Gas Injection into Geological Formations and Related Topics

Scrivener Publishing
100 Cummings Center, Suite 541J
Beverly, MA 01915-6106

Publishers at Scrivener
Martin Scrivener (martin@scrivenerpublishing.com)
Phillip Carmical (pcarmical@scrivenerpublishing.com)

Gas Injection into Geological Formations and Related Topics

Edited by

Ying (Alice) Wu, John J. Carroll, Mingqiang Hao and Weiyao Zhu

WILEY

This edition first published 2020 by John Wiley & Sons, Inc., 111 River Street, Hoboken, NJ 07030, USA and Scrivener Publishing LLC, 100 Cummings Center, Suite 541J, Beverly, MA 01915, USA

For more information about Scrivener publications please visit www.scrivenerpublishing.com.

Wiley Global Headquarters
111 River Street, Hoboken, NJ 07030, USA

For details of our global editorial offices, customer services, and more information about Wiley products visit us at www.wiley.com.

Library of Congress Cataloging-in-Publication Data

ISBN 9781119592068

Cover image: Jim J. Caroll
Cover design by Kris Hackerott

Set in size of 11pt and Minion Pro by Manila Typesetting Company, Makati, Philippines

Printed in the USA

10 9 8 7 6 5 4 3 2 1

Contents

Preface

The eighth edition of the International Acid Gas Injection Symposium (AGIS VIII) was held at the end of September 2019 in Calgary, Canada. Presentations and posters covered various topics related to (1) acid gas injection [AGI], (2) carbon capture and storage [CCS], and (3) the use of CO_2 for enhanced oil recovery [EOR]. This volume contains select papers presented at the Symposium. These included primary research such as the solubility of CO_2 and the ionic speciation of CO_2 in amine solutions. It also includes safety considerations such as pipeline leak detection and the dealing with a blowout from an acid gas well. And through to applications, including field projects. It is worth noting that Chap 1 is the paper that was presented by Mitch Stashick and was awarded the Best Student Paper at the Symposium.

YW, JJC, MH & WZ
October 2019

1

Modifying Effects of Hydrogen Sulfide When Contemplating Subsurface Injection of Sulfur

Mitchell J. Stashick, Gabriel O. Sofekun and Robert A. Marriott*

Department of Chemistry, University of Calgary, Calgary, Alberta, Canada

Abstract

Transportation and handling of molten sulfur is inevitably challenging due to the anomalous rheological behaviour of sulfur with changing temperature. After melting at 115 °C, sulfur's viscosity remains close to 10 cP. The onset of the λ-transition region is observed at $T \approx 160$ °C. The viscosity drastically rises in this region, increasing to a maximum of about 93000 cP at 187 °C. This anomaly is due to the cleavage of sulfur rings and production of reactive diradical sulfur species that concatenate to create sulfur polymers. The entanglement of these sulfur chains causes the dramatic rise in viscosity. Within this work, new data is reported that examines the modifying effects of hydrogen sulfide (H_2S) within liquid sulfur. This may be used when considering the potential injection of liquid sulfur into depleted reservoirs for safe long-term storage. H_2S, when present in liquid sulfur, can either physically dissolve or chemically react to generate polysulfane. The chemical reaction causes significant changes in the sulfur chain distribution and consequently changes the viscosity curve of liquid sulfur as a function of temperature. This study reports viscosity measurements performed from $120 < T < 280$ °C with concentrations of H_2S in sulfur ranging from 0 ppmw to 284 ppmw.

Keywords: Rheology, viscosity, λ-transition, sulfur, polymers, hydrogen sulfide

**Corresponding author*: rob.marriott@ucalgary.ca

Ying Wu, John J. Carroll, Mingqiang Hao and Weiyao Zhu (eds.) Gas Injection into Geological Formations and Related Topics, (1–8)

1.1 Introduction

Sulfur requires transportation and handling on an industrial scale. After acknowledging that there were approximately eighty million metric tons of elemental sulfur produced globally in 2018, this becomes abundantly clear [1]. Sulfur recovery from oil refineries and sour gas treatment plants (sour gas is natural gas with hydrogen sulfide (H_2S) > 5.7 $mg{\cdot}m^{-3}$) has continued to increase, bringing about more deliberation on the utilization and/or storage of sulfur product. When the value of sulfur is not high enough to economically justify transportation and sale of the material, it is often common to block pour for long-term storage. Block pouring sulfur is a relatively inexpensive method where sulfur is solidified within retaining walls on large plots of land. However, there are some disadvantages to this technique. The land on which the blocks are poured must be leased or owned and this can cause some financial strain. Also, bacteria classified as Thiobacilli are known to metabolize sulfur by oxidizing the material to sulfate $\left(SO_4^{2-}\right)$ and in doing so produce sulfuric acid (H_2SO_4). This along with rain and further weathering results in the need for water treatment of the acid runoff, incurring additional cost. Lastly, large amounts of weathering sustained by sulfur blocks can yield high content of materials such as dirt, sand and moisture. This can create issues of purity if the price of sulfur rises and it makes economic sense to sell the product again [2]. Alternatively, producers have chosen to inject H_2S (acid gas injection) to mitigate stranded sulfur. With acid gas injection, one needs to consider the energy required for compression of gas, storage under pressure and the loss of energy due to eliminating the Claus plant.

In future operations, an alternative to block pouring or acid gas injection could include the potential injection of liquid elemental sulfur into depleted reservoirs for safe long-term storage. This method would diminish some of the issues experienced with block pouring, but would likely sustain other costs needed for infrastructure and operation. Also, other fundamental understanding is currently lacking in order to pursue this approach. The conditions under which an injection such as this would take place must be known and understood in how they will impact the rheological behavior of sulfur.

One of several conditions to consider is that all sulfur produced in Sulfur Recovery Units at refineries and gas processing facilities will contain some residual H_2S. This is because sulfur is recovered before complete conversion from H_2S. Generally, recovered sulfur from a plant process can have up to 380 ppmw of dissolved H_2S depending on the facility set up [3].

Another condition to consider is the temperature of the depleted underground reservoir. For this, the range of interest for potential injection was found to be around $120 < T < 280$ °C. It should be recognized that this temperature range includes the λ-transition region of liquid sulfur. Also, high shear must be considered as this will be encountered in sulfur pumps and the near-wellbore region. Studying sulfur's shear flow with and without H_2S over the specified temperature range could therefore greatly improve the fundamental understanding needed for injection of molten sulfur.

The viscosity temperature dependence of sulfur within the λ-transition region can be explained by a scission-recombination equilibrium for polymers and the term reptation. In this occurrence, reptation is defined as the thermal motion of entangled macromolecular sulfur chains. At $T > 160$ °C, cleavage of sulfur S_8 rings results in the generation of reactive diradical sulfur species that combine to create sulfur polymers [4]. The average polymer chain lengths increases as a function of temperature leading to more entanglement and higher viscosity values. At 187°C, the maximum polymer chain length is reached, along with the maximum viscosity. Beyond this temperature, the viscosity decreases due to the thermal scission of polymer chains; however, if H_2S is present, the viscosity profile of sulfur changes depending on concentration. H_2S is known to chemically react with diradical sulfur species during the λ-transition to produce polysulfane, as shown in Eq. (1-1). This reaction terminates the polymerization, which reduces the average sulfur polymer chain length. Therefore, a reduction in the viscosity of the liquid is observed [5-7].

$$H_2S + \cdot S \cdot_x \rightleftharpoons H_2S_{x+1} \tag{1.1}$$

1.2 Experimental

1.2.1 Materials

Oxygen-free, nitrogen gas (N_2; 99.998% as per certificate of analysis) was purchased from Praxair Technology, Inc. Hydrogen sulfide gas (H_2S; 99.6% containing N_2, Ar and trace CO_2 as per certificate of analysis and in-house gas chromatography analysis) was purchased from Praxair Technology, Inc.

Sulfur used for this study was air prilled and supplied by Keyera Energy from their Strachan, Alberta, gas plant in 2017. Analyses of the air prills were performed and reported in Table 1.1. Moisture (volatiles) content,

Table 1.1 Analytical results of the Keyera air prilled sulfur.

Moisture Content (wt. %)	Purity (wt. %)	Ash Content (ppmw)	Total Carbon Content (ppmw)	Total H_2S Content (ppmw)
0.14	99.995	8	34	< 0.2

total nonpolymer sulfur content/overall purity, and ash content were determined by methods used at ASRL, reported by Sofekun *et al.* [4]. Total carbon content and H_2S content were also performed on the sulfur prills. Additionally, it was necessary to perform analyses of H_2S content before and after rheometric measurements. Total carbon content was measured using an analysis method established by Dowling *et al.* [8]. H_2S content was measured using an analysis method detailed by Sofekun *et al.*, Marriott *et al.*, and Tuoro and Wiewioroski [3, 4, 9, 10]. Large sulfur samples that had been equilibrated with H_2S were partially used to record infrared spectra (six total measurements) prior to each set of rheometric measurements. All samples were analyzed using a Nicolet 380 FT-IR (Thermo Electron Corp.) spectrometer.

1.2.2 Rheometer

The experimental system was composed of an Anton-Paar MCR 302 rheometer with a custom built gravity-fed charging rig, a high-pressure N_2 cylinder and a thermostated Fourier Transform Infrared (FT-IR) cell used from previous studies [4, 9, 10]. A head pressure tee for inducing H_2S partial pressures along with a purging setup connected to KOH traps for removal of H_2S before venting was added. This permitted the safe introduction of differing concentrations of H_2S in liquid sulfur samples. All valves and tubing used for both the pressure tee and gravity-fed charging rig were made of 316L stainless steel. The system was housed inside a negative-pressure bay equipped with automatic toxic gas detectors.

Geometry and measuring limitations for the Anton-Paar MCR 302 were detailed by Sofekun *et al.* [4]. Air checks and motor adjustments were performed at a rotational speed of 0.3 min^{-1} at set time intervals as recommended by the instrument manufacturer. This confirmed on a regular basis that the rheometer was in good working condition.

The procurement of viscosity data sets corresponding to each differing H_2S concentration in sulfur were carried out using the following experimental procedure: Two hundred grams of high purity sulfur prills were

placed in an oven overnight at 135 °C. The experimental system was prepared for rheometric measurements of liquid elemental sulfur by inputting set points for the temperature controllers on the gravity-fed charging rig and rheometer cylinder jacket of 135 °C. After being held at the set temperature for 2 hrs, the pressure tee was removed from the top of the reservoir. The reservoir was then filled with 80 mL of liquid elemental sulfur. Following this, the pressure tee was reconnected to the top of the reservoir, purged and pressurized with pure H_2S or a H_2S/N_2 mixture. The gases in the headspace of the reservoir were then allowed to equilibrate with the sulfur for at least 24 hrs. Following equilibration, the H_2S dissolved in sulfur was extremely stable. This allowed the pressure tee to be purged with N_2 and subsequently, the safe loading of the rheometer cell.

To load the rheometer cell, a plug on the sample cell was removed and the pressure tee was disconnected. This allowed for liquid sulfur to be transported through the charging rig by gravity after opening a valve on the sulfur reservoir. This valve was metered until sulfur filled the rheometer cell. Analyses by FT-IR to determine the concentration of dissolved H_2S in sulfur were performed by sampling twice through a drain valve below the rheometer before filling the rheometer cell once more with a final sample used for viscosity measurements. The plug on the sample cell was then retightened, all valves were confirmed closed, and the sulfur reservoir was capped.

For measurement and recording of data, the desired T and shear rate, γ, were programmed using the Rheoplus software interface. Heating of the sample was done at 5 °C intervals from 120 to 280 °C. The measurements at each temperature were made after specified equilibration times. Average Newtonian viscosities were obtained at each temperature using a data processing code written in Microsoft Visual Basic for Applications in Excel. The code yields uncertainty in each viscosity value at a 95% confidence interval.

1.3 Results and Discussion

Four charges of liquid sulfur without H_2S were measured to compare the maximum viscosity value, η_{max}, with the previous study [4] and values reported by Bacon and Fanelli, Doi, and Ruiz-Garcia *et al.* [11-13]. At 187 °C, the values were in agreement with past studies, $\eta_{max} \approx 93000$ cP. When comparing the η_{max} of Sofekun *et al.* to the average viscosity value of the four charges in this study, there was a relative change of 2.10%. This indicated that no hydrocarbon impurities were present in the rheometer cell

during this study [4]. Average Newtonian viscosities were then measured at every 5 °C across the λ-transition of sulfur containing differing concentrations of H_2S. The average Newtonian viscosity data for each specified H_2S concentration in this study, was plotted as a function of temperature (Figure 1.1). The data plotted for sulfur with approximately no H_2S present was reported by Sofekun *et al.* [4].

Some general trends were gathered from Figure 1.1. One clear deduction was that as H_2S concentration increases, the viscosity of liquid sulfur decreases. Another definitive trend was that the viscosity curve or peak maximum shifted to higher temperatures with larger concentrations of dissolved H_2S. Although measured viscosity values by Fanelli and Rubero were much lower due to high concentrations of H_2S, the trends reported were in accordance with trends found in these studies [5, 7]. This study reports reliable data with more industrially-relevant concentrations of H_2S in sulfur. The concentrations from this study would be more commonly found in recovered sulfur from natural gas processing plants or oil refineries and therefore would be more relevant in consideration of storage by subsurface injection.

To speculate on the trends or changes in viscosity observed upon the addition of H_2S in sulfur, Eq. (1-1) must once again be contemplated. The

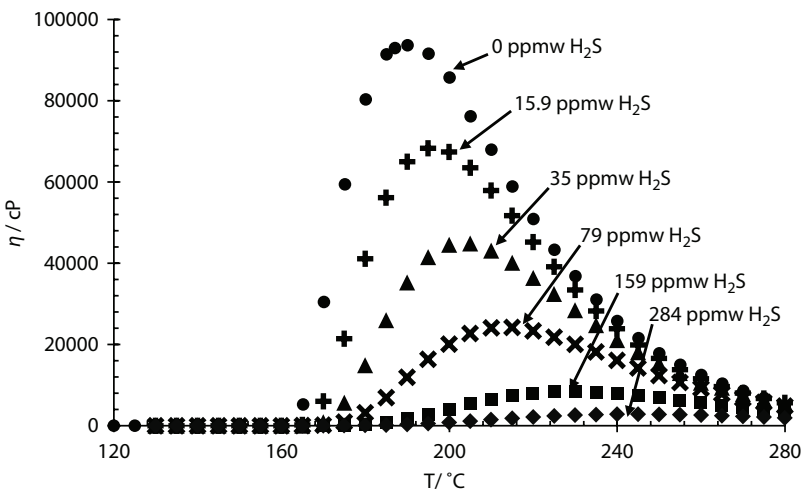

Figure 1.1 Average Newtonian viscosity versus temperature for liquid sulfur containing different concentrations of H_2S. ●, heating run of 0 ppmw H_2S in sulfur; +, heating run of 15.9 ppmw H_2S in sulfur; ▲, heating run of 35 ppmw H_2S in sulfur; ×, heating run of 79 ppmw H_2S in sulfur; ▪, heating run of 159 ppmw H_2S in sulfur; ◆, heating run of 284 ppmw H_2S in sulfur [4].

H_2S present in sulfur acts as another reaction pathway where polymerization is terminated to form a shorter polysulfane chain. Normally, without H_2S, the sulfur chain length distribution at each temperature would be determined by the chemical equilibrium established by scission and recombination of polymers. However, due to the new reaction pathway, the kinetic rate of termination interferes with the rate of recombination and/or polymerization resulting in a shift of the viscosity-temperature profile. Besides the profile shape change, there was a reduction in viscosity. As mentioned before, this can be attributed to shorter polymer chain lengths. Shorter polymers results in less entanglement which influences the reptative behavior. With fewer entangled macromolecular chains, there are less intermolecular interactions to break allowing for an ease of thermal motion. Chain relaxation is faster and fluid deformation requires less force.

1.4 Conclusions

The rheometric properties of liquid sulfur with varying concentrations of dissolved H_2S were measured. This was accomplished by using an Anton-Paar MCR 302 rheometer with a custom built gravity-fed charging rig and a head pressure tee for inducing H_2S partial pressures. Sulfur with H_2S concentrations ranging from 0 ppmw to 284 ppmw were measured at 5 °C intervals over temperatures of 120 °C to 280 °C. This permitted investigation of the impact of H_2S on the λ-transition region of sulfur. Introduction of H_2S led to overall reductions in viscosity, as well as a peak shift to higher temperatures for the entire viscosity profile of sulfur. This was presumed to be due to H_2S terminating the polymerization of sulfur, which gave shorter polymer chain lengths and altered each temperature's chemical equilibrium.

The rheometric data presented within this study for liquid sulfur with industrially relevant concentrations of H_2S should help in understanding the feasibility of operations contemplating this materials subsurface injection into depleted reservoirs. Currently, more efforts are being made to produce a semi-empirical correlation model based on the reptation model of Cates to estimate the properties discussed in this study [4, 14]. A semi-empirical model could aid in the simulation of subsurface injection or assist operators in the use of sulfur pumps. Future research could also include investigating the impact of other impurities on liquid sulfur's rheometric properties. If experimental data were available, these properties could be estimated using a similar model.

References

1. Sulfur Statistics and Information. National Minerals Information Center. USGS, https://www.usgs.gov/centers/nmic/sulfur-statistics-and-information (accessed May 6, 2019).
2. Davis, P., Marriott, R.A., Fitzpatrick, E., Wan, H., Bernard, F., Clark, P.D., Fossil Fuel Development Requires Long-Term Sulfur Strategies. *Oil Gas J.*, 106, 29, 45, 2008.
3. Marriott, R.A., Fitzpatrick, E., Lesage, K.L., The solubility of H_2S in liquid sulfur. *Fluid Phase Equilib.*, 269, 1-2, 69–72, 2008.
4. Sofekun, G.O., Evoy, E., Lesage, K.L., Chou, N., Marriott, R.A., The rheology of liquid elemental sulfur across the λ-transition. *J. Rheol.*, 62, 2, 469–476, 2018.
5. Fanelli, R., Modifying the viscosity of sulfur. *Ind. Eng. Chem.*, 38, 1, 39–43, 1946.
6. Farr, C.C. and Macleod, D.B., On the viscosity of sulfur. *Proc. R. Soc. Lond. A*, 97, 682, 80–98, 1920.
7. Rubero, P.A., Effect of Hydrogen Sulfide on the Viscosity of Sulfur. *J. Chem. Eng. Data*, 9, 481–484, 1964.
8. Dowling, N.I., Bernard, F., Leung, J., Lesage, K.L., Analytical procedure for the determination of trace carbon impurity in elemental sulfur. *J. Sulfur Chem.*, 29, 2, 129–137, 2008.
9. Wiewiorowski, T.K., Matson, R.F., Hodges, C.T., Molten Sulfur as a Solvent in Infrared Spectrometry. *Anal. Chem.*, 37, 1080–1080, 1965.
10. Wiewiorowski, T.K. and Touro, F.J., The Sulfur – Hydrogen Sulfide System. *J. Phys. Chem.*, 70, 1, 234–238, 1966.
11. Bacon, R.F. and Fanelli, R., The Viscosity of Sulfur. *J. Am. Chem. Soc.*, 65, 639–648, 1943.
12. Doi, T., Physico-chemical properties of sulfur: IV. Critical polymerization temperatures and polymerization equilibrium constants of sulfur. *Rev. Phys. Chem. Jpn.*, 35, 1, 18–24, 1965.
13. Ruiz-Garcia, J., Anderson, E.M., Greer, S.C., Shear viscosity of liquid sulfur near the polymerization temperature. *J. Phys. Chem.*, 93, 19, 6980–6983, 1989.
14. Cates, M.E., Theory of the viscosity of polymeric liquid sulfur. *Europhys. Lett. (EPL)*, 4, 4, 497–502, 1987.

2

Experimental Determination of CO_2 Solubility in Brines At High Temperatures and High Pressures and Induced Corrosion of Materials in Geothermal Equipment

Marie Poulain[1,2], Jean-Charles Dupin[1], Hervé Martinez[1] and Pierre Cézac[2]

[1]Univ Pau & Pays Adour / E2S UPPA, IPREM – CNRS, UMR, Pau, France
[2]Univ Pau & Pays Adour / E2S UPPA, Laboratoire de Thermique, Energétique et Procédés – IPRA, Pau, France

Abstract
In this study, a high pressure and high temperature apparatus has been used to reproduce the subsoil conditions. CO_2 solubility data have been determined by conductimetric titration in Na-Ca-(K)-Cl brines at 323, 373 and 423 K up to 20 MPa. Obtained results have shown good agreements with scarce ones available in the literature. Then, a new device has been developed to conduct corrosion tests on a carbon steel DC01 in geothermal environments. Surface analyses, using X-Ray Photoelectron Spectroscopy (XPS) and Scanning Electron Microscopy (SEM), allowed the identification of corrosion product on the steel surface at the end of the corrosion test. This deposit consists of a mixture of calcium carbonate $CaCO_3$ and iron carbonate $FeCO_3$.

Keywords: CO_2, brine, solubility, corrosion, experimental

2.1 Introduction

Global warming has been observed for many years and has brought about important climate change. A major cause of global warming is the steady increase of greenhouse gases emissions and particularly CO_2. One of the objectives of the Paris agreement, whose purpose is to fight against global

Ying Wu, John J. Carroll, Mingqiang Hao and Weiyao Zhu (eds.) Gas Injection into Geological Formations and Related Topics, (9–20) © 2020 Scrivener Publishing LLC

warming, is to keep the increase of the general temperature below 2°C by 2100 [1].

To lessen the emissions of this greenhouse gas and thus reduce global warming, the capture, recovery and storage of carbon dioxide is an increasingly studied option. Carbon dioxide can be stored in deep saline formations which have a large capacity. Nevertheless, the amount of carbon dioxide dissolved in the water depends on the pressure, temperature and composition of the water.

Another studied option to reduce global warming is to develop renewable energy. The use of geothermal energy in the world is still in development, both for the production of electricity and heat. In 2015, the total energy produced by geothermal power throughout the world was around 74,000 GWh [2]. The deep geothermal energy to produce electricity or heat for large complexes is under development. In France, more precisely in the Upper Rhine Graben region, several projects have been carried out, in Soultz-sous-Forêts, for instance. The aim is to recover a hot fluid from deep subsoil. This fluid passes through a heat exchanger where the energy is released to a secondary fluid. The cooled geothermal fluid is then reinjected into a second well [3]. It is very important to have a good knowledge of the fluid behaviour to better design equipment and reduce the cost of the installations. Another crucial point is to prevent installations from corrosion. Material choice remains difficult due to the fluid composition, the operating temperatures and pressures and the presence of acid gas dissolved.

A good knowledge of the liquid-vapour equilibrium, particularly gas solubility, for these two different applications is essential. Models allowing the prediction of carbon dioxide solubility in brines have been previously developed [4–8]. However, they are fitted from experimental data. Experimental measurements of carbon dioxide in brines are therefore needed. The determination of gas solubility at high temperatures and pressures is quite complex. Although many data are available in the literature for the CO_2 solubility in pure water [9–13] or single salt solutions [10–18], data for carbon dioxide solubility in mixed-salt solutions remain scarce [7, 19, 20]. The aim of the first part of this study was to use a simple method previously developed [13, 15, 18] to determine the carbon dioxide solubility in brines at high temperatures and high pressures. The results of this study are available in a previous paper [21] and are summarized here.

The second part of this work consists of studying the material corrosion in these particular environments (high temperature, high pressure, brines). The goal of this study is to better understand the corrosion phenomena induced by geothermal fluid on a carbon steel. Previous studies conducted at the Soultz-sous-Forêts geothermal power plant have allowed

a first step towards the understanding of corrosion processes and mechanisms [22–24]. In this study, a new device has been developed to conduct investigations on materials.

Usually, weight loss measurements and electrochemical analysis are used to determine the corrosion rate. In this work, surface analysis is carried out to identify corrosion products and their composition. This method allows a better comprehension of the corrosion mechanism and process. This leads to the determination of the most appropriate material from a technico-economic point of view: resistance to corrosive medium vs. cost of material.

2.2 Experimental Section

2.2.1 Chemicals

Carbon dioxide is provided by Air Liquide with a certified purity of 99.7%. Water is purified by a Smart2Pure system with a resistivity of 18.2 MΩ.cm. Sodium chloride (NaCl, 99%), calcium chloride ($CaCl_2$, 96%) and potassium chloride (KCl, 99%) salts are provided by Acros Organics. Sodium hydroxide is prepared from a 46/51 %wt solution of NaOH provided by ThermoFisher. Hydrochloric acid (0.1 mol/L ± 0.2%) for the titration is provided by VWR.

2.2.2 Test Solutions

The composition of the brines was based on the Soultz-sous-Forêts (Upper Rhine Graben) water. The fluid of Soultz is classified as Na-Ca-Cl type with a TDS (Total Dissolved Solids) around 90 $g.L^{-1}$ [25]. The first synthetic brine consists in a mixture of NaCl and $CaCl_2$ salts, respectively at concentration of 1.2 $mol.kg^{-1}$ and 0.2 $mol.kg^{-1}$. The second brine is made of 1.2 $mol.kg^{-1}$ of NaCl, 0.2 $mol.kg^{-1}$ of $CaCl_2$ and 0.1 $mol.kg^{-1}$ of KCl. The conditions of experiments are given in the Table 2.1. Solubility measurements have been carried out on a wide range of temperature and pressure to characterize the fluid behaviour during its rising. Corrosion tests have been realized on surface condition at low temperature and low pressure.

2.2.3 Metals

In this study, a carbon steel DC01 was tested in geothermal brine environment. Chemical composition of the metal is given in Table 2.2.

Table 2.1 Conditions of experiments for solubility measurements and corrosion tests.

Solubility measurements			
CO_2-NaCl-$CaCl_2$	323 K	373 K	423 K
	1-20 MPa	1-20 MPa	1-20 MPa
CO_2-NaCl-$CaCl_2$-KCl	323 K	373 K	423 K
	1-20 MPa	1-20 MPa	1-20 MPa
Corrosion tests			
CO_2-NaCl-$CaCl_2$	323 K		
	2 MPa		

Table 2.2 Chemical composition (in %wt) of the carbon steel DC01 obtained by Spark Atomic Emission Spectroscopy.

Fe	**C**	**Si**	**Mn**	**P**	**S**	**Cr**
99.6	0.039	0.022	0.210	0.0078	0.0028	0.0127
Mo	**Ni**	**Al**	**Co**	**Cu**	**Nb**	**Ti**
0.0017	0.0035	0.0371	0.0032	0.0110	0.0033	0.0020

The dimensions of the specimens were 1.9 cm x 1.9 cm x 2 mm. The samples were prepared according the ASTM G1-03 standard [26]. They were polished with abrasive paper (500, 800, 1000 grit), degreased in acetone, washed with pure water, dried in a desiccator and weighed before exposure.

2.2.4 CO_2 Solubility Measurements

A high pressure and high temperature apparatus has been used to reproduce the subsoil conditions and obtain the thermodynamic equilibrium. The experimental device (provided by Top Industrie) used for carbon dioxide solubility determination in brine at high pressure and high temperature has been previously described in detail in several studies [13, 15, 18]. It is based on a cell of 1000 cm^3 made in Hastelloy C-276. This device can be used from 293 to 423 K and pressure up to 20 MPa. A thermostated volumetric pump (PMHP 200-200) is used to load the carbon dioxide in the

equilibrium cell and allows the pressure compensation during the sampling phase.

After the establishment of the vacuum in the autoclave and the lines, the synthetic brine is introduced into the cell. Then, the temperature is fixed and the carbon dioxide is added. A heavy stirring (800 rpm) is applied to reach the equilibrium faster. Once, the thermodynamic equilibrium is reached, a sample of liquid phase is withdrawn. The sampling process is based on the trapping method: the sample is taken in a syringe containing a solution of NaOH. The carbon dioxide dissolved reacts with hydroxide ions to form carbonate ions CO_3^2 (Eqn. 2.1). In presence of calcium ions in the aqueous solution, a precipitate of calcium carbonate appears (Eqn. 2.2). Conductimetric titration coupled with pH-measurements was realized to determine carbon dioxide solubility in brine. A 0.1 mol.L^{-1} of hydrochloric acid solution is used as a titrant. This method has been used in previous studies [15, 18].

$$CO_2 + 2OH^- \leftrightarrow CO_3^{2-} + H_2O \tag{2.1}$$

$$CO_3^{2-} + Ca^{2+} \leftrightarrow CaCO_{3(s)} \tag{2.2}$$

2.2.5 Material Corrosion Study

In this study, a pilot (provided by Armines), presented in Figure 2.1, has been developed to conduct investigations on material corrosion. Four autoclaves made of titanium are divided two by two in ovens. An autoclave can operate until 473 K and 20 MPa. Temperature probes and pressure sensor enable the monitoring of experimental conditions. An inert insert is placed in the cell to avoid the contact between the titanium and the fluid or the exposed coupons. Test specimens are placed in a PTFE support.

The operating procedure for corrosion study is similar to the procedure for solubility measurement. It consists of making the vacuum, introducing the brine, fixing the temperature and adding the carbon dioxide. A stirring of 200 rpm is applied. The equilibrium is kept constant during the time of the experiment. In this study, the material has been exposed for 500 hours. At the end of the experiment, the specimen is removed from the reactor, rinsed with water, dried in a desiccator and finally weighed.

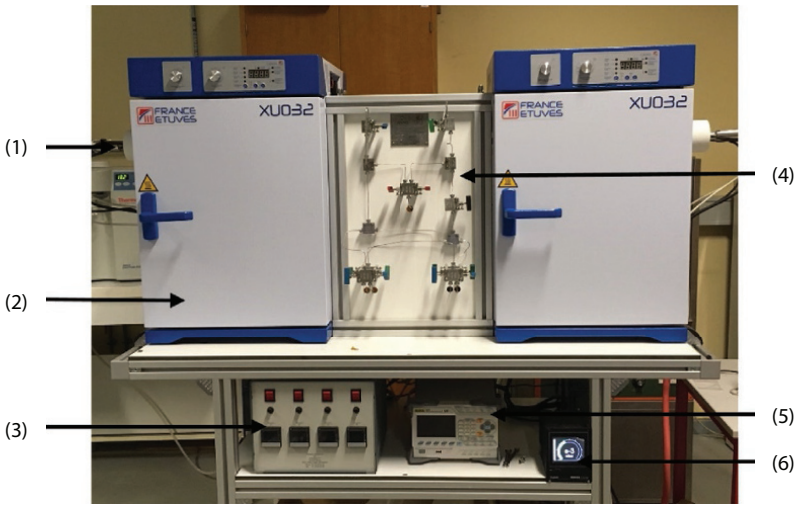

Figure 2.1 Photograph of the corrosion device. (1) Pressure sensor Keller PAA 35 XHTC; (2) Oven 'France Etuves'; (3) Temperature controller Fuji model PXF4; (4) Fluids charging circuit; (5) RIGOL Data acquisition; (6) Vacuum pump controller.

The material surface was analysed by X-Ray Photoelectron Spectroscopy (XPS) and Scanning Electron Microscopy (SEM).

XPS analyses were conducted with a Thermo K-alpha spectrometer (ThermoFisher Scientific) using monochromatized Al-Kα radiation (1485,6 eV) and operating under a residual pressure of 10^{-9} mbar. The radiation is microfocused on the sample (400µm diameter microspot). A charge compensation system using low energy electrons has been used. Survey spectra were recorded from 0 to 1350 eV with a pass energy (PE) of 200 eV and core ionization peaks were recorded at PE of 40 eV. CasaXPS software © was used to fit spectra. Peaks were fitting with a non-linear Shirley type background. Mathematical components were optimized by a weighted least-squares fitting method using 70% Gaussian and 30% Lorentzian GL(30) line shapes. For metallic core line Fe(0), assymmetry was defined in the form LA(1.2,4.8,3). The other representative components of iron were fitting with an asymetry A(0.15, 0.65, 0)GL(0).

SEM analyses were performed with a JEOL JEAMP 9500F Auger spectrometer (JEAOL Ltd, Tokyo, Japan) working under UHV conditions ($P < 2.10^{-7}$ Pa). SEM images were recorded at several magnifications using the following probe conditions : 15 kV acceleration woltage and a low current of 1 nA.

2.3 Results and Discussion

2.3.1 CO_2 Solubility Measurements

CO_2 solubility has been measured in two synthetic brines. Both CO_2-H_2O-NaCl-$CaCl_2$ and CO_2-H_2O-NaCl-$CaCl_2$-KCl systems have been studied at three temperatures: 323, 373 and 423 K and up to 20 MPa. 48 experimental solubility data have been obtained and are presented in a previous paper [21]. Obtained results are summarized in the Figure 2.2.

The results have been compared to the data obtained by Li *et al.* [19] and Zhao *et al.* [7]. Their data have been acquired in brines whose composition were close to our study. Observed trends show a good agreement. For instance, our values are higher than those of Li *et al.* [19]. This could be explained because their study has been carried out at 332 K in a brine containing other salts. In their work, Zhao *et al.* [7] have also measured carbon dioxide solubility in a synthetic solution mostly composed of Na-Ca-Cl species at 323K. A deviation of 3.5% is observed with our values. The results are in good agreement.

In this study, two brines with and without KCl have been compared. The results have shown that at this salt concentration (0.1 $mol.kg^{-1}$), the influence of the potassium chloride salt on the carbon dioxide solubility can be neglected. In this context, the values obtained in Na-Ca-Cl solution give a reasonable estimation of carbon dioxide solubility in Upper Rhine Graben water.

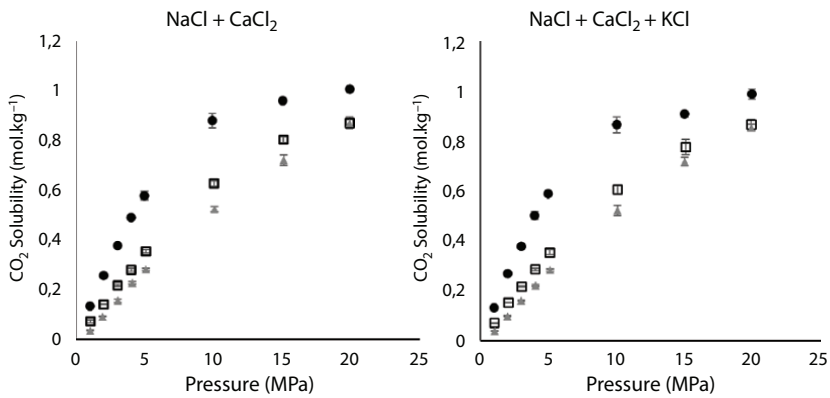

Figure 2.2 Experimental CO_2 solubility measurements in the two synthetic brines at 323 K (●), 373 K (□) and 423 K (▲) up to 20 MPa.

Experimental results have been compared with two different models (PhreeSCALE and PSUCO2). This comparison between measured and calculated values show a good agreement with a maximum deviation of 10%.

2.3.2 Material Corrosion Study

Carbon steel DC01 have been exposed to Na-Ca-Cl synthetic brine saturated with 2 MPa of carbon dioxide for 500 hours.

Surface analyses before and after coupon exposure have been carried out to highlight surface modification induced by geothermal environment. The evolution of core ionisation peaks for the carbon, the oxygen, the iron and the calcium are shown in Figure 2.3. Table 2.3 listed the binding energies of the components and the corresponding chemical environment identified by XPS.

The C 1s spectrum displays four components before exposure: the main one at 285 eV corresponds to adventitious hydrocarbon, the ones at 286.5 and 288.5 eV are respectively attributed to **C**-O and O-**C**=O which are characteristics of adsorbed contaminants species. The last peak is detected at 282.9 eV corresponding to carbide environment due to the inclusion of SiC at the top of the metal during the surface preparation. After the immersion of the specimen in the geothermal environment during 500 hours, the C 1s spectrum displays modifications compared to before exposure, meaning there is chemical evolution of the metal surface. First, the

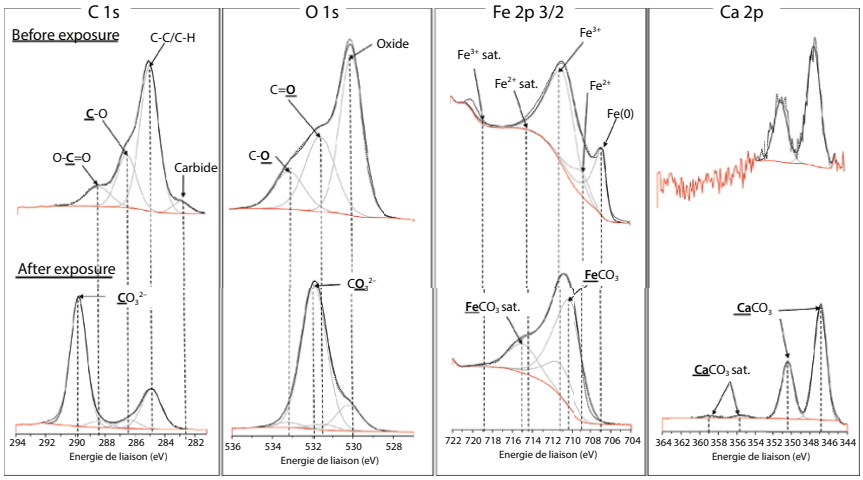

Figure 2.3 C1s, O1s, Fe 2p3/2 and Ca 2p XPS spectra of the DC01 surface before and after exposure to geothermal environments.

Table 2.3 Binding energies and assignment of the different chemical environments identified by XPS at the DC01 surface before and after exposure to geothermal environments.

	Before exposure		After Exposure	
Orbital	**Binding energy (eV)**	**Assignment**	**Binding energy (eV)**	**Assignment**
C 1s	282.9	Carbide	285	**C**-C/**C**-H
	285	**C**-C/**C**-H	286.5	**C**-O
	286.5	**C**-O	288.5	**C**=O
	288.5	**C**=O	289.9	**C**O_3^{2-}
O 1s	530	Oxide	530	Oxide
	531.5	C=**O**	531.2	C=**O**
	533	C-**O**	531.9	C**O**$_3^{2-}$
			533	C-**O**
Fe 2p3/2	706.7	Fe(0)	710.3	**Fe**CO_3
	709	Fe^{2+}	711.2	Fe^{3+}
	711.2	Fe^{3+}	715	**Fe**CO_3 sat.
	714.5	Fe^{2+} sat.	719.2	Fe^{3+} sat.
	719.2	Fe^{3+} sat.		
Ca 2p	347.3	Ca	347.5	**Ca**CO_3
	350.8	Ca	351	**Ca**CO_3
			355.4	**Ca**CO_3 sat.
			359	**Ca**CO_3 sat.

peak assigned to carbide is no longer detected. Moreover, a peak appears at 289.9 eV corresponding to carbonate environment.

The O 1s spectrum displays three components before exposure located at 530, 531.5 and 533 eV corresponding respectively to iron oxide, C-**O** and C=**O** environments. These three components are also visible on the spectrum of the surface analysis after exposure. A supplementary peak is

located at 531.9eV assigned to carbonate environment in agreement with C 1s peak.

Before exposure, the Fe 2p3/2 spectrum shows several components. Among them, the first situated at 706.7 eV represents the metallic iron Fe(0). This component disappears on the spectrum after exposure. It is due to the corrosion process with the oxidation of iron metal following Eqn. 2.3.

$$Fe \rightarrow Fe^{2+} + 2e^{-} \tag{2.3}$$

The other main components are detected at 709 and 711.2 eV corresponding to iron oxide with Fe^{2+} and Fe^{3+}. The satellite peaks of these two components are located at 714.5 and 719.2 eV. After the corrosion test, the environment associated to Fe^{2+} have disappeared whereas the peaks assigned to Fe^{3+} are always detected. Nevertheless, the results show the presence of two new peaks at 710.3 and 715 eV, which can be attributed to the main peak and satellite peak of iron carbonate $FeCO_3$. Passive film of iron carbonate on the surface of mild steels has already been shown by Heuer and Stubbins [27]. This corrosion product is formed following Eqn. 2.4.

$$Fe^{2+} + CO_3^{2-} \rightarrow FeCO_{3(s)} \tag{2.4}$$

The analysis of the calcium Ca 2p peak reveals that after exposure, the binding energies of the main and satellite components are characteristic of the presence of calcium carbonate $CaCO_3$. This result shows that the corrosion product on the metal surface is composed of a mixture of iron and calcium carbonate.

SEM images have been realized to characterize the surface morphology of the sample (Figure 2.4). SEM images display the presence of rhomboedral and hexagonal crystals at the surface of the carbon steel. $CaCO_3$ has a

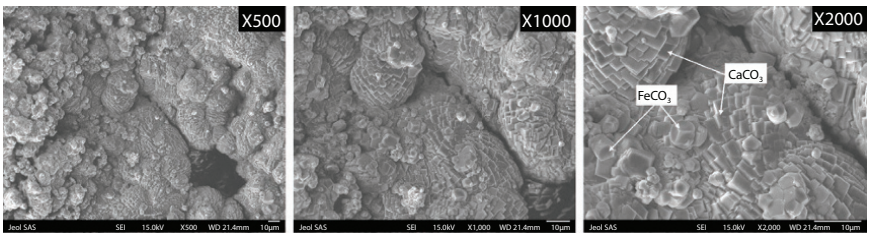

Figure 2.4 SEM images of $CaCO_3$ and $FeCO_3$ crystals on the surface of corroded DC01 carbon steel.

rhomboedral crystal structure and $FeCO_3$ a hexagonal one. The information given by the microscopic analysis technic confirm that the corrosion product is constituted by a mixture of calcium and iron carbonate.

2.4 Conclusion

Carbon dioxide solubility data have been acquired in two brines containing Na-Ca-(K)-Cl salts at 323, 373 and 423 K up to 20 MPa. In this range of temperature and pressure, the results show that an increase in temperature implies a decrease of CO_2 solubility; an increase in pressure improves the carbon dioxide solubility and the increase of salinity involves a diminution of the gas solubility. Nevertheless, in this study the concentration of KCl does not involve a significant modification of the CO_2 solubility in brine. A good estimation of the carbon dioxide solubility in the Upper Rhine Graben can be obtained in Na-Ca-Cl solution.

A new corrosion device has been used in this study to investigate the corrosion of a carbon steel DC01 in geothermal environments. The surface of the sample has been analysed by XPS and SEM to identify the corrosion product. The results have shown that at the end of the experiment, the surface of the carbon steel was covered by a mixture of calcium and iron carbonate deposit. Further investigations will be done in different conditions and on other steels to better understand corrosion phenomena and chose the appropriate material to resist to geothermal environments.

2.5 Acknowledgments

This work was supported by ANR grant SIGARRR, TOTAL SA, GIS GEODENERGIES (Project Carphymcheau) and Institut Carnot ISIFoR.

References

1. Rogelj, J., den Elzen, M., Höhne, N., Fransen, T., Fekete, H., Winkler, H. *et al.*, *Nature*, 534, 631, 2016.
2. Bertani, R., In: *Proceedings World Geothermal Congress*, Melbourne (Australia), p. 19, 2015.
3. Agemar, T., Weber, J., Schulz, R., *Energies*, 7, 4397, 2014.
4. Duan, Z., Sun, R., Zhu, C., Chou, I.-M., *Mar. Chem.*, 98, 131, 2006.
5. Spycher, N. and Pruess, K., *Transport Porous Med.*, 82, 173, 2010.

6. Springer, R.D., Wang, Z., Anderko, A., Wang, P., Felmy, A.R., *Chem. Geol.*, 322–323, 151, 2012.
7. Zhao, H., Dilmore, R., Allen, D.E., Hedges, S.W., Soong, Y., Lvov, S.N., *Environ. Sci. Technol.*, 49, 1972, 2015.
8. Appelo, C.A.J., Parkhurst, D.L., Post, V.E.A., *Geochim. Cosmochim. Acta*, 125, 49, 2014.
9. Bamberger, A., Sieder, G., Maurer, G., *J. Supercrit. Fluids*, 17, 97, 2000.
10. Hou, S.-X., Maitland, G.C., Trusler, J.P.M., *J. Supercrit. Fluids*, 73, 87, 2013.
11. Tong, D., Trusler, J.P.M., Vega-Maza, D., *J. Chem. Eng. Data*, 58, 2116, 2013.
12. Zhao, H., Fedkin, M.V., Dilmore, R.M., Lvov, S.N., *Geochim. Cosmochim. Acta*, 149, 165, 2015.
13. Messabeb, H., Contamine, F., Cézac, P., Serin, J.P., Gaucher, E.C., *J. Chem. Eng. Data*, 61, 3573, 2016.
14. Zhao, H., Dilmore, R.M., Lvov, S.N., *AIChE J*, 61, 2286, 2015.
15. Messabeb, H., Contamine, F., Cézac, P., Serin, J.P., Pouget, C., Gaucher, E.C., *J. Chem. Eng. Data*, 62, 4228, 2017.
16. Yan, W., Huang, S., Stenby, E.H., *Int. J. Greenh. Gas Con.*, 5, 1460, 2011.
17. Bastami, A., Allahgholi, M., Pourafshary, P., *Pet. Sci.*, 11, 569, 2014.
18. Poulain, M., Messabeb, H., Cézac, P., Serin, J.P., Dupin, J.C., Martinez, H., *Cutting-Edge Technology for Carbon Capture, Utilization, and Storage*, K. Ballerat-Busserolles, Y.A. Wu, J.J. Carroll (Eds.), p. 123, John Wiley & Sons, Inc., Hoboken, NJ, USA, 2018.
19. Li, Z., Dong, M., Li, S., Dai, L., *J. Chem. Eng. Data*, 49, 1026, 2004.
20. Liu, Y., Hou, M., Yang, G., Han, B., *J. Supercrit. Fluids*, 56, 125, 2011.
21. Poulain, M., Messabeb, H., Lach, A., Contamine, F., Cézac, P., Serin, J.-P. *et al.*, *J. Chem. Eng. Data*, 64, 2497, 2019.
22. Mundhenk, N., Huttenloch, P., Sanjuan, B., Kohl, T., Steger, H., Zorn, R., *Corros. Sci.*, 70, 17, 2013.
23. Mundhenk, N., Huttenloch, P., Kohl, T., Steger, H., Zorn, R., *Geothermics*, 46, 14, 2013.
24. Mundhenk, N., Huttenloch, P., Bäßler, R., Kohl, T., Steger, H., Zorn, R., *Corros. Sci.*, 84, 180, 2014.
25. Sanjuan, B., Millot, R., Innocent, Ch, Dezayes, Ch, Scheiber, J., Brach, M., *Chem. Geol.*, 428, 27, 2016.
26. Standard Practice for Preparing, Cleaning, and Evaluating Corrosion Test Specimens. ASTM G1-03, ASTM International, West Conshohocken, PA, 2018.
27. Heuer, J.K. and Stubbins, J.F., *Corros. Sci.*, 41, 1231, 1999.

3

Experimental Study of the Liquid Vapour Equilibrium of the System Water-CO_2-O_2-NO_x Under Pressure at 298 K

Esther Neyrolles[1]*, Georgio Bassil[2], François Contamine[1], Pierre Cézac[1] and Philippe Arpentinier[3]

[1]Univ Pau & Pays Adour/E2S UPPA, Laboratoire de Thermique, Energétique et Procédés- IPRA, PAU, France
[2]Faculty of Engineering, Univ Libano-Canadienne, LCU, Zouk Mikael, Aintoura, Kesrouan Lebanon, Liban
[3]Air Liquide, Paris Innovation Campus, Direction Scientifique, 1 chemin de la Porte des Loges, Jouy-en-Josas Cedex, France

Abstract

The sequestration of CO_2 fumes from an oxyfuel combustion is used to reduce significantly CO_2 emissions. Impurities like nitric oxide can cause technical difficulties during the capture, treatment, transport and storage steps of CO_2 fumes. In order to reduce these risks, the system CO_2-NO_x-H_2O is studied under pressure. The measurements are performed in an equilibrium cell. Ion chromatography is used to analyze the aqueous phase and infrared spectrometry is used to analyze the gas phase. The use of mechanisms that take place in the aqueous phase and the experimental measurements allowed us to estimate the concentration of all the nitrogen species in the aqueous phase. The presence of nitrogen oxides has no impact on the CO_2 solubility. The distribution of the NO_x in the aqueous phase shows that the nitrogen dioxide, absorbed in the aqueous phase, reacts to form mostly nitric and nitrous acid.

Keywords: Carbon dioxide, nitrogen oxides, liquid vapor equilibrium, high pressure, Henry constant

**Corresponding author*: esther.neyrolles@univ-pau.fr

Ying Wu, John J. Carroll, Mingqiang Hao and Weiyao Zhu (eds.) Gas Injection into Geological Formations and Related Topics, (21–40) © 2020 Scrivener Publishing LLC

3.1 Introduction

The emission of greenhouse gases is a factor in global warming. At the COP21 in Paris in 2015, 195 countries agreed to reduce their greenhouse emission. Carbon dioxide is one of the most emitted greenhouse gases. It principally comes from the burning of fossil fuel. To reduce its emission in the atmosphere, a solution is to capture it for geological storage. The process is known as Carbon Capture and Storage (CCS). One of the main challenges in the recovery of carbon dioxide in gaseous effluents from coal or oil-fired power plants comes from the low molar fractions of CO_2 in these effluents. To remedy this, one of the solutions consists of using oxygen instead of air as the main oxidant for the combustion reaction. Oxy-combustion significantly increases the molar fraction of CO_2 in the fumes and significantly improves the efficiency of CO_2 separation and purification techniques. But even when this technique is used, there are still impurities in the flue gas like NO_x, SO_x, O_2, Hg, water, etc., which come from the fossil fuels burned. To produce CO_2 at food grade or at specifications required for storage, the flue gas has to be treated. During this process the fumes are washed with a soda aqueous solution in order to almost completely eliminate the sulfur compounds. Then the desulfurized fumes are compressed before being cooled down at 223 K. During this compression step, the water and most of the nitrogen oxides are eliminated. Then, the carbon dioxide is distillated in order to separate nitrogen dioxide and nitrogen tetroxide on one hand, and the most volatile compounds (NO, Ar, O_2, N_2) on the other hand. During all the steps of the CO_2 purification process, the nitrogen oxides are in the presence of residual gaseous oxygen and water in the vapor state or in the liquid state (absorption column and condensates after the cooling steps). Consequently, to design the process, it is important to know the evolution of the composition of the mixture and in particular, the formation of nitric acid and nitrous acid in the aqueous phase and the distribution of the nitrogen oxides in the vapor phase (NO, NO_2, N_2O_3, N_2O_4). This information will not only allow the calculation the NO_x abatement rates in the various sections of the installation and consequently to correctly size the CO_2 separation and purification unit, but also to choose the appropriate materials to minimize the risks of corrosion. This system is complex because reactions are numerous between nitrogen oxides and water in the aqueous phase and in the gaseous phase. In this paper, an experimental study of the liquid vapor and the thermochemical equilibriums of the system H_2O-CO_2-O_2-NO_x under pressure at 298 K is presented.

3.2 Literature Review

3.2.1 Carbon Dioxide and Water System

The solubility of carbon dioxide in water has been studied over a large range of pressure and temperature over the last century [1]. Four studies [2–5], at 298.15 K and pressure range of interest (from 5 to 30 bar) have been selected. The range of temperature and pressure of these studies are reported in Table 3.1.

In water, carbon dioxide could appear under three form: aqueous carbon dioxide $CO_{2(aq)}$, bicarbonate ion $HCO^-_{3(aq)}$ and carbonate ion $CO^{2-}_{3(aq)}$. In the aqueous phase, the equilibrium reactions between each species follow:

$$CO_{2(aq)} + H_2O_{(aq)} \overset{K_{CO2}}{\longleftrightarrow} HCO^-_{3(aq)} + H^+_{(aq)} \tag{3.1}$$

$$HCO^-_{3(aq)} \overset{K_{HCO3-}}{\longleftrightarrow} CO^{2-}_{3(aq)} + H^+_{(aq)} \tag{3.2}$$

The distribution of carbonate species in the aqueous phase is dependent on the pH. In acidic aqueous solution (pH < 5), the species mainly present in solution is the aqueous carbon dioxide [6].

Kawazuishi and Prausnitz [7] have studied these equilibrium reactions at different temperatures: 273 K to 498 K. At 298 K, they have established: $K_{CO2} = 4.42 \times 10^{-7}$ mol.L^{-1} and $K_{HCO3-} = 4.40 \times 10^{-11}$ mol.L^{-1}.

Table 3.1 Literature data for the carbon dioxide water system in our experimental conditions.

Author	Temperature (K)	Pressure (bar)
Zel'venskii [2]	273 – 373	5 – 30
Houghton *et al.* [3]	273 – 373	10 – 36
Valtz *et al.* [4]	287 – 318	5 – 80
Lucile *et al.* [5]	298 – 393	5 – 50

3.2.2 Nitrogen Oxides and Water System

In the aqueous phase, the nitrogen oxides can be present under several forms: $NO_{(aq)}$, $NO_{2(aq)}$, $N_2O_{4(aq)}$, $N_2O_{3(aq)}$, $N_2O_{5(aq)}$, $HNO_{2(aq)}$, $HNO_{3(aq)}$, $NO^-_{2(aq)}$ and $NO^-_{3(aq)}$. Many reactions can occur between them in the aqueous phase, except for $N_2O_{5(aq)}$ which formation is negligible in the liquid phase. Joshi *et al.* [8] and Schwartz and White [9] identified eleven equilibrium reactions:

$$2\ NO_{2(aq)} \overset{K_1}{\leftrightarrow} N_2O_{4(aq)} \tag{3.3}$$

$$NO_{(aq)} + NO_{2(aq)} \overset{K_2}{\leftrightarrow} N_2O_{3(aq)} \tag{3.4}$$

$$N_2O_{3(aq)} + H_2O_{(aq)} \overset{K_3}{\leftrightarrow} 2\ HNO_{2(aq)} \tag{3.5}$$

$$N_2O_{4(aq)} + H_2O_{(aq)} \overset{K_4}{\leftrightarrow} HNO_{2(aq)} + HNO_{3(aq)} \tag{3.6}$$

$$HNO_{2(aq)} \overset{K_5}{\leftrightarrow} NO^-_{2(aq)} + H^+_{(aq)} \tag{3.7}$$

$$HNO_{3(aq)} \overset{K_6}{\leftrightarrow} NO^-_{3(aq)} + H^+_{(aq)} \tag{3.8}$$

$$3\ NO_{2(aq)} + H_2O_{(aq)} \overset{K_7}{\leftrightarrow} 2\ HNO_{3(aq)} + NO_{(aq)} \tag{3.9}$$

$$NO_{(aq)} + NO_{2(aq)} + H_2O_{(aq)} \overset{K_8}{\leftrightarrow} 2\ HNO_{2(aq)} \tag{3.10}$$

$$2\ NO_{2(aq)} + H_2O_{(aq)} \overset{K_9}{\leftrightarrow} HNO_{2(aq)} + HNO_{3(aq)} \tag{3.11}$$

$$3\ HNO_{2(aq)} \overset{K_{10}}{\leftrightarrow} HNO_{3(aq)} + 2\ NO_{(aq)} + H_2O_{(aq)} \tag{3.12}$$

$$NO_{2(aq)} + HNO_{2(aq)} \overset{K_{11}}{\leftrightarrow} HNO_{3(aq)} + NO_{(aq)} \tag{3.13}$$

Six equations are independents: equation 3.3 to 3.8. The equilibrium constants of each reaction at 298 K are presented in Table 3.2.

3.2.3 Nitric Oxide Henry Constant at 298 K

Henry's law states that the amount of dissolved gas in an aqueous phase is proportional to its partial pressure in the gas phase above at constant temperature, for a low amount of this gas. We are assuming the

Table 3.2 Equilibrium constants of nitrogen oxides reaction in the aqueous phase at 298 K.

Equilibrium constant	Value	Unit	Reference
K_1	6.54×10^4	$L.mol^{-1}$	[10]
K_2	1.37×10^4	$L.mol^{-1}$	[11]
K_3	3.30×10^2	$mol.L^{-1}$	[12]
K_4	3.77×10^3	$(mol.L^{-1})^2$	[a]
K_5	5.1×10^{-4}	$mol.L^{-1}$	[13]
K_6	15.4	$mol.L^{-1}$	[14]
K_7	1.35×10^{10}	$(mol.L^{-1})^2$	[b]
K_8	4.52×10^6	–	[c]
K_9	2.47×10^8	$mol.L^{-1}$	[15]
K_{10}	1.21×10^{-5}	$mol.L^{-1}$	[d]
K_{11}	54.6	$mol.L^{-1}$	[e]

[a] Estimated from: K_9/K_1
[b] Estimated from: K_9^2/K_8
[c] Estimated from: $K_3 \cdot K_2$
[d] Estimated from: K_9/K_8^2
[e] Estimated from: K_9/K_8

hypothesis of an ideal solution. Sander [16] compiled Henry's constant values in water of the nitrogen monoxide involved in previous reactions at 298 K. The nitric oxide Henry's constant listed are under the form:

$$H_{NO}^{298K} = \frac{[NO]}{P_{NO}} \tag{3.14}$$

with [NO]: concentration of nitric oxide in the aqueous phase in $mol.L^{-1}$

P_{NO}: partial pressure of nitric oxide in the gas phase in bar

In this review, Sander [16] has reported fourteen references of NO Henry constant at 298 K. Twelve of them present the same data: $1.9x10^{-3}$ $mol.L^{-1}.bar^{-1}$ at 298 K. We use this NO Henry's constant as a reference.

3.3 Experimental Section

3.3.1 Chemicals

Air Liquide provided all the gases. Carbon dioxide has a certified purity of 99.7 vol-% (CAS registry No. 124-38-9). Oxygen has a certify purity of 99.5 vol-% (CAS registry No. 7782-44-7). The gas mixture was a CRYSTAL quality mix CO_2-NO (50 270 ± 1 005 vol-ppm). The water used in the experiments is deionized water at 18.2 MΩ.cm produced by a Barnstead™ Smart2Pure™ water purifier system from Thermo Fischer. Sodium hydroxide (CAS registry No. 1310-73-2) for ion chromatography is provided by Fischer Scientific with a certified purity of 50 ± 2.5 wt%. Sulfuric acid (CAS registry No. 7664-93-9) for ion chromatography is provided by VWR with a certified purity of 96 ± 1 wt%. Sodium nitrate (CAS registry No. 7631-99-4) for the calibration curve of ion chromatography is provided by ACROS Organics with a certified purity of 99 wt%. Sodium nitrite (CAS registry No. 7632-00-0) for the calibration curve of ion chromatography is provided by ACROS Organics with a certified purity of 97 wt%. Sodium carbonate (CAS registry No. 497-19-8) for the calibration curve of ion chromatography is provided by VWR with a certified purity of 99 wt%.

3.3.2 Apparatus

The apparatus has already been described [5]. A scheme of the experimental equipment is presented in Figure 3.1.

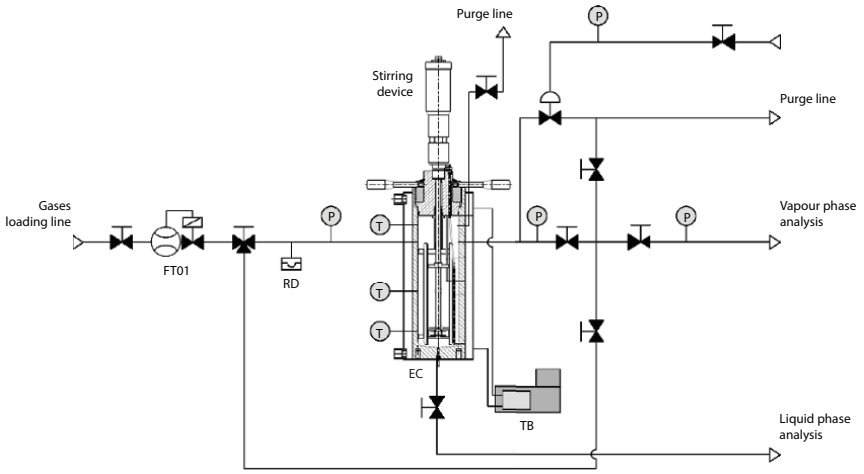

Figure 3.1 Scheme of the experimental equipment: FT01: mass flow meters; RD: rupture disk; EC: equilibrium cell; TB: thermostatic bath; P: pressure transducer or manometers; T: temperature probes ([5]).

It is an equilibrium cell made in Hastelloy C276 with a double jacket and a volume of 2 400 cm^3. The operating conditions of the device go from 288 to 393K and it can be operated up to 90 bar. A thermostatic bath controls the temperature in the cell. The thermal gradient between the top and the bottom of the cell is ± 0.5 K. The temperature is measured at three locations (at the top, at the bottom and also to two-thirds of the cell) by three Pt100 probes with an accuracy of ± 0.1 K. The pressure is measured by a high temperature pressure transmitter (PA-25HTT) from Keller with an accuracy of ± 0.5 % of the full scale. To ensure the mixture homogeneity in the cell, a stirrer is used. It is composed by a Rushton turbine at the bottom of the cell and a four blades impeller at the top. A mass flow meter Brooks® SLA5850S (FT01), is placed on the gas loading line and have a volumetric counter to know the volume of gas injected in the cell. Between the cell and the gas phase analyzer, a regulator and a valve allow to control the pressure before the gas phase analyzer. The temperature between the cell and the gas phase analyzer is controlled by an electrical tracing. A rupture disk is also implemented on the apparatus for safety.

3.3.3 Operating Procedure

The cell and the line are first swept with nitrogen to eliminate residues from the previous experiment. Then the cell is dry to eliminate any traces

of water. The cell is put under vacuum at 0.1 bar with a vacuum pump. Then the purified water is introduced. The temperature is fixed at 298 K. When the temperature is reached, the oxygen is introduced. After the oxygen, the gas mixture is introduced until the desire pressure is reached. Once the two mixtures are in the cell, nitrogen dioxide is formed following the reaction:

$$2\,NO_{(g)} + O_{2(g)} \rightarrow 2\,NO_{2(g)} \tag{3.15}$$

In order to observe nitrogen dioxide in the gas phase at the end of the experiment, we need a large quantity of NO_2 to inject initially (at least 5% of NO_2). For reasons of feasibility, Air Liquid cannot provide a gas cylinder with 5% of nitrogen dioxide in mixture with carbon dioxide, so we decided to produce nitrogen dioxide in situ. Once the gas phase and the aqueous phase are in contact in the cell, a stirring of 700 rpm is applied until the liquid/vapor and thermochemical equilibriums are reached. The experimental follow-up is achieved by the analysis of the aqueous phase. When the aqueous phase concentrations are constants, we assume that the equilibriums are reached. The time for the equilibriums to be reached can take more than two weeks. The follow-up of an experiment is presented in Figure 3.2. When the equilibriums are reached, the gas phase is analyzed.

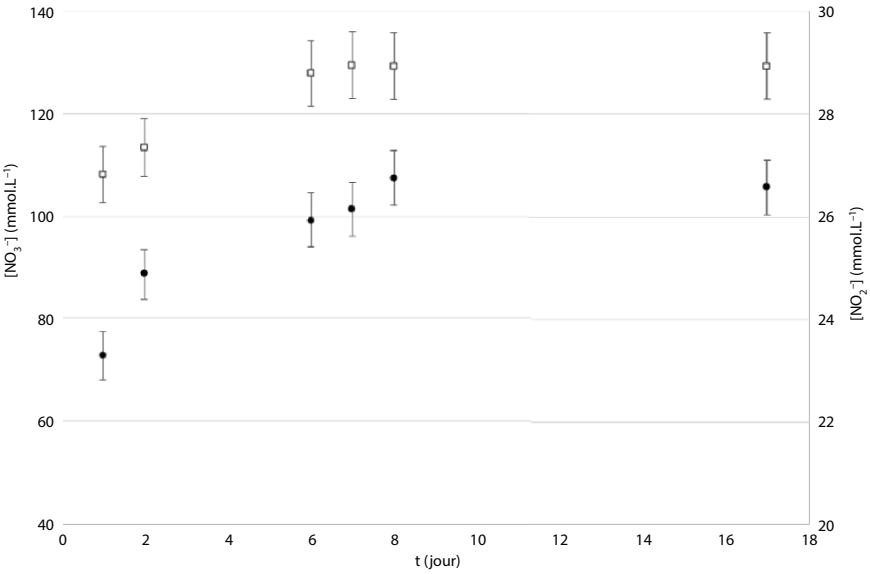

Figure 3.2 Nitrites and nitrates concentrations in the aqueous phase according to the time of the experiment: ▲, nitrate; ●, nitrite.

3.3.4 Experimental Analysis

3.3.4.1 Aqueous Analysis

3.3.4.1.1 Carbon Dioxide

The analysis of the aqueous phase is done by an original on-line ion chromatography already described in a previous paper [5]. The calibration curves are obtained from aqueous solutions of sodium carbonate. The volume of the sample introduced in the injection valve is 0.4 µL. No manual injections occurred because the chromatograph is directly connected to the equilibrium cell. Samples are pushed in the injection valve thanks to the pressure in the cell.

3.3.4.1.2 Nitrogen Oxides

This analysis is also done by on-line ion chromatography. The liquid chromatography system used is a Dionex ICS-900 equipped with an IonPac AS14A column (4 × 250 mm). The IonPac AS14A column is specific for anions like NO_2^- and NO_3^- which are eluted by a NaOH eluent (0.01 mol.L^{-1}). A regenerating solution of H_2SO_4 is used to decrease the conductivity of the eluent due to sodium and hydroxide ions and to stabilize the baseline. Calibration curves are obtained from aqueous solution of $NaNO_3$ and $NaNO_2$. The volume of the sample introduced in the injection valve is 0.4 µL. Like for carbon dioxide analysis, samples are directly pushed in the injection valve.

Different nitrogen oxides are present in the aqueous phase ($NO_{(aq)}$, $NO_{2(aq)}$, $N_2O_{4(aq)}$, $N_2O_{3(aq)}$, $HNO_{2(aq)}$, $HNO_{3(aq)}$, $NO_{2(aq)}^-$ and $NO_{3(aq)}^-$) and most of them react with the NaOH eluent [17] according to the following reactions:

$$2\ NO_{2\,(aq)} + 2\ OH^-_{(aq)} \rightarrow NO^-_{2\,(aq)} + NO^-_{3\,(aq)} + H_2O_{(aq)} \qquad (3.16)$$

$$N_2O_{3\,(aq)} + 2\ OH^-_{(aq)} \rightarrow 2\ NO^-_{2\,(aq)} + H_2O_{(aq)} \qquad (3.17)$$

$$N_2O_{4\,(aq)} + 2\ OH^-_{(aq)} \rightarrow NO^-_{2\,(aq)} + NO^-_{3\,(aq)} + H_2O_{(aq)} \qquad (3.18)$$

$$HNO_{2\,(aq)} + OH^-_{(aq)} \rightarrow NO^-_{2\,(aq)} + H_2O_{(aq)} \qquad (3.19)$$

$$HNO_{3\,(aq)} + OH^-_{(aq)} \rightarrow NO^-_{3\,(aq)} + H_2O_{(aq)} \quad (3.20)$$

From reactions 3.16 to 3.20, all nitrogen oxides, absorbed in a solution containing hydroxide ions, react to form nitrite and nitrate ions, **except nitric oxide**.

The nitrite and nitrate concentration measured by ion chromatography are not the concentration of nitrite and nitrite in the aqueous phase of the cell but the sum of all the nitrogen oxides that have reacted with OH^- to form nitrite and nitrate. From the reactions presented here above, the concentrations of nitrite (α) and nitrate (β) measured by ion chromatography are expressed according to the equations below:

$$\alpha = \frac{1}{2} * [NO_2] + \left[NO_2^-\right] + 2 * [N_2O_3] + [N_2O_4] + [HNO_2] \quad (3.21)$$

$$\beta = \frac{1}{2} * [NO_2] + \left[NO_3^-\right] + [N_2O_4] + [HNO_3] \quad (3.22)$$

Therefore, the experimental results given by ion chromatography about nitrites and nitrates concentrations correspond to the concentration of the nitrogen species that react to form nitrites and nitrites in the aqueous phase in contact with the basic eluent, except nitric oxide. The concentration of all nitrogen oxides in the aqueous phase estimation is described in section 3.3.5 of this chapter.

3.3.4.2 Gas Phase Analysis

Two infrared spectrometers Proceas® from the company Ap2e are used to determine the vapor composition of the cell. The Proceas® spectrometers have longer optic path than classical spectrometer in order to have a sensibility of the order of the volume fraction (% or ppm). The two infrared spectrometers give, respectively, the volume fraction of NO_2, CO_2 and NO and SO_2, O_2 and H_2O. The range of volume fraction and measurement accuracies are presented in Table 3.3. The response time of the Proceas® to reach 98% of carbon dioxide is less than 40 seconds.

During the different experiments, we have noticed that the ProCeas® analyzer measurements on nitrogen dioxide did not stabilize over time. Measurements obtained on nitrogen dioxide are unreliable.

Table 3.3 Range of volume fraction and measurement accuracies of the Proceas® infra-red spectrometers.

	y_{NO2} (ppm)	y_{CO2} (%)	y_{NO} (ppm)	y_{SO2} (ppm)	y_{O2} (%)	y_{H2O} (%)
range	0 – 500	0 – 100	0 – 10 000	0 – 100	0 – 10	0 – 15
accuracy[a]	± 5	± 1	± 100	± 1	± 0.1	± 0.15

[a] given by the manufacturer

3.3.5 Estimation of the Concentrations of All the Species in the Aqueous Phase

The aqueous phase, from the dissolut ion of NO_2 and CO_2 in water, contains several species: $NO_{(aq)}$, $NO_{2(aq)}$, $N_2O_{4(aq)}$, $N_2O_{3(aq)}$, $HNO_{2(aq)}$, $HNO_{3(aq)}$, $NO^-_{2(aq)}$, $NO^-_{3(aq)}$, $CO_{2(aq)}$, $HCO^-_{3(aq)}$, $CO^{2-}_{3(aq)}$, $H^+_{(aq)}$ and $OH^-_{(aq)}$.

The aqueous phase is acidified by the absorption of carbon dioxide [18] and also by the formation of nitric oxide and nitrous oxide [9], so the $OH^-_{(aq)}$ and $CO^{2-}_{3(aq)}$ concentrations are neglected. We have 11 unknowns in the aqueous phase: $NO_{(aq)}$, $NO_{2(aq)}$, $N_2O_{4(aq)}$, $N_2O_{3(aq)}$, $HNO_{2(aq)}$, $HNO_{3(aq)}$, $NO^-_{2(aq)}$, $NO^-_{3(aq)}$, $CO_{2(aq)}$, $HCO^-_{3(aq)}$, and $H^+_{(aq)}$.

We have three equations from the experimental measurements: equation 3.21 and 3.22 from the nitrite and nitrate ion chromatography and from the carbon dioxide chromatography analysis:

$$\alpha = \frac{1}{2} * [NO_2] + \left[NO_2^-\right] + 2 * [N_2O_3] + [N_2O_4] + [HNO_2] \quad (3.21)$$

$$\beta = \frac{1}{2} * [NO_2] + \left[NO_3^-\right] + [N_2O_4] + [HNO_3] \quad (3.22)$$

$$\gamma = [CO_2] + \left[HCO_3^-\right] + \left[CO_3^{2-}\right] \quad (3.23)$$

We also consider the electroneutrality equation of the solution:

$$[H^+] = \left[NO_2^-\right] + \left[NO_3^-\right] + \left[HCO_3^-\right] \quad (3.24)$$

The seven remaining equations are from the thermochemical equilibria taking place in the aqueous phase detailed in the section 3.2 of this chapter. These seven reactions were chosen because they are independent of each other:

$$CO_{2(aq)} + H_2O_{(aq)} \overset{K_{CO2}}{\longleftrightarrow} HCO^-_{3(aq)} + H^+_{(aq)} \tag{1.1}$$

$$2\ NO_{2(aq)} \overset{K_1}{\leftrightarrow} N_2O_{4(aq)} \tag{1.3}$$

$$NO_{(aq)} + NO_{2(aq)} \overset{K_2}{\leftrightarrow} N_2O_{3(aq)} \tag{1.4}$$

$$N_2O_{3(aq)} + H_2O_{(aq)} \overset{K_3}{\leftrightarrow} 2\ HNO_{2(aq)} \tag{1.5}$$

$$N_2O_{4(aq)} + H_2O_{(aq)} \overset{K_4}{\leftrightarrow} HNO_{2(aq)} + HNO_{3(aq)} \tag{1.6}$$

$$HNO_{2(aq)} \overset{K_5}{\leftrightarrow} NO^-_{2(aq)} + H^+_{(aq)} \tag{1.7}$$

$$HNO_{3(aq)} \overset{K_6}{\leftrightarrow} NO^-_{3(aq)} + H^+_{(aq)} \tag{1.8}$$

Taken into account this mechanism characterized by the above eleven equations we can estimate the concentration of the eleven species in the aqueous phase.

3.3.6 Uncertainties

The calculation of uncertainties for the carbon dioxide chromatography analysis has already been described [5]. The ANOVA method was used and an average uncertainty of 3.4% was obtained.

The calculation of uncertainties for the nitrite and nitrate chromatography analysis is based on the determination of a coefficient of variation

(C_V), also known as the relative standard deviation. The definition of C_V is the ratio of the standard deviation to the average:

$$C_V(\%) = \frac{Standard\ deviation\ (x)}{\bar{x}} * 100 \tag{3.25}$$

With

$$Standard\ deviation\ (x) = \sqrt{\frac{\sum (x - \bar{x})^2}{p - 1}} \tag{3.26}$$

$\bar{x}$: average
p: number of analyze

For each experiment, five ion chromatography measurements were made. The results presented in this chapter are the average of these five measurements $(\bar{x})$. C_v is also obtained with the five measurements. The uncertainties of nitrate and nitrite chromatography measurements are respectively 5% and 2%.

3.4 Results and Discussion

Two experiments have been conducted on the CO_2-NO_x-O_2-H_2O system, at respectively 5 and 30 bar and at 298 K. The initial conditions (the amount of water, carbon dioxide, nitric oxide and oxygen introduced in the cell and the pressure in the cell) and the experimental results from the aqueous and the gas phase are reported in Table 3.4.

For these two experiments, the oxygen was introduced in stoichiometric proportion according to reaction 3.15 in order to convert almost all the nitric oxide into nitrogen dioxide.

3.4.1 Solubility of Carbon Dioxide

The experimental solubility of carbon dioxide in the presence of nitrogen oxides is compared with the data from the literature on the CO_2-H_2O system [2–5] in Figure 3.3.

Table 3.4 Specifics of the experiments on the CO_2-NO_x-O_2-H_2O system at 298 K.

P (bar)	w_w (kg)	n_{CO2} (mol)	n_{NO} (mol)	n_{O2} (mol)	γ (mol.L^{-1})	α (mol.L^{-1})	β (mol.L^{-1})	y_{NO} (ppm)
5.1	0.521	0.489	1.72x10^{-2}	8.48x10^{-3}	0.183	7.12x10^{-4}	2.98x10^{-2}	793
29.1	0.545	3.110	1.09x10^{-1}	5.45x10^{-2}	0.841	2.50x10^{-2}	1.25x10^{-1}	9000

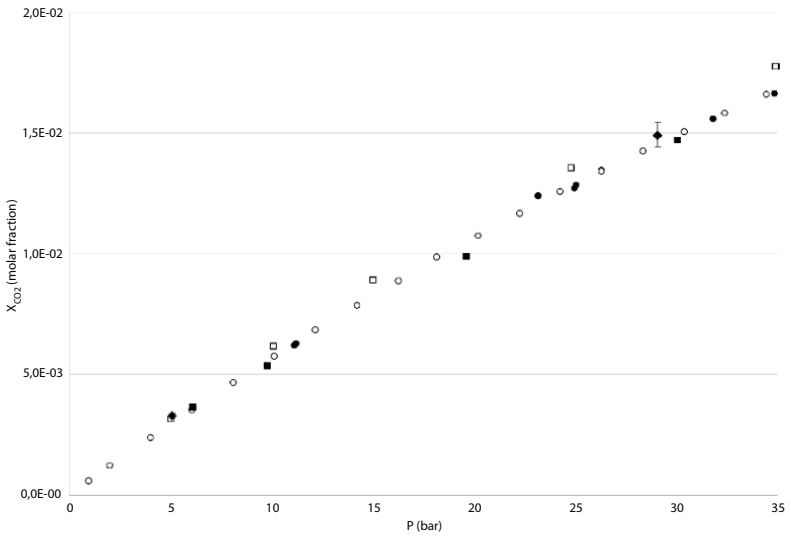

Figure 3.3 Experimental solubility of carbon dioxide on the CO_2-NO_x-O_2-H_2O system compared with data from the literature on the CO_2-H_2O system at 298 K: ◆, this work; ■, Lucile *et al.* [5]; ▫, Valtz *et al.* [4]; o, Houghton *et al.* [3]; •, Zel'venskii [2].

From the Figure 3.3, we can notice that the carbon dioxide solubility increases with the pressure. The experimental measurements are in good agreement with the literature. The presence of nitrogen oxides does not seem to have any influence on the carbon dioxide solubility in our experimental conditions.

3.4.2 Nitrogen Oxides Repartition in the Aqueous Phase

The aqueous phase, from the dissolution of NO_x and CO_2 in water, contains molecular species, as well as ionized species: $NO_{(aq)}$, $NO_{2(aq)}$, $N_2O_{4(aq)}$, $N_2O_{3(aq)}$, $HNO_{2(aq)}$, $HNO_{3(aq)}$, $NO^-_{2(aq)}$, $NO^-_{3(aq)}$, $CO_{2(aq)}$, $HCO^-_{3(aq)}$, and $H^+_{(aq)}$. With the chosen reaction mechanism and measurements by ion chromatography described in section 3.3.5 of this chapter, we estimated the concentrations of all the species in the aqueous phase. Data are presented in Table 3.5.

From the data in Table 3.4 it is possible to classify the nitrogenous species, in the increasing order: $NO^-_{3(aq)} > HNO_{2(aq)} > HNO_{3(aq)} > NO_{(aq)} > NO^-_{2(aq)} > N_2O_{3(aq)} > NO_{2(aq)} > N_2O_{4(aq)}$.

Table 3.5 Estimated concentration of all the aqueous species at 298 K.

Pressure (bar)	pH[a]	Concentration (mol.L^{-1})				
		$[CO_2]$	$[NO_3^-]$	$[HNO_2]$	$[HNO_3]$	[NO]
5.1	1.5	1.83×10^{-1}	2.98×10^{-2}	7.01×10^{-4}	5.77×10^{-5}	8.49×10^{-6}
29.1	0.9	8.41×10^{-1}	1.25×10^{-1}	2.55×10^{-2}	1.01×10^{-3}	4.45×10^{-4}
Pressure (bar)	**pH[a]**	**Concentration (mol.L^{-1})**				
		$[NO_2^-]$	$[HCO_3^-]$	$[N_2O_3]$	$[NO_2]$	$[N_2O_4]$
5.1	1.5	1.05×10^{-5}	2.61×10^{-6}	1.49×10^{-9}	1.28×10^{-8}	1.07×10^{-11}
29.1	0.9	9.11×10^{-5}	2.88×10^{-6}	1.96×10^{-6}	3.22×10^{-7}	6.79×10^{-9}

[a] Estimated with the equation pH = - log([H$^+$]) (Hypothesis: ideal solution).

This distribution is almost the same of the one proposed by Schwartz and White [9]: $NO^-_{3(aq)} > HNO_{2(aq)} > NO^-_{2(aq)} > N_2O_{4(aq)} > N_2O_{3(aq)} > NO_{2(aq)} > NO_{(aq)}$.

Schwartz and White [9] considered that the nitric acid is completely dissociated into nitrate according to equation 3.8. That is why they did not take it into account in their distribution. Their distribution was established from the absorption of nitrogen dioxide. In our experiments, a large amount of nitric oxide is still present in the gas phase at the end of the experiment. For this reason, the amount of nitric oxide in the aqueous phase is higher. We also disagree on the distribution of the three last nitrogen species, but we agree that these species are less present in solution. We also agree on the two predominant nitrogen species in the aqueous phase: nitrate and nitrous acid.

In order to better visualize the trend of the main species, the concentrations are represented in Figure 3.4.

From the Figure 3.4, we can notice that the concentration of nitrate and nitrous acid increases within the pressure. The aqueous phase is also acidified, the pH goes from 1.5 to 0.9. The absorption of carbon dioxide acidifies the aqueous phase to a pH around three [18]. The absorption of nitrogen dioxide and nitric oxide increase the acidification of the aqueous phase, especially by the formation of nitrous and nitric acid.

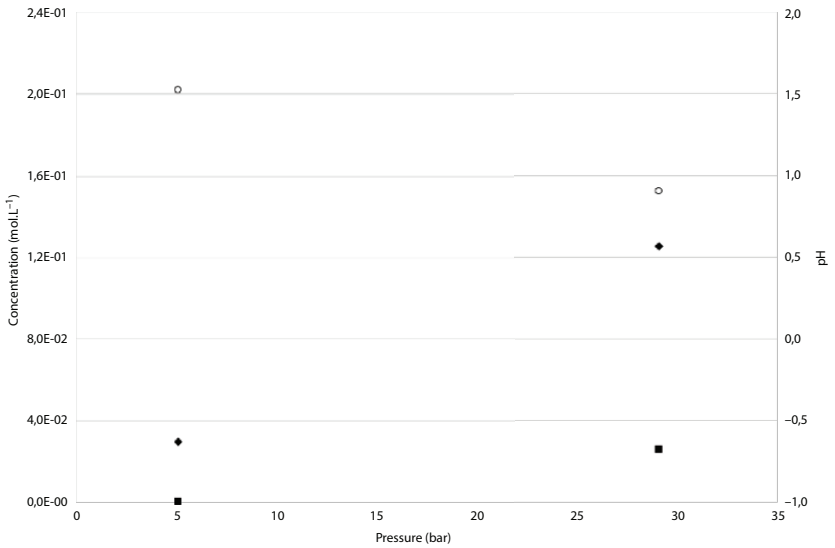

Figure 3.4 Estimated concentrations of the predominant nitrogen species in the aqueous phase according to the pressure in the cell: ○, pH; ◆, $\left[NO_3^-\right]$; ▪, $[HNO_2]$.

3.4.3 Nitric Oxide Henry Constant at 298 K

The partial pressure of nitric oxide in the gas phase is known thanks to the infrared spectrometers:

$$P_{NO} = P^{\star}\, y_{NO} \tag{3.27}$$

The nitric oxide concentration is known from the estimation of all the nitrogen species in the aqueous phase. The nitric oxide Henry constant is estimated at 298 K with equation 3.14 and compared with the most used value in the literature [16]: $H_{NO,lit}^{298k} = 1.9 \times 10^{-3}$ mol.L^{-1}.bar^{-1}. The data are presented in Table 3.6.

The nitric oxide Henry constant found are closed to the literature, the relative difference being lower than 13%. This agreement with the literature allows us to validate our experimental protocol and our way of estimation of the concentration of all the aqueous species.

The determination of the nitrogen dioxide Henry constant at 298 K cannot be assessed because the measurements obtained on the nitrogen dioxide by the infrared spectrometers are unreliable.

Table 3.6 Estimation of the nitric oxide Henry constant at 298 K and comparison with literature.

Pressure (bar)	**[NO] (mol.L^{-1})**	**P_{NO} (bar)**	**H_{NO}^{298K} (mol.L^{-1}. bar^{-1})**	**Literature gap (%)**
5.1	$8.49x10^{-6}$	$4.04x10^{-3}$	$2.10x10^{-3}$	**+ 12.4**
29.1	$4.45x10^{-4}$	0.26	$1.70x10^{-3}$	**- 8.3**

3.5 Conclusion

The equilibrium between nitrogen oxides, carbon dioxide, oxygen and water have been studied at 298 K and at 5 and 29,1 bar. The experimental protocol and our way of analysis have been validated with the nitric oxide Henry constant estimation.

The presence of nitrogen oxides in the system does not seem to have any influence on the solubility of the carbon dioxide in the experimental conditions studied. The distribution of nitrogen species in the aqueous phase has been estimated. The absorption of nitrogen dioxide acidifies the aqueous phase by the formation of nitric and nitrous acid. These experiments bring new data in the literature on the solubility of nitrogen oxides and allow us to understand better the reactions that take place during the steps of compression and cooling during the CCS process.

To go further, this system should be studied at different temperatures and at higher nitric oxide partial pressure. It would be interesting to study the system with other impurities present in the oxy-combustion fumes like the sulfur dioxide.

3.6 Acknowledgements

This work was supported by Air Liquide and the Conseil Régional d'Aquitaine, France.

References

1. Mao, S., Zhang, D., Li, Y., Liu, N., An improved model for calculating CO2 solubility in aqueous NaCl solutions and the application to CO2–H2O–NaCl fluid inclusions. *Chem. Geol.*, 347, 43–58, Jun. 2013.

2. Zel'venskii, Y.D., Measurements of carbon dioxide solubility in water. *Zhurm Khim Prom*, 14, 1250–1257, 1937.
3. Houghton, G., McLean, A.M., Ritchie, P.D., Absorption of carbon dioxide in water under pressure using a gas-bubble column. *Chem. Eng. Sci.*, 7, 1, 26–39, Jan. 1957.
4. Valtz, A., Chapoy, A., Coquelet, C., Paricaud, P., Richon, D., Vapour–liquid equilibria in the carbon dioxide–water system, measurement and modelling from 278.2 to 318.2K. *Fluid Phase Equilib.*, 226, 333–344, Dec. 2004.
5. Lucile, F., Cézac, P., Contamine, F., Serin, J.-P., Houssin, D., Arpentinier, P., Solubility of Carbon Dioxide in Water and Aqueous Solution Containing Sodium Hydroxide at Temperatures from (293.15 to 393.15) K and Pressure up to 5 MPa: Experimental Measurements. *J. Chem. Eng. Data*, 57, 3, 784–789, Mar. 2012.
6. Lucile, F., *Etude thermodynamique des équilibres liquide-vapeur des systèmes complexes CO2-eau-impuretés à haute pression. Expérimentation et modélisation*, thesis, Pau, 2012.
7. Kawazuishi, K. and Prausnitz, J.M., Correlation of vapor-liquid equilibria for the system ammonia-carbon dioxide-water. *Ind. Eng. Chem. Res.*, 26, 7, 1482–1485, Jul. 1987.
8. Joshi, J.B., Mahajani, V.V., Juvekar, V.A., Invited Review Absorption of NOx Gases. *Chem. Eng. Commun.*, 33, 1–41–92, Feb. 1985.
9. Schwartz, S.E. and White, W.H., Solubility Equilibria of the Nitrogen Oxides and Oxyacids in Dilute Aqueous Solution. *Adv. Env. Sci. Eng. U. S.*, 4, Jan. 1981.
10. Gratzel, M., Pulse radiolytic investigation of some elementary processes of oxidation of nitrie ion. *Ber Bunsen Ges.*, 73, 646–653, 1969.
11. Graetzel, M., Taniguchi, S., Henglein, A., Pulse radiolytic study of NO oxidation and of the equilibrium N2O3. dbr. NO+ NO2 in aqueous solution. *Berichte Bunsen Ges.*, 74, ARTICLE, 488–92, 1970.
12. Markovits, G.Y., Schwartz, S.E., Newman, L., Hydrolysis equilibrium of dinitrogen trioxide in dilute acid solution. *Inorg. Chem.*, 20, 2, 445–450, 1981.
13. Vassian, E.G. and Eberhardt, W.H., The Spectrophotometric Determination of the Dissociation Constant of a Cadmium–Nitrite Complex. *J. Phys. Chem.*, 62, 1, 84–87, 1958.
14. Davis, W., Jr. and De Bruin, H.J., New activity coefficients of 0–100 per cent aqueous nitric acid. *J. Inorg. Nucl. Chem.*, 26, 6, 1069–1083, 1964.
15. Vetter, K., Das Gleichgewicht zwischen Stickstoffdioxyd und salpetriger Säure in Salpetersäure. *Z. Für Anorg. Chem.*, 260, 4–5, 242–248, 1949.
16. Sander, R., Compilation of Henry's law constants (version 4.0) for water as solvent. *Atmos. Chem. Phys.*, 15, 8, 4399–4981, Apr. 2015.
17. Pradhan, M.P. and Joshi, J.B., Absorption of NOx gases in aqueous NaOH solutions: Selectivity and optimization. *AIChE J.*, 45, 1, 38–50, Jan. 1999.
18. Meyssami, B., Balaban, M.O., Teixeira, A.A., Prediction of pH in model systems pressurized with carbon dioxide. *Biotechnol. Prog.*, 8, 2, 149–154, Mar. 1992.

4

The Use of IR Spectroscopy to Follow the Absorption of CO_2 in Amine Media – Evaluation of the Speciation with Time

E. Brugère, J-M. Andanson and K. Ballerat-Busserolles*

Institute of Chemistry of Clermont-Ferrand, UMR CNRS, University of Clermont Auvergne, Sigma Clermont, Aubière, France

Abstract

Carbon Capture and Storage (CCS) is a concrete option for CO_2 mitigation in the atmosphere. One option is the CO_2 capture from post-combustion industrial effluents followed by storage in secured sites. Capture processes can be based on selective absorption/desorption cycles of gas into aqueous solutions of alkanolamines [1]. The cost of CO_2 treatment with classical alkanolamines is a limitation for the intensive use of this technology. The SIMODEX project is dealing with coupling experimental developments, molecular simulation and thermodynamic modeling to understand structure-properties relationships, and to develop transferable conclusions to optimize processes at low costs.

This chapter will focus on the use of ATR-IR (Attenuated Total Reflection-infrared) spectroscopy to quantify the speciation in mixtures containing alkanolamine and CO_2, in absence of water, in order to validate the thermodynamic models already used, and to give crucial information for molecular simulation developments.

Keywords: Infrared, spectroscopy, carbon dioxide, amine, speciation

4.1 Introduction

Carbon Capture and Storage (CCS) is a solid option for CO_2 mitigation in the atmosphere. One option is the CO_2 capture from post-combustion industrial effluents followed by utilization or storage in secured sites.

**Corresponding author*: karine.ballerat@uca.fr

Ying Wu, John J. Carroll, Mingqiang Hao and Weiyao Zhu (eds.) Gas Injection into Geological Formations and Related Topics, (41–54) © 2020 Scrivener Publishing LLC

Capture processes are generally based on selective absorption/desorption cycles of gas into aqueous solutions of alkanolamines [1]. The following scheme shows the principle of the process (see Figure 4.1).

In this treatment scheme, the industrial effluent is entering in the absorber at atmospheric pressure and at temperature close to 40°C. Due to favorable chemical reactions, and physical absorption, the CO_2 is selectively captured into the aqueous solution, while the other gases are rejected to the atmosphere. The CO_2 rich solvent is then transported to the stripper, where the loaded solution is heated up to 120°C using a countercurrent steam. The CO_2 is then desorbed from the solvent, separated, compressed and transported for further use, while the lean solvent is returned to the absorber. This last step is the most critical in the process cost, as it necessitates high energy consumption for heating up the system. The cost of CO_2 treatment using classical alkanolamine solutions as absorbent is prohibitive and is a clear limitation for the intensive use of this technology.

In order to provide optimized treatment processes, it is necessary to have a comprehensive understanding of the chemical and physical interactions taking place in the mixture. SIMODEX project is a joint program between ANR (Agence Nationale de la Recherche) in France and NSERC (Natural Sciences and Engineering Research Council of Canada) in Canada dealing with coupling experimental developments, molecular simulation and modeling to understand structure-properties relationships, and to develop transferable conclusions to optimize processes at low costs. The objectives

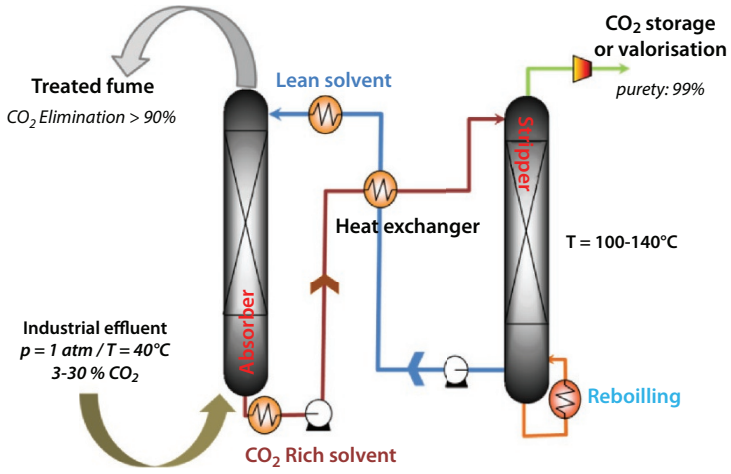

Figure 4.1 Schematic view of the amine based post-combustion CO_2 capture process.

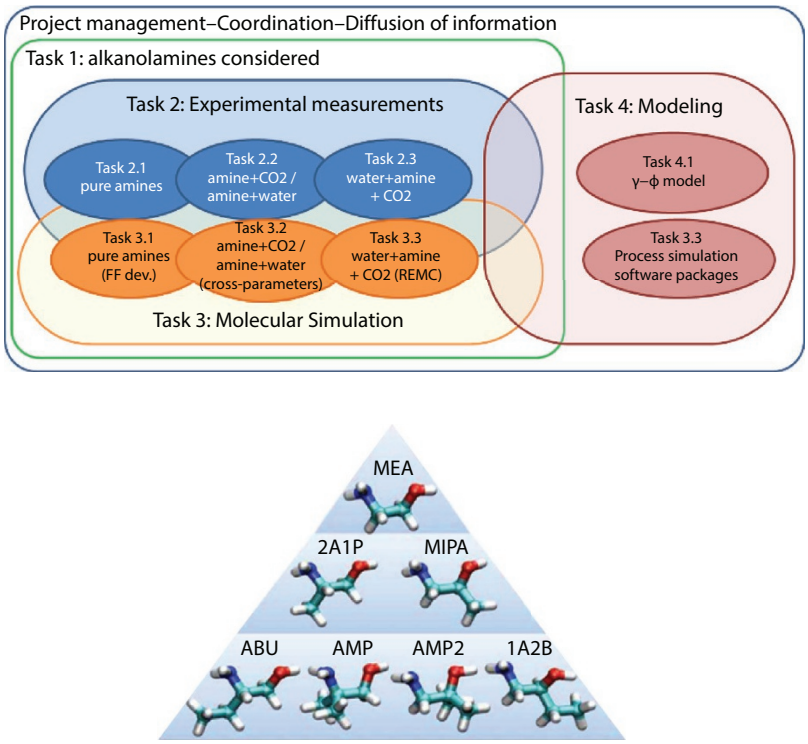

Figure 4.2 Structuration of the SIMODEX project and amine family to be studied.

of the project are to understand the complex equilibria taking place in the ternary water-alkanolamine-CO_2 system by studying the elementary mixtures starting with pure compounds and going through binary ones as shown in Figure 4.2.

This chapter will focus on the use of IR spectroscopy to quantify the speciation in solutions, in order to validate the thermodynamic models already used, and to give crucial information for molecular simulation developments. The mixtures chosen are binary systems containing initially only amine and CO_2, where there is almost no publication in the literature. For this binary mixture the only reaction that may happen during the mixing process is the formation of the carbamate that can be written as following:

$$2 \cdot HOCH_2CH_2CH_2NH_2 + CO_2 \rightarrow HOCH_2CH_2CH_2NHCOO^- + HOCH_2CH_2CH_2NH_3^+ \quad (4.1)$$

As experimental issues happened when studying CO_2-monoethanolamine (MEA) mixtures, such as high increase in viscosity or solid phase formation, a physical solvent, known for not interacting with amine or CO_2 was used. Then ethylene glycol was chosen to dilute the system [2].

More specifically, the speciation in mixtures containing MEA + ethylene glycol + CO_2 will be studied using IR-spectroscopy, and a new *in situ* cell designed for following absorption of gas in liquid mixtures versus time will be described and first promising results presented.

4.2 Materials and Methods

4.2.1 Chemicals

Monoethanolamine (MEA) was purchased in TCI-europe (purity >99%), ethylene glycol is from Riedel and Haën (purity 99.5%) and CO_2 from air products (99.995%). The water quantities in liquids were verified using Karl Fisher measurements, and correspond to 300 ppm and 1000 ppm respectively for amine and glycol.

4.2.2 Sample Preparation

As direct measurements of MEA+CO_2 mixtures were not possible due to increase of viscosity and solid phase generation, the MEA was first mixed with a CO_2 physical solvent, namely the ethylene glycol. A first concentration of 30% of MEA in ethylene glycol was chosen as this is comparable to the classical concentration of MEA in water when studying the solvents used in the process. Then a second concentration of 10% MEA in ethylene glycol was considered to reach more easily the complete stoichiometric reaction of the CO_2 on MEA.

4.3 Experimental Device

The spectroscopic measurements, realized at atmospheric pressure and room temperature, were performed using a heatable Golden Gate™ accessory (Specac, Ltd., UK) with a diamond as ATR (Attenuated Total Reflection) crystal. The ATR-IR spectra were collected by means of Thermo Nicolet™ 380 FT-IR spectrometer with a DTGS (deuterated triglycine sulfate) detector. The spectra were obtained with a resolution of 4 cm^{-1}, 32 co-added scans and were recorded in the range of 4000–500 cm^{-1}. The measurement of one spectrum takes around 50 seconds.

For the spectroscopic measurements under pressurized CO_2 a heatable Golden Gate™ accessory (Specac, Ltd., UK) equipped with a home-designed pressurized cell was used. Briefly, the Golden Gate™ was used to hold the ATR crystal with an incident angle of 45° below the liquid phase of interest. Some modifications on the design of the bridge were realized to support a customized sapphire cell as shown in Figure 4.3. Two aluminum arms (1) were added to the bridge to increase the space between the thumb screw and the diamond in order to fit with the new high volume cell (2+4) and a stirring mechanism (3).

The liquid cell was installed on the top of the heating plate of the Golden Gate™ as shown on Figure 4.3. The internal volume of the cell is about 2 ml. The cell is composed of a sapphire cylinder surrounded by an inox block. Heating cartridges and PT100 resistances are inserted in the inox cylinder to control the temperature of the sample. Two windows are present in the inox cylinder, so the inside of the cell can be observed during the whole experiment. A Teflon ring was installed between the cell and the plate to prevent leaking.

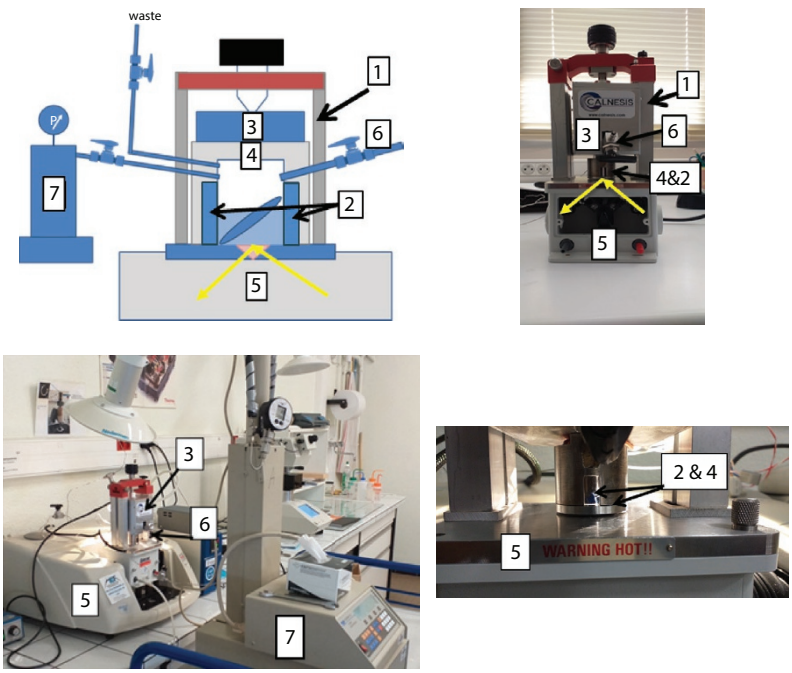

Figure 4.3 New experimental setup for gas absorption : 1. Aluminum arms; 2. sapphire cylinder; 3. magnetic stirrer; 4. inox cell, surrounding sapphire cylinder; 5. ATR-IR spectrometer; 6. liquid injection valve; 7. high pressure pump equipped with pressure transducer and gas injection valve.

The liquid is inserted using the injection valve (6) until the needed volume of liquid is obtained. About 1 mL of liquid is introduced in the cell. After reaching the temperature equilibrium, the gas is added using the gas injection valve, while the pressure is maintained constant using the high-pressure syringe pump. As the magnetic stirrer is agitating the solution, the diffusion of the gas in the liquid starts immediately.

The IR spectra are then recorded every minute from the beginning of the experiment. When the evolution of the peaks is reduced, the spectra are measured every 5 minutes, until the signal becomes constant, or when the gas contained in the high-pressure pump is consumed.

4.4 Results and Discussion

4.4.1 Kinetic of Absorption

A first kinetic experiment was realized using a liquid mixture containing initially MEA (10% w/w) and ethylene glycol (90% w/w). IR spectra of direct measurements are reported on the top Figure 4.4. The mixture was introduced in the cell, and a first spectrum was realized. Then the valve isolating the CO_2 from the system was open and the gas started flowing in the head space of the cell.

In order to interpret the results, the spectrum obtained for the binary mixture without gas (t=0 minute) was subtracted to the subsequent spectra as shown on the bottom Figure 4.4. All positive peaks after subtraction are characteristics of new species appearing in the liquid during the sorption while negative peaks correspond to the disappearance of pre-existing species. In order to quantify the speciation versus time in such systems, it is necessary to determine a relation between the intensity of the IR signals and the quantity of each species.

4.4.2 Calibration of Speciation

4.4.2.1 Sample Preparation

In order to realize the calibration of the absorption of CO_2 in MEA as function of the loading charge, it was necessary to record spectra containing very well-known concentrations of MEA and CO_2. For that purpose, a mixture of MEA + ethylene glycol was prepared by weight. Then CO_2 was added above the liquid sample, for 12 hours, under a pressure of CO_2 of 0.2 MPa (2 bar), while the liquid phase was agitated using a magnetic stirrer. Then

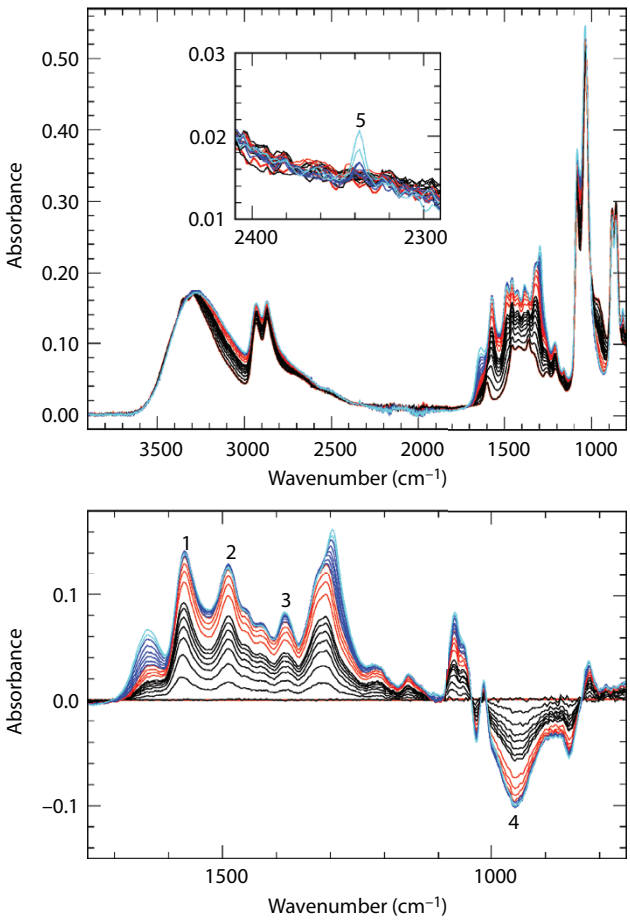

Figure 4.4 IR spectra during the kinetic of the sorption of CO^2 in MEA-Ethylene glycol mixture (top) and MEA-Glycol-CO_2 after subtraction of the MEA-Glycol spectrum (bottom) at different time; 1-3 peaks: characteristic peaks for carbamates; 4: characteristic peak for non-protonated amine; 5: asymmetric stretching vibration band for physically absorbed CO_2. The spectra obtained during the first 10 minutes are the black ones. The red spectra are obtained for a time from 10 to 40 minutes, while blue ones are for times longer than 40 minutes after the beginning of the CO_2 sorption.

the mixture was returned to atmospheric pressure. The sample was then weighted, and the mass difference with the sample without CO_2 was considered as corresponding to the mass of CO_2 absorbed in the sample. This very concentrated sample was diluted using the initial mixture of MEA+Glycol, in different proportions to reach various CO_2 loading charges.

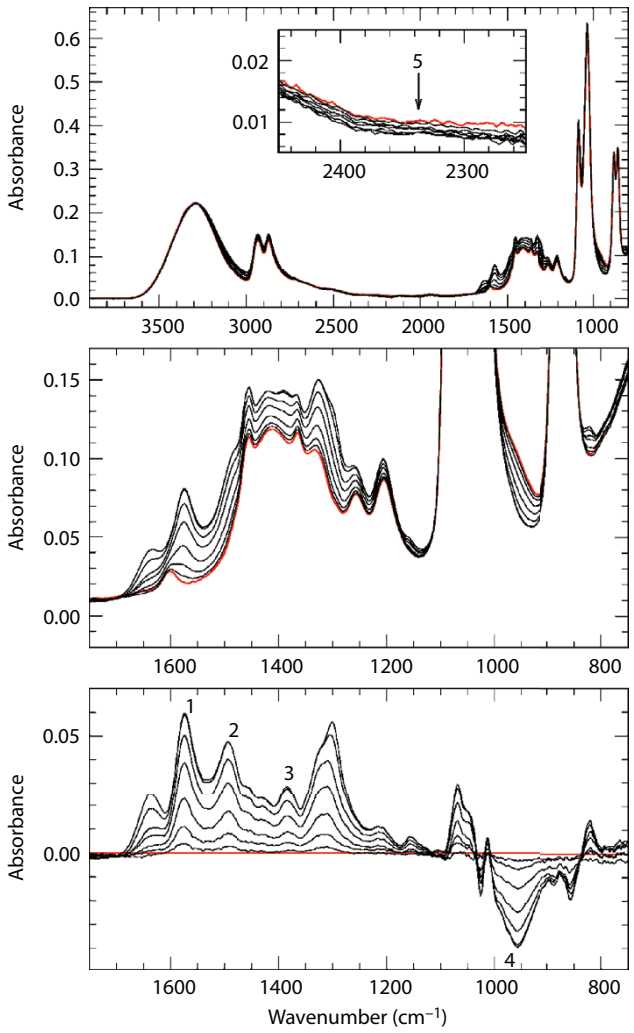

Figure 4.5 IR spectra for mixtures containing MEA (30%) ethylene glycol (70%), at different and well known loading charges from a = 0 up to a = 0.53. Top figure: direct spectra; middle figure: zoom of the spectra in the range of 1700-750 cm^{-1}; bottom figure: fingerprint region of the IR spectra of the MEA-ethylene glycol-CO_2 mixtures after subtraction of the MEA-ethylene glycol spectrum.

4.4.2.2 Spectra and Results

The spectra obtained for the calibration are given in Figure 4.5. The first graph shows the direct spectra obtained for mixtures at known loading charge, from α =0 to 0.5 (α = mol of CO_2 / mol of amine) while the

second one present a zoom of the fingerprint region (1700–750 cm^{-1}), where most of the bands of organic compounds are regrouped. The red spectrum corresponds to the sample obtained for MEA+Glycol solution without CO_2.

As previously described, and in order to be able to analyze the results, the red spectrum was subtracted to the others as shown on the third graphic of Figure 4.5. On this graph, 4 peaks have been identified and used to calibrate the amount of absorbed CO_2. Peaks labelled from 1 to 3 correspond to peaks characteristic of vibration in carbamate molecules [3]. The peak 4 centered at 960 cm^{-1} is characteristic of non-protonated nitrogen of MEA [3]. When increasing CO_2 loading charge, the height of all those peaks increases. Peaks 1 to 3 are more and more positive while the peak 4 is more and more negative. This corresponds naturally to the generation of carbamate and consumption of non-protonated MEA following the equation 1 shown above. The signal corresponding the physisorbed CO_2 (band label 5 in Figure 4.5 at around 2340 cm^{-1}) has not been detected for the concentrations realized during the calibration.

In order to calibrate the system, it is necessary to relate the height (or the area) of each peak to the loading charge. The peak 4 was truncated on the left side due to peak displacements during the absorption. Then, for this peak we considered the height of the peak as the characteristic data. For peaks 1 to 3 it was possible to use the integration that reduces the uncertainty on the result. The curves representing area of peaks 1 to 3, and height of peak 4 versus loading charge are given in Figure 4.6.

From those calibrations, it is then possible to recalculate at any time of a kinetic experiment the quantity of each species formed when the loading charge is below 0.45. When the concentration of CO_2 is higher the increase of the IR signals are much slower, probably part of the CO_2 does not react but is physisorbed. Furthermore, it was not possible to prepare mixtures containing high amount of CO_2 physically absorbed in the binary mixture. For that purpose, CO_2 was then absorbed in pure ethylene glycol under higher pressure directly in the ATR-IR cell.

4.4.2.3 Physisorption

As it can be seen on Figure 4.7, during the kinetic of the CO_2 sorption in the MEA-Ethylene glycol mixture, after one hour, it is possible to observe a small signal at around 2340 cm^{-1} corresponding to the asymmetric stretching vibration of the CO_2 physically absorbed in the mixture. In order to quantify this CO_2, it is then necessary to calibrate this band. For that purpose, a mixture of ethylene glycol + CO_2 was measured at high pressure.

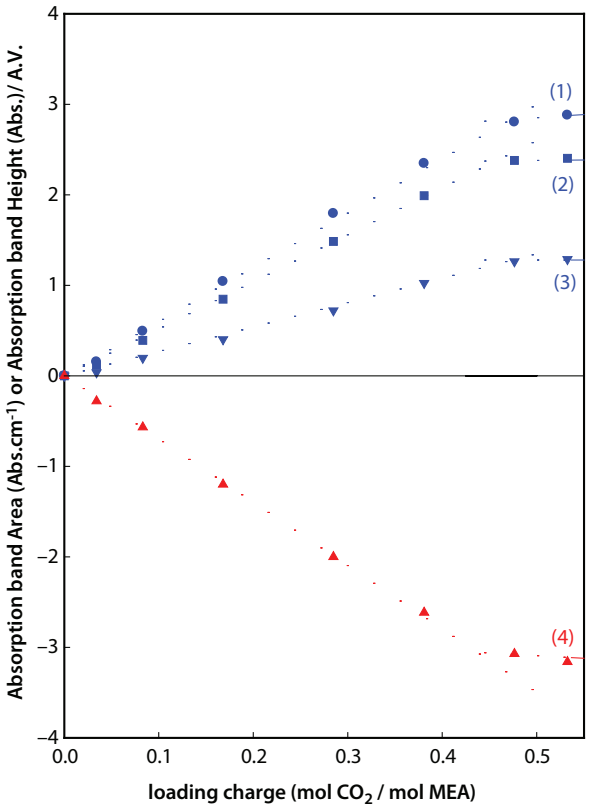

Figure 4.6 Area (peak 1 to 3) and height (peak 4) of the IR signals characteristic to chemical reaction occurring in the mixture.

On Figure 4.7, the black curve shows the signal obtained for pure ethylene glycol. Measurements have then been realized for mixtures of CO_2 + glycol, at 2.0 MPa, 35°C at different times. Two spectra obtained for different times are shown on Figure 4.7 (red and blue spectra). Two phenomena have to be observed. The intensity of all bands corresponding to the ethylene glycol is decreasing with the sorption of CO_2. These decreases of intensity are explained by the swelling of the solvent due to the presence of CO_2. This phenomenon is well known and documented in the literature, particularly in the case of liquid [4, 5].

When looking at absorbance close to 2340 cm^{-1} it is easy to observe an intense peak corresponding to the CO_2 physically absorbed in ethylene glycol. The rest of the spectra is identical with and without CO_2, apart from the decreasing of the intensity of bands corresponding to

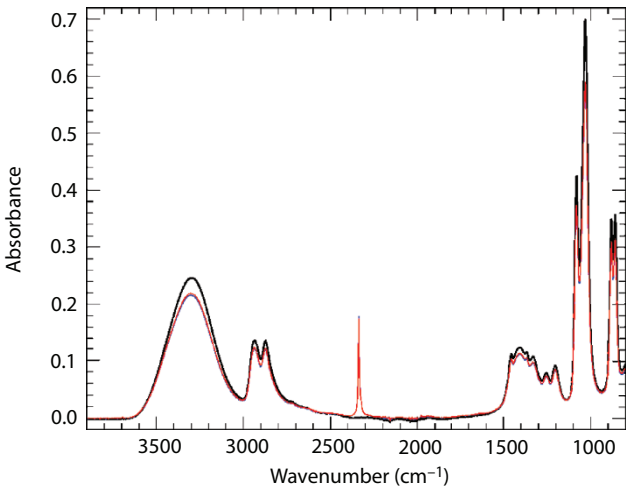

Figure 4.7 IR spectra for pure ethylene glycol (black curve) and CO_2 in ethylene glycol (red and blue curve) at 20.0 bar and 35°C.

the swelling of the ethylene glycol, meaning that no chemical reaction happened in those mixtures. The area of the CO_2 peak at 2340 cm^{-1} can then be directly associated to the solubility of CO_2 in ethylene glycol using literature value [6]; at this temperature and pressure, the solubility of CO_2 in ethylene glycol is $x_{CO2} = 0.0369 \pm 0.0006$. Admitting that the absorption of CO_2 in ethylene glycol follow the Beer-Lambert law, a linear regression was determined between zero and this concentration to estimate the quantity of CO_2 absorbed in solutions of interest.

4.4.2.4 Full Curve Speciation

The evolution of absorptions of the characteristic bands of different species versus time shown in Figure 4.5, were plotted in Figure 4.8. Carbamate vibrations are shown in blue, while the vibration of the none-protonated amine group of MEA is in red. The signals of the physically absorbed CO_2 in the MEA-Glycol mixture correspond to the black empty circle.

On this figure one can see that the absorbance area for peaks corresponding to carbamate increases quickly during the first 20 minutes. The quantity of none protonated amine decreases synchronously to the appearance of carbamate. All the blue and the red curves reach a plateau after 30 minutes. Using the calibration curves shown before, at this time, the value of absorbance correspond to a loading charge of about 0.4. Parallel, during the first 40 minutes, no peak for physical absorption is observed. After this time, the

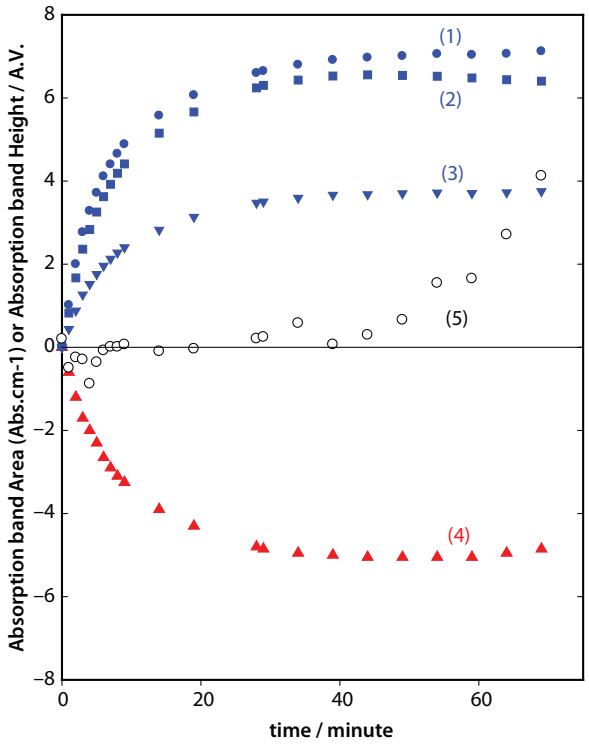

Figure 4.8 Area/height of the peaks versus time. Blue curves: area of characteristic peaks for carbamate (wavelength 1573, 1495 and 1385 cm^{-1} respectively for peaks 1 to 3); red curve: height of characteristic peak for non-protonated MEA (peak 4); black circle: area of characteristic peak for physically absorbed CO_2 (peak 5; signal multiply by 100 for visibility).

intensity of the band starts to increase continuously. After 70 minutes the CO2 physically absorbed corresponds to a molar fraction of 0.002. With this graph, it is confirmed that the chemical reaction is the first step of the process, while the physical absorption starts only when most of the non-protonated amine has reacted with CO_2 to form carbamate and protonated amine.

4.5 Conclusion

In situ ATR-IR spectroscopy has been used successfully to follow the absorption of CO_2 in binary liquids containing MEA and ethylene glycol. The spectra obtained have shown peaks characteristic of carbamate formation, and none protonated amine consumption. After calibrating the signal, the area of the peaks linked to carbamates, and the height of the

peak corresponding the none protonated amine has been associated to an advancement of the reaction of formation of carbamate.

The same experiments will be carried out with amines with a skeleton similar to MEA, as shown on Figure 4.2. The results obtained will allow evaluating the influence of the substituents on the carbons of the MEA on the chemical reaction leading to carbamate formation. It will be possible to compare the kinetic of the reaction as well as the final advancement of the reaction.

4.6 Acknowledgments

This work is part of the international project SIMODEX supported by ANR in France and NSERC in Canada. The authors also acknowledge the financial support received from the Agence Nationale de la Recherche of the French government through the program "Investissements d'Avenir" (16-IDEX-0001 CAP 20-25).

References

1. Raynal, L., Bouillon, P.-A., Gomez, A., Broutin, P., *Chem. Eng. J.*, 171, 742, 2011.
2. Yu, C.-H., Huang, C.-H., Tan, C.-S., *Aerosol Air Qual. Res.*, 12, 745–769, 2012.
3. Sun, C., Dutta, P.K., *Ind. Eng. Chem. Res.*, 55, 22, 6276-6283, 2016.
4. Pasquali, I., Andanson, J.-M., Kazarian, S.G., Bettini, R., *J. Supercrit. Fluids*, 45, 3, 384–390, 2008.
5. Andanson, J.-M., Jutz, F., Baiker, A., *J. Phys. Chem. B*, 113, 30, 10249–10254, 2009.
6. Gui, X., Tang, Z.G., Fei, W., *J. Chem. Eng. Data*, 56, 2420–2429, 2011.

5

Solubility of Methane, Nitrogen, Hydrogen Sulfide and Carbon Dioxide in Mixtures of Dimethyl Ethers of Polyethylene Glycol

Alan E. Mather[1] and Kurt A. G. Schmidt[2]*

[1]Department of Chemical and Materials Engineering, University of Alberta, Edmonton, AB, Canada
[2]Schlumberger, Calgary, AB, Canada

Abstract

Mixtures of dimethyl ethers of polyethylene glycol (DMPEG) are physical solvents which have been used for the separation of acid gases from gas streams. An advantage of DMPEG mixtures is the high solubility of acid gases compared with the low solubility of light hydrocarbons. The solubility of the light hydrocarbons in DMPEG is important, as the hydrocarbons constitute a loss to the process, and result in hydrocarbon emissions to the atmosphere.

The design of separation facilities with mixtures of DMPEG requires accurate modelling techniques that can capture the vapor-liquid equilibrium properties of these systems over the appropriate operating conditions. An exhaustive review of the data available in the literature revealed a limited number of experimental points for these systems. Since only limited data exist in the open literature, new solubility measurements were performed on binary mixtures of nitrogen, methane, carbon dioxide and hydrogen sulfide with a mixture of DMPEG. A solubility model based on the Peng-Robinson Equation of State was developed from literature data and the new experimental data.

The ability of the Peng-Robinson Equation of State to calculate the solubility of N_2, CH_4 and acid gases (CO_2 and H_2S) in a mixture of DMPEG will be shown. Henry's law constants obtained from the approach will be compared with those previously reported in the literature.

Keywords: Vapor-liquid equilibrium, separations, equation of state, Krichevsky-Ilinskaya, methane, nitrogen, hydrogen sulfide, carbon dioxide, dimethyl ethers of polyethylene glycol mixtures

**Corresponding author*: kschmidt@slb.com

Ying Wu, John J. Carroll, Mingqiang Hao and Weiyao Zhu (eds.) Gas Injection into Geological Formations and Related Topics, (55–76) © 2020 Scrivener Publishing LLC

5.1 Introduction

This work was undertaken to determine if the Peng-Robinson Equation of State (EoS) [1] could be used to model the solubility of nitrogen, methane, carbon dioxide, hydrogen sulfide in a mixture of polyethylene glycol dimethyl ethers, a solvent commonly used for the removal of acid gases (H_2S and CO_2) from natural gas streams [2]. Unfortunately, there are few data sets which contain the solubility of nitrogen, methane, carbon dioxide, hydrogen sulfide in mixtures of DMPEG. In order to provide data needed for validate models used in important design decisions, this laboratory at the University of Alberta embarked on a research program to fill the voids in the existing literature data sets and test the most common EoS (PR EoS) used in gas treating.

5.2 Experimental

The apparatus and experimental techniques that were used are similar to those described by Jou *et al.* [3]. The equilibrium cell was mounted in an air bath. The temperature of the contents of the cell was measured by a calibrated iron-constantan thermocouple and the pressure in the cell was measured by digital Heise gauges. The uncertainty in the pressure was ±0.1% of full scale by comparison with a dead-weight gauge. The experimental uncertainty in the temperature was ±0.1 K by comparison with a platinum resistance thermometer. A magnetically driven piston pump was used to circulate the gas phase and bubble it through the liquid solution. The physical solvent (a mixture of dimethyl ethers of polyethylene glycol) was obtained from Exxon. The other chemicals were obtained from Praxair: nitrogen with a purity of 99.99%, methane with a purity of 99.97%, carbon dioxide with a purity of 99.9% and hydrogen sulfide with a purity of 99.5%.

Approximately 100 cm^3 of the physical solvent was charged to the evacuated cell. Gases were added in an amount determined by observation of the pressure. To ensure that equilibrium was reached, the vapor was bubbled through the liquid for at least 8 h prior to sampling the vapor and liquid phases. The vapor phase was analysed by gas chromatography. For nitrogen and methane, the liquid phase was analysed by a volumetric method. A sample was taken into a sample bomb that had previously been evacuated and weighed. The bomb was reweighed to determine the mass of the sample and was attached to a vacuum rack. The gas was allowed to evolve from the liquid into a buret, which was maintained at the local atmospheric pressure and room temperature. The moles collected were calculated from

Table 5.1 Experimental conditions.

Solute	Temperature (°C)	Partial pressure range (MPa)
H_2S	0, 25, 37.8, 60, 100 & 150	3.3×10^{-4} – 14.4
CO_2	-20, 0, 15.6, 25, 37.8, 60, 80, 100, 125 & 150	1.1×10^{-3} – 20.0
CH_4	-20, -15, 0, 10, 15.6, 25, 40, 60, 80, 100, 125 & 150	1.0×10^{-1} – 20.5
N_2	0, 15.6, 37.8, 60, 80, 100, 125 & 150	8.7×10^{-2} – 20.0

the P-V-T data, assuming ideal gas behavior. A correction was made for the residual nitrogen or methane left in the sample at atmospheric pressure by injection of an aliquot into the gas chromatograph.

For carbon dioxide and hydrogen sulfide, a known weight of loaded solution was drawn into a 1 M NaOH solution to form Na_2CO_3 or Na_2S. The concentration of CO_2 in an aliquot of liquid sample was determined by mixing the liquid with 0.1 N $BaCl_2$ solution to form a precipitate of $BaCO_3$. This precipitate was filtered and washed. It was titrated with 0.1 N HCl using methyl orange-xylene cyanol indicator. The concentration of H_2S in an aliquot of liquid sample was determined by mixing the liquid with an excess of acidic 0.1 N I_2 solution. The excess I_2 was back-titrated with 0.1 N $Na_2S_2O_3$ solution using a starch indicator. The uncertainty in the liquid phase analyses is estimated to be +/- 3%.

The conditions of the experiments for each gas solute are presented in Table 5.1.

5.3 Equation of State Development

The approach of Jou *et al.* [4] was used to model the phase equilibrium data. This approach uses the Peng–Robinson (1976) EoS:

$$P = \frac{RT}{V-b} - \frac{a(T)}{V(V+b)+b(V-b)} \tag{5.1}$$

The parameters a_{22} and b_2 of nitrogen, carbon dioxide, methane and hydrogen sulfide were obtained from the critical constants and acentric

factors found in Rowley *et al.* [5]. Consistent with that modelling approach, the parameters a_{11} and b_1 for the solvent (DMPEG mixture) were obtained directly from the vapor pressure and liquid density of the solvent. Due to the lack of these properties being directly measured by this laboratory, values from the literature were used.

Although not directly related to the modelling approach the composition of the mixture of polyethylene glycol dimethyl ethers used in the experimental work is presented in Table 5.2.

The DMPEG mixture has a measured molar mass of 277.5. This fluid was also used by Schmidt and Mather [6]. Compositions of DMPEG mixtures have also been presented by Michaeli and Stein [7], Wölfer [8], van Deraerschot [9], Wölfer [10], Wölfer [11], Stöll and Röper [12], Herraiz *et al.* [13], Conesa *et al.* [14] and Nannan *et al.* [15]. As can be seen in Table 5.2 (and the above references), the solvent is a multicomponent mixture consisting of DMPEG ranging from di-ethylene glycol dimethyl ether, n=2, to undeca-ethylene glycol dimethyl ether, n=11. The range of ethylene glycol dimethyl ethers or glymes (and their relative concentrations) in commercially available mixtures of DMPEG is not standardized. As such each mixture has different volatilities and volumetric properties.

Table 5.2 Composition of DMPEG mixture used in this investigation.

n-DMPEG	**wt %**
2	6.0
3	19.6
4	25.7
5	22.3
6	14.7
7	7.3
8	3.2
9	1.2
10	0.2
11	6.0

Unfortunately, there is only a limited amount of vapor pressure and density data for DMPEG mixtures in the open literature. Vapor pressure data were found in the following sources: Clare and Valentine [16], van Deraerschot [9], Wölfer [8], Wölfer [10], Wölfer *et al.* [17], Wölfer *et al.* [18], Kuwairi [19], Bucklin and Schendel, [20], Demyanovich and Lynn [21], Shah and Szymborski [22], Stüven [23] and Chen [24]. Unfortunately, most of the vapor pressure data of DMPEG mixtures had to be inferred from digitized figures and from vapor pressure data of a variety of mixtures (e.g., Selexol, PEGDME 250 and Genosorb 1753). Density data were found in the following sources: Sweeny and Brooks [25], Clare and Valentine [16], Wölfer [8], van Deraerschot [9], Wölfer [10], Bucklin and Schendel [20], Demyanovich and Lynn [21], Esteve *et al.* [26], Esteve *et al.* [27], Conesa *et al.* [14], Pereira *et al.* [28], Li *et al.* [29]. Similar to the vapor pressure data set, the volumetric data used in this study came from a variety of DMPEG mixtures.

The style and the paucity of data makes the determination of EoS parameters for such mixtures challenging. Based on the available information, a detailed solvent characterization, similar to a multicomponent characterization of oils in the petroleum industry [30], could not be used for the DMPEG mixture. In this investigation, a pseudo-component with pure EoS properties (Tc, Pc, ω) was used to represent the mixture of DMPEG.

The vapor pressure and density of the pseudo-DMPEG mixture, used to represent the solvent used in the experiments, were determined at each temperature from smoothed equations of the respective vapor pressure and density datasets described above. The saturation pressure algorithm of Wisniak *et al.* [31] was used to calculate the saturation properties of the DMPEG mixture and regress the a_{11} and b_1 parameters. Figures 5.1 and 5.2 compare the difference between the literature data, the pure glymes, tri, tetra and penta (Rowley *et al.* [5]), the smoothed correlations and those calculated by the Peng Robinson EoS.

The binary interaction parameter for each solute, k_{12}, which appears in the mixing rule of the equation of state

$$b = \sum_{i=1}^{NC} x_i b_i \tag{5.2}$$

$$a(T) = \sum_{i=1}^{NC}\sum_{j=1}^{NC} x_i x_j \sqrt{a_{ii}a_{jj}}\,(1-k_{ij}) \tag{5.3}$$

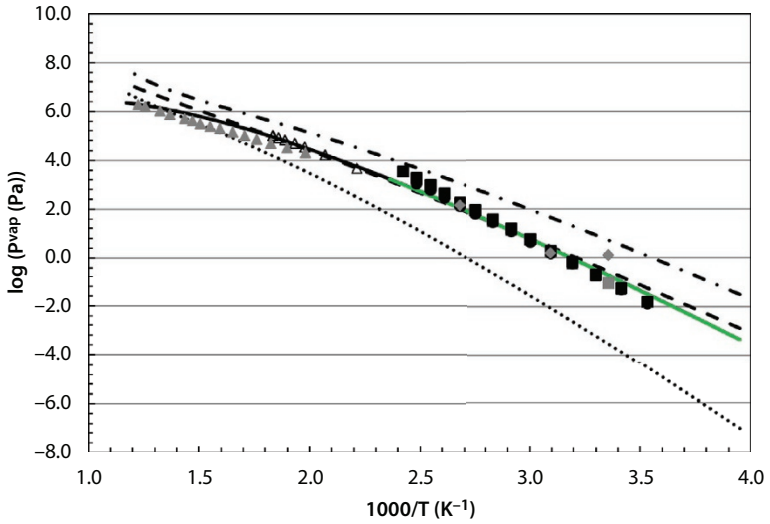

Figure 5.1 DMPEG mixture vapor pressures comparison. ◇, Clare and Valentine [16]; ○, van Deraerschot [9]; ◆, Wölfer [8]; ●, Wölfer [10]; ▲, Wölfer *et al.* [17]; ■, Wölfer *et al.* [18]; △, Kuwairi [19]; □, Bucklin and Schendel [20]; grey ◆, Demyanovich and Lynn [21]; ●, Shah and Szymborski [22]; ▲, Stüven [23]; ■, Chen [24]. Solid line, Smoothed vapor pressure correlation; round dot line, pentaglyme [5]; dash line, tetraglyme [5]; dash dot line, triglyme [5]; solid line, EoS.

was regressed from the experimental solubility data. In all the binary solute-solvent systems, a linear temperature dependent binary interaction parameter was used.

The data span many orders of magnitude, so minimizing the sum of the squares of the differences between measured and fitted values would weight the high pressure data almost to the exclusion of the low pressure data. The simple unbiased objective function used by Weiland *et al.* [32] weights all data equally.

$$\boldsymbol{c}_{\text{Relative Difference Regression}} = \arg\min_{c} \sum_{i} \left(\frac{\left(yc_i - f(xc_i, \boldsymbol{c}) \right)^2}{\left| (yc_i) \cdot f(xc_i, \boldsymbol{c}) \right|} \right) \tag{5.4}$$

Where $\boldsymbol{c}$ is the parameter vector, f is the model function and (xc_i, yc_i) are the experimental data. The denominator is designed to give equal weight to all the data, regardless of the magnitude of the measured quantity. The robust regression algorithm of Schmidt *et al.* [33] was used to minimize the

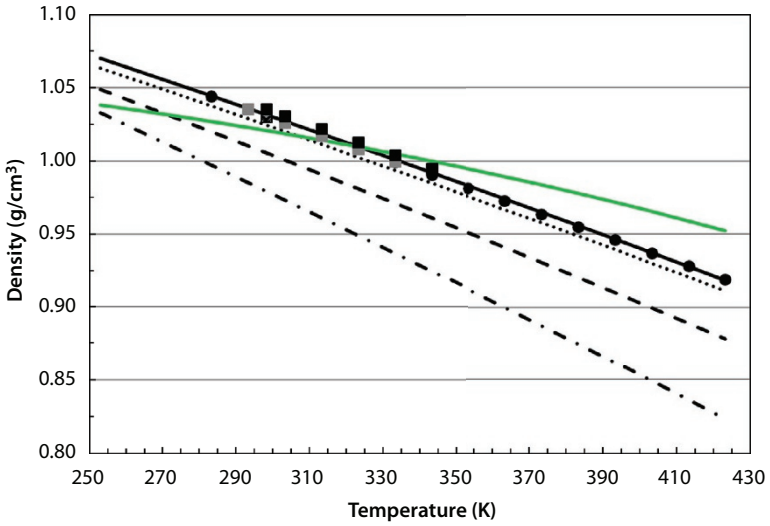

Figure 5.2 DMPEG mixture mass density comparison. grey ●, Sweeny and Brooks, [25]; ◇, Clare and Valentine [16]; ○, van Deraerschot [9]; ◆, Wölfer [8]; ■, Wölfer *et al.* [18]; □, Bucklin and Schendel [20]; ◈, Demyanovich and Lynn [21]; △, Esteve *et al.* [26]; ▲, Esteve *et al.* [27]; ●, Conesa *et al.* [14]; ■, Pereira *et al.* [28]; ▲, Li *et al.* [29]. Solid line, Smoothed mass density correlation; round dot line, pentaglyme [5]; dash line, tetraglyme [5]; dash dot line, triglyme [5]; solid line, EoS.

objective function. This regression routine incorporates an outlier detection routine based on the Benjamini-Hochberg [34] test for significance. Use of this robust regression technique improves the parameterization of the model because the data points with significant deviations are excluded from the regression. This results in the final regression equation given by Equation (5.5), where M experimental measurements out of N total measurements are excluded.

$$\boldsymbol{c}_{\text{Robust Regression}} = \arg\min_{c} \sum_{i}^{N-M} \left(\frac{\left(yc_i - f(xc_i, \mathbf{c}) \right)^2}{\left| yc_i \cdot f(xc_i, \mathbf{c}) \right|} \right) \tag{5.5}$$

In this investigation, the objective function which related the differences between the calculated saturation pressures and the experimental values was used. A saturation pressure calculation was performed at each measured experimental liquid phase composition and temperature. A modified saturation pressure algorithm presented by Whitson and Brulé [35] was

used. The modified algorithm used the stability test approach described in Saber and Shaw [36].

5.4 EoS Model Results

With the regression approach described above, all the experimental saturation pressures could be calculated to within an overall average absolute percentage deviation (AAPD, denoted Δ),

$$\Delta = \frac{100}{N} \sum_{i=1}^{N} \left| \frac{yc_i - f(xc_i, \boldsymbol{c})}{yc_i} \right| \tag{5.6}$$

of 2.6, 4.0, 20.5, 14.5% for N_2, CH_4, H_2S and CO_2, respectively. The AAPD between the optimal model and that of the data used in the parameterization (i.e., data points not deemed outliers) was 2.2, 2.8, 13.9, 11.1% for N_2, CH_4, H_2S and CO_2, respectively. The model results are compared with the experimental results in Figures 5.3–5.6. As can be seen in Figures 5.5 and 5.6, H_2S and CO_2 have four orders of magnitude difference in partial pressures and have solute liquid mole fractions which range from 0.001 to ~0.99. The temperature range of the data is 150 K (H_2S and N_2) and 170 K (CO_2 and CH_4). This is an exceptional range of solubility measurements for these systems.

This modelling approach reproduces the CH_4 and N_2 experimental data very well (to within the experimental uncertainty) and H_2S and CO_2 experimental data reasonably well. It appears that the modelling approach does not capture the solubility of the highly soluble solutes (H_2S and CO_2) as well as it captures the solubility of CH_4 and N_2 over the extreme ranges of data. Based on the regression results, the inconsistency between the model and the data (H_2S and CO_2) is most likely attributed to a combination of the limitation of the model's performance and the higher experimental uncertainty at the far ends of the concentration interval for these acid gases.

There may be a number of reasons for the poorer performance of the model for the CO_2 and H_2S systems. Due to insufficient data of the DMPEG mixture, the EoS characterization of the DMPEG mixture may not capture the chemical physics of the solvent and hence the interactions of the highly soluble solutes. Additionally, the EoS, with van der Waals mixing rules, may be insufficient for the significant ranges (temperature, pressure and composition), which were covered in the measurements.

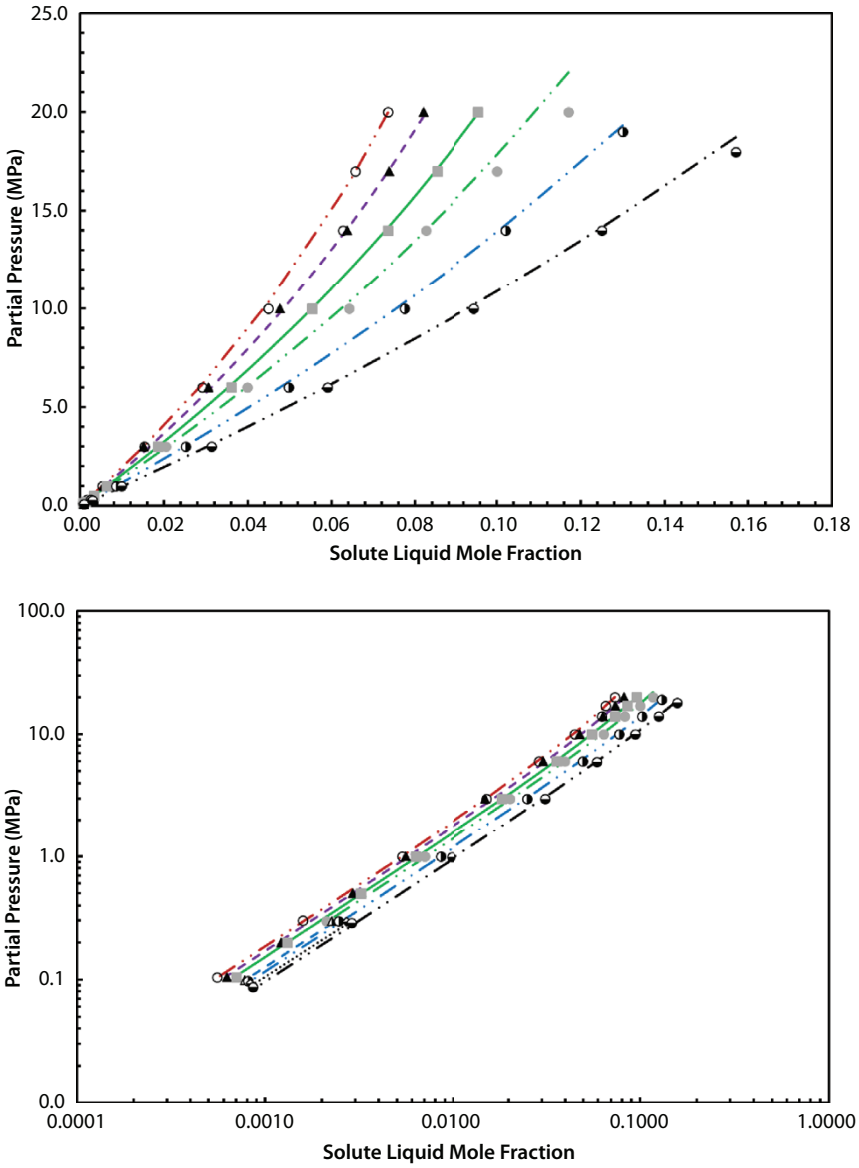

Figure 5.3 Experimental data for nitrogen (1) + DMPEG (2) system compared with correlated values using the Peng-Robinson equation of state. Experimental data: ○, 273.15 K; ▲, 288.75 K; ■, 310.95 K; ●, 333.15 K; ◮, 353.15 K; ◑, 373.15 K; ◆, 398.15 K; ◒, 423.15 K; Peng-Robinson equation of state: long dash dot dot, 273.15 K; dash, 288.75 K; solid line, 310.95 K; long dash dot dot, 333.15 K; dash, 353.15 K; long dash dot dot, 373.15 K; round dot, 398.15 K; long dash dot dot, 423.15 K.

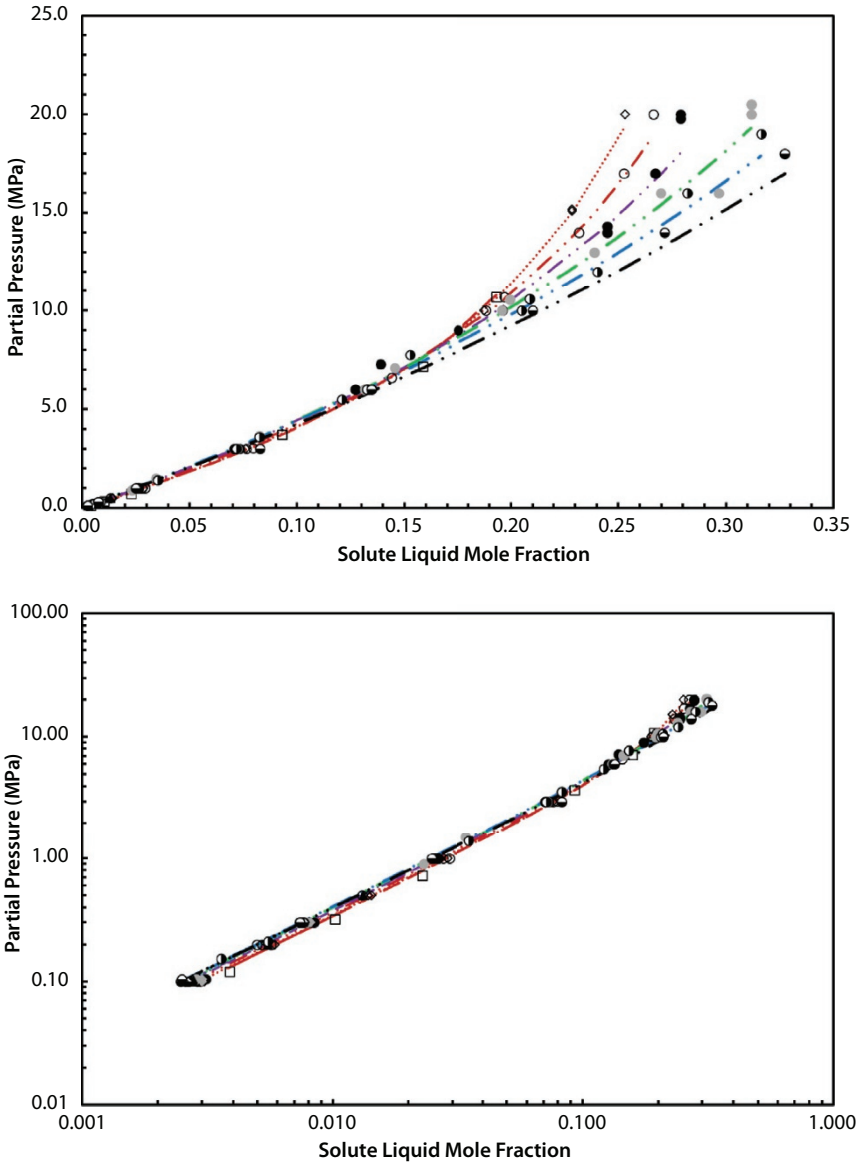

Figure 5.4 Experimental data for methane (1) + DMPEG (2) system compared with correlated values using the Peng-Robinson equation of state. Experimental data: □, 253.15 K; ◇, 258.15 K; ○, 273.15 K; ▲, 288.75 K; ●, 298.15 K; ◆, 313.15 K; ●, 333.15 K; ◭, 353.15 K; ◑, 373.15 K; ◆, 398.15 K; ◒, 423.15 K; Peng-Robinson equation of state: solid line, 253.15 K; round dot, 258.15 K; long dash dot dot, 273.15 K; dash, 288.75 K; long dash dot dot, 298.15 K; round dot, 313.15 K; long dash dot dot, 333.15 K; dash, 353.15 K; long dash dot dot, 373.15 K; round dot, 398.15 K; long dash dot dot, 423.15 K.

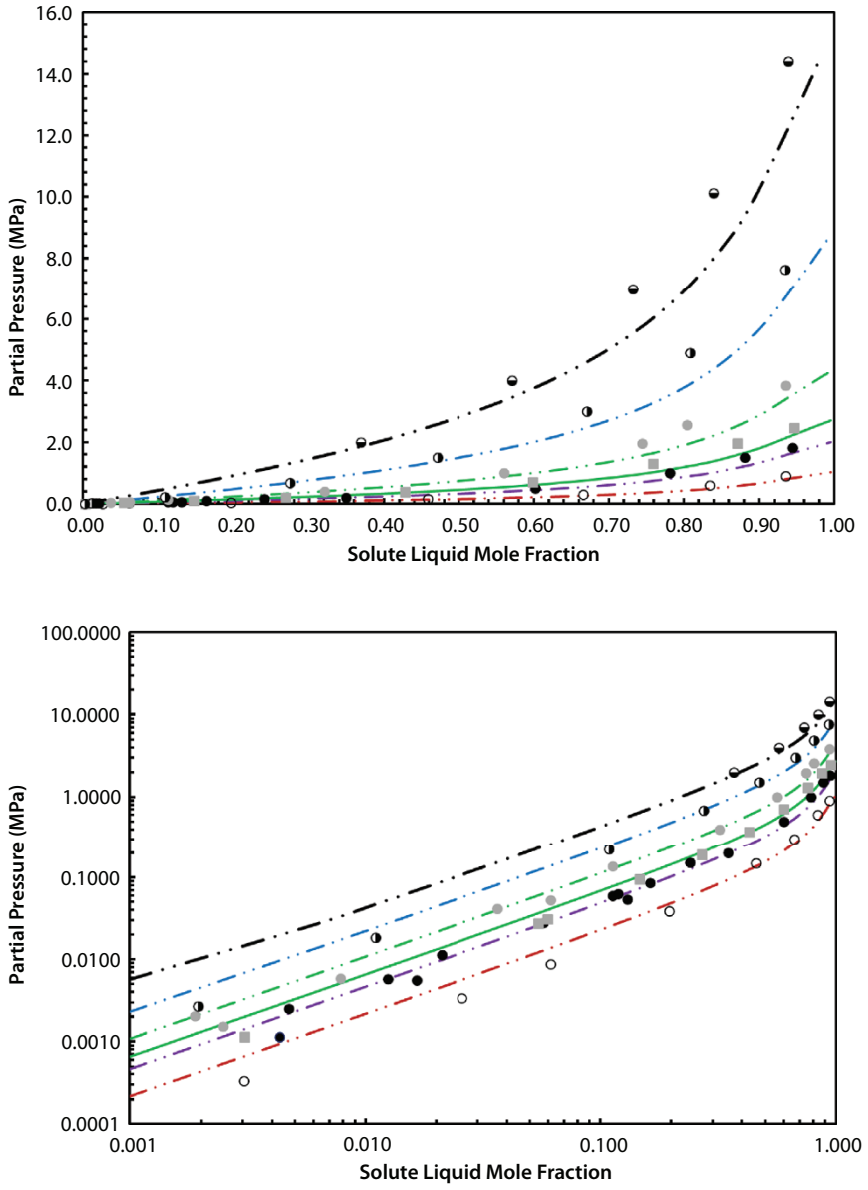

Figure 5.5 Experimental data for hydrogen sulfide (1) + DMPEG (2) system compared with correlated values using the Peng-Robinson equation of state. Experimental data: ○, 273.15 K; ●, 298.15 K; ■, 310.95 K; ●, 333.15 K; ◑, 373.15 K; ◒, 423.15 K; Peng-Robinson equation of state: long dash dot dot, 273.15 K; long dash dot dot, 298.15 K; solid line, 310.95 K; long dash dot dot, 333.15 K; long dash dot dot, 373.15 K; long dash dot dot, 423.15 K.

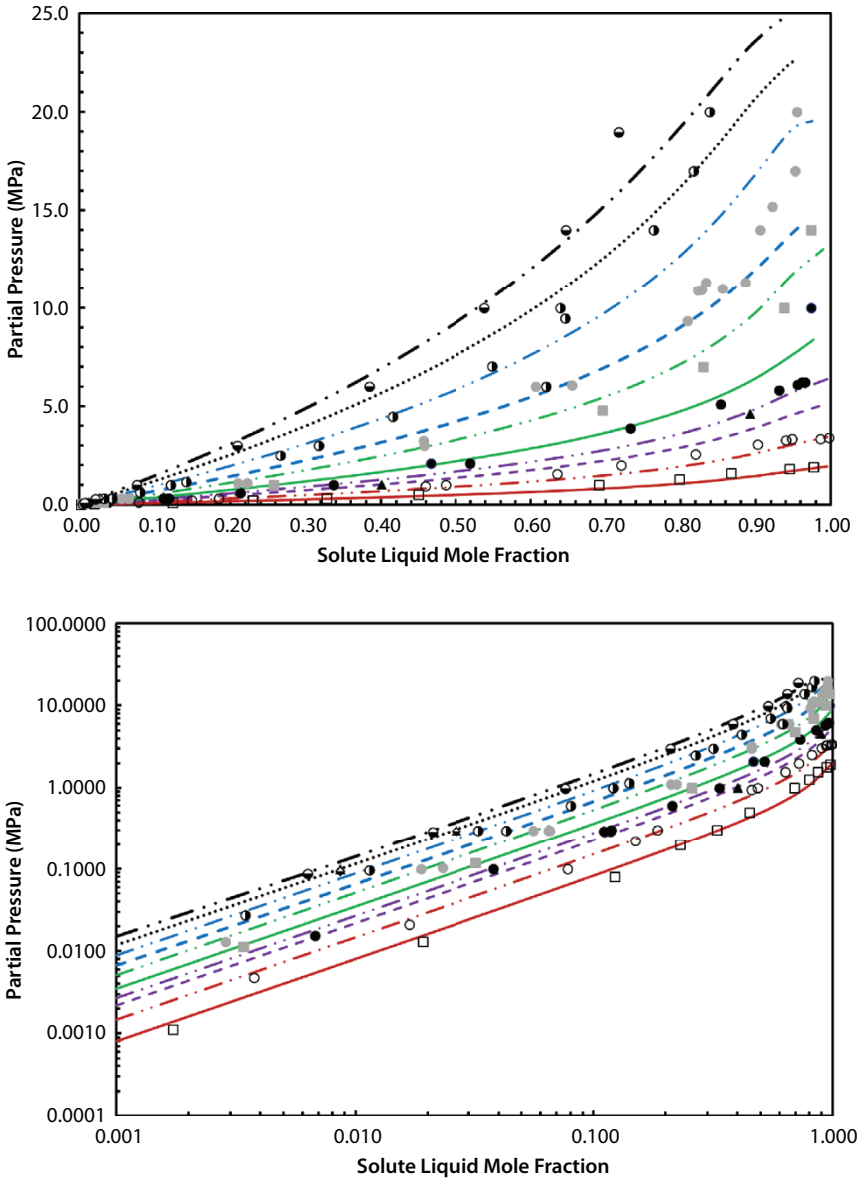

Figure 5.6 Experimental data for carbon dioxide (1) + DMPEG (2) system compared with correlated values using the Peng-Robinson equation of state. Experimental data: □, 253.15 K; ○, 273.15 K; ▲, 288.75 K; ●, 298.15 K; ■, 310.95 K; ●, 333.15 K; ◭, 353.15 K; ◑, 373.15 K; ◆, 398.15 K; ◒, 423.15 K; Peng-Robinson equation of state: solid line, 253.15 K; long dash dot dot, 273.15 K; dash, 288.75 K; long dash dot dot, 298.15 K; solid line, 310.95 K; long dash dot dot, 333.15 K; dash, 353.15 K; long dash dot dot, 373.15 K; round dot, 398.15 K; long dash dot dot, 423.15 K.

However, it should be noted that the model does a very good job reproducing the data in the region of interest to the gas treating industry [10, 11, 17, 18, 37–39].

If the full region of solute partial pressures is important, alternative modelling approaches could be tried (e.g., different mixing rules, activity coefficient model approaches [6, 40] and the SAFT EoS [15]). As this investigation was to supply phase behaviour data and correlate the data with the Peng-Robinson EoS with the van der Waals mixing rules different modelling approaches were not tested. Based on the variability of DMPEG solvents, caution should be used when extending the model results from this investigation to other mixtures of DMPEG.

5.5 Krichevsky-Ilinskaya Equation

Bender *et al.* [41, 42] have shown the connection between the Peng-Robinson EoS, the binary interaction parameter and the three parameters in the Krichevsky-Ilinskaya equation. The Krichevsky-Ilinskaya equation is given by:

$$\ln\left(\hat{f}_2 / x_2\right) = \ln H_{21} + \frac{\overline{v}_2^{\infty}\left(P - P_1^s\right)}{RT} + \frac{A}{RT}\left(x_1^2 - 1\right) \tag{5.7}$$

where the three parameters are the Henry's law constant, H_{21}, the partial molar volume at infinite dilution, $\overline{v}_2^{\infty}$, and the Margules activity coefficient parameter, A. With this connection, the regressed binary parameter can not only be used to calculate Henry's law constant and the partial molar volume of the solute at infinite dilution but also the Margules activity coefficient parameter. These parameters can then be used in the Krichevsky-Ilinskaya equation to calculate gas solubilities. The calculated parameters for each binary system (N_2, CH_4, H_2S and CO_2) + DMPEG mixture are compared with literature values in Figures 5.7–5.9.

The relative solubility, defined in this investigation as:

$$H_{21}^{i}(T = 298.15K) \Big/ H_{21}^{CO_2}(T = 298.15K) \tag{5.8}$$

was determined to be 5.8 for H_2S, 0.07 for CH_4 and 0.02 for N_2. The average values reported in the literature are 8.9 for H_2S, 0.07 for CH_4 and

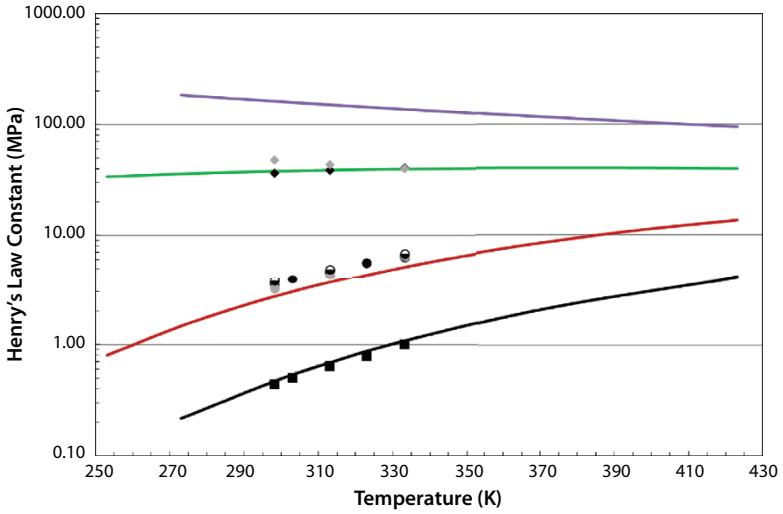

Figure 5.7 The temperature dependence of the Henry's law constants of nitrogen (1), methane (1), hydrogen sulfide (1) and carbon dioxide (1) in DMPEG (2). Carbon dioxide: ●, Xu *et al.* [51]; ●, Henni *et al.* [52]; ◒, Rayer *et al.* [53]; ○, Rayer *et al.* [40]; solid line, Peng-Robinson equation of state; Hydrogen sulfide: ■, Xu *et al.* [51]; solid line, Peng-Robinson equation of state; Methane: ◆, Rayer *et al.* [53]; ◆, Henni *et al.* [54]; solid line, Peng-Robinson equation of state; Nitrogen: solid line, Peng-Robinson equation of state.

0.02 for N_2 [20, 37, 38, 43–49]. However, most of the reported relative solubilities in the literature do not indicate the conditions of comparison (other than 298.15 K, Bucklin and Schendel [20] and Burr and Lyddon [49]. For example, if the temperature of consideration as 273.15 K, the value for H_2S increases to 6.8. Relative solubilities could also be different if reported at elevated pressures. The calculated relative solubilities at 298.15 K, and Figure 5.7, indicate the high selectivity of H_2S and CO_2 compared with CH_4 and N_2. The high selectivity of H_2S to CO_2 is also advantageous.

The solubility of methane has a minimum around 373 K as evidenced by the Henry's law constant reaching a maximum value at this temperature. At lower pressures ($P < 7$ MPa), the solubility of methane essentially remains temperature independent as evidenced by solubility data, Figure 5.4, and the Henry's law constant variation with temperature shown in Figure 5.7. This solubility phenomena was also seen with propylene carbonate [50]. At higher pressures, the solubility of methane increases with increasing temperature. The solubility of nitrogen increases with temperature at all

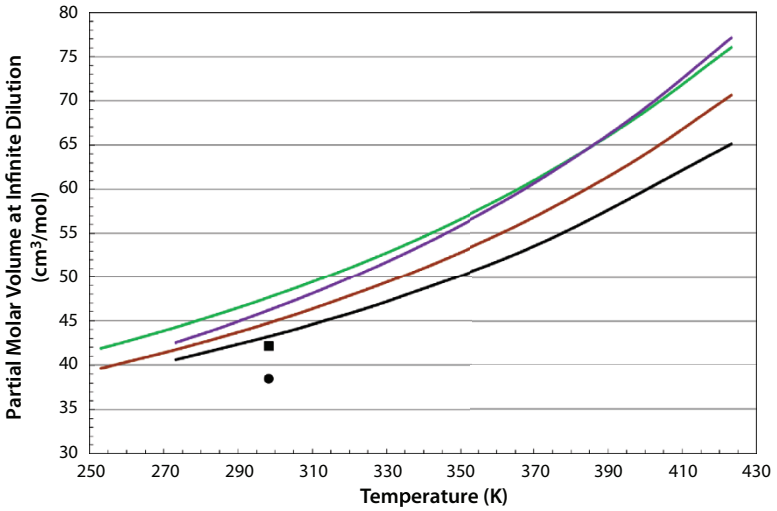

Figure 5.8 The temperature dependence of the partial molar volume at infinite dilution of nitrogen (1), methane (1), hydrogen sulfide (1) and carbon dioxide (1) in DMPEG (2). Carbon dioxide: ●, Xu *et al.* [55]; solid line, Peng-Robinson equation of state; Hydrogen sulfide: ■, Xu *et al.* [55]; solid line, Peng-Robinson equation of state; Methane: solid line, Peng-Robinson equation of state; Nitrogen: solid line, Peng-Robinson equation of state.

measured pressures. The opposite trend with temperature occurs with the more soluble gases, carbon dioxide, and hydrogen sulfide. As expected [4], the Henry's law constant and the high pressure solubility both increase with temperature.

Enthalpies of solution were calculated from the dependence of the Henry's constant with temperature according to:

$$\left(\frac{\partial \ln H_{21}}{\partial(1/T)}\right)_P = \frac{\Delta\bar{h}_2}{R} \tag{5.9}$$

The calculated enthalpies of solution, at 298.15 K, for H_2S, CO_2, CH_4 and N_2 are -20.1, -16.0, -1.3, 3.4 kJ/mol respectively. These compare well with previously reported values of (-)15.1 kJ/mol [16, 37], and -19.1 kJ/mol [51] for H_2S and (-)16.4 kJ/mol [16, 37], -14.3 kJ/mol [51] and -14.5 kJ/mol [40] for CO_2 (no temperature was specified for these reported values – presumably an average value over the full temperature range investigated).

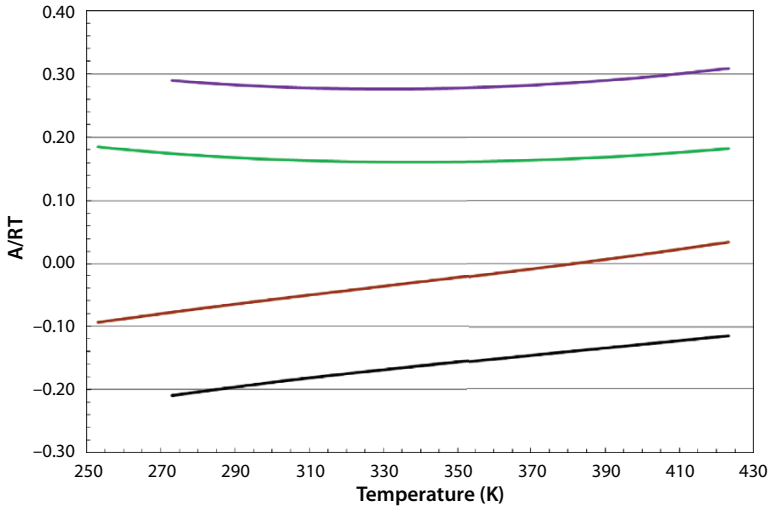

Figure 5.9 The temperature dependence of A/RT of nitrogen (1), methane (1), hydrogen sulfide (1) and carbon dioxide (1) in DMPEG (2). Carbon dioxide: solid line, Peng-Robinson equation of state; Hydrogen sulfide: solid line, Peng-Robinson equation of state; Methane: solid line, Peng-Robinson equation of state; Nitrogen: solid line, Peng-Robinson equation of state.

5.6 Conclusions

New experimental phase behaviour measurements were performed to expand gas solubility data in the areas of interest for gas treating processes involving mixtures of DMPEG. New solubility data were obtained for the binary N_2, CO_2, CH_4, and H_2S + the DMPEG mixture systems. The solubility was measured at several temperatures in the range of 253.15 K to 423.15 K at pressures up to 20.5 MPa.

A solvent characterization approach combined with the Peng-Robinson equation of state with a temperature dependent binary interaction parameter reproduces most of the experimental data quite well. The relative solubility of the gases in the DMPEG mixture was (253.15 to 423.15 K) determined to be: Nitrogen < Methane < Carbon Dioxide < Hydrogen Sulfide.

The new solubility data and models are important for the evaluation of DMPEG mixtures as a solvent in gas treating plant design.

5.7 Nomenclature

a_{11} parameter in the Peng-Robinson equation, Pa·m^6/mol^2 (Solvent)
a_{22} parameter in the Peng-Robinson equation, Pa·m^6/mol^2 (Solute)
A Margules parameter, J/mol
b_1 parameter in the Peng-Robinson equation, cm^3/mol (Solvent)
b_2 parameter in the Peng-Robinson equation, cm^3/mol (Solute)
$\boldsymbol{c}$ parameter vector
f model function
$\hat{f}_{i\_}$ fugacity of component *i* in a mixture, MPa
Δh_2 enthalpy of solution, J/mol
H_{21} Henry's law constant of solute 2 in solvent 1 at P_1^s, MPa
k_{ij} binary interaction parameter in the Peng-Robinson equation
M excluded experimental measurements out of N total measurements
N total experimental measurements
NC number of components
P pressure, MPa
P_c critical pressure, MPa
R gas constant, J/mol·K
T absolute temperature, K
T_c critical temperature, K
V molar volume of the mixture, cm^3/mol
$\overline{v}_2^{\infty}$ partial molar volume at infinite dilution, cm^3/mol
x_i mole fraction of component *i*
xc_i experimental data (independent data)
yc_i experimental data (dependent data)

Greek letters
Δ *o*verall absolute percentage deviation
ω acentric factor

References

1. Peng, D.-Y. and Robinson, D.B., A new two-constant equation of state. *Ind. Eng. Chem. Fundam.*, 15, 1, 59–64, 1976.
2. Maddox, R.N. and Morgan, D.J., *Gas Conditioning and Processing Volume 4, Gas Treating and Sulfur Recovery*, John M. Campbell and Company, Norman, Oklahoma, 1998.
3. Jou, F.-Y., Carroll, J.J., Mather, A.E., Otto, F.D., The solubility of nitrous oxide in water at high temperatures and pressures. *Z. Phys. Chem.*, 177, 225–239, 1992.
4. Jou, F.-Y., Mather, A.E., Schmidt, K.A.G., The solubility of hydrogen sulfide and carbon dioxide in propylene carbonate. *J. Chem. Eng. Data*, 60, 12, 3738–3744, 2015.
5. Rowley, R.L., Wilding, W.V., Oscarson, J.L., Yang, Y., Zundel, N.A., Daubert, T.E., Danner, R.P., *DIPPR Data Compilation of Pure Component Properties*, Design Institute for Physical Properties, AIChE, New York, New York, 2003.
6. Schmidt, K.A.G. and Mather, A.E., Solubility of sulphur dioxide in mixed polyethylene glycol dimethyl ethers. *Can. J. Chem. Eng.*, 79, 6, 946–960, 2001.
7. Michaeli, W. and Stein, W.H., Das Selexol-Verfahren – Ein Beitrag zur Selektiven Aufbereitung von Saurem Erdgas. *Erdoel-Erdgas-Z.*, 95, Oktober, 341–347, 1975.
8. Wölfer, W., Erdgasreinigungsanlage Rütenbrock Modifikationen der SELEXOL® - Regeneration. *Erdoel-Erdgas-Z.*, 92, Juni, 183–187, 1976.
9. Van Deraerschot, R., The SELEXOL® Solvent Process for Selective Removal of Sulfur Compounds, in: *2nd International Conference on The Control of Gaseous Sulphur and Nitrogen Compound Emission*, Salford, England, pp. 1–17, 1976.
10. Wölfer, W., Construction and Operation of SELEXOL Natural Gas Purification Plant, in: *27th Canadian Chemical Engineering Conference*, Calgary, Alberta, pp. 2–25, 1977.
11. Wölfer, W., Bau und lnbetriebnahme der SELEXOL-Erdgaswasche Duste II der Wintershall Aktiengesellschaft. *Erdoel-Erdgas-Z.*, 93, Dezember, 421–427, 1977.
12. Stöll, R.D. and Röper, S., Reinigung von Sauergas Darstellung der wichtigsten Verfahren. *Erdoel Kohle, Erdgas – Petrochem.*, 35, 8, 380–385, 1982.
13. Herraiz, J., Shen, S., Coronas, A., Vapor-liquid equilibria for methanol + poly(ethylene glycol) 250 dimethyl ether. *J. Chem. Eng. Data*, 43, 2, 191–195, 1998.
14. Conesa, A., Shen, S., Coronas, A., Liquid densities, kinematic viscosities, and heat capacities of some ethylene glycol dimethyl ethers at temperatures from 283.15 to 423.15 K. *Int. J. Thermophys.*, 19, 5, 1343–1358, 1998.
15. Nannan, N.R., De Servi, C.M., Van Der Stelt, T., Colonna, P., Bardow, A., An equation of state based on PC-SAFT for physical solvents composed of

polyethylene glycol dimethylethers. *Ind. Eng. Chem. Res.*, 52, 51, 18401–18412, 2013.
16. Clare, R.T. and Valentine, J.P., Acid Gas Removal using the Selexol Process. *Energy Process./Can.*, 67, 6, 38–43, 1975.
17. Wolfer, W., Schwartz, E., Vodrazka, W., Volkamer, K., Solvent Shows Great Efficiency in Sweetening of Gas. *Oil Gas J.*, 78, 3, 66–70, 1980.
18. Wolfer, W., Schwartz, E., Vodrazka, W., Volkamer, K., Helpful hints for physical solvent absorption. *Hydrocarb. Process.*, 61, 11, 193–197, 1982.
19. Kuwairi, B.S., *Vapor Pressure of Selected Materials and Mixtures*, Ph.D. Dissertation, Oklahoma State University, Stillwater, Oklahoma, 1983.
20. Bucklin, R.W. and Schendel, R.L., Comparison of FLUOR Solvent and SELEXOL Processes. *Energy Prog.*, 4, 3, 137–142, 1984.
21. Demyanovich, R.J. and Lynn, S., Use of Polar Solvents to Control Emissions from a Sulfuric Acid Plant, in: *Coal Science and Technology - Processing and Ultilization of High Sulfur Coals*, Attia, Y.A. (Ed.), pp. 547–562, 1985.
22. Shah, V.A. and Szymborski, P.A., SELEXOL® Solvent Process for Combined Gas Treating and Hydrocarbon Recovery. *Energy Process./Can.*, 79, 4, 8–10, 35, 1987.
23. Stüven, U., Entwicklung und Erprobung eines neuen Stoffsystems für den Einsatz in Absorptionswärmetransformatoren. *Chem. Ing. Tech.*, 61, 6, 492–493, 1989.
24. Chen, C.A., *Technical and Economic Assessment of CO_2 Capture Technology for IGCC Power Plants*, Ph.D. Dissertation, Carnegie Mellon University, Pittsburgh, Pennsylvania, 2005.
25. Sweeney, J.L. and Brooks, G.E., Selexol at Fort Stockton, in: *Laurance Reid Gas Conditioning Conference Proceedings*, Norman, Oklahoma, 1970.
26. Esteve, X., Boer, D., Patil, K.R., Chaudhari, S.K., Coronas, A., Densities, Viscosities, and Enthalpies of Mixing of the Binary System Methanol + Polyethylene Glycol 250 Dimethyl Ether at 303.15 K. *J. Chem. Eng. Data*, 39, 4, 767–769, 1994.
27. Esteve, X., Olive, F., Patil, K.R., Chaudhari, S.K., Coronas, A., Densities and viscosities of the binary mixtures of interest for absorption refrigeration systems and heat pumps. *Fluid Phase Equilib.*, 110, 1-2, 369–382, 1995.
28. Pereira, S.M., Iglesias, T.P., Legido, J.L., Rodríguez, L., Vijande, J., Changes of refractive index on mixing for the binary mixtures {xCH_3OH + (1 - x) $CH_3OCH_2(CH_2OCH_2)_3CH_2OCH_3$} and {x$CH_3OH$ + (1 - x) $CH_3OCH_2(CH_2OCH_2)_nCH_2OCH_3$} (n = 3-9) at temperatures from 293.15 K to 333.15 K. *J. Chem. Thermodyn.*, 30, 11, 1279–1287, 1998.
29. Li, J., Mundhwa, M., Henni, A., Volumetric properties, viscosities, refractive indices, and surface tensions for aqueous genosorb 1753 solutions. *J. Chem. Eng. Data*, 52, 3, 955–958, 2007.
30. Quiñones-Cisneros, S.E., Schmidt, K.A.G., Creek, J., Deiters, U.K., Friction theory modeling of the non-Newtonian viscosity of crude oils. *Energ. Fuel.*, 22, 2, 799–804, 2008.

31. Wisniak, J., Apelblat, A., Segura, H., Application of cubic equations of state to the fit of vapor pressures of pure components. *Chem. Eng. Sci.*, 53, 4, 743–751, 1998.
32. Weiland, R.H., Chakravarty, T., Mather, A.E., Solubility of carbon dioxide and hydrogen sulfide in aqueous alkanolamines. *Ind. Eng. Chem. Res.*, 32, 7, 1419–1430, 1993.
33. Schmidt, K.A.G., Pagnutti, D., Curran, M.D., Singh, A., Trusler, J.P.M., Maitland, G.C., McBride-Wright, M., New experimental data and reference models for the viscosity and density of squalane. *J. Chem. Eng. Data*, 60, 1, 137–150, 2015.
34. Benjamini, Y. and Hochberg, Y., Controlling the False Discovery Rate: A Practical and Powerful Approach to Multiple Testing. *J. R. Stat. Soc. B Methodol.*, 57, 1, 289–300, 1995.
35. Whitson, C.H. and Brulé, M.R., *Phase Behavior*, Society of Petroleum Engineers, Richardson, TX, 2000.
36. Saber, N. and Shaw, J.M., Rapid and robust phase behaviour stability analysis using global optimization. *Fluid Phase Equilib.*, 264, 1-2, 137–146, 2008.
37. Valentine, J.P., Gas Purification with a Physical Solvent, in: *Laurance Reid Gas Conditioning Conference Proceedings*, Norman, Oklahoma, 1973.
38. Sweny, J.W., High CO_2-High H_2S Removal with SELEXOL Solvent, in: *GPA Annual Convention Proceedings*, Houston, Texas, pp. 163–166, 1980.
39. Sweny, J.W. and Valentine, J.P., Physical Solvent Stars in Gas Treatment/Purification. *Chem. Eng.*, 77, 19, 54–56, 1970.
40. Rayer, A.V., Henni, A., Tontiwachwuthikul, P., High pressure physical solubility of carbon dioxide (CO_2) in mixed polyethylene glycol dimethyl ethers (Genosorb 1753). *Can. J. Chem. Eng.*, 90, 3, 576–583, 2012.
41. Bender, E., Klein, U., Schmitt, W.P., Prausnitz, J.M., Thermodynamics of gas solubility: Relation between equation-of-state and activity-coefficient models. *Fluid Phase Equilib.*, 15, 3, 241–255, 1984.
42. Schmidt, K.A.G., Erratum: Thermodynamics of gas solubility: Relation between equation-of-state and activity-coefficient models (*Fluid Phase Equilibria* (1984) 15 (241-255)). *Fluid Phase Equilib.*, 236, 1-2, 268–269, 2005.
43. Sweny, J.W., Gas Treating with a Physical Solvent, in: *Acid and Sour Gas Treating Processes*, S.A. Newman (Ed.), pp. 1–41, Gulf Publishing Company, Houston, Texas, 1985.
44. Shah, V.A. and McFarland, J., Low Cost Ammonia and CO2 Recovery. *Hydrocarb. Process.*, 67, 3, 43–46, 1988.
45. Hernandez, R.J. and Huurdeman, T.L., Solvent Unit Cleans Synthesis Gas. *Chem. Eng.*, 96, 2, 154–156, 1989.
46. Judd, B., Mercaptan removal rate exceeds 99% at Canadian gas plant. *Oil Gas J.*, 91, 33, 81–83, 1993.

47. Epps, R., Use of SELEXOL Solvent for Hydrocarbon Dewpoint Control and Dehydration of Natural Gas, in: *Laurance Reid Gas Conditioning Conference Proceedings*, Norman, Oklahoma, 1994.
48. Breckenridge, W., Holiday, A., Ong, J.O.Y., Sharp, C., Use of SELEXOL Solvent for Hydrocarbon Dewpoint Control and Dehydration of Natural Gas, in: *Laurance Reid Gas Conditioning Conference Proceedings*, Norman, Oklahoma, 2000.
49. Burr, B. and Lyddon, L., A comparison of physical solvents for acid gas removal, in: *GPA Annual Convention Proceedings*, pp. 100–113, 2008.
50. Jou, F.-Y., Mather, A.E., Schmidt, K.A.G., Solubility of methane in propylene carbonate. *J. Chem. Eng. Data*, 60, 4, 1010–1013, 2015.
51. Xu, Y., Schutte, R.P., Hepler, L.G., Solubilities of carbon dioxide, hydrogen sulfide and sulfur dioxide in physical solvents. *Can. J. Chem. Eng.*, 70, 569–573, 1992.
52. Henni, A., Tontiwachwuthikul, P., Chakma, A., Solubilities of carbon dioxide in polyethylene glycol ethers. *Can. J. Chem. Eng.*, 83, 2, 358–361, 2005.
53. Rayer, A.V., Henni, A., Tontiwachwuthikul, P., High-pressure solubility of methane (CH_4) and ethane (C_2H_6) in mixed polyethylene glycol dimethyl ethers (Genosorb 1753) and its selectivity in natural gas sweetening operations. *J. Chem. Eng. Data*, 57, 3, 764–775, 2012.
54. Henni, A., Tontiwachwuthikul, P., Chakma, A., Solubility study of methane and ethane in promising physical solvents for natural gas sweetening operations. *J. Chem. Eng. Data*, 51, 1, 64–67, 2006.
55. Xu, Y., Li, L., Hepler, L.G., Partial molar volumes of acidic gases in physical solvents and prediction of solubilities at high pressures. *Can. J. Chem.*, 70, 55–57, 1992.

6

Water Content of Hydrogen Sulfide – A Review

Eugene Grynia[1]* and Bogdan Ambrożek[2]

[1]Gas Liquids Engineering Ltd., Calgary, Alberta, Canada
[2]West Pomeranian University of Technology in Szczecin, Poland

Abstract

The knowledge of the phase behavior of the water-hydrogen sulfide system is important in the design and operation of pipelines and production and processing facilities handling sour reservoir fluids containing the two compounds. The formation of condensed water may lead to corrosion or ice formation, and sufficient amount of water in the vapor phase may lead to hydrate formation. When acid gas is removed from sour gas, one option for its disposal is by injection into an underground reservoir. Acid gas is normally saturated with water in gas treatment units, so designing acid gas disposal schemes requires the knowledge of the phase equilibrium in H_2O-H_2S systems [1]. In addition, water content data in the gas phase is useful for tuning binary interaction parameters between water and gaseous H_2S in equations of state.

A thorough literature review was conducted to find all of the measured data for water content of hydrogen sulfide. Only experimental data was collected. The paper did not include the solubility of hydrogen sulfide in water. Experimental data for more complex mixtures were not reviewed at this time.

The data from the various sources were compared and notes were made which one deviated from the rest. A regression model was used to plot the data as isotherms. A seminal paper by Selleck *et al.* [25] served as a benchmark in this paper.

Keywords: Water, hydrogen sulfide, solubility, experimental methods

6.1 Introduction

Natural gas reservoirs have always associated water; therefore the gas produced from the reservoirs is water saturated. The same can be said of sour

**Corresponding author*: egrynia@gasliquids.com

Ying Wu, John J. Carroll, Mingqiang Hao and Weiyao Zhu (eds.) Gas Injection into Geological Formations and Related Topics, (77–114) © 2020 Scrivener Publishing LLC

natural gas. Water in sour natural gas is a concern due to the potential for corrosion and hydrate formation during production, transmission and processing – the H_2S-H_2O hydrate persists to temperatures as high as +30°C.

Hydrogen sulfide is often extracted from sour natural gas in amine sweetening units and is also water saturated.

Hydrogen sulfide and water is also used in the dual temperature process for the production of heavy water. This process involves the transfer of deuterium atoms between H_2S and H_2O and is carried out in high columns, therefore for optimum design and operation of the process accurate phase and chemical equilibrium data are required.

The presence of hydrogen sulfide in geochemical environment like hot aqueous solutions may result in formation of sulfide minerals. An understanding of the phase behavior in the system H_2O-H_2S helps analyze these mineral forming processes.

Experimental data is used to fine-tune empirical correlations for calculating water content of H_2S. It is also used to validate the models for calculating water content of H_2S.

The solubility of water in hydrogen sulfide is higher than the solubility of water in carbon dioxide and in hydrocarbons, which can be explained by the different molecular structure of these compounds. Hydrogen sulfide possesses higher polarity than hydrocarbons because of the asymmetric arrangement of its atoms. Since water is strongly polar, it will have higher solubility in substances with higher polarity [2].

Experimental work is also available on water content of mixtures of hydrogen sulfide and other gases. This work has not been reviewed in the present review.

Water content of hydrogen sulfide had previously been reviewed by Clark [3], Carroll [4] and Chapoy [1], and also summarized in IUPAC Solubility Data Series [5]. Some of the information presented in this paper is taken from the above references.

6.2 Literature Review

The early investigations of the hydrogen sulfide-water system were mainly concerned with the study of hydrates and the development of generalizations of phase behavior for binary systems, e.g., Forcrand [6] and Scheffer [7]. The first paper dealing with water content of hydrogen sulfide was apparently that of Wright and Maas [8]. The first that became a benchmark for other investigators was a paper by Selleck *et al.* [25].

Chapoy *et al.* [1] listed Burgess and Germann [9] data as experimental, but those are calculated values based on the correlation of data obtained by Selleck *et al.*

There is some difficulty with the interpretation of the water content of H_2S reported by Clarke and Glew [10]. The data seem to be experimentally obtained but the authors of this literature review are not that certain, as Clark and Glew discussed in their paper the method for deriving fugacities, phase compositions and Henry's Law constants.

There are some papers in which experimental data are used to calculate water content of H_2S. For example, Zezin *et al.* [11] made in situ determination of the pressure developed by H_2O-H_2S mixtures of variable compositions for temperatures from 150 to 325°C, and measured the volumes of the fluid mixtures, and then calculated the compositions of liquid and vapor by modelling the bulk fluid composition using the Stryjek-Vera modification of the Peng-Robinson equation of state in conjunction with the density-dependent mixing rules of Panagiotopoulos, obtaining 77 data points. Such data are not included in the present paper.

6.2.1 Wright and Maass (1932)

a. Purpose for the Study
Previously recorded data on the solubility of H_2S in water suffered from the incorporation of Henry's law as an implicit assumption, a part of the experimental method. Since Wright and Maass had found that the law was not strictly obeyed, the last significant figures of the accepted values were probably invalidated at atmospheric pressure, and most certainly so at all other pressures. The authors carried out a series of measurements of the solubility of hydrogen sulfide in water at various temperatures and pressures other than atmospheric and determined the degree to which Henry's law was applicable.

b. Experimental Method
Wright and Maass conducted their measurements based on the determination of the equilibrium pressures of known mixtures of hydrogen sulfide and water confined in an especially designed all-glass vapor pressure cell of known volume (a synthetic experimental method). The authors used a new type of glass diaphragm manometer, with a glass pointer affixed to the inside of the diaphragm. They also used the

magic lantern principle to magnify the movements of the pointer (a lens system projected on a screen some distance away the enlarged images of the blackened tips of the pointer and index). The glass material was used to minimize the possibility of stray reactions between the gas and mercury, or stopcock grease.

A measured quantity of water was run into the cell. Dissolved air was removed by repeated freezing and melting in vacuo. A measured amount of H_2S was condensed in the cell by liquid air and the cell sealed. The temperature of the cell and manometer were controlled to 0.1°C. Partial pressure of hydrogen sulfide P_{H2S} was calculated by subtracting vapor pressure of pure water P_{H2O} from the total pressure P_{total}. The weight of hydrogen sulfide in the gas phase was calculated from P_{H2S} and the volume of the gas phase. The difference between the total weight of H_2S used in the experiment and the weight of H_2S in the gas phase was the weight of H_2S in the solution.

The authors claimed that the results given by this method were more directly applicable than those obtained by the usual gravimetric and volumetric procedures.

c. Results

Wright and Maass measured the vapor pressures of six mixtures of H_2S and water (H_2S in water) confined in a vapor pressure cell at nine different temperatures between 5°C and 60°C. From the total pressures, observed or interpolated, the internal volume of the cell and the amounts of material in it, they calculated the concentration of the solution using the following equation:

$$P_1 - P_2 - \frac{W \cdot R}{M \cdot V} \cdot T + \frac{w \cdot R}{M \cdot V} \cdot T = 0 \qquad (6.1)$$

where:

P_1 – observed total pressure, mm Hg at 0°C

P_2 – vapor pressure of water, mm Hg at 0°C, at temperature T in K

W – total weight of hydrogen sulfide in the cell

w – weight of dissolved hydrogen sulfide in the solution

R – gas constant in cc-mm

M – apparent molecular weight of H_2S at temperature T and pressure P_1 – P_2 (calculated from the data from a previous paper)
V – volume of the vapor phase in cc, calculated

They solved the equation for *w* and calculated the concentration of the solutions in moles of H_2S per liter of vapor at actual conditions of pressure and temperature. The authors of this review calculated the volume of vapor at standard conditions using Symmetry simulation program and converted Wright and Maass results to g of water per Sm^3 of the vapor.

Figure 6.1 summarizes the results obtained by Wright and Maass and converted to g/Sm^3.

Symmetry was also used to estimate the water content of H_2S and volume of vapor using the experimental data from Wright and Maass paper, i.e., temperature, pressure and moles of H_2S per liter of vapor. The largest relative error between the calculated and simulated water content values

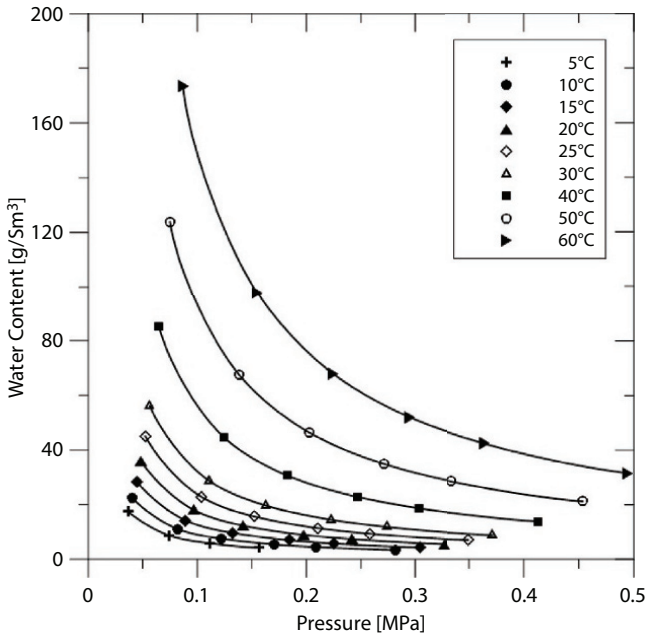

Figure 6.1 Water content of H_2S, Wright and Maass [8].

was 0.7%. The largest relative error between the measured and calculated volume of vapor was 0.3%.

6.2.2 Selleck *et al.* (1951, 1952)

d. Purpose for the Study
Selleck *et al.* reviewed earlier work regarding the hydrogen sulfide-water system and concluded that only limited data concerning the solubility of hydrogen sulfide in water had been obtained.

e. Experimental Method
The study by Selleck *et al.* [25] determined the composition of the coexisting phases in a two-phase equilibrium involving an aqueous liquid and a gas phase for temperatures between 100 and 340°F (37.8°C and 171.1°C) and pressures up to 5121.6 psia (35.312 MPa). They used an isochoric spherical stainless-steel pressure vessel (a bomb). The pressure within the bomb was determined with the aid of an aneroid-type diaphragm. The isochoric bomb was not appropriate for measurements of bubble point pressures of the H_2S-H_2O system therefore they used a variable volume glass equipment.

The composition of the dew point gas was determined by withdrawing samples from a heterogeneous equilibrium mixture in the spherical bomb. The quantity of water in the gas phase sample withdrawn was determined by passing it over anhydrous calcium sulfate (a desiccant) and condensing the dried gas in a weighing bomb near the temperature of liquid nitrogen.

Note: the solubility data listed in IUPAC Solubility Data Series [5] are the smoothed ones, not the raw ones.

f. Results
The work of Selleck *et al.* [12, 25] is considered the benchmark study for the system water – H_2S. Data in the 1952 paper were smoothed and extrapolated from the raw data. It is the smoothed data that are often quoted. However, some problems with the smoothed data for the fluid phase equilibria were demonstrated by Carroll and Mather [13]. A thorough review and reinterpretation of the raw data of Selleck *et al.* [12] was done by Carroll [14].

Selleck *et al.* divided the measurements they made in three classes:

1. The determination of the equilibrium pressure as a function of temperature for homogeneous and heterogeneous mixtures under isochoric conditions. The results established the locus of three-phase states and volumetric data for the one-, two-, and three-phase regions.
2. Measurements of the pressure as a function of specific volume for several predetermined temperatures. The study was limited to gas-aqueous liquid equilibria for compositions rich in water. The objective was to determine the bubble point pressure as a function of temperature and composition.
3. Direct measurement of the composition of individual phases when forming a part of a heterogeneous equilibrium.

Of interest to the present review paper is the third class. The authors presented the raw data in a paper published by the American Document Institute [12] and smoothed data a year later in *Industrial and Engineering Chemistry* [25].

The data obtained by Selleck *et al.* were used by a number of authors, including Burgess and Germann [9] who correlated Selleck's data to derive equations for H_2S humidity and solubility. The knowledge of hydrogen sulfide-water compositions at equilibrium is needed for calculations concerning the production of heavy water by the hydrogen sulfide dual-temperature exchange process which requires precise data on hydrogen sulfide-water mixtures between 25 and 170°C and 200 and 340 psia (1.379 – 2.344 MPa). Burgess and Germann commented that the Selleck's data were presented in such large intervals of pressure and temperature that precise plots could not be adequately interpolated for the narrow ranges of temperature and pressure needed. They made more precise interpolations with correlating equations. However, they did not find a single equation which correlated either the humidity or the solubility using all of the published information. So, they first plotted isotherms from all of Selleck's data, and from these obtained points for isobars. Then the data from the isobars were correlated with three equations: for the humidity of H_2S, for the solubility of H_2S at low temperatures (from hydrate point to 100°C), and for the solubility of H_2S at high temperatures (from 100°C to 171°C).

The raw data obtained by Selleck *et al.* are presented in Figure 6.2.

Since it may not be easy to access Selleck's raw data, this data is provided in the table below (Table 6.1), which in the original document is numbered as Table III.

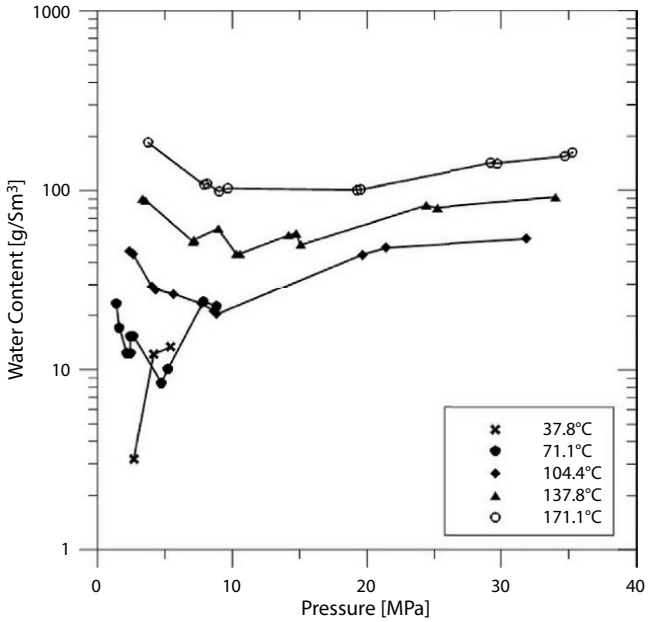

Figure 6.2 Water content of H_2S – raw data, Selleck *et al.* [25].

6.2.3 Kozintseva (1964)

a. Purpose for the Study

The knowledge of physiochemical properties of gases at high temperatures and pressures is essential for the understanding of migration and deposition of sulfide ores and for the interpretation of the processes of gas-liquid separation.

Selleck *et al.* [25] studied the phase equilibria in the H_2S-H_2O system between 37.8°C and 171.1°C and pressures from 2.7 MPa to 35.3 MPa. The existing data for this system did not cover the temperature range encountered in geological investigations, for the formation of polymetallic ores extends into a region of higher temperatures. It was believed that the pressure of H_2S in natural solutions was of the order of a few atmospheres. To approximate the conditions of deposition of sulfide ores the solubility of H_2S in water was studied at temperatures from 160°C to 330°C.

Table 6.1 Raw data from Selleck *et al.* for the water content of H_2S.

Pressure psia	H_2S Wt. Fraction	H_2S Mole Fraction	Pressure psia	H_2S Wt. Fraction	H_2S Mole Fraction
	100°F			280°F	
390.67	0.9978	0.9958	484.5	0.9337	0.8816
604.9[a]	0.9915[a]	0.9840[a]	518.3	0.9349	0.8836
791.9[a]	0.9906[a]	0.9824[a]	1030.0	0.9626	0.9315
	160°F		1036.5	0.9616	0.9298
201.4	0.9835	0.9692	1297.2	0.9556	0.9191
236.7	0.9881	0.9777	1491.5	0.9681	0.9413
316.1	0.9913	0.9837	1535.4	0.9680	0.9412
351.3	0.9913	0.9837	2056.1	0.9593	0.9257
355.4	0.9892	0.9798	2139.5	0.9581	0.9236
388.3	0.9892	0.9798	2182.9	0.9642	0.9344
688.4	0.9941	0.9889	3532.6	0.9394	0.8913
759.1	0.9929	0.9867	3657.1	0.9412	0.8943
1142.4[a]	0.9831[a]	0.9685[a]	4937.1	0.9324	0.8794
1279.1[a]	0.9842[a]	0.9705[a]			
	220°F			340°F	
346.4	0.9672	0.9397	547.6	0.8551	0.7573
380.8	0.9680	0.9412	1145.5	0.9198	0.8584
586.5	0.9794	0.9617	1181.3	0.9185	0.8563
626.2	0.9802	0.9632	1307.5	0.9266	0.8696
822.5	0.9814	0.9654	1399.9	0.9236	0.8647
1117.6	0.9836	0.9694	2795.7	0.9249	0.8669
1254.3	0.9851	0.9722	2833.7	0.9248	0.8667
1285.4	0.9857	0.9733	4246.5	0.8916	0.8130

(*Continued*)

Table 6.1 Raw data from Selleck *et al.* for the water content of H_2S. (*Continued*)

Pressure psia	H_2S Wt. Fraction	H_2S Mole Fraction	Pressure psia	H_2S Wt. Fraction	H_2S Mole Fraction
2848.5	0.9684	0.9419	4310.3	0.8922	0.8140
3108.6	0.9655	0.9367	5037.6	0.8810	0.7965
4625.9	0.9614	0.9294	5121.6	0.8745	0.7865

[a] Hydrogen sulfide-rich liquid phase

b. Experimental Method

The solubility experiments were made in the laboratory of magmatic processes in Moscow.

A two-chamber bomb was used for simultaneous sampling of both phases, gas and liquid. The bomb was purged with nitrogen to remove oxygen. 50 ml of water was added and the apparatus was saturated with H_2S under unknown (not specified) pressure. The bomb and the contents were heated in a stirrer-furnace to the required temperature for 25 to 50 hours. Then a sample of the liquid phase was passed into a system of traps (anhydron, iodine solution, potassium iodide crystals). A sample of the hot gas phase was passed into a glass condenser connected to traps for absorption of hydrogen sulfide. The condensate and the liquid sample were weighed and hydrogen sulfide was determined iodometrically.

c. Results

Kozintseva determined the compositions of the coexisting gas and liquid phases in mole H_2S/L for temperatures of 160°C – 330°C but did not state the pressures at which the measurements were made. She provided H_2S partial pressures for 14 data points, the lowest being 0.085 MPa and the highest 0.210 MPa.

The authors of this paper calculated the pressure using the Dalton's law of partial pressures:

$$P_{total} = \frac{P_{H_2S}}{y_{H_2S}} \tag{6.2}$$

Where:
P_{total} – total pressure of the H_2S-H_2O system (gas phase)
P_{H_2S} – partial pressure of H_2S in the gas phase (reported by Kozintseva)
y_{H_2S} – mole fraction of H_2S in the gas phase

$$y_{H_2S} = \frac{Y}{1+Y} \tag{6.3}$$

$$Y = \frac{n_{H_2S}}{n_{H_2S}} \tag{6.4}$$

The values of Y are also reported by Kozintseva for each temperature at which the experiments were conducted.

The data obtained by Kozintseva, with the pressures calculated, are shown in Figure 6.3.

Suleimenov and Krupp [15] made a comment that the data by Kozintseva contained major inconsistencies that

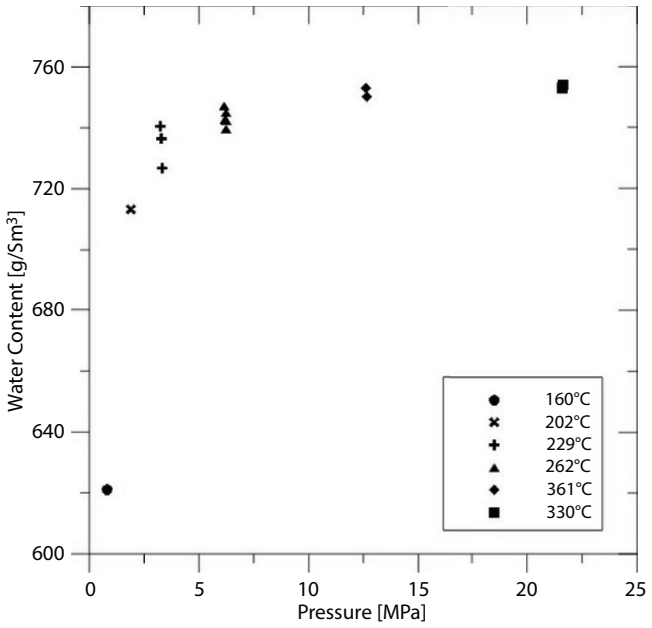

Figure 6.3 Water content of H_2S, Kozintseva [19].

become apparent when the H_2S partial pressures and vapor phase compositions reported by Kozintseva are used to reconstruct total pressure and by subsequent comparison of the difference of total gas pressure minus H_2O partial pressure with the reported H_2S partial pressure.

Experimental data obtained by Kozintseva can also be found in IUPAC Solubility Data Series, Vol 32, *Hydrogen Sulfide in Aqueous Solvents*, page 11 [5].

6.2.4 Clarke and Glew (1971)

a. Purpose for the Study

The authors required values for the solubility of deuterium sulfide in deuterium oxide while evaluating thermodynamic functions for the formation of deuterium sulfide deuterate. It seemed to them that this solubility might be obtained by the application of isotope correction factors to the well-known solubility of hydrogen sulfide in water. They made a literature search to find the magnitude, direction and temperature coefficient for these isotopic effects but could not find reliable estimates.

b. Experimental Method

Clarke and Glew conducted low pressure solubility measurements for H_2S in water. They designed and constructed a new solubility apparatus to measure the small solubility differences between deuterium sulfide in deuterium oxide and hydrogen sulfide in water. The apparatus was capable of 0.1% accuracy in the 0°C – 50°C range. The main pieces of their solubility apparatus consisted of a precision variable piston of known volume, a solubility cell containing magnetic stirring bar and a thermostat bath. The bath temperature adjacent to the solubility cell was measured with a precision of 0.001°C by a platinum resistance thermometer. Pressure was measured with an accuracy of 0.02% by a 0 – 16 psi range fused quartz precision Bourdon gauge.

In their experiments, they brought the known weight of water and volume of hydrogen sulfide to pressure equilibrium and measured the equilibrium pressure and temperature.

c. Results

The vapor and liquid phase compositions seem to be not experimentally determined but calculated, starting with the solubility expressed as the Henry Law constant:

$$H = \frac{f_2}{a_2} \tag{6.5}$$

where:
f_2 – the solute vapor fugacity, in atm
a_2 – its equilibrium solution activity

The activity is defined as

$$a_2 = x_2 \cdot e^{\frac{(P-1)\cdot \bar{v}_2}{R\cdot T}} \tag{6.6}$$

where:
x_2 – the mole fraction of un-ionized solute in solution
$\bar{v}_2$ – the partial molar volume of the un-ionized solute in solution
P – the total pressure

The authors evaluated the fugacities and volumetric properties of all components from the Redlich-Kwong equation of state. They calculated the values of the RK EOS constants for the binary vapor mixtures from the pure component values using relations from Spear *et al.* [16]. They derived equations for the fugacity f_1 and f_2 in a binary mixture. They wrote an iterative computer program that enabled them to obtain values for the vapor and liquid phase compositions.

In this manner, they obtained water content of H_2S at temperatures from 0°C to 50°C and pressures from 0.047 to 0.096 MPa – a total of 36 data points.

The results of their calculations are shown in Figure 6.4.

6.2.5 Lee and Mather (1977)

a. Purpose for the Study

Lee and Mather measured the mole fraction of hydrogen sulfide in vapor at 90°C, 120°C and 150°C and pressures from 1.921 MPa to 3.401 MPa. This measurement was part of a broader investigation of the solubility of hydrogen sulfide in water between 10°C and 180°C and 158.4 kPa to 6670.4 kPa.

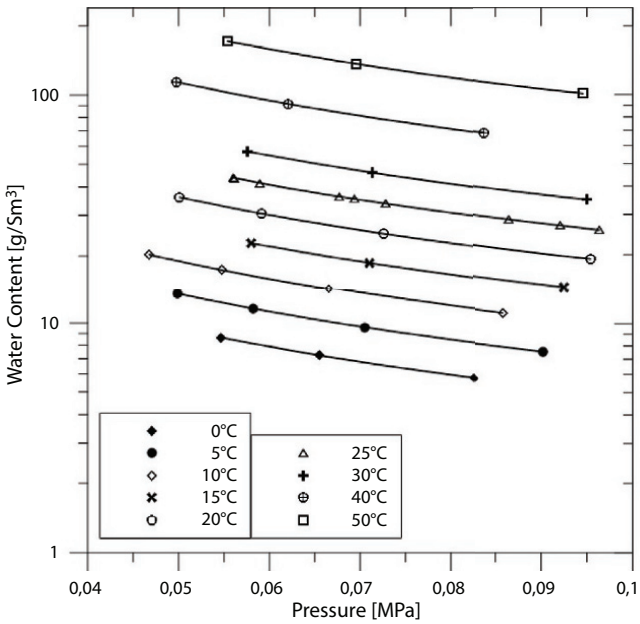

Figure 6.4 Water content of H_2S, Clarke and Glew [10].

What prompted the study by Lee and Mather was the observation made by Burgess and Germann [9] that the data of Selleck *et al.* [25] were at such large intervals of temperature and pressure that it was difficult to interpolate accurately to find solubilities in the narrow range of interest to the dual temperature process of producing heavy water.

b. Experimental Method

Lee and Mather used a recirculating equilibrium cell which consisted of a high-pressure liquid level gauge and a vapor reservoir. The gas was circulated by a magnetic pump. The temperature of the cell was measured by duplicate ten-junction copper-constantan thermopiles. The total pressure was measured by a Heise bourdon tube gauge. Samples of the liquid phase were withdrawn to determine the amount of H_2S dissolved. The pressure drop in the cell during sampling was about 10 kPa. The total quantity of H_2S was the gas evolved from the sample when its pressure was dropped to atmospheric and the residual gas in the liquid. The amount of H_2S which evolved was calculated from P-V-T information and the amount of liquid determined by reweighing the liquid sampler; the residual

H_2S in the liquid was measured by gas-liquid chromatography (Hewlett-Packard 5750). The vapor samples were withdrawn from the cell directly into the chromatograph. The sample line was heated to avoid condensation.

c. Results

The number of experimental data point obtained by the authors was 15. The authors noted that satisfactory analysis of the vapor phase was difficult; reproducible results at high hydrogen sulfide concentration could not be obtained.

Tabulations of the original experimental data were filed with the National Depository of Unpublished Data, National Science Library, National Research Council, Ottawa, Ontario. Their data were also published in IUPAC Solubility Data Series, Vol 32, *Hydrogen Sulfide in Aqueous Solvents*, page 19 [5].

The authors stated that their work was in good agreement with earlier values at low temperatures and was consistent with the higher temperature values of Selleck *et al.* and Kozintseva.

The results of Lee and Mather's work are presented in Figure 6.5.

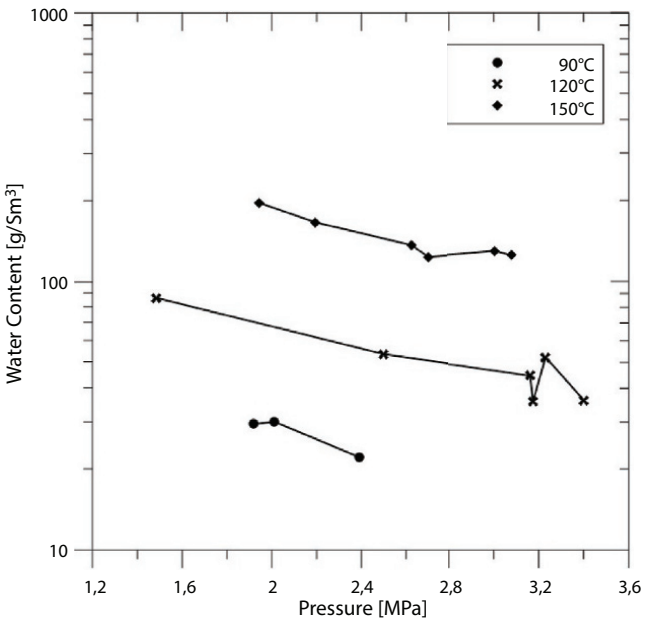

Figure 6.5 Water content of H_2S, Lee and Mather [20].

6.2.6 Gillespie and Wilson (1982)

a. Purpose for the Study

Gas Processors Association's Research Report 36 (Literature Survey for Synthetic Gas Components – Thermodynamic Properties) indicated that limited data existed for water-hydrocarbon systems and that quality ranged from average to poor. As a result of these findings, GPA initiated an experimental program, called Project 758 – Measurement of Vapor-Liquid Equilibrium Data for Water with Gaseous Components, with the purpose to generate phase equilibrium data on gaseous components with water.

Results of the initial investigation were reported in Research Report 41 – Vapor-Liquid Equilibrium Data on Water-Substitute Gas Components N_2-H_2O, H_2- H_2O, CO-H_2O, H_2-CO-H_2O, and H_2S-H_2O. The data obtained from the second of a series of investigations were summarized in Research Report 48 (RR-48) – Vapor-Liquid and Liquid-Liquid Equilibria: Water-Methane, Water-Carbon Dioxide, Water-Hydrogen Sulfide, Water-nPentane, Water-Methane-nPentane. The authors of RR-48 were Paul C. Gillespie and Grant M. Wilson.

b. Experimental Method

The water-hydrogen sulfide system was brought to equilibrium in an aluminum-jacketed stainless-steel cylinder of 1 L volume. The aluminum jacket was effective in eliminating temperature gradients and fluctuations. The vapor and aqueous liquid phases were sampled and analyzed by two different procedures. When conditions were such that the gaseous component existed as a liquid phase (liquid H_2S), the phase was sampled and analyzed in the same manner as the vapor phase.

The equilibrium cell (the stainless-steel cylinder) was heated with heating wire wrapped around the jacket and the temperature was measured and controlled with Chromel-Alumel thermocouples. The pressure was measured with a 3-D Instruments precision pressure gauge.

For sampling and analysis of the vapor or second liquid phase (H_2S-rich), the equilibrium cell was used as a flow cell. Gaseous H_2S was charged to the bottom of the cell with water in it and passed from the top of the cell, as water-saturated

vapor, through two drying tubes with $Mg(ClO_4)_2$, where water in the sample was absorbed, to a calibrated wet test meter. Both drying tubes were weighed before and after each run. The barometric pressure and the temperature of the water in the wet test meter were recorded during the run. The number of moles of gas in the sample was calculated from this information. And the number of moles of water was calculated from the weight of the water collected in the drying tubes. It is to be noted that H_2S was absorbed slightly by magnesium chlorate and by absorbed water in the drying tubes.

c. Results

The results obtained by Gillespie and Wilson are summarized in Figure 6.6. All the data points for 37.8, 71.1, 93.3, 98.9 and 100.4°C lie in the H_2S-rich liquid region. One point (above

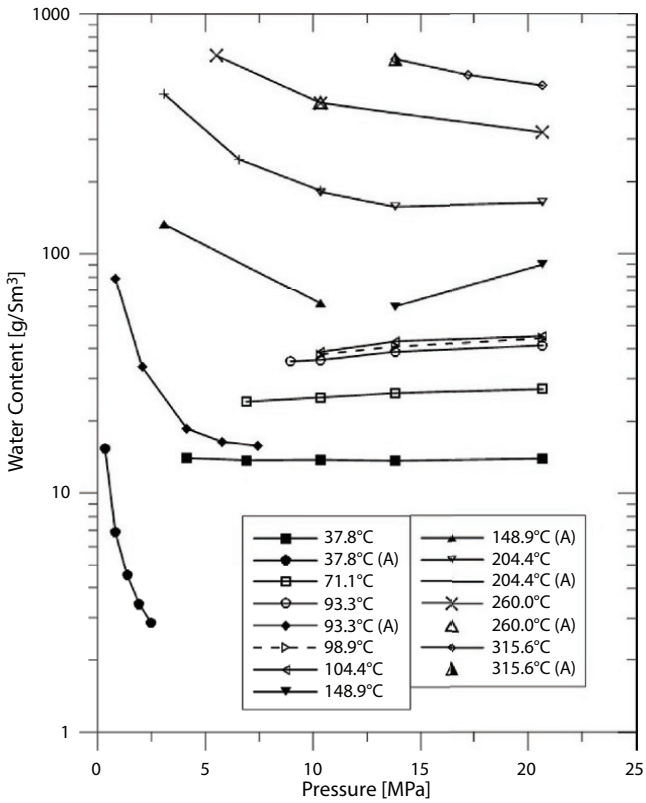

Figure 6.6 Water content of H_2S, Gillespie and Wilson [21] (A in curve description means Appendix in RR-48).

20 MPa) for 148.9°C also lies in this region. The number of experimental data point obtained by the authors is 47.

Gillespie and Wilson examined the measured data and made the following conclusions:

- The Henry's constants go through a maximum as a function of temperature (maximum Henry's constant means minimum solubility)
- The Henry's constants increase with increasing pressure
- The mutual solubilities of hydrogen sulfide and water are similar in the temperature range studied.

6.2.7 Carroll and Mather (1989)

a. Purpose for the Study

Carroll and Mather presented experimental data for the liquid-liquid-vapor (LLV) equilibrium for the system water-hydrogen sulfide. Conditions ranged from the hydrate-liquid-liquid-vapor quadruple point (29.4°C and 2.23 MPa) to beyond the critical temperature of hydrogen sulfide (100.3°C).

What led to the investigation of the LLV equilibrium was a discrepancy between the smoothed data of Selleck *et al.* [25] and the observations of Vogel [17], who made some bubble point measurements for H_2S in water.

b. Experimental Method

Carroll and Mather made the measurements of pressure and temperature along the LLV locus and established the critical end point. They conducted their experiments in a flow-type cell. The cell was a high-pressure liquid level gauge. A vapor reservoir was attached to the top of the cell to ensure sufficient mass within the system. Vapor was drawn off the reservoir and circulated through the condensed phases to ensure that equilibrium is attained.

The cell, reservoir and pump were housed in a constant temperature air bath. Pressure was measured using two Heise bourdon tube gauges and temperature was measured with an iron/constantan thermocouple. Performing a run consisted in placing approximately 20 mL of water and bubbling H_2S through the liquid. During sampling, the pressure drop was never higher than 0.07 MPa.

Compositions were measured by absorbing samples of each phase into a 1 mol/L NaOH solution. The H_2S content of the solution was determined by iodometric titrations. The amount of water was obtained by measuring the mass of the sample and subtracting the amount of H_2S. The authors intended initially to use gas chromatography to measure the compositions of the H_2S-rich phases but this proved unreliable because they could not obtain reproducible results.

The authors also calculated, from the correlation of Goodwin [18], the vapor pressure of H_2S, because of its proximity to the three-phase locus for this system.

c. Results

Regarding the compositions of coexisting phases along the LLV locus, the authors commented that at the lowest two temperatures, 40°C and 60°C, the determination of the water content of the vapor was inaccurate. For that reason, the results were given as 0.99+ mole fraction of H_2S.

The water content of the H_2S-rich phase and the vapor phase are shown in Figure 6.7. V in the legend in the graph

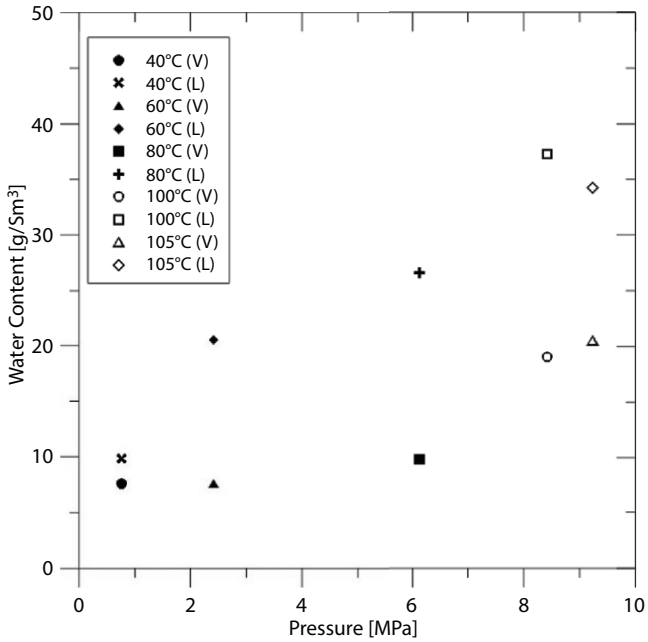

Figure 6.7 Water content of H_2S in H_2S-rich phase and in vapor phase, Carroll and Mather [13].

denotes the vapor phase and L denotes the H_2S-rich liquid phase. For each pressure, the water content of H_2S-rich phase is higher than the water content of the vapor phase.

6.2.8 Suleimenov and Krupp (1994)

a. Purpose for the Study

Hydrogen sulfide and its dissociation products are important constituents of hydrothermal solutions. Reliable thermodynamic data are therefore required to model processes of ore formation and water-rock interaction in active and fossil hydrothermal systems as well as diagenetic and metamorphic processes.

Suleimenov and Krupp studied experimentally the solubility of hydrogen sulfide in pure water and in NaCl solutions from 20°C to 320°C and at saturation pressures. They measured equilibrium vapor pressure, volume, temperature and bulk compositions. Values of the Henry constants were derived from those measurements. They calculated the molar volume of the gas mixture using the PRSV-EOS and partial molar volumes of H_2S in aqueous solutions using a polynomial fit based on data by a number of researchers. They also calculated Henry constants from their P-V-T-X measurements using an iterative procedure known as liquid-vapor flash calculations by an algorithm of successive substitution.

b. Experimental Method

The approach to the study was to measure equilibrium vapor pressures of the water-rich, liquid-vapor, two-phase system, temperature, volume and bulk compositions, which would provide the basis for the calculation of the Henry constants and salting coefficients.

The main part of the experimental apparatus consisted of a titanium pressure vessel which was subdivided by a titanium membrane bellows of 55 mL volume. The bellows contained the H_2S-H_2O two-phase system. The bellows was surrounded by a heat resistant, low-pressure hydrocarbon oil that acted as a pressure medium. The inside pressure vapor was transmitted by the bellows, *via* the oil, to a high-precision pressure sensor. Temperatures were measured by a sheathed thermocouple immersed into the oil surrounding the bellows.

Fourteen hydrogen sulfide solutions in water were prepared, from 0.6297 to 2.6446 mol% H_2S. For each solution, a weighted amount of degassed water was transferred into the bellows followed by introduction of H_2S gas from a 10 mL stainless-steel cylinder. The filled quantities were determined by weight differences.

A HPLC pump was employed to inject measured solution volumes under run conditions for various purposes, including neutralization of H_2S gas before disassembling. After run completion and cooling of the autoclave to room temperature, the fully neutralized H_2S solution was immediately sampled and analyzed for its H_2S content by iodometric titration.

The researchers claimed that thanks to their specially designed equipment they avoided some of the experimental problems encountered in previous high-temperature studies, like corrosion and concomitant formation of hydrogen gas.

c. Results

The water content for different mixtures and at different temperatures is shown in Figure 6.8. Isotherms and isobars could not be constructed as all 49 experimental points were measured at different temperatures and pressures.

Suleimenov and Krupp plotted the Henry constants obtained in their study, together with experimental values of earlier investigations (e.g., Kozintseva [19], Lee and Mather [20], Selleck *et al.* [25]) and concluded that there was a good agreement between the different studies at low temperatures but at higher temperatures the different data sets became increasingly discrepant. They commented that the reason could be the generation of hydrogen gas due to corrosion of Cr-plated stainless steel vessels and the use of nitrogen for flushing of the experimental equipment. Since hydrogen and nitrogen are much less soluble in water than H_2S, traces of these gases generated high partial pressures that interfered with the determination of H_2S partial pressures.

6.2.9 Chapoy *et al.* (2005)

a. Purpose for the Study

Chapoy *et al.* gathered experimental data from a bibliographic study on the solubility of hydrogen sulfide in water and the water content of gaseous hydrogen sulfide,

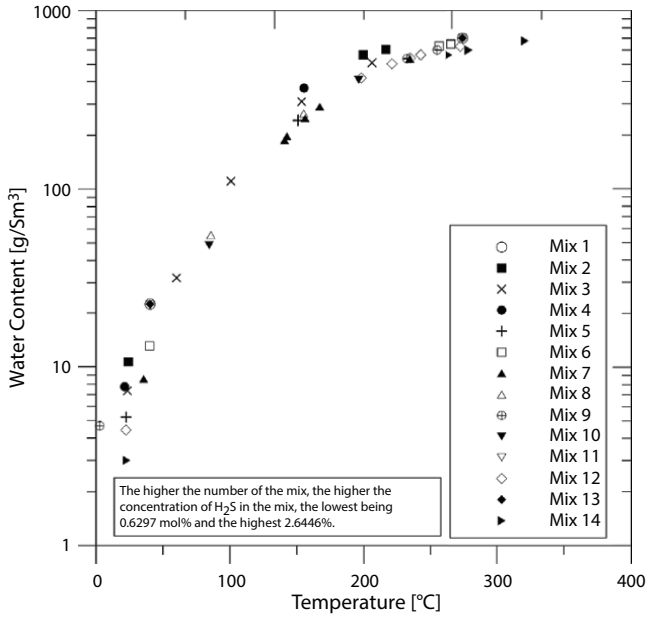

Figure 6.8 Water content of H_2S in the vapor phase, Suleimenov and Krupp [15].

as well as hydrate dissociation conditions. Their main objective was to identify inconsistencies and gaps in the available data to build a reliable database. As a result of the study, they concluded that it was necessary to determine complementary vapor-liquid equilibrium data for the H_2S-H_2O binary mixture because measurements at low temperatures (below 25°C) and intermediate pressures were scarce and some of the data reported at higher temperature were scattered.

Chapoy *et al.* reported new vapor-liquid equilibrium data of the H_2S-H_2O binary system over the 25.06 – 65.19°C temperature range for pressures up to 3.962 MPa.

b. Experimental Method

The experimental method is based on a static analytic apparatus with fluid phase sampling – taking advantage of two ROLSI (Rapid On-Line Sampler-Injector) pneumatic capillary samplers. The phase equilibrium is achieved in a cylindrical cell made of sapphire immersed in Ultra-Kryomat Lauda constant-temperature liquid bath that controls and maintains the desired temperature within ± 0.01K. The

pressure is measured by means of a Druck pressure transducer connected to a HP data acquisition unit. The analytical work was carried out using a GC (VARIAN Model CP-3800) equipped with a thermal conductivity detector connected to a data acquisition system fitted with BORWIN software.

c. Results

Chapoy *et al.* used the experimental gas solubility data to tune the binary interaction parameters between H_2S and H_2O in the Valderrama-Patel-Teja equation of state to predict H_2S solubility in water and the water content of the H_2S vapor phase, as well as the H_2S hydrate phase boundary, over wide ranges of temperature and pressure. The authors concluded that the predictions, from the model, were in good agreement with the experimental data, demonstrating the reliability of the techniques used in their work.

The experimental water content obtained by Chapoy *et al.* is presented in Figure 6.9. All the 15 data points lie in the region of gaseous H_2S.

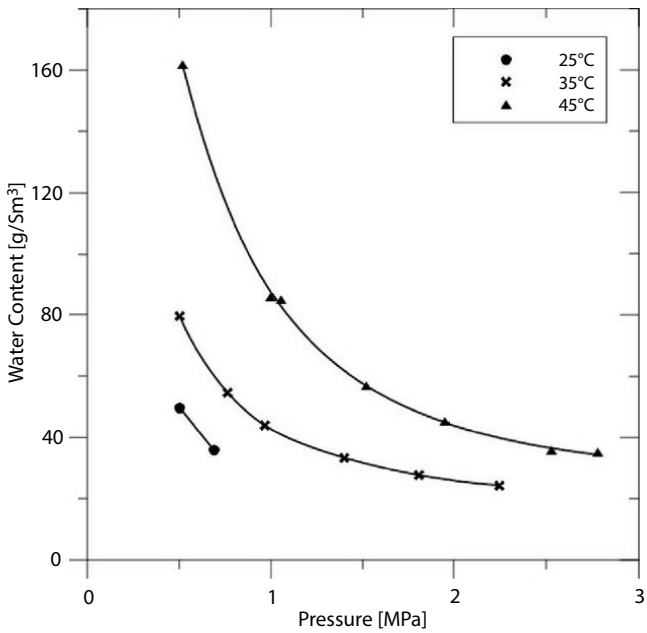

Figure 6.9 Water content of H_2S, Chapoy *et al.* [1].

6.2.10 Marriott *et al.* (2012)

a. Purpose for the Study

Insufficient data on H_2S-H_2O system at pressures relevant to injection schemes and target reservoir pressures.

Marriott *et al.* are part of the Alberta Sulphur Research Ltd., where techniques for the measurement of water carrying capacity of gases, liquids and supercritical fluids are being developed. They completed initial measurements for the H_2S-H_2O system at 50°C and 100°C and from 3.8 MPa to 70.5 MPa (their paper does not include all the data reported to date). These new measurements added solubility information at conditions which were not covered by the existing literature. But with the current experimental method, water content measurements at pressures up to 100 MPa and at temperatures up to 150°C are being carried out.

The new data is useful in the design of acid gas compression, injection and transport facilities because, as the authors stated in their paper – although many data are available for natural gas systems in open literature, there are limited reported data on the H_2S-H_2O system at pressures relevant to injection schemes and target reservoir pressures. Before Marriott's work, the highest pressure for which water content of H_2S was available, was 35.3 MPa [25]. Marriott himself commented that there were no data above ca. 30 MPa and experimental data in the liquid H_2S region were mostly those of Gillespie and Wilson [21].

The water content data allows to estimate saturation water content of acid gas in the inter-stages of multiple stage acid gas compressors, as oftentimes acid gas can be dehydrated by compression alone. Sending acid gas without free water and without water condensation *via* a transmission pipeline to an injection well allows to use carbon steel thus avoiding the need for installing expensive stainless steel pipelines.

Marriott *et al.* also pointed out that even though 75 MPa extends beyond compressor discharge pressures, the degree of sub-saturation in the near wellbore region is useful for reservoir modelling, because – as the fluid arrives in the reservoir – it will have capacity to take up additional reservoir water.

b. Experimental Method

The experimental equipment consisted of a high-pressure equilibrium vessel sampled through a capillary dip-tube and into a gas chromatograph with a thermal conductivity detector. The researchers had to overcome the most difficult issue for measuring water content in an acid gas sample, which is the transfer of the high-pressure sample to the low-pressure gas chromatograph. They developed a technique of injecting the high-pressure samples directly onto the GC column.

c. Results

The results obtained by Marriott *et al.* are presented in Figure 6.10. A preliminary thermodynamic model was reported which can be used to calculate the partitioning of H_2S and H_2O over a wide range of temperatures and pressures. The authors compared their own experimental results with those of Selleck *et al.* [25] and Gillespie and Wilson [21], along with the calculated water content using three different models: AQUAlibrium 3.0, Alami *et al.* [22] and their own model described in their paper. AQUAlibrium

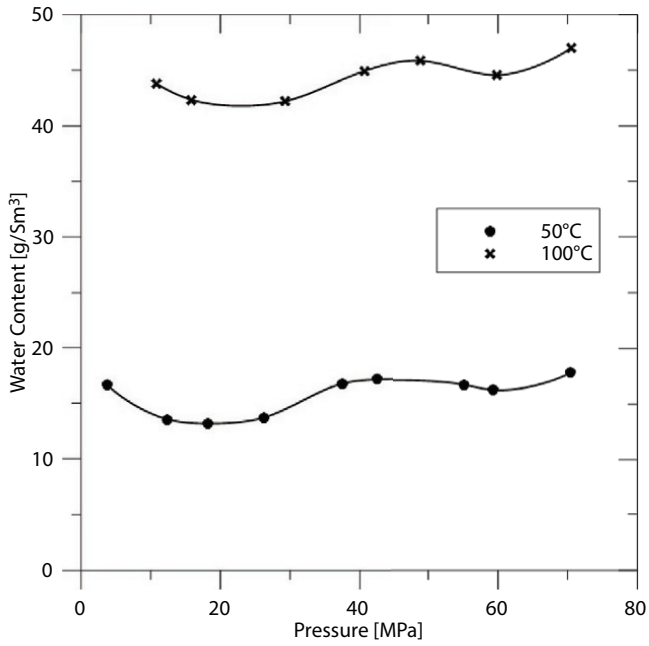

Figure 6.10 Water content of H_2S, Marriott *et al.* [23].

and their own model tend to overestimate the new data at 50°C and 100°C. The new data is also slightly below the data reported by other authors in the high-pressure region.

6.3 Discussion of the Results

The experimentally obtained water content of hydrogen sulfide (or in some cases calculated, based on other experimental data) are compared in the following three plots, Figures 6.11, 6.12, and 6.13. All these figures present the data in form of the isotherms. The data obtained by Suleimenov and Krupp [15] could not be presented in that form as each data point is for a different temperature. These data points, 49 in total, are presented in Figure 6.8.

Figure 6.11 shows the data for the temperatures of or below 60°C and pressures above 1 MPa. There are 32 data points in that region, 7 of which are common to both Figures 6.11 and 6.12. These 7 points lie in the region between 1 MPa and 2 MPa.

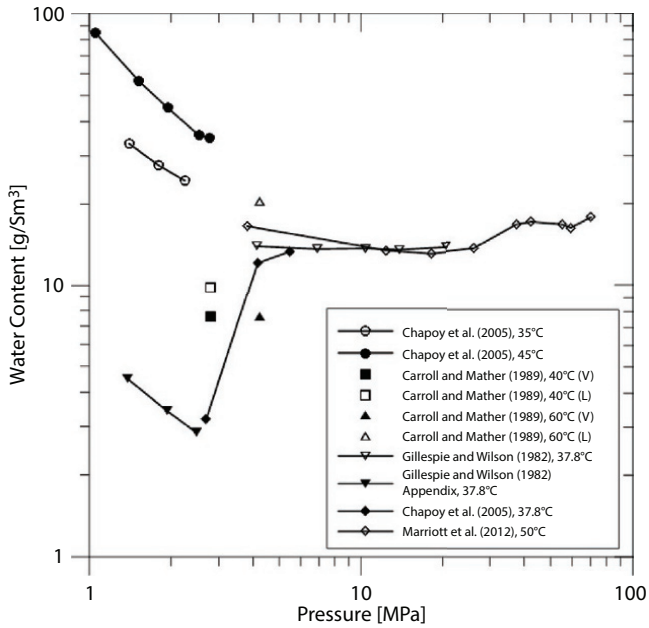

Figure 6.11 Water content of H_2S for T ≤60°C and P > 1 MPa. L stands for liquid phase; V stands for vapor phase.

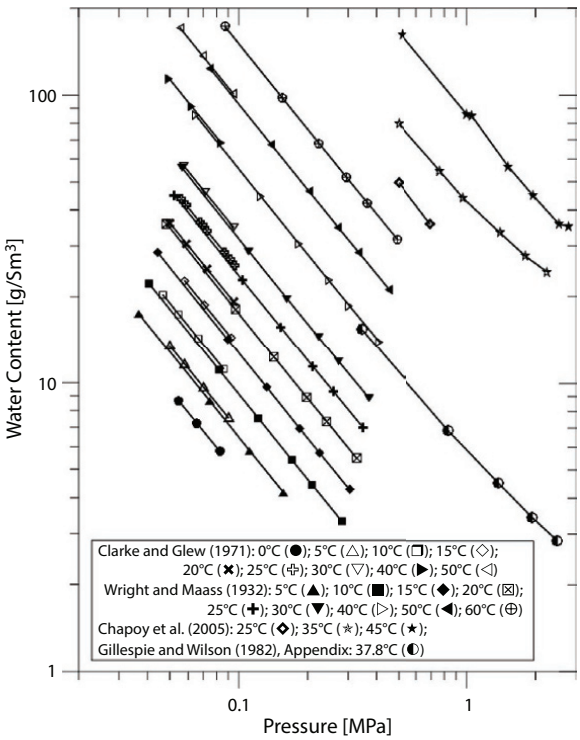

Figure 6.12 Water content of H_2S for T ≤60°C and P < 2 MPa.

Figure 6.12 shows the data for the temperatures of or below 60°C and pressure below 2 MPa. There are 104 data points in that region.

Figure 6.13 shows the data points for the temperatures above 60°C. There are 124 data points in that region. 4.

Figure 6.14 summarizes all the 302 experimental data points. Most of the water content is for pressures below 30 MPa. Only 13 points, or 4% of all the points, lie above 30 MPa.

The experimental data, for the pressures up to 0.8 MPa, were also compared using a regression model represented by Eqn. (6.7):

$$W = \exp\{a + b\ln(p) + c[\ln(p)]^2 + d[\ln(p)]^3\} \tag{6.7}$$

where: W – water content, g/S m^3
p – pressure, MPa
a, b, c, d – parameters

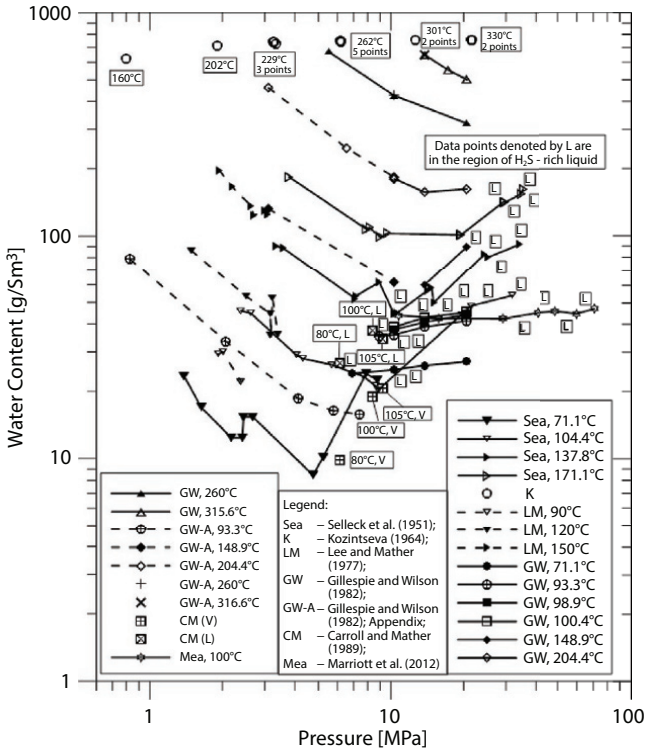

Figure 6.13 Water content of H_2S for T > 60°C.

The parameters of Eqn. (6.7) were determined by minimizing the objective function:

$$S = \sum_{i=1}^{n} \left(W_i^{exp} - W_i^{cal} \right)^2 \tag{6.8}$$

where: W_i^{exp} – the experimentally measured water content, g/Sm^3
W_i^{cal} – the corresponding model calculated water content, g/Sm^3
n – the number of experimental points
i – data index

The average relative percentage error, δ, which is a measure of accuracy of the model fitting to the experimental data, was calculated as:

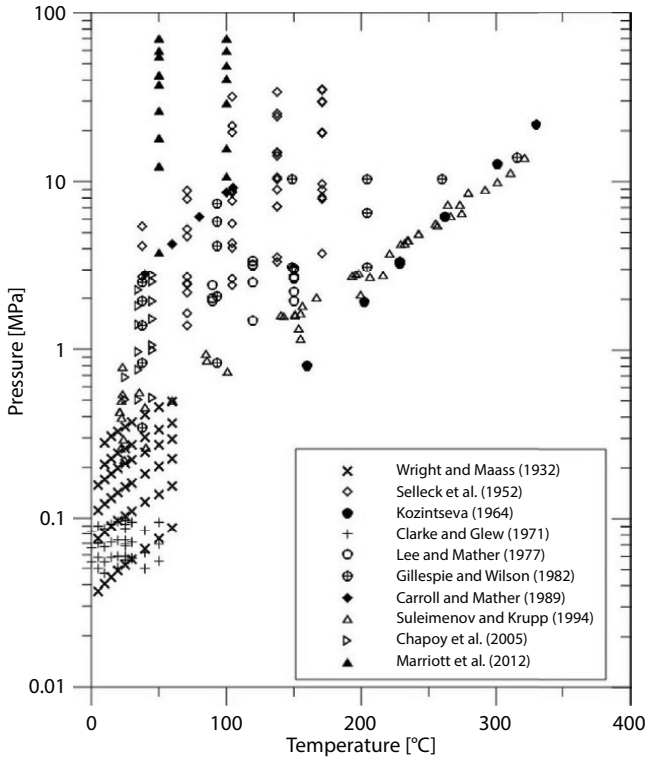

Figure 6.14 Summary of all the experimental data points for water content of H_2S.

$$\delta\% = \frac{\sum_{i=1}^{n} \left| \frac{W_i^{exp} - W_i^{cal}}{W_i^{exp}} \right|}{n} 100\% \tag{6.9}$$

The obtained parameters of Equation (6.7) and average relative percentage errors are given in Table 6.2. The model used gives an excellent description of experimental data, as shown in Figure 6.15. As can be seen from Table 6.2, the average relative error, δ, is not higher than 1.69% for each tested temperature.

The experimental data can also be described by a multi-temperature model that includes temperature-dependent parameters. In applying Eqn. (6.7) over a tested temperature range, the parameters *a*, *b*, *c*, and

Table 6.2 Model (Eq. 6.7) Parameters and Average Relative Errors for different temperatures.

T [°C]	a	b	c	d	d%
5	1.6358	1.6470	1.1090	$1.5099 \cdot 10^{-1}$	1.11
10	1.3520	1.0717	$9.4964 \cdot 10^{-1}$	$1.3859 \cdot 10^{-1}$	1.69
15	1.2240	$4.8919 \cdot 10^{-1}$	$7.1935 \cdot 10^{-1}$	$1.1022 \cdot 10^{-1}$	1.29
20	1.4855	$4.3045 \cdot 10^{-1}$	$7.0114 \cdot 10^{-1}$	$1.0861 \cdot 10^{-1}$	1.49
25	1.7854	$4.7011 \cdot 10^{-1}$	$7.4356 \cdot 10^{-1}$	$1.1864 \cdot 10^{-1}$	1.22
30	1.8316	$1.0354 \cdot 10^{-1}$	$5.7439 \cdot 10^{-1}$	$9.4233 \cdot 10^{-2}$	1.43
40	1.7695	$-9.5149 \cdot 10^{-1}$	$1.4169 \cdot 10^{-2}$	$6.4494 \cdot 10^{-4}$	0.76
50	2.3065	$-9.2007 \cdot 10^{-1}$	$3.0559 \cdot 10^{-2}$	$3.3960 \cdot 10^{-3}$	0.58
60	2.7859	$-9.2719 \cdot 10^{-1}$	$2.6804 \cdot 10^{-2}$	$3.7920 \cdot 10^{-3}$	0.47

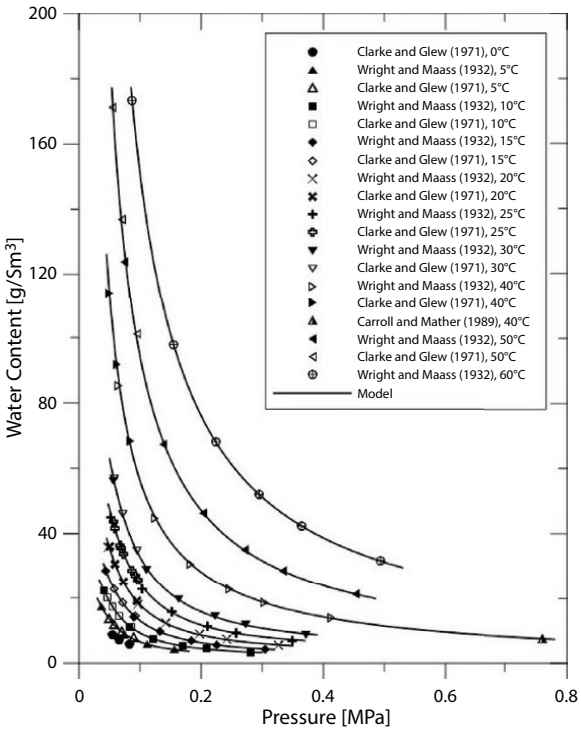

Figure 6.15 Comparison of experimental data with model predictions using Eqn. (6.7).

d can be considered temperature dependent, according to the following equations:

$$a = A_1 + B_1(T + 273) + C_1(T + 273)^2 + D_1(T + 273)^3 \quad (6.10)$$

$$b = A_2 + B_2(T + 273) + C_2(T + 273)^2 + D_2(T + 273)^3 \quad (6.11)$$

$$c = A_3 + B_3(T + 273) + C_3(T + 273)^2 + D_3(T + 273)^3 \quad (6.12)$$

$$d = A_4 + B_4(T + 273) + C_4(T + 273)^2 + D_4(T + 273)^3 \quad (6.13)$$

where: T – temperature, °C
$A_1, A_2, \ldots, D_4$ – parameters

The optimal values of parameters of Eqn. (6.10-6.13), calculated using the objective function (8), are:

$A_1 = -133.7566$
$B_1 = 1.2429$
$C_1 = -3.9290 \cdot 10^{-3}$
$D_1 = 4.2856 \cdot 10^{-6}$

$A_2 = -212.6590$
$B_2 = 2.2061$
$C_2 = -7.5460 \cdot 10^{-3}$
$D_2 = 8.4999 \cdot 10^{-6}$

$A_3 = -137.7600$
$B_3 = 1.4051$
$C_3 = -4.7220 \cdot 10^{-3}$
$D_3 = 5.2414 \cdot 10^{-6}$

$A_4 = -26.0027$
$B_4 = 2.6209 \cdot 10^{-1}$
$C_4 = -8.7221 \cdot 10^{-4}$
$D_4 = 9.6000 \cdot 10^{-7}$

The average relative error, δ, was found to be 5.35%. All experimental data, over a temperature range 0 °C - 60 °C, are well described by the multi-temperature model, as shown in Figure 6.16. The obtained results

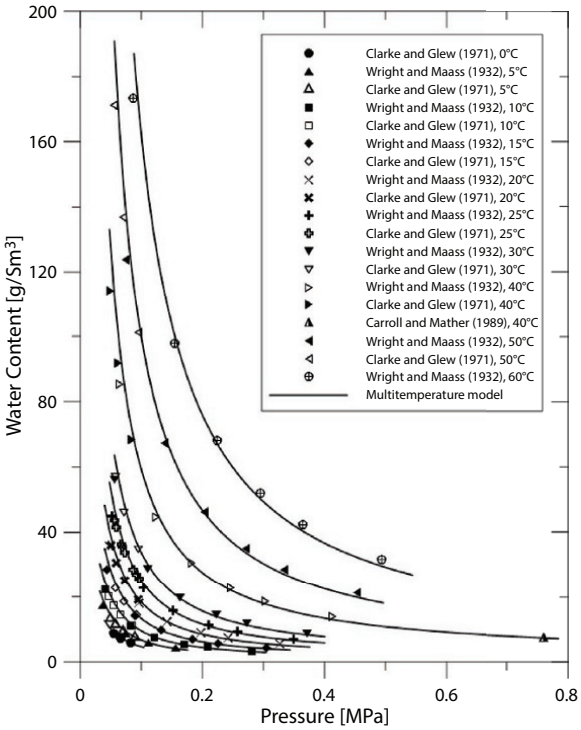

Figure 6.16 Comparison of experimental data with model predictions using a multi-temperature model.

show a good agreement of the model with the experimental data, for the pressures up to 0.8 MPa. Eqn. (6.7) can be used to calculate the water content of H_2S as a function of pressure at a constant temperature. The system of equations [Eqn. (6.7), (6.10) - (6.13)] (multi-temperature model) can be used to calculate the water content of H_2S as a function of pressure and temperature.

The information presented in this review can be condensed in Table 6.3.

6.4 Conclusions

Only 10 papers were identified regarding experimentally obtained water content of hydrogen sulfide, the first being written in 1932 and the last in 2012. Of 891 citations listed in Google Scholar on August 15, 2019, for the ten papers, 277 (31%) were regarding the paper by Selleck *et al.* [25], confirming its status as a benchmark study. A number of researchers

Table 6.3 Condensed summary of the papers reviewed.

Author	Temp. °C	Pressure MPa	No. of Points	Experimental Approach	Measured Values	Calculated Values
Wright and Maass [8]	5–60	0.0366–0.4942	52	Synthetic. All-glass vapor pressure cell	P, T, weight of water	Weight of H_2S, volume of vapor phase
Selleck *et al.* [25]	37.8–171.1	2.694–35.312	48	Spherical pressure bomb	P, T, weight of water in gas phase by anhydrous $CaSO_4$, condensing gas in a weighing bomb	
Kozintseva [19]	160–330	0.797–21.639	14	Static apparatus. A two-chamber bomb	T, weight of water, H_2S - iodometric	P (not stated in paper, calculated by reviewers)
Clarke and Glew [10]	0–50	0.047–0.096	36	Solubility cell	P, T, weight of water, volume of H_2S	Phase compositions, fugacities, Henry's law constants.

(*Continued*)

Table 6.3 Condensed summary of the papers reviewed. (*Continued*)

Author	Temp. °C	Pressure MPa	No. of Points	Experimental Approach	Measured Values	Calculated Values
Lee and Mather [20]	90–150	1.486–3.401	15	Recirculating equilibrium cell	T, P, vapor composition	H_2S evolved from liquid from PVT information
Gillespie and Wilson [21]	37.8–315.6	0.345–20.684	47	Equilibrium cell, used as a flow cell for sampling	T, P, weight of water, flowrate of gas sample	Moles of water from weight, moles of gas from flowrate, P and T
Carroll and Mather [13]	40–105	2.80–9.24	10	Flow-type cell	P, T of three-phase locus, compositions of the co-existing phases	Vapor pressure of H2S from correlation of Goodwin.

(*Continued*)

Table 6.3 Condensed summary of the papers reviewed. (*Continued*)

Author	Temp. °C	Pressure MPa	No. of Points	Experimental Approach	Measured Values	Calculated Values
Suleimenov and Krupp [15]	2.8–321	0.222–13.861	49	Reaction vessel with membrane bellows	T, P, volume, bulk composition – fully neutralized H_2S (by NaOH), by iodometric titration	Molar volume of gas mixture using PRSV-EOS, Henry constants, partial molar volumes of H_2S in aqueous solutions using a polynomial fit
Chapoy *et al.* [1]	25–45	0.503–2.778	15	Static analytic apparatus with fluid phase sampling	P, T, compositions of co-existing phases using a gas chromatograph	
Marriott *et al.* [23]	50–100	3.81–70.55	16	High pressure equilibrium vessel	P, T, compositions of co-existing phases using a gas chromatograph	

used Selleck's data to derive equations for water content of H_2S as a function of pressure and temperature, for example Pohl [24] and Burgess and Germann [9].

The total number of experimental points were 302, scattered between 0°C and 330°C and between 0.0366 MPa and 70.55 MPa.

The reason for a limited number of experimental data is likely the risk involved in working with high pressure H_2S and a limited number of laboratories in the world that are equipped to perform the measurements in the water-hydrogen sulfide systems. Besides, measuring gas solubility in water is easier than measuring water content of gases.

Water is more soluble in liquid hydrogen sulfide than in vapor hydrogen sulfide.

References

1. Chapoy, A., Mohammadi, A.H., Tohidi, B., Valtz, A., Richon, D., Experimental Measurement and Phase Behavior Modeling of Hydrogen Sulfide-Water Binary System. *Ind. Eng. Chem. Res.*, 44, 7567–7574, 2005.
2. Lukacs, J. and Robinson, D.B., Water Content of Sour Hydrocarbon Systems. *Soc. Pet. Eng. J.*, 3, 12, 293, 1963.
3. Clark, M.A., *Experimentally obtained Saturated Water Content, Phase Behavior and Density of Acid Gas Mixtures*, A Thesis, University of Calgary, 1999.
4. Carroll, J.J., The Water Content of Acid Gas and Sour Gas from 100° to 220°F and Pressures to 10,000 psia. *81st GPA Convention*, Dallas, TX, March 11-13, 2002.
5. IUPAC Solubility Data Series, *Hydrogen Sulfide, Deuterium Sulfide and Hydrogen Selenide*, vol. 32, 1988.
6. Forcrand, R. de, *Ann. Chim. Phys.*, 5, 17, 5, 1883.
7. Scheffer, F.E.C., Das System Schwefelwasserstoff-Wasser. *Z. Phys. Chem.*, 84, 707, 1913.
8. Wright, R.H. and Maass, O., The Solubility of Hydrogen Sulphide in Water from the Vapor Pressures of the Solutions. *Can. J. Res.*, 6, 1, 94–101, 1932.
9. Burgess, M.P. and Germann, R.P., Physical Properties of Hydrogen Sulfide-Water Mixtures. *AIChE J.*, 15, 272–275, 1969.
10. Clarke, E.C.W. and Glew, D.N., Aqueous Nonelectrolyte Solutions. Part VIII. Deuterium and Hydrogen Sulfides Solubilities in Deuterium Oxide and Water. *Can. J. Chem.*, 49, 1971.
11. Zezin, D.Y., Migdisov, A.A., Williams-Jones, A.E., PVTx properties of H2O-H2S fluid mixtures at elevated temperature and pressure based on new experimental data. *Geochim. Cosmochim. Acta*, 75, 5483–5495, 2011.

12. Selleck, F.T., Carmichael, L.T., Sage, B.H., *Some Volumetric and Phase Behavior Measurements in the Hydrogen Sulfide-Water System*, Document No. 3570, American Document Institute, Washington D. C, 1951.
13. Carroll, J.J. and Mather, A.E., Phase Equilibrium in the System Water-Hydrogen Sulphide: Modelling the Phase Behavior with an Equation of State. *Can. J. Chem. Eng.*, 67, December. 1989.
14. Carroll, J.J., *Phase Behaviour in the System Water-Hydrogen Sulphide*, Ph.D. Thesis, Department of Chemical Engineering, University of Alberta, Edmonton, AB, 1990.
15. Suleimenov, M. and Krupp, R.E., Solubility of Hydrogen Sulfide in Pure Water and in NaCl Solutions, from 20 to 320°C and at Saturation Pressures. *Geochim. Cosmochim. Acta*, 58, 11, 2433–2444, 1994.
16. Spear, R.R., Robinson, R.L., Jr., Chao, K.C., Critical States of Mixtures and Equations of State. *Ind. Eng. Chem. Fundamen.*, 8, 2, 1969.
17. Vogel, J.L., *An Experimental Study of the Solubilities of Pure Hydrogen Sulfide in Water and of Methane-Hydrogen Sulfide Gas Mixtures in Water and Brines at Reservoir Conditions*, M.S. Thesis, Dept. of Petroleum Engineering, University of Tulsa, Tulsa, OK, 1971.
18. Goodwin, R.D., *Hydrogen Sulfide Provisional Thermophysical Properties from 188 to 700 K at pressures to 75 MPa*, Report No. NBSIR 83-1694, National Bureau of Standards, Boulder, CO, 1983.
19. Kozintseva, T.N., Solubility of Hydrogen Sulfide in Water at Elevated Temperatures. *Geokhimiya*, 8, 758–765, 1964.
20. Lee, J.I. and Mather, A.E., Solubility of Hydrogen Sulfide in Water. Ber. Bunsenges. *Phys. Chem.*, 81, 1021–1023, 1977.
21. Gillespie, P.C. and Wilson, G.M., *Vapor-Liquid and Liquid-Liquid Equilibria: Water-Methane, Water-Carbon Dioxide, Water-Hydrogen Sulfide, Water-Npentane, Water-Methane-Npentane*, Research report RR-48, Gas Processors Association, Tulsa, 1982.
22 Alami, I.A., Monnery, W.D., Svrcek, W.Y., Model predicts equilibrium water content of high-pressure acid gases. *Oil Gas J.*, July 11, 2005.
23. Marriott, R.A., Bernard, F., Giri, B.R., The Equilibrium between H_2S and Water at High-Pressures. *3rd International Acid Gas Injection Symposium*, Banff, 2012, (also published in Sour Gas and Related Technologies, Wiley 2012).
24. Pohl, H.A., Thermodynamics of the Hydrogen Sulfide-Water System Relevant to the Dual Temperature Process for the Production of Heavy Water. *J. Chem. Eng. Data*, 6, 4, October 1961.
25. Selleck, F.T., Carmichael, L.T., Sage, B.H., Phase Behavior in the Hydrogen Sulfide-Water System. *Ind. Eng. Chem.*, 44, 9, 2219–2226, September 1952.

7

Acid Gas Injection at SemCAMS Kaybob Amalgamated (KA) Gas Plant Operational Design Considerations

Rinat Yarmukhametov[1]*, James R. Maddocks[1] and Jason Lui[2]

[1]Gas Liquids Engineering Ltd., Calgary, AB, Canada
[2]SemCAMS, Calgary, AB, Canada

Abstract

SemCAMS currently owns and operates the Kaybob Amalgamated (KA) sour gas processing facility, located near Fox Creek, Alberta. The gas plant takes gas from various sweet and sour inlets and processes these streams to produce sales specification gas, LPG and C5+ products.

With reduced plant throughput and lower H_2S concentration in the feed stream to the Sulfur Recovery Unit, the existing sulfur plant was operating below the design turndown rates, which impacts the performance and reliability of the entire facility.

SemCAMS decided to decommission the sulfur plant in Q2 2018 and replace it with acid gas compression that will inject acid gas into a disposal well drilled on the plant lease.

The GLE scope of work was to complete detailed engineering (process, civil, mechanical, electrical, instrumentation and controls) of the two acid gas injection compressors, including the suction piping from the existing acid gas knockout drum, the discharge piping to the wellhead, as well as utility piping to/from the compressors (instrument air, fuel gas, flare, drains, etc.).

Major project decisions and design aspects are reviewed and discussed with a focus on capital & operational cost, challenges, issues, and lessons learned relating to process modelling and operational design.

Process modelling topics discussed include: steady state and dynamic modelling for the AGI system; flare system design; compression capacity control; hydrate formation prevention during system blowdown; methanol injection for hydrate prevention; prediction of water content/hydrate formation temperatures within

**Corresponding author*: RYarmukhametov@gasliquids.com

Ying Wu, John J. Carroll, Mingqiang Hao and Weiyao Zhu (eds.) Gas Injection into Geological Formations and Related Topics, (115–136) © 2020 Scrivener Publishing LLC

the AGI system and finally overpressure protection of compression equipment and the injection line.

Operational design topics discussed include: Inherently Safety Design (ISD) strategies; material selection for compression equipment and the injection line, air cooler design, impact of leak scenarios on the existing plant and AGI system design; freeze protection; considerations for depressurization duration and acid gas flaring scenarios; and impact of the existing plant safety practises on the addition of the AGI system.

Keywords: Acid gas injection, Kaycob sour gas plant, project management, project execution

7.1 Project Drivers

SemCAMS currently owns and operates the Kaybob Amalgamated (KA) sour gas processing facility, located approximately 8 km (5 miles) southwest of Fox Creek, Alberta, Canada. The gas plant takes gas from various sweet and sour inlets and processes these streams to produce sales specification gas, LPG, and C5+ products.

The sour gas is sweetened through the use of a traditional amine system. The amine is regenerated for reuse, and through this process, acid gas (mixture of H_2S and CO_2) is liberated. Currently the acid gas is processed for sulfur recovery through the existing "Claus" and "Sulfreen" units. The acid gas flow from this facility will be piped to the new acid gas compressors for sub-surface injection, allowing the sulphur plants to be shut down. The normal flowrate of acid gas is 75 e^3m^3/day and the design flowrate of acid gas is 105 e^3m^3/d (calculated on a dry basis; however, the actual design will be larger due to being water saturated).

With reduced plant throughput and lower H_2S concentration in the feed stream to the Sulfur Recovery Unit, the existing sulfur plant is currently operating below the design turndown rates, which impacts the performance of the entire facility.

The proposed acid gas injection scheme is intended to replace the plant's existing sulphur recovery process by offering an alternative method for reducing the emissions of sulphur-containing compounds at the plant and achieving the sulphur recovery requirements set in the AER's Interim Directive Sulphur Recovery Guidelines for the Province of Alberta.

SemCAMS will be drilling a new acid gas injection well on the plant lease. The sulfur pit will remain in use to allow third-party liquid sulfur to be brought in from other facilities for prilling and export.

7.2 Process Design Basis

The range of acid gas compositions used for the design of the acid gas injection facilities varies widely from 30% H_2S (balance mostly CO_2) up to 60% H_2S. However the inlet compositions of the lines coming into the KA plant are varied, and it is possible that during upset or start-up conditions, or through future field development, that the acid gas composition may be as high as 82% H_2S. This is not considered a normal operating condition and therefore is not incorporated as a design case; however, the operation of the acid gas injection compressors and associated equipment with acid gas compositions of 70% and 85% H_2S content was investigated for feasibility.

7.2.1 Acid Gas Inlet Design Conditions

Acid gas from the Plant 1 & 2 amine reflux accumulators enters the existing acid gas knockout drum. Acid gas (Table 7.1) leaving the knockout drum will then be routed to the new acid gas compression suction header. It is important to note that the design inlet operating temperature of 30°C from the reflux accumulators is achieved through the use of cooling water for amine stripper reflux condensing.

7.2.2 Acid Gas Compositions

The following table defines the Inlet Acid gas composition (Table 7.2) for all design cases. It should be noted that water concentration reflects "saturation" condition of the streams at suction conditions.

Table 7.1 Inlet acid gas design conditions.

Operating Condition	**30% H_2S**	**60% H_2S**	**70% H_2S**	**85% H_2S**
Standard Volume Flow Rate (Note 1)	105 e^3Sm^3/d	105 e^3Sm^3/d	105 e^3Sm^3/d	105 e^3Sm^3/d
Operating Inlet Pressure	55 kPag	55 kPag	55 kPag	55 kPag
Operating Inlet Temperature Range	30°C	30°C	30°C	30°C

Note 1: Dry basis (stream is not water saturated).

Table 7.2 Inlet acid gas composition.

Component (mole %)	30% H_2S Design Case	60% H_2S Design Case	70% H_2S Case (Note 1)	85% H_2S Case (Note 1)
H_2O	1.60	1.60	1.60	1.60
H_2	0.00	0.00	0.00	0.00
He	0.00	0.00	0.00	0.00
N_2	0.07	0.04	0.03	0.02
CO_2	66.29	35.96	24.83	11.90
H_2S	**29.52**	**59.87**	**70.33**	**83.94**
C1	1.53	1.53	1.95	1.54
C2	0.49	0.49	0.63	0.49
C3	0.22	0.22	0.28	0.22
iC4	0.04	0.04	0.05	0.04
nC4	0.09	0.09	0.11	0.09
iC5	0.02	0.02	0.03	0.02
nC5	0.02	0.02	0.03	0.02
C6	0.02	0.02	0.03	0.02
C7	0.09	0.09	0.11	0.09
Total	100.00	100.00	100.00	100.00

Note 1 – The 70% H_2S and 85% H_2S cases are **not** used as a design basis cases. They are used strictly for sensitivity studies on the acid gas compression operation at a higher H_2S content.

7.2.3 Acid Gas Compressor Discharge

7.2.3.1 Acid Gas Conditions

The acid gas fluid (Table 7.3) leaving the acid gas compressors will have the following properties:

7.2.3.2 Acid Gas Composition

The acid gas at the discharge of the final stage (Table 7.4) will have the following composition:

Table 7.3 Acid gas discharge conditions.

Acid Gas Discharge Conditions	
Design Volume Flow Rate	105 e^3Sm^3/d (Note 1)
Maximum Operating Pressure (upstream of backpressure control valve)	11,000 kPag
Fluid Density Range (at surface)	617-754 kg/m^3
Water Content Range	2583-4306 mg/m^3 (159-265 lb/MMSCF)

Note 1: Actual discharge flow rate is dependent on compressor performance, inlet composition and water content in the inlet stream.

Table 7.4 Acid gas discharge composition.

Component (mole %)	**30% H_2S design case**	**60% H_2S design case**	**70% H_2S case**	**85% H_2S case**
H_2O	0.33	0.35	0.46	0.46
H_2	0.00	0.00	0.00	0.00
He	0.00	0.00	0.00	0.00
N_2	0.07	0.04	0.03	0.02
CO_2	67.14	36.42	25.12	12.04
H_2S	**29.90**	**60.64**	**71.15**	**84.92**
C1	1.55	1.55	1.97	1.56
C2	0.50	0.50	0.63	0.50
C3	0.22	0.22	0.28	0.22
iC4	0.04	0.04	0.05	0.04
nC4	0.09	0.09	0.11	0.09
iC5	0.02	0.02	0.03	0.02
nC5	0.02	0.02	0.03	0.02
C6	0.02	0.02	0.03	0.02
C7	0.09	0.09	0.11	0.09
Total	100.00	100.00	100.00	100.00

7.3 Acid Gas Compression Description

Five-stage acid gas compression will be required to achieve the range of injection wellhead pressures associated with the different design compositions. A consistent backpressure will be maintained on the compressors above the wellhead pressure to ensure consistent, steady and predictable compressor operation. Maintaining backpressure fixes the inter-stage pressures, which ensures that aftercooler outlet temperature set points are well defined relative to the acid gas phase envelope and avoids any incursions into the phase envelope.

Dehydration of the acid gas will be accomplished strictly through compression, after cooling, and water removal in the suction scrubbers. Sufficient hydrate and water dew point suppression is achieved in this manner and no external acid gas dehydration is required. Stainless steel piping will be required between the acid gas compressors and the injection well and methanol injection will be provided for further hydrate suppression during shut down situations.

The compressor package is to be equipped with inlet and outlet ESD valves, auto-recycles, fuel gas purge and backpressure control for maximum system response. Acid gas after-cooling shall take place in air coolers with variable speed fan drives, warm air recirculation, and auxiliary heating.

The Gas Liquids team completed a comparison in terms of cost, operation, maintenance and risk with regards to the type of compressor driver and recommended to install electric drive motors for this application.

The electric drive motor with variable speed drive offers superior operating performance, flexibility, reliability, maintenance and a reduced capital cost vs. the gas drive option.

Reliability is the key design feature of any acid gas compressor installation. One of the design features of the SemCAMS units is to use a reduced piston speed for the compressor. This was accomplished by utilizing a short stroke compressor at 2/3 of its design speed.

7.4 AGI System Capacity Control

Acid gas leaves the amine sweetening system via either the normal acid gas suction line or via an overpressure relief in the event of a compressor flow restriction or inability to move the required volume of acid gas. Both streams are electronically metered and pressure controlled.

Acid gas is compressed in five (5) stages of compression with intercooling on each stage. The design philosophy of the compressor capacity control system is to automatically maintain a constant suction pressure at or near the

desired regeneration system set point with minimum operator intervention. The primary capacity control is to vary the compressor speed using the AC variable frequency controller to adjust the speed of the motor and the gas flow.

Compressor capacity is controlled per the following series of interlinked PID loops:

- On declining suction pressure, the electric motor will slow automatically to reduce capacity and to maintain system suction pressure as gas throughput decreases. Once the motor speed is at a predetermined minimum, the auto-recycle system will begin bypassing discharge gas to maintain adequate suction pressure. The 1st stage suction pressure is maintained by bypassing a mix of cold and hot 5th stage discharge gas back to the 1st stage suction.

Due to the varying inlet composition, the acid gas fluid responds differently during a pressure let-down. High H2S content acid gas experiences a much higher differential temperature than high CO2 acid gas. Thus, it was impossible to construct a system with a single bypass that would operate for all compositions. The following graph shows the differences in outlet temperatures for differing compositions during a pressure reduction from 11,000 kPag to suction conditions (Figure 7.1; Graph 1).

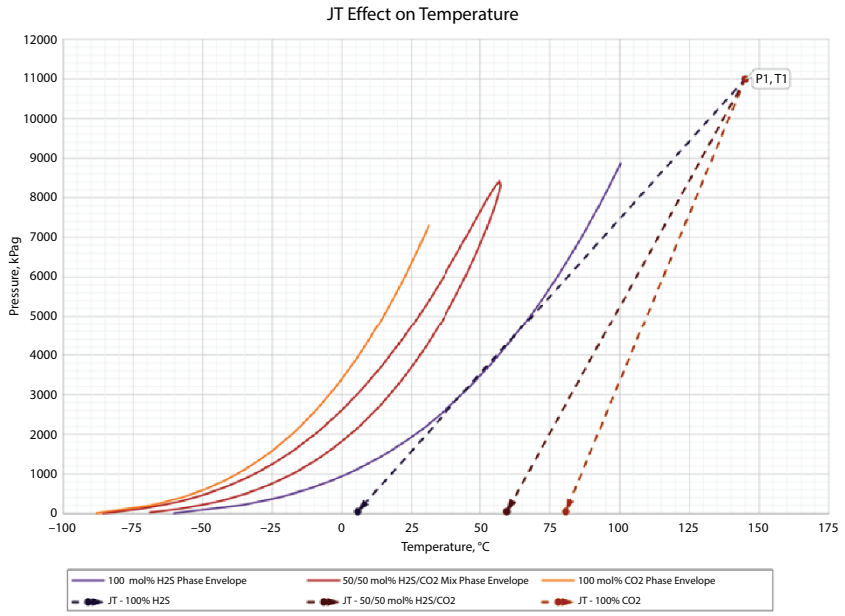

Figure 7.1 Acid Gas JT effect as the result of pressure reduction.

The capacity control bypass valve located in the compressor building recycles mixed 5th stage hot and cold acid gas back to the first stage suction scrubber. Specifically, the hot side temperature control valve and cold side temperature control valve will be actuated by the temperature transmitter located downstream of the capacity valve. The hot side valve is a fail-open valve while the cold side valve is fail-closed to prevent overcooled discharge fluid from returning to the compressor suction during a shutdown or control system failure/upset.

The control of bypass fluid temperature is sensitive, requiring a careful selection of set points to achieve the following goals:

- Primary – maintain the overall temperature of the bypass gas to keep the mixed suction gas in the correct range and below the High Temperature Shutdown set point
- Secondary – maintain the overall temperature of the bypass gas above hydrate formation.

A typical suction set point is 20-30°C. The intent of this system is such that the compressor is unaware of the bypassing fluid and continues to function normally.

Due to wide variations of the H_2S /CO_2 ratio, the final water content of the discharge acid gas will mean variations in the hydrate formation temperature of the acid gas. The temperature control system will attempt to ensure a constant bypass fluid temperature regardless of the composition and flow.

- On increasing suction pressure, the recycle valves will close in reverse order and the motor will speed up to increase compressor delivery capacity.
- On increasing discharge pressure beyond normal limits, the auto-recycle valves will also open to begin bypassing acid gas to avoid a unit shutdown or a PSV release on discharge. The suction pressure will increase and the acid gas to flare pressure control valve (located in the amine plant) will begin to open allowing metered flaring of acid gas.

It should be noted that either suction pressure dropping below a control set point or discharge pressure rising above a high set point can result in both speed (first) and recycle (second) being activated almost simultaneously. If the pressures either decrease or increase

quickly, there will be an offset between speed and bypass that will result in both being activated to meet the set point. If the upset happened at a slower rate, then the compressor would go first to minimum speed, then to recycle. This control offset can be adjusted to maximize performance.

During winter and/or low flow conditions, the aerial coolers will be vastly oversized. This combined with the normal air leakage can result in a low plenum temperature and consequently acid gas overcooling and condensation.

In order to minimize the risk of acid gas condensation due to low ambient and low plenum temperatures, two Ruffneck heaters were added per cooler section. These steam heaters use 700 kPag saturated steam from the KA Plant utility system to provide artificial heat in the plenum during very cold ambient temperatures.

7.5 Project Execution

Front End Loading (FEL). Early involvement of GLE AGI experts at earlier stages of the project minimizes the need for changes during the project cycle. A good definition and early scoping of the project allows for project execution with minimal changes. FEL helps to achieve fast cycle times, lowers the cost and ensures excellent operability and safe design.

Engineering standards and specifications can affect the total installed cost (TIC) of the project, construction efficiency, operating cost and employee safety. Comparing an AGI system installation to a typical gas processing project, certain design features of the AGI project can be viewed as "gold plating" or even as non-value adding investments.

While the project team strives to avoid multiple levels of conservatism, the stringent safety requirements for high concentration/high pressure H_2S service would require a more conservative approach in certain areas such as safety equipment, materials, valves and instrumentation. As well, it should be noted, that performance of the AGI system is integral to the reliability and performance of the KA processing facility.

Purchasing from reliable manufacturers with the long-term cost of ownership (life cycle) in mind is essential to ensure safe operation and maintenance of the AGI equipment. It is important for the end user to pay careful attention to parameters beyond initial cost.

Point Cloud: A 3D model is a key project deliverable which has a significant impact on piping design, plot plan development, operations reviews and tie-ins reviews.

Brownfield projects present certain challenges when it comes to 3D modelling. To address the integration of the AGI 3D model into the existing plant, GLE used a point cloud method.

The final point cloud file is a set of data points in a three-dimensional coordinate system. Point cloud files were created by 3D laser scanners of the KA facility. Integration of the existing plant data (Figure 7.2) into the AGI 3D Model allows a reduction of project costs and schedule while maintaining high engineering integrity and quality. The use of an integrated 3D model assists in constructability reviews, operator reviews, and improves planning, safety and accuracy during construction.

Modular design for pipe racks: a cost benefit analysis demonstrated that small pipe racks will cost less if constructed in the field, but the cost reduction for larger modules (Figure 7.3) justified the project decision to use a modular rack design for AGI system pipe racks. Another major driver in selecting modular method for the AGI piperack design was a higher assurance of quality of the final product. Shop fabrication allows the use of stringent quality systems and testing to ensure that finished systems conform to technical requirements. Building the modules offsite also resulted in minimal plant site interruption, a smaller labour force and lower manhours during the construction phase.

Figure 7.2 Produced water storage bullets.

Figure 7.3 Modular piperack on site.

7.6 Risk Assessment Strategy

H_2S is extremely hazardous even in very low concentrations. Hence, plant personnel and public safety must take priority over all other concerns. In the developing and implementing an acid gas injection project within an operating asset, it is critical to identify hazards associated with a proposed change as part of the management of change process. This can be challenging in legacy facilities.

For the KA AGI system project, a Hazard Identification (HAZID) study was conducted during the early stages of the project development to ensure that the potential hazards of the proposed design are identified and managed appropriately in the detailed design. The HAZID was used to develop the initial hazard and risk register.

The project decision to conduct a HAZID earlier allowed the project team and owner to examine all possible sources of hazards, including the process design itself and hazards external to the process and helped to include additional layers of protection and procedural controls into final design.

The SemCAMS and GLE project team held numerous design and operational safety reviews during the entire project duration. As a result of the HAZID reviews and dynamic modelling, the final facility design includes the following additional design features to mitigate the potential hydrogen sulfide release on site:

- Added a line heater to heat the process fluid prior to blowdown to minimize the risk of hydrate formation during cold fluid blowdowns.
- The injection line is installed within a Utilidor with multipoint H_2S detection
- Additional automated methanol injection points
- Permissive for line heater minimum temperature and fluid level in order to operate
- Discharge line is maintained above hydrate point all the time with the addition of insulation and tracing.
- Additional ambient H_2S detectors

7.7 Utilities & Tie-Ins

Tie-ins were executed during a scheduled wide plant shutdown in spring 2018. Installing tie-ins ahead of major AGI equipment and pipe racks helped to minimize plant disruptions during the installation of the new equipment. Construction drawings were issued well in advance which allow operational and construction teams to plan activities around each tie-in point.

One of the critical element of the tie-in construction phase was the flare system tie-in (Figure 7.4). Due to flare system considerations, the hot tap method was selected in lieu of modifications of the existing header. The flare header cut and weld option was rejected due to risk and additional engineering and construction cost. The intent all the tie-in work was to minimize operational upsets to the KA facility.

The existing plant flare system serves more than one process unit. Block valves at each unit's battery limits are usually necessary to allow the unit to be taken out of service for turnarounds without having to take down all units connected to the flare system. All block valves in a flare system must be locked open and be subject to a strict lockout/tagout control program. The block valves may only be closed after the unit has been completely shut down and secured. Usually this will be after all blinds necessary to open equipment for inspection have been installed.

To avoid partial or complete line blockage due to a detached gate, all gate valves used for flare header isolation must be installed with their stems in the horizontal (preferable) or downward vertical position.

Figure 7.4 Completed flare system tie-in.

7.8 Relief System Design

7.8.1 KA Gas Plant Flare System

The existing KA Facility flare system consists of:

- 356 mm Ø (14″) main HP Flare header
- 610 mm Ø (24″) main LP Flare header
- 324 mm Ø (12″) main MP Flare header
- 4877 mm S/S x 2743 mm ID vertical flare liquids knockout drum
- 7315 mm S/S x 3658 mm OD horizontal flare liquids knock-out drum
- 762 mm (30”) OD x 53,340 mm (175’-00”) tall Flare Stack

There are three flare systems (headers) on site based on the set pressure of PSVs tied into the headers:

Low pressure:	0-17 50 kPag
Medium Pressure:	1751 – 4500 kPag
High Pressure:	4501+ kPag

Each of these headers are combined into several flare KO drums and a single flare stack. The existing flare header piping material is ASTM A53 SMLS which has an MDMT of - 29°C.

7.8.2 AGI System Flare System

Individual AGI compressor unit flare headers will collect the following sources of acid gas to be flared:

- PSVs installed on Stages 1-5 of compressors (hot side)
- Automated blowdown valves
- Manual vents and blowdowns
- Utility PSVs
- Highline PSV

The new common acid gas flare header is routed to the existing flare system. Acid gas flare metering is provided for the new acid gas flare header as well as fuel gas mixing to ensure adequate heating value and flare stack tip velocities are maintained to meet ground-level SO_2 dispersion requirements during acid gas flaring events.

The PSVs, laterals and main flare header associated with the acid gas injection system are constructed of 316/316L dual certified material.

7.8.3 Evaluation of Existing Plant Blowdowns Concurrent with the AGI Compressors Blowdown

GLE reviewed the overall impact of the AGI system blowdown on the flare system when the existing plant equipment is depressurized simultaneously. SemCAMS identified 4 (four) existing scenarios where current plant equipment is depressurized.

The blowdown cases were modelled in Flare Net using the following assumptions:

- Blowdown cases considered instantaneous peak flow for all sources.
- The comparison pressure sensing point is at the vertical FKOD.
- AGI blowdown cases include the addition of fuel gas (FG) with the requisite 2:1 ratio (FG:AG).

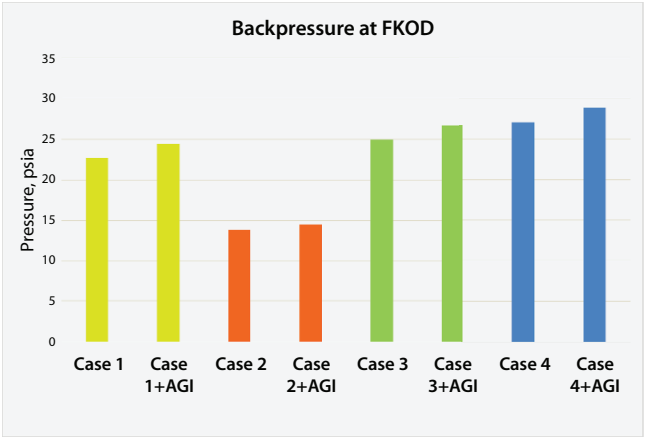

Figure 7.5 Backpressure at FKOD.

Figure 7.5 shows the backpressure at the comparison sensing reference point for the four (4) base line cases and 4 (four) additional cases where the AGI system blowdown volumes were considered. Results clearly demonstrate that even for the worst case scenario the additional backpressure at the FKOD will not exceed 14 kPag and does not impact the flare system performance with higher blowdown rates.

7.8.4 Inherently Safer Design (ISD) Strategies in Pressure Relief System Design for AGI Systems

Pressure relief systems are emergency systems whose only function is to prevent internal pressures in process vessels and equipment from rising to levels which could cause severe damage or catastrophic failure. These systems are relied upon for ultimate protection when normal process system interlocks, controls, and operating practices have failed to maintain a process at safe pressures. In essence, they are intended to perform only when the operation of a process runs out of control, and equipment and personnel safety can only be maintained through emergency release of process material. Operation of a pressure relief system may pose hazards in itself, but these hazards are usually overshadowed by the greater danger of continued pressure build-up.

Properties of acid gases under relief conditions are very different from normal operation. Acid gases expanding across a relief device or a

blowdown valve into a low pressure system will experience substantial cooling due to the Joule-Thomson (J-T) effect and can lead to flare system mechanical damage due to hydraulic surge of liquid slugs, impact from solid ice slugs or hydrates and low temperature embrittlement through auto refrigeration.

The most common approach for process systems handling acid gases at elevated pressures is to locate relief devices in the part of the process where the relieving fluid will be at relatively high temperature as it is relieved. Using the AGI compressor discharge piping upstream of the cooler is the preferred location of the pressure safety valve (PSV) as well as the compressor blowdown assembly.

The AGI injection header, running at a cooler temperature (43°C), presents a challenge for flare system design, since discharging a PSV on the highline as the result of possible wellhead blockage will result in two phase flow potentially involving cryogenic conditions of acid gas relief. A flare header blockage as the result of plugging with solids (hydrates, ice buildup) is the potential scenario and the flare system design should ensure that sufficient mitigation steps are in place on the AGI system to limit the consequences of the multiphase cold relief.

The ISD strategy for acid gas relieving systems is to design the systems to prevent a two phase relief scenario, as downstream handling systems, such as piping and liquid disposal, require additional design measures to ensure that the fluids can be handled safely.

To address the injection line relief scenario, the GLE team included the following design features into the AGI flare relieving system to significantly reduce or eliminate the probability of a PSV relief event:

- The AGI compressor stage five cooler design pressure is 15 MPag. The final discharge header (1500#) has an MAWP of 18.1 MPag which is piping class 1500# derated to the highest temperature that is expected to exist coincident with the design pressure. Thus, the compressor PSV's (warm location) will relieve initially prior to the injection line PSV.
- Pressure relief devices themselves require some margin between operating pressure and the device set pressure. If this margin is not observed, leakage or premature operation (simmering) of the device may occur. Process stability is a significant concern with very narrow differences between operating pressure and set pressure.
- The normal injection pressure of the AGI system is 11 MPag.

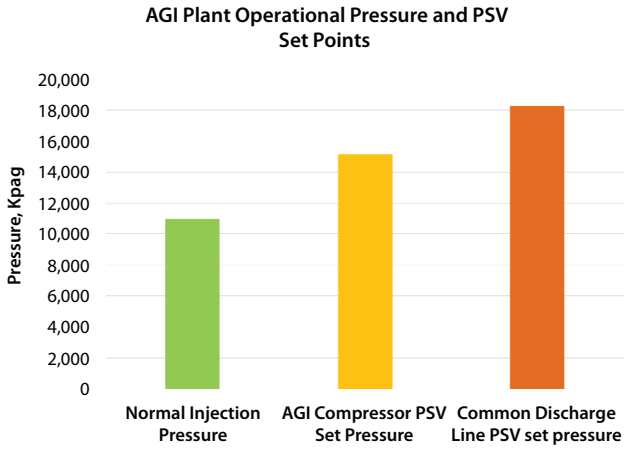

Figure 7.6 AGI System PSV set points.

- The injection line PSV set pressure was raised to provide a sufficient margin between the AGI compressor PSV set pressures and the injection line safety valve PSV set pressure (Figure 7.6).

If there is a blockage at the injection well, the expectation is to lift a PSV on the compressor initially and relieve hot acid gas while maintaining PSV integrity and protection on the injection line. In an ideal case, the injection line PSV will never be required to function.

7.8.5 MDMT Evaluation

There are certain activities such as start-up, upset conditions, or maintenance activities around the acid gas injection piping and AGI wellhead which will require the depressurization of the system containing acid gas in the dense phase. Since there can be appreciable temperature effects when acid gas fluids are reduced in pressure, the relieving system design and the suitability of the materials of construction to adequately facilitate the depressurization of the system will be considered.

A dynamic study was completed for the Acid Gas Flare Header which routes acid gas blowdown fluids from the wellhead piping to the existing plant flare system. The piping system consists of 10 meters of 114 mm dia stainless steel piping which connects to 200 meters of 273 mm dia stainless steel piping prior to connecting to the existing plant flare system. The study

estimated the temperature at the location of the 114 mm and 273 mm new flare piping connection which is 10m/200m away respectively from the existing flare system.

The objective of this study was to estimate the wall temperature profile of the flare header to ensure that controlled depressurization of the system will not create a brittle fracture condition for the existing flare header which has a minimum design metal temperature (MDMT) of -29 °C.

The temperature of the piping wall at the tie-in to the 24" flare system is estimated to be 9°C as the result of controlled depressurization. The temperature reduction due to auto refrigeration from cold depressurization will not result in temperatures below the MDMT of the existing flare system.

7.8.6 Drain Management

Pocketed flare system header piping, including any underground piping, is not allowed for flare systems due to the increased corrosion risks and increased system backpressures that may result. Increases in system backpressure due to liquid accumulation and solids deposition has the negative effect of a reduction of the flare system design capacity and raises the possibility of exceeding the flare system pipe rating during a flaring event. Also, it can lead to unstable facility operation and a lack of flare system reliability.

Lateral, blowdown valves and PSV tie-in connections into the flare header should be sloped downwards into the flare header where practical; however, level lateral connections will be accepted without a specification waiver. Any risks associated with liquid accumulation resulting in backpressure/blockage in lateral and PSV tie-ins that are not sloped continuously into the flare header must be mitigated by design (manual low point drains, heat trace, build/design to match full upstream MOP, etc.).

Traditionally, Acid Gas compressor PSVs are located at the compressor skid floor level and the design team must ensure that PSV performance is not impacted by any liquids accumulation in low points of the header as the fluid is travelling up to the primary flare header.

Each compressor flare sub header is equipped with a drain pot. A similar arrangement is also used on distance piece vent line to allow the removal of accumulated liquids.

Heat traced and insulated drain pots are equipped with a level gauge and level switch. LP fuel gas is used to push any liquids accumulated toward the high points of the flare header and pots are routinely checked by Operators every shift.

7.9 Discussion

Relief system design is based on the as-built capabilities of existing plant equipment, controls, and piping systems. To maintain the integrity of overpressure protection, any change to the physical plant (apart from replacement in kind) must be assessed for its impact on relief requirements. Under current KA Plant process safety management practices, this evaluation should be part of a documented Management of Change (MOC) review, followed by a relief system design revalidation.

Late design of the relief system has historically caused significant additions to project costs, as well as a less than ideal technical and cost solution. Early development of the AGI system relief protection philosophy allowed the project team to prevent costly rework or add-ons and minimized the risk of late changes.

Flare system design modelling and assessment of the existing relieving system clearly demonstrated that additional volumes from the AGI system does not hinder the functionality of the existing safety system. Modifications of the plant flare system as part of addition of AGI equipment are consistent with the original relief and overpressure design basis, with no negative impact on the original design intent.

7.10 Start-Up

A successful start-up is one that covers all aspects of operational excellence: safety, environment performance, reliability, schedule, cost and quality. A thorough commissioning and start-up planning process is an essential part of any AGI project. Commissioning start-up is always a consideration in every facet of the project design and construction.

Starting up a new process unit within an existing facility can present certain challenges that were never considered during all phases of the project. Legacy processing facilities may inadvertently have hidden characteristics which can be found under certain conditions or circumstances.

Data collected during the AGI Plant start-up demonstrates that even meticulous planning and attention to all aspects of a project cannot always address operational hazards that are not known to operational and start-up teams.

During start-up, the acid gas compression equipment experienced an unusually high differential pressure between the Amine Plant Regenerator and the suction of the acid gas compressors. Using drain valves on the suction line, operators ensured that there was no accumulation of liquids in

the low points of the suction header. The AGI system start up resumed but pressure losses in the suction header remained higher than expected.

The AGI compressors were stopped and 1st stage suction strainers were removed for visual inspection. Both strainers were covered with a sludge type material which caused a significant blockage and resulted in excessive pressure drop in the suction line. A sample was sent to the lab and subsequent analysis showed that the bulk of the substance collected is the silicon and iron with some traces of precious metals and asphaltenes.

One of the possible explanations for the origin of the material collected on suction strainers is the result of dislodged materials sitting in the existing acid gas piping during commissioning and start-up. An anti-foaming agent, sand, corrosion products, iron sulphides and hydrocarbons collected in the piping for the last number of decades are believed to have contributed to the formation of the substance caught in the suction strainers (Figure 7.7).

Suction strainers were kept in place on both units and the current design has provisions in place to monitor differential pressure to allow early detection of accumulation of any foreign materials on the surface of the witches hat strainers.

Figure 7.7 Suction Strainer.

7.11 Conclusions

Acid gas injection is a reliable, safe, and cost-effective long-term solution for disposal of acid gases. Reinjection of acid gases into an underground formation releases the minimum amount of greenhouse gases into an atmosphere compared with options for sulfur recovery and thermal sulphur destruction.

Brownfield projects present certain challenges for both technical and project execution aspects of the addition of new process equipment to the existing site.

A thorough engineering review of existing plant infrastructure and process equipment along with detailed commissioning and start-up planning is the key factor for safe, efficient operation and to maintain the high integrity demanded of acid gas injection facilities.

8

Reciprocating Compressors in Acid Gas Service

Dan Hannon

Ariel Corporation, Mount Vernon, Ohio

Abstract

Hydrogen sulfide and carbon dioxide are both corrosive when in contact with water. Hydrogen sulfide is lethal and interactive with the mechanical properties of high-strength carbon steel. This paper will discuss the influence hydrogen sulfide and carbon dioxide have on the safety, design, and selection of reciprocating compressors.

Reciprocating compressors include dynamic seals at the piston rod. This seal will see increased leakage through the life of the seal. Due to the lethal and corrosive nature of H_2S, a purge and vent system is required to route the leakage to a safe location for collection or disposal.

Hydrogen sulfide can embrittle high-strength, high-carbon steel. NACE MR-0175, ISO-15156, discusses the materials that are compatible with H_2S. Several items within a reciprocating compressor include high-strength, high-hardness carbon steel. We will review the materials of construction for acid gas service, referencing NACE MR-0175.

Acid gas injection service includes gas compositions mainly comprised of hydrogen sulfide and carbon dioxide. These influence the selection of reciprocating compressors in several ways. The heavier mole weight of these gasses may require operating at slower speeds. The higher pressures of injection service may also require operating at slower speeds. The dewpoint of both hydrogen sulfide and carbon dioxide are near normal operating pressures and temperatures typically found in acid gas injection services. We will discuss how the different proportions of H_2S and CO_2 affect the dewpoint of the gas, and how to avoid condensates between stages of compression.

Keywords: Reciprocating compressor, acid gas

Email: dhannon@arielcorp.com

Ying Wu, John J. Carroll, Mingqiang Hao and Weiyao Zhu (eds.) Gas Injection into Geological Formations and Related Topics, (137–144) © 2020 Scrivener Publishing LLC

8.1 Introduction

Hydrogen sulfide is naturally occurring in natural gas gathering services in many regions. Reciprocating compressors must handle hydrogen sulfide in various quantity, and various pressures; from gathering services through injection/disposal services. Gas gathering applications can have as little as ppm, while injection for disposal can have as much as 100%. Sour gas gathering services typically consist of 100 pm hydrogen sulfide to 5% hydrogen sulfide, and pressures of 1200 to 1500 psi. Injection for disposal, acid gas services, will see a combination of hydrogen sulfide and carbon dioxide, in any combination, and pressures of 1200 to 5000 psi. There are several considerations when applying a reciprocating compressor into sour, or acid gas services. This paper will discuss these considerations, from safety, design, materials, condensate/dew point, and compressor selection perspectives.

8.2 Reactivity

Hydrogen sulfide and carbon dioxide are both acidic gasses, they create sulfuric and carbonic acid when combined with water. Both gasses will require special materials due to their corrosive nature. Apart from the corrosive attach on materials, hydrogen sulfide can attack high-hardness, high-strength martensitic materials, causing embrittlement. Further, hydrogen sulfide is a lethal gas, requiring a very low exposure level to be fatal.

8.3 Safety

Hydrogen sulfide can be lethal at very low exposure levels. Uncontrolled emissions can be a concern for the health and safety of personnel. Reciprocating compressors contain the process gas within the cylinder, with o-rings or metallic gaskets at the piping connections, heads and valve caps. However, the seal at the piston rod, the pressure packing case, is a dynamic seal. The packing case controls the leakage, but not to a zero leakage level. Gas leaking past this seal must be routed to safe collection or disposal location. This requires a suitable vent and purge system (see Figure 8.1).

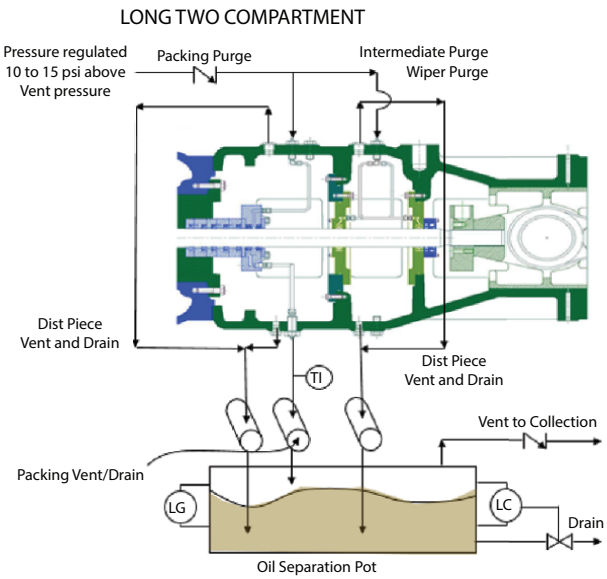

Figure 8.1 Safety – purge and vent system.

The packing case vents must be routed to a separation pot, separating the cylinder and packing lube oil from the vent gas, then routed to safe collection or disposal, such as a flare system. A purge is introduced at the packing case, just downstream of the packing vent. The purge is a supply of inert or sweet natural gas 15 psi (1 bar) above the vent pressure. This purge pressure helps eliminate vent gas from being introduced further along the piston rod, and eventually into the compressor crankcase and operators work space.

8.4 Design

The reciprocating compressor is designed with a separation between the compressor cylinder containing the gas pressure, and the crankcase containing the rotating to reciprocating running gear. This separation, or distance piece compartment, can be provided in several different configurations. There are specific configurations for sour gas services. The long two compartment is applied for the higher levels of hydrogen sulfide (see Figure 8.2).

The two compartment distance pieces are applied for sour gas, allowing more than one buffer compartment of separation between the cylinder and crankcase.

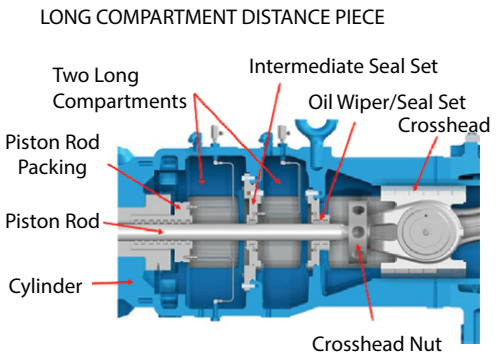

Figure 8.2 Distance piece – long two compartment.

8.5 Materials

Carbon dioxide and hydrogen sulfide are both corrosive gasses. Materials of construction of the wetted components must be taken into consideration. Further, hydrogen sulfide can embrittle certain commonly applied materials within the cylinder. NACE MR-0175 ISO-15156 provides guidance on materials that are suitable for hydrogen sulfide service.

Components in contact with the process gas include the cylinder body, cylinder heads, clearance pockets, valves, valve caps, valve retainers, piston, piston rod, and packing case (See Figure 8.3). Common cylinder body, cylinder head, valve caps, valve retainers, and clearance pocket materials are nodular and gray iron. These are suitable for sour service. Higher pressure cylinders will be of steel. MR-0175 allows steel when hardness is limited to

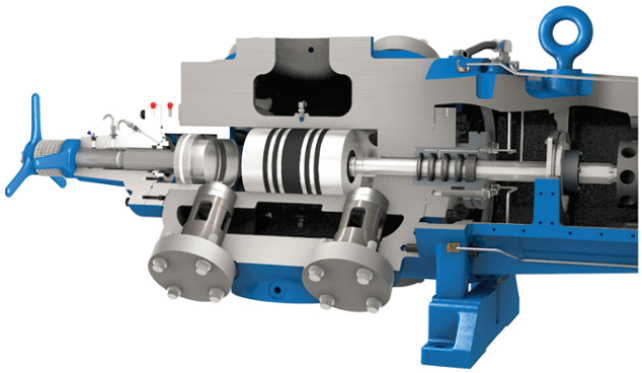

Figure 8.3 The compressor cylinder.

22 Rc (Rockwell hardness C) and below. Pistons are generally nodular and gray iron.

Piston rods are typically 4100 series carbon steel. As this is unsuitable for sour gas service, steel with hardness limited to 22 Rc can be applied. This can reduce the rod load capability of a reciprocating compressor. Stainless steel can be applied, eliminating the derate of rod load capability. MR-0175 specifically addresses both CC450 and 17-4PH stainless steel with specific heat treatment and hardness levels as acceptable in sour gas service.

Valve seats and guards are generally higher strength materials, unsuitable for sour gas service. As with the piston rods, carbon steel limited to 22 Rc, or stainless steel as noted above can be applied.

Most reciprocating compressor cylinder components are suitable for both carbon dioxide and hydrogen sulfide, with special attention required for the piston rod, valves, and higher strength forged steel cylinder bodies.

8.6 Condensate/Dewpoint

The dewpoint for carbon dioxide and hydrogen sulfide are at temperatures and pressures common to the compression process. Cooling the gas between stages of compression can be in the proximity of the dewpoint for the gas. When the gas composition is primarily carbon dioxide and hydrogen sulfide, the dewpoint and bubble point are very close, the phase envelope is very narrow. Small changes in temperature can result in large quantities of condensate.

The areas of interest include the dewpoint, critical point, and dense phase region (see Figure 8.4). Operating close to the critical point results in large changes in gas properties with small changes in temperature or pressure. This makes the prediction model less accurate and can result in very dense gas through the compressor. Operation above the critical pressure requires review to ensure the gas is warm enough to "act like a gas". The properties of the gas can look and act more like a liquid as the temperatures are reduced.

Awareness of the dewpoint margin is critical in the design of the interstage equipment. The interstage coolers are often fan driven ambient air to gas coolers. Colder ambient conditions results in colder process gas, with the potential for condensing the gas stream. Interstage coolers are most often designed for a minimum approach at a maximum ambient. Acid gas coolers must also be reviewed for a controlled minimum gas outlet temperature at minimum ambient conditions. This may require

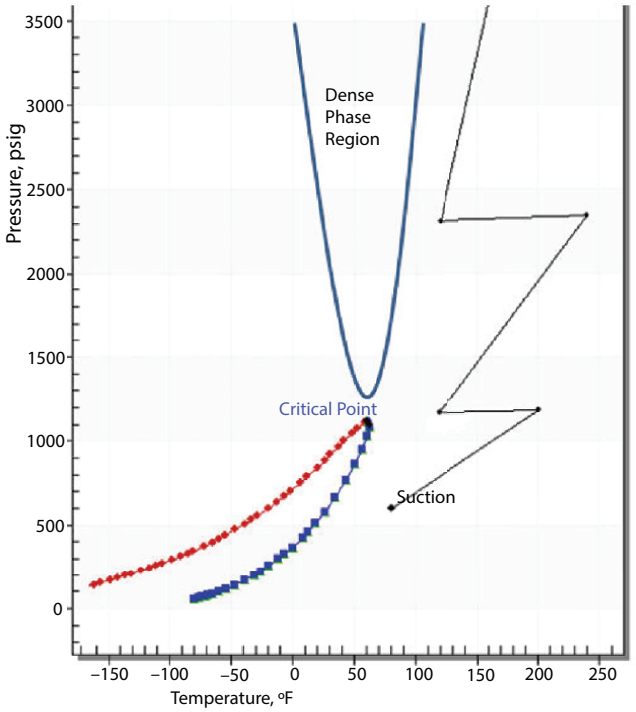

Figure 8.4 Acid gas phase envelope with compression sawtooth.

automated louvre controls, automated fan speed control, hot air recirculation within the cooler plenum, and potentially heaters within the plenum.

As the percentage of H_2S increases, the phase envelope shifts right and upwards (higher temperature and higher pressure). Avoiding condensates can be very difficult at the higher pressures as the compressor interstage temperatures must be quite high. It may be necessary to consider compressing to a pressure where the process stream is all liquid at ambient temperatures and apply a pump to the final injection pressure.

8.7 Compressor Selection

There are various guidelines and requirements for applying reciprocating compressors in acid gas service. The heavier gas often requires slower operating speeds. The interstage pressures and temperatures can be coincident with the dewpoint of the gas. Careful scrutiny of the

phase envelope and interstage conditions is required (for example, see Figure 8.5).

Reduced piston speeds are often necessary. Several reasons account for this need:

Heavier gasses can result in greater pressure losses across the cylinder and valves. Reduced piston speeds allow for the cylinder and valves to breathe, and reduce valve impact stresses. Compressor valves are sized for each cylinder based upon natural gas and rated frame speeds. With heavier gasses, speeds may need to be reduced. Lower piston speeds offer lower losses through the cylinder and valves. This may be necessary for valve life, or may be desired for extending time between maintenance for this hazardous service.

Most injection service compressors operate at higher discharge pressures. Often speeds need to be reduced to maintain appropriate piston rod packing wear life.

Operating speed may also need to be reduced when the cylinder bore is quite large and the gas is heavy. This reduces the possibility for choked flow across the face of the piston.

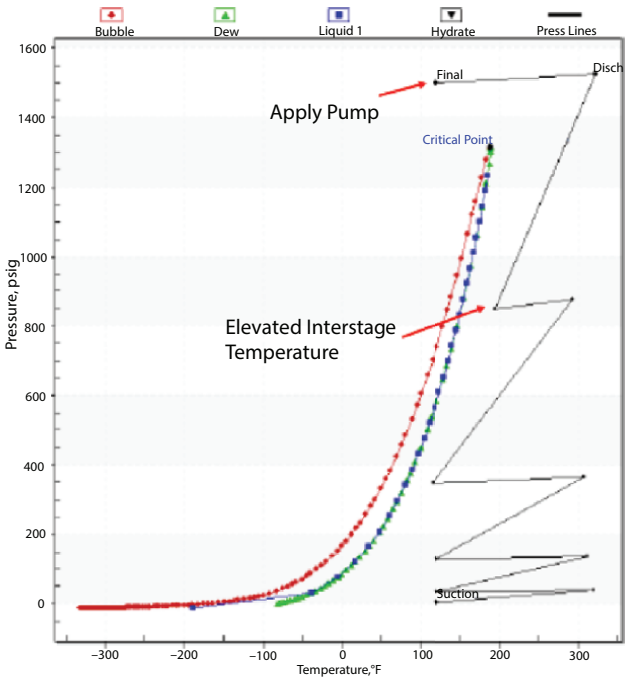

Figure 8.5 Acid gas phase envelope and compressor sawtooth (avoid Phase Envelope).

Interstage cooling requires attention to ensure condensates are avoided. This requires a review of the phase envelope for dewpoint, critical point, and dense phase region.

8.8 Conclusion

Reciprocating compressors are well suited for acid gas compression. Hundreds of reciprocating compressors have been applied on carbon dioxide and hydrogen sulfide service successfully. Full consideration must be made for safety, gas properties and materials of constructions.

9

Case Study: Wellbore Thermodynamic Analysis of Erhao Acid Gas Injection Project

Zhu Zhu[1] and Shouxi Wang[1,2]*

[1]Xi'an Shiyou University, Xi'an, China
[2]PipePlus Technology Ltd, Xi'an, China

Abstract
After nearly 5 years of discussion, disputing, preparation, and application, the first acid gas injection (AGI) project in China is on the way to being implemented in Xinjiang province in northwest China by Sinopec Northwest Company. AGI is in response to the emission of hydrogen sulfide (H_2S) produced as a by-product from oil and gas production. Compressing acid gas for transport via pipeline to an injection well and into a deep geological formation has been proved to be an economical and effective acid gas disposal method. The key concerns were focused on the estimation of wellhead injection pressure, the behavior of the acid gas flow, and phase profile along the deep, slightly inclined wellbore. Presented here is a case study based on an AGI application in Erhao station to reveal the wellbore thermodynamic features with using the GLEWpro program.

Keywords: Acid gas injection, wellbore, GLEWpro, thermodynamic analysis

9.1 Introduction

By August 2017, Sinopec Northwest Company produced 7 million tons of crude oil and 1.5 billion m^3 of natural gas annually. Most of these products contain sulfur with maximum hydrogen sulfide concentration of 1500 mg/L in heavy oil and 12×10^4 mg/m^3 in associated natural gas.

Up to now, 70% of hydrogen sulfide was recovered by many small sulfur recovery systems built earlier with high operation cost. Besides, the uncertainty of the sulfur market produced large quantities of stockpiling of the

**Corresponding author*: wangsx@yahoo.com

Ying Wu, John J. Carroll, Mingqiang Hao and Weiyao Zhu (eds.) Gas Injection into Geological Formations and Related Topics, (145–160)

elemental sulfur that is another source of potential environmental pollution. So acid gas injection (AGI) was considered and expected to replace the traditional recovery process to handle the waste gases [1, 2, 3].

With almost 30 years of research and practice, acid gas injection technology has been mature and widely used. In China, the first AGI project was implemented in the Sinopec Northwest Company in 2018. This paper takes Tahe oilfield Erhao light-hydrocarbon station (Erhao station) AGI project as an example, with the help of GLEWpro program, analyzing the thermodynamic features and estimating the wellhead pressure.

Now Erhao station has formed a complete AGI system (see Figure 9.1). After desulfurization, the initial acid gas is saturated with water. The initial acid gas contains 45.87% H_2S, 46.14% CO_2 and 0.28% hydrocarbon. The operator needs to inject 0.424 MMscfd of initial acid gas into the reservoir. The bottom hole pressure is 60.07 MPa and temperature is 100°C, the wellhead temperature is 20°C. GLEWpro estimated the wellhead injection pressure is 11.284 MPa and carried out a detailed analysis of the flow and phase profile along the wellbore. Through thermodynamic analysis of the initial acid gas along the wellbore, the preliminary pressure required in the AGI system is determined. Then the initial saturated water acid gas is compressed and dehydrated. With other conditions unchanged, the composition of compressed and dehydrated acid gas changes to 49.4622% H_2S, 49.7811% CO_2 and 0.3022% hydrocarbon. The final injection rate changes to 0.393 MMscfd. GLEWpro estimates the wellhead injection pressure is 11.463 MPa, analysis the thermodynamic profile along the wellbore. When comparing the initial acid gas with compressed acid gas in the pressure and temperature profile along the wellbore, it could be concluded that the water content has a greater impact on the temperature profile.

Although the estimated wellhead pressure is 11.463 MPa in a specific condition, many factors will change (composition, injection rate, wellhead

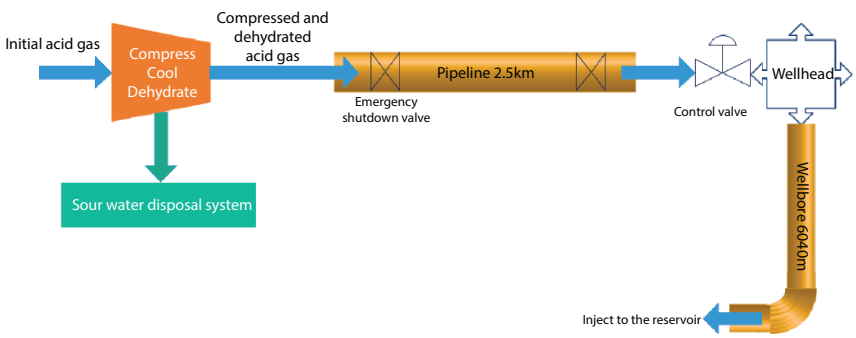

Figure 9.1 The AGI System at the Erhao Station.

temperature, bottom-hole pressure, etc.) in future production and operation. So this paper also analyzes the influence of different acid gas composition and different wellhead temperature on wellhead injection pressure.

9.2 Erhao Station Process and Injection Basic Data

Erhao station started construction in July 2004 and was put into operation in April 2005. In 2006, the light-hydrocarbon recovery system was upgraded. To deal with the associated gas with high hydrogen sulfide, the MDEA desulfurization system was expanded in 2010. In 2011, a new sulfur recovery system was established. Using a complex iron desulfurization technology with a sulfur recovery scale of 2000t/a. After years of expansion and reconstruction, the current Tahe oilfield Erhao combined station has formed the natural gas treatment process shown in Figure 9.2 to produce purified natural gas, liquefied petroleum gas (LPG), light hydrocarbons, sulfur and other products. The main production data are shown in Table 9.1.

Due to the sluggish sulfur market, the sulfur quality produced by the small sulfur recovery systems is poor, resulting in a long-term large backlog of sulfur products, huge sulfur stocks and secondary environmental

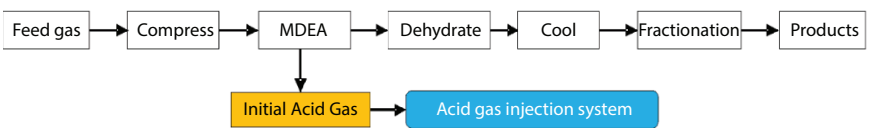

Figure 9.2 Natural Gas Process in Erhao Station.

Table 9.1 Erhao station production data.

No	Content	Amount	Unit
1	Feed natural gas	7.77	MMscfd
2	Output natural gas	3.531	MMscfd
5	LPG	44.78	t/d
6	Light hydrocarbons	14.21	t/d
7	Acid gas (45.87% H_2S, 46.14% CO_2)	0.424	MMscfd
8	Sulfur recovery	2000	t/a

pollution, which affects normal natural gas production. Therefore, the AGI system was applied to replace the small sulfur recovery system in Erhao station to seal harmful acid gas in the underground reservoir permanently to solve the problem of acid gas disposal in the production process of sulfur-containing natural gas. The AGI system process is shown in Figure 9.1. The initial saturated water acid gas enters into the AGI system after desulfurization in MEDA unit. In the AGI system, the compressed and dehydrated acid gas is transported to the wellhead through the pipeline and injected to the reservoir via wellbore. Several emergency shutdown valves are set along the pipeline to limit the amount of acid gas emptying in the accident state Pressure, flow and temperature sensors are installed at both ends of the pipeline to detect the acid gas leakage. A pressure regulating valve is installed in front of the wellhead to control the injection pressure and rate.

The initial saturated water acid gas composition is shown in Table 9.2. The acid gas pressure is 90-100 kPa and temperature is 41.7°C, which belongs to wet acid gas and the injection rate is 0.424 MMscfd.

9.3 Acid Gas Injection Well and Reservoir

The selection of the injection well and reservoir are the first thing to be concerned about in the AGI project. According to the selection principle of the injection well and reservoir, combined with the production situation, ZD8-212 was selected as the injection well, and the Ordovician was selected as the injection reservoir.

9.3.1 Injection Well

ZD8-212 was selected as the injection well. This well has complete production data and is located 2.5km south downwind from Erhao station (Figure 9.3). It is currently the production well of the Ordovician, with little potential to develop, and belongs to the same formation with the Ordovician system.

Table 9.2 Initial saturated water acid gas composition.

Component	Methane	Ethane	Propane	Nitrogen	CO_2	H_2S	Water
Mol%	0.22	0.04	0.02	0.01	46.14	45.87	7.7

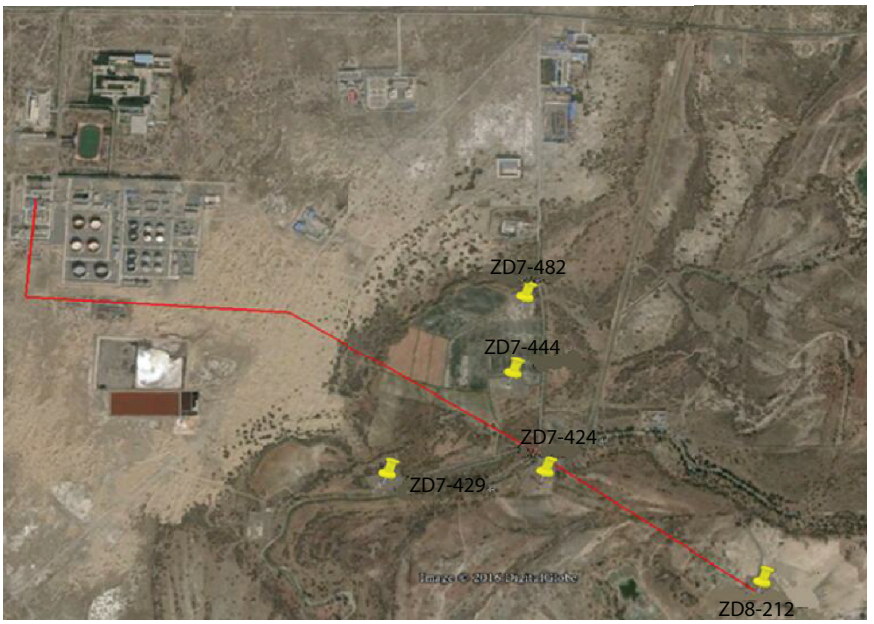

Figure 9.3 The location of ZD8-212.

9.3.1.1 Basic Data

- Well depth: 6040m inclined and 5547.44m vertical depth. The elevation distribution is shown in Table 9.3.
- Inner diameter: 3½-in tubing.
- Bottom hole: The actual pressure is 60.70 MPa and the temperature is 100°C.

9.3.1.2 Characteristics

- ZD8-212 is 2.5 km away from the Erhao station, close to the source of acid gas and there are no obstacles in the middle.
- ZD8-212 is relatively isolated. When injecting water to adjacent well ZD7-429 and ZD7-424, ZD8-212 has no dynamic

Table 9.3 Elevation Distribution for the Injection Well.

Location (m)	0	1000	2000	3000	4000	5000	5217.5	5603.5	6040
Elevation (m)	0	-1000	-2000	-3000	-4000	-5000	-5217.5	-5514.5	-5547.4

response. The injection well also has a bad connection with adjacent well ZD7-444 (see Figure 9.4).

- According to acid frac completion and reservoir characteristics, the reservoir near the injection well is well developed so that can realize the continuous injection.
- The injection well region has strong bottom water and large reservoir space, the injection pressure is relatively stable.
- No leakage and emptying in the production process along the wellbore.

9.3.2 Injection Reservoir

The selection of the injection reservoir is determined by geological and non-geological factors, mainly considering the source-ground proximity, caprock sealing capacity, reservoir flow properties, chemical effects of acid gas on the reservoir rock matrix and native fluids, protection of energy, mineral and groundwater resources, drilling integrity, public safety and other factors.

Based on various factors, the project selected the Ordovician as the injection reservoir. The Ordovician meets the requirements of the acid gas injection.

- The Ordovician has a vertical depth of 5547.44m, the actual pressure is 60.07 MPa and the temperature is 100°C.
- The apparent volume is 670,000 m^3 and the estimated actual space volume is more than 135,000 m^3. Therefore, the Ordovician is conducive to long-term and large-scale acid gas injection.
- The Ordovician is the production horizon, the injected acid gas has the least chemical interactions with the reservoir rocks and native fluids.

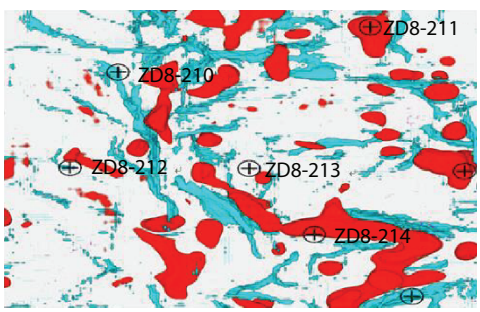

Figure 9.4 The connection between other wells.

- The Ordovician is well developed so it is convenient for permanent acid gas sealing.
- No leakage through the caprock.

9.4 Thermodynamic Analysis and Injection Pressure

The thermodynamic analysis from the wellhead to total depth and wellhead pressure estimation are key points in AGI system designing and operating [4].

A program, called GLEWpro, was developed based upon a new comprehensive model for the multiphase flow to provide phase and flow profiles along the wellbore.

9.4.1 Comprehensive Model

The new comprehensive model combined the tubular flow model and fluid model seamlessly, precisely modelling the flow in tubular and estimating the fluid properties [5].

Fluid flow behaviour in tubular is governed by mass, momentum and energy conservation laws. These three fundamental equations can illustrate the flow features of flow states, fluid phase and tubular orientation without the limitations. So it's suitable not only for the vertical, horizontal and inclined tubular segment. But also for production and injection wellbore. The model also considers the bulk modulus, thermal transmission, and the effects of pressure and temperature on fluid properties.

AQUAlibirum is designed specifically for gas, liquid, and supercritical phase to calculate equilibrium in systems containing acid or sour gas and water. It provides a smooth transmission when the phase changing and do help to understand the physics of the injection well and solve the flow equations.

This new comprehensive model (Equation 9.1) facilitates an accurate thermodynamic analysis of the wellbore and phase equilibrium calculation.

$$\begin{cases} \dfrac{\partial(V_m A\rho_m)}{\partial x} = 0 \\ V_m\rho_m \dfrac{\partial V_m}{\partial x} + \dfrac{\partial P}{\partial x} + g\rho_m \dfrac{\partial z}{\partial x} + \dfrac{\rho_m f_m V_m^2}{2D} = 0 \\ V_m\rho_m \dfrac{\partial h_m}{\partial x} = V_m \dfrac{\partial P}{\partial x} + gV_m\rho_m \dfrac{\partial z}{\partial x} + \dfrac{\rho_m f_m V_m^3}{2D} + \dfrac{1}{A}\dfrac{\partial Q_m}{\partial x} = 0 \end{cases} \tag{9.1}$$

where: A: Flow area of the tube, m^2
D: Tubing inside diameter, m
f: Darcy friction factor
h: Acid gas enthalpy
g: Acceleration due to gravity, m/s^2
P: Pressure, Pa
V: Velocity, m/s
x: Coordinate along the tube, m
z: Elevation, m
ρ: Acid gas density, kg/m^3

subscripts
m: Acid gas with multi-component

In the comprehensive model, the pressure *P*, temperature *T*, the mixture mass flow rate W_m are basic variables. AQUAlibrium calculates the mixture properties based on composition and condition.

$$V_m = \frac{W_m}{A\rho_m} \tag{9.2}$$

Equation 9.2 is used to estimate the mixture velocity V_m, and the Colebrook-White equation is selected to calculate the friction factor.

9.4.2 Initial Acid Gas

According to the initial acid gas composition (Table 9.2), the operator needs to inject 0.424 MMscfd of acid gas into the bottom hole. The bottom hole pressure is 60.07 MPa and temperature is 100°C, the wellhead temperature is 20°C.

The GLEWpro estimated the flow and phase profile along the wellbore. Figure 9.5 shows the input interface, Figure 9.6 shows the flow and phase profile, Figure 9.7 shows the temperature profile, Figure 9.8 shows the pressure and density profile.

Figures 9.7 and 9.8 show the flow profile and phase change process of initial acid gas injection. The process has the following characteristics:

- The injected acid gas is a liquid phase and the estimated wellhead pressure is 11.284 MPa.

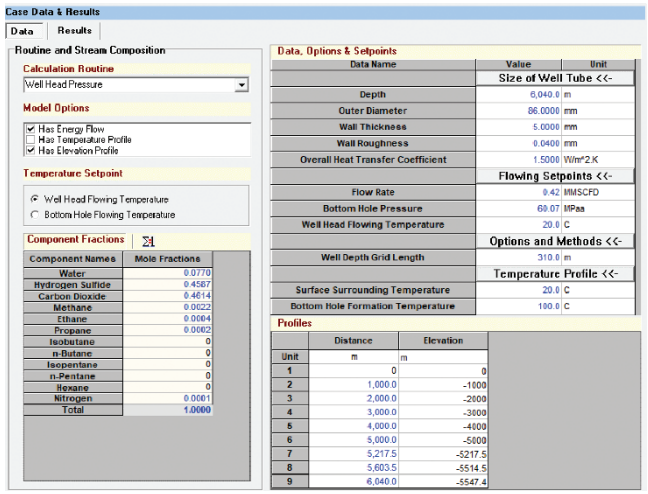

Figure 9.5 GLEWpro Input Interface-1.

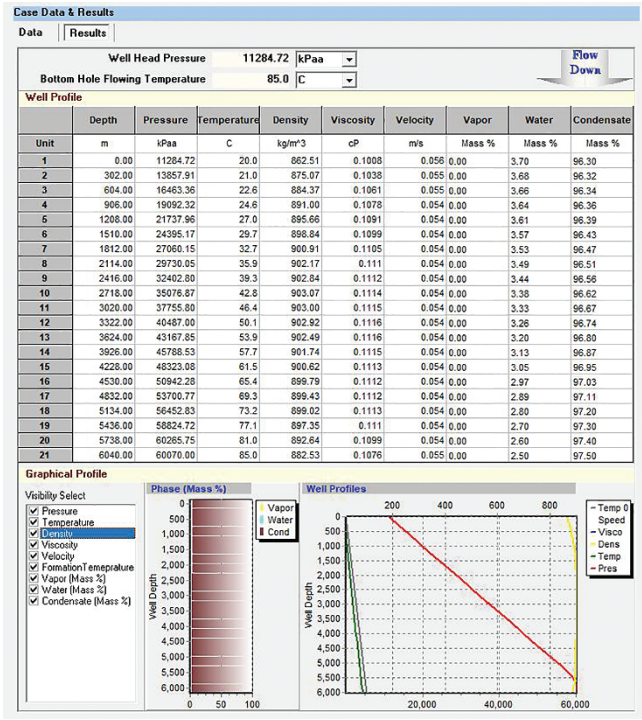

Figure 9.6 GLEWPro Flow and Phase Profile-1.

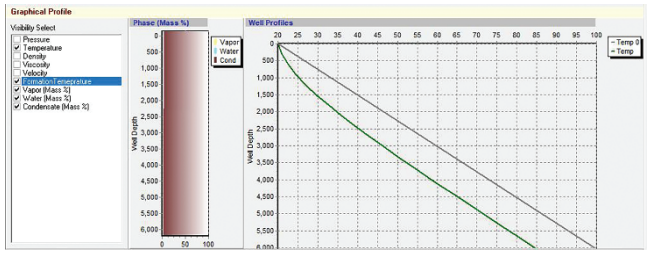

Figure 9.7 GLEWpro Temperature Profile Along the Wellbore-1.

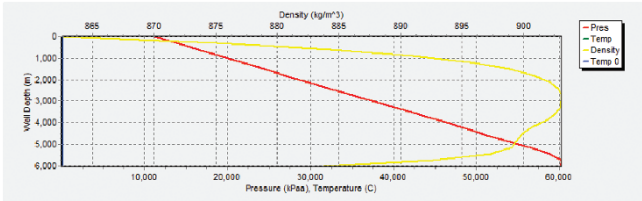

Figure 9.8 GLEWPro Pressure and Density Profile Along the Wellbore-1.

- The liquid column static pressure in wellbore is 48.1 MPa. The wellhead pressure is mainly determined by liquid column static pressure, and the contribution of friction loss of wellbore flow is small.
- Without dehydration, the initial acid gas contains about 3.2% free water throughout the injection wellbore.
- With a small injection rate, the average flow velocity in the wellbore is 0.054 m/s. Slow-moving leads to the full heating of acid gas in the wellbore, the temperature in the bottom hole reaches 85.0°C.
- The setting wellhead temperature is 20°C, the formation temperature is 100°C. The lower the wellhead temperature is, the lower the estimated wellhead injection pressure required; the higher the formation temperature is, the higher the estimated wellhead injection pressure required. Therefore, wellhead pressure decreases with the decrease of wellhead temperature and wellbore temperature distribution.

Through the estimation of wellbore injection pressure and the analysis of flow in the tubular profile, the preliminary pressure required in the

AGI system can be determined, the compression, dehydration and pipeline transportation process analysis and design can be carried out accordingly [6].

9.4.3 Compressed and Dehydrated Acid Gas

The estimated wellhead pressure of initial acid gas is 11.878 MPa. Considering the dehydration, pipeline transportation and other pressure requirements, the initial acid gas was compressed and dehydrated from 0.1 MPa to 15 MPa.

After compressing and dehydrating, the composition, properties and injection rate of initial acid gas all changed. The compressed and dehydrated acid gas composition is shown in Table 9.4. When 712.466 kg/d of acid water was removed, the actual final injection rate changes to 0.393 MMscfd.

With other conditions unchanged, the GLEWpro estimated the flow and phase profile along the wellbore. Figure 9.9 shows the input interface, Figure 10.10 shows the flow and phase profile, and Figure 9.11 shows the pressure and density profile.

Table 9.4 Compressed and dehydrated acid gas composition.

Component	Methane	Ethane	Propane	Nitrogen	CO_2	H_2S	H_2O
mol%	0.2374	0.0432	0.0216	0.0117	49.7811	49.4622	0.4428

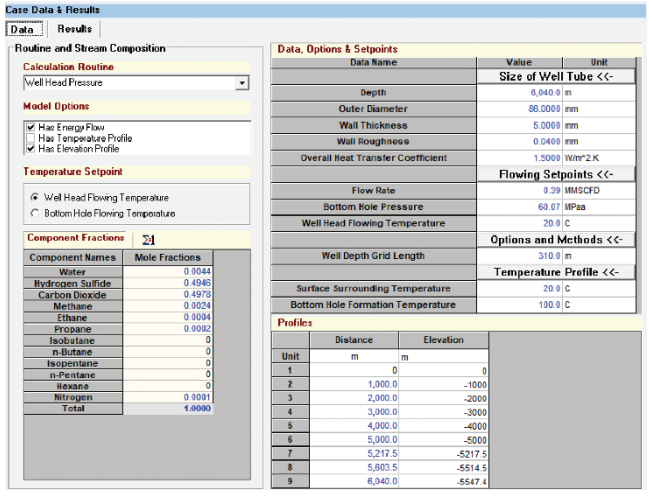

Figure 9.9 GLEWpro Input Interface-2.

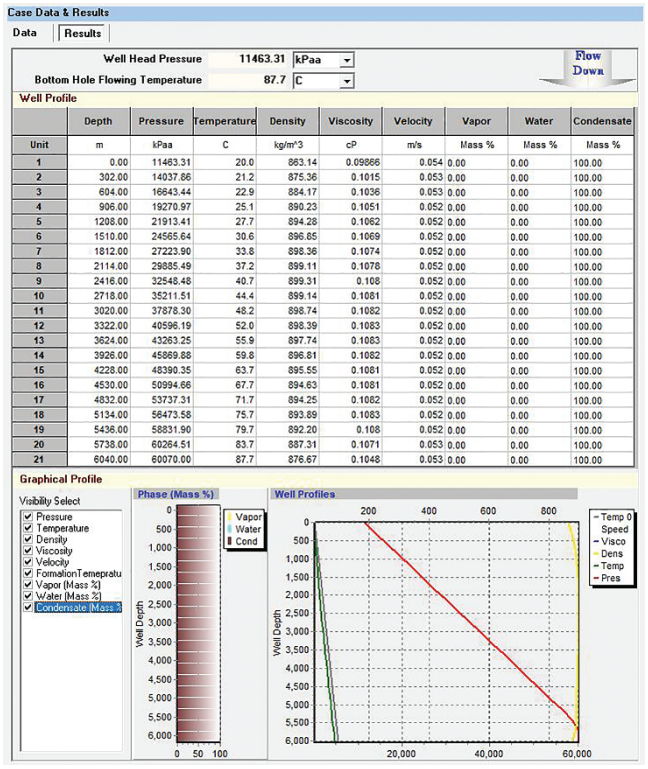

Figure 9.10 GLEWpro Flow and Phase Profile-2.

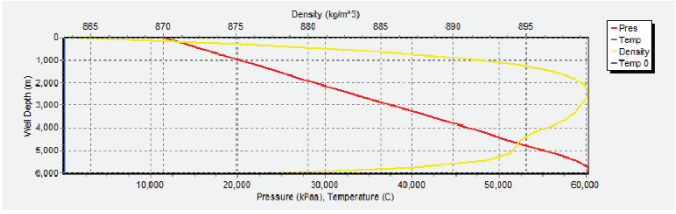

Figure 9.11 GLEWpro Pressure and Density Profile-2.

Figures 9.10 and 9.11 show the flow profile and phase change process of initial acid gas injection. The process has the following characteristics:

1. The injected acid gas is the liquid phase and the estimated wellhead pressure is 11.463 MPa. Compared with the initial

acid gas, the compressed and dehydrated acid gas has a small amount of injection but a high estimated wellhead injection pressure. The reason is that the acid gas density decreases after dehydration (Figure 9.11), and the temperature of the acid gas in the wellbore is high at a small flow rate.

2. No free water generated because of the through dehydration, the acid gas corrosion problem could be ignored.

Figure 9.12 shows the compressed and dehydrated acid gas pressure and density profile. Pressure changes in the inclined section at the bottom of the well are obviously slowed down. Figure 9.12 also compares the initial acid gas with compressed gas in the pressure and temperature profile along the wellbore. After compression, the pressure profile has only a slight change, the temperature profile along the wellbore increases slightly. It could be concluded that the water content has a greater impact on the temperature profile.

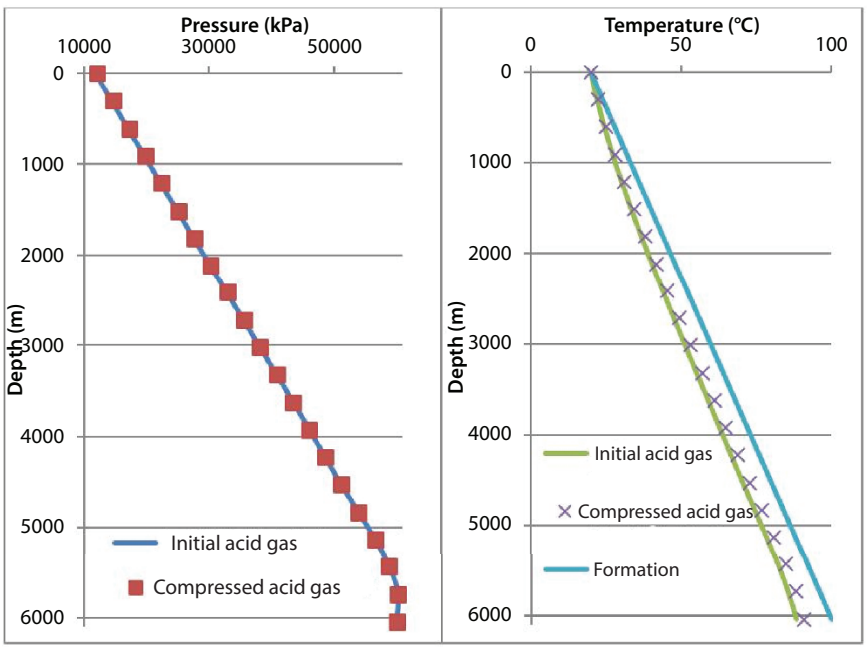

Figure 9.12 The comparison of pressure and temperature profile.

9.4.4 Comparison of Different Acid Gas Composition

Although the estimated wellhead pressure is 11.463 MPa in a specific condition, many factors will change (composition, injection rate, wellhead temperature, bottom-hole pressure, etc) in future production and operation. So that the wellhead pressure should have a range to adapt to different operating conditions.

With other conditions unchanged, changing the acid gas composition to estimate wellhead pressure (Table 9.5).

It can be concluded that the higher the H_2S content is, the higher the wellhead pressure needs; the higher the CO_2 content is, and the lower the wellhead pressure needs.

9.4.5 Comparison of Different Wellhead Temperature

The acid gas is compressed and cooled to 50°C, then transported via pipeline to ZD8-212 injection well. The wellhead temperature always changes with the environment temperature. Table 9.6 shows the estimated wellhead pressure in different wellhead temperature.

It can be concluded that the wellhead pressure increases with the increase of the wellhead temperature.

Table 9.5 Wellhead pressure in different composition.

Mol%	CO_2	0	30	50	70	100
	H_2S	100	70	50	30	0
Wellhead pressure (MPa)		15.31	13.29	12.23	11.24	9.49
Bottom hole temperature (°C)		90.7	90.8	90.8	90.9	90.9

Table 9.6 Wellhead pressure in different temperature.

Wellhead temperature(°C)	5	10	15	20	25	30	35
Wellhead pressure (MPa)	10.255	10.857	11.071	12.089	12.719	13.357	14.001
Bottom hole temperature(°C)	88.4	89.2	89.2	90.8	91.6	92.4	93.2

9.5 Conclusion

1. Each AGI project is independent and different. The process schemes are decided by the acid gas composition, property, injection reservoir, wellbore configuration, etc.
2. The key problems should be solved in the AGI project, which is the selection of the injection reservoir and the estimation of the wellhead pressure, as they would affect the following gas compression, dehydration, and transportation.
3. Public safety is as vital as the AGI process flow. Although the toxic gas is involved in the process, there have not been any incidents or negative results so far.
4. Compared with the traditional sulfur recovery system, the AGI system has its advantages; it is not only economically efficient but also environmentally friendly. Based on the high hydrogen sulfide contained in oil and gas field status in China, the application of AGI technology will bring great economic and social benefits.

References

1. Shouxi, W., Lin, T., Carroll, J., A State of the art of Acid Gas Injection and Its Application Prospects in China. *Nat. Gas Ind.*, 1, 33, 1, 105–111, 2013.
2. Carroll, J.J., Shouxi, W., Lin, T., Acid Gas Injection – Another way of Acid Gas Processing. *Nat. Gas Ind.*, 11, 29, 10, 96–100, 2009.
3. Bachu, S. and Gunter, W.D., Overview of acid-gas injection operations in Western Canada. *Greenhouse Gas Control Technol.*, 1, 443–448, 2005.
4. Shouxi, W. and Carroll, J.J., Model Calculates Acid-Gas Injection Profiles. *Oil Gas J.*, 4, 104, 33, 61–69, 2006.
5. Shouxi, W., Carroll, J.J., Lin, T., The Flow and Phase Profiles of the Acid Gas Injection Well. *Nat. Gas Ind.*, 3, 30, 3, 87–92, 2010.
6. Shouxi, W. and Carroll, J.J., Blowout Calculations for Acid Gas Well with High Water Cut. *AGIS III. Third International Acid Gas Symposium*, Banff Canada, May 29 to June 1, 2012, 2012.

10

Selecting CO_2 Sinks CCUS Deployment in South Mid-West Kansas

Eugene Holubnyak*, Martin Dubois and Jennifer Hollenbach

Kansas Geological Survey, Lawrance, Kansas

Abstract

The goal of the Integrated CCS for Kansas (ICKAN), a Phase I project under CarbonSAFE, was to evaluate and develop a plan and strategy to address the challenges and opportunities for commercial-scale Carbon Capture and Storage (CCS) in Kansas. Four separate geologic structures were identified as each having potential for storing 50Mt of CO_2. The four structures, aligned on the same regional geologic structure, are similar in size, have more than 100 ft of closure, and have similar geologic histories, and storage reservoirs, Mississippian Osage, Ordovician Viola, and Cambrian-Ordovician Arbuckle at depths from 5200-6400 ft.

In addition to the saline storage targets, there are many CO_2 EOR opportunities in southwest Kansas, four of which were part of a DOE-funded study (DE-FE0002056) conducted by the Kansas Geological Survey [1]. The CO_2 EOR market for CO_2 could help the economics of transporting CO_2 to the Patterson site through economies of scale and the reduction of market risk.

Keywords: CO_2 sinks, Kansas carbon capture, storage and utilization

10.1 Introduction

The Integrated CCS for Kansas project (ICKan) is a Phase I pre-feasibility study under DOE-NETL Carbon Storage Assurance Facility Enterprise (CarbonSAFE) program. The Kansas Geological Survey (KGS) and The University of Kansas (KU) together with a Carbon Capture and Storage (CCS) Coordination Team executed the study. The goal of Phase I activity under CarbonSAFE is to identify and critically evaluate challenges and opportunities

**Corresponding author*: eugene@kgs.ku.edu

Ying Wu, John J. Carroll, Mingqiang Hao and Weiyao Zhu (eds.) Gas Injection into Geological Formations and Related Topics, (161–182) © 2020 Scrivener Publishing LLC

for commercial-scale Carbon Capture and Storage (CCS) in Kansas. The objectives include identifying, evaluating, and addressing the major technical and non-technical challenges for implementing commercial-scale, CO_2 capture, transport, and secure geologic storage of 50 million tonnes CO_2 in Kansas.

This feasibility study examined three of Kansas' largest CO_2 point sources, nearby and distant storage sites, where an estimated storage capacity was equal to or greater than 50 million tonnes (Table 10.1), and prospective CO_2 transportation networks. Westar Energy's Jeffrey Energy Center—Kansas' largest coal-fired electrical generating facility—near St. Marys, Kansas, served as the primary site because of its size (2.16 GigaWatt and 12.5 million metric tons of CO_2 emissions) and strategic location along the eastern margin of Kansas' aerially extensive and vertically stacked, reservoir complexes. Sunflower Electric Cooperative's Holcomb coal-fired plant near Garden City in southwest Kansas and one of Kansas' largest oil refineries, CHS Refinery, near McPherson in central Kansas were secondary sites. Because of the high cost of capture and compression from power plants and refineries, the study also considered ethanol plant sources where capture and compression costs are significantly lower.

The KGS undertook highly technical, subbasinal evaluations of CO_2 storage building upon prior regional characterization studies conducted under DOE-NETL project DE-FE0002056. Site-specific, risk assessments incorporated "lessons learned" by the KGS during the final EPA (Region 7) review of the Class VI geosequestration permit for storage of 26,000 tonnes of CO_2 within the Arbuckle saline aquifer at Wellington Field (DE-FE0006821) [2]. The success of the recent Class II CO_2 Enhanced Oil Recovery (EOR) injection in the overlying Mississippian oil reservoir at Wellington, Kansas, supports the viability of the stacked reservoir concept. The experience and knowledge gained established a foundation for planning to address post-injection site care, site closure, financial assurance, and long-long-term liability.

The Patterson site is one of several geologic sites that has been demonstrated by initial simulation analysis to be capable of injecting and storing 50Mt of CO_2 in a 25- to 30-year timeframe. However, the analyses in this study are based on limited subsurface well, core, and injectivity data, and in the case of the Patterson, no seismic data. Considerable additional data need to be collected and technical analysis performed to validate the Patterson site. Key questions that need to be resolved are 1) the geometry of the Patterson site structure, hence potential volume of CO_2 stored, 2) injectivity in the target reservoirs, in particular in the Osage, and 3) integrity of the caprock and seals. The current model was built without the advantage of having 3-D seismic to locate the bounding fault on the southwest side and knowing the overall geometry of the geologic structure.

Table 10.1 Results of initial numerical simulation for five geologic sites evaluated.

Storage Complex	Geologic Site	Volume Stored (Mt)	Injection Wells	Injection Zones	Years of Injection
North Hugoton Storage Complex	**Rupp**	36.6	4	Osage, Viola, Arbuckle	30
	Patterson	60.7	4	Osage, Viola, Arbuckle	30
	Lakin	30.8	3	Osage, Viola, Arbuckle	25
	Pleasant Prairie	67.4	3	Osage, Viola, Arbuckle	25
Forest City Basin	**Davis Ranch - John Creek**	24.6	6	Simpson, Arbuckle	25

Questions remain about the injectivity and capacity at the site, particularly in the Osage. Closest core analysis in the Osage suggests low permeability, despite porosity in the range of 25–30%. There is currently no geomechanical nor capillary pressure data for the caprock seals for the reservoirs, although indirect data discussed below suggest that the seals are effective to the vertical migration of hydrocarbons and mixing of brines.

A primary driver for CCS implementation in Kansas is the cost of CO_2 capture and compression. The focus for CO_2 sources in the ICKan project were initially coal-fired power plants and a refinery (Figure 10.1 for locations) because of CarbonSAFE FOA stipulations. However, under current market conditions in the midcontinent region, the aggregation of CO_2 captured from multiple ethanol plants provides the most economical, and frankly, the only viable option for a CCS project of the scale envisioned by CarbonSAFE without substantially more subsidy than currently available. Preliminary technical and economic evaluations of two coal-fired power plants and a refinery in this study suggest that CO_2 capture from these sources is cost prohibitive, even when 45Q tax incentives are applied.

Having EOR CO_2 as part of the system is accompanied by economic gains from scale and, potentially, additional subsidy for CO_2 destined for

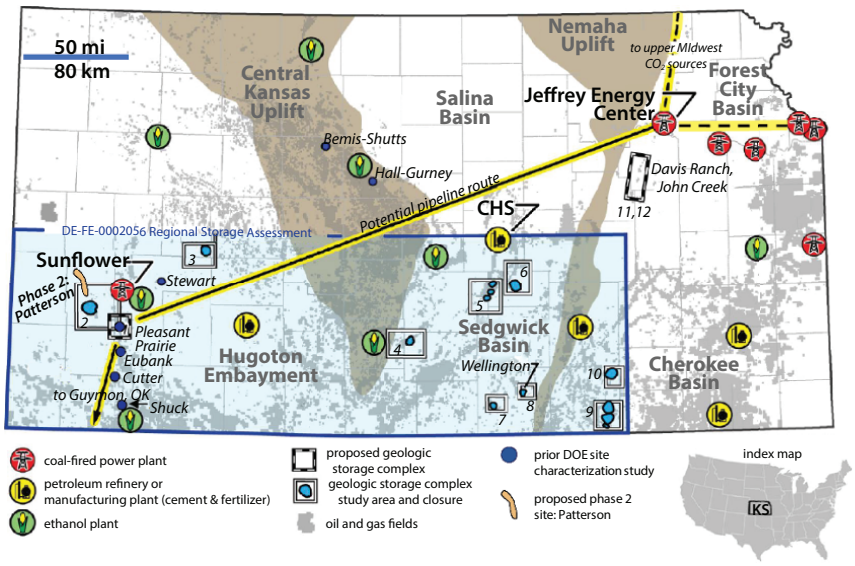

Figure 10.1 Kansas map showing location of the Patterson site, a variety of CO_2 sources, possible CO_2 pipeline routes, other possible CO_2 injections sites (numbered 1–12) identified in (1) located inside the DE-FE0002056 study areas (blue), and oil fields (gray). The primary sources in this study are labeled. The figure is modified from ICKan proposal SF 424 R&R, 2016 [3].

saline storage. In the most economically favorable case. Five fields within or nearby the NHSC could readily take 1.8 to 2.3 Mt/yr for EOR. They include the Patterson Morrow waterflood and the Chester and Morrow waterfloods in four fields studied for EOR as part of a DOE-funded study (DE-FE0002056).

10.2 Process for Determining Potential Phase II Sites

We went into this study with two geologic complexes in mind, FCB and Pleasant Prairie, on the basis of prior DOE-funded Kansas Geological Survey studies and the proximity to coal-fired powerplant source industry partners. The Pleasant Prairie site was determined by CO_2 injection simulation studies to have the capacity to store >50Mt CO_2. However, the operator of the Pleasant Prairie Field determined that they and their business partners could not commit to Phase 2 of a CarbonSAFE program operational and financial obligations that would be required. Thus, the Pleasant Prairie site could not be considered as a Phase 2 site.

Alternative sites were evaluated for capacity and willingness of oil field operators to participate in a Phase 2 project. A starting point were sites evaluated in an earlier DOE-funded study (DE-FE0002056) on regional saline aquifers [1] that identified 10 sites possibly capable of storing 50+Mt CO_2. Most of the sites were eliminated from consideration for a variety of reasons. The site numbered 2 did not meet the 50Mt minimum in the aforementioned study, sites 1 and 5 are in an area of significant seismic activity induced by high-rate injection of produced brines into the Arbuckle, sites 9, and 10 were given lower priority because of proximity Class I Arbuckle disposal wells with rising water levels, and site 3 was downgraded because of its proximity to an operating gas storage field. At sites 4 and 8, the structures are relatively small and storage reservoir shallow (~3,200 ft), and site 7 had very limited well control and no available seismic data needed to estimate the size of the geologic structure. Thus sites 4, 7, and 8 were downgraded. Site 6, the Lakin site, was characterized, modeled and a numerical simulation of CO_2 injection was performed, along with other potential sites in the NHC, the Rupp and Patterson (Figure 10.2).

10.2.1 Geologic Setting

The Patterson site is situated in southwest Kansas at the northern end of the giant Hugoton Gas Field in the Hugoton Embayment of the Anadarko Basin (see Figure 10.3). The Patterson site comprises three closely spaced

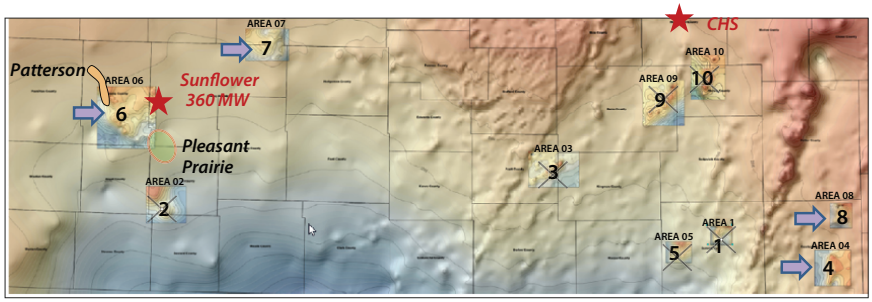

Figure 10.2 Location of 10 potential CO_2 storage sites (numbered) studied by Watney *et al.* [1] and further evaluated in this study. Map is the structure on top of the Arbuckle. Modified from [1]. Map area is the study area shaded blue in Figure 10.1.

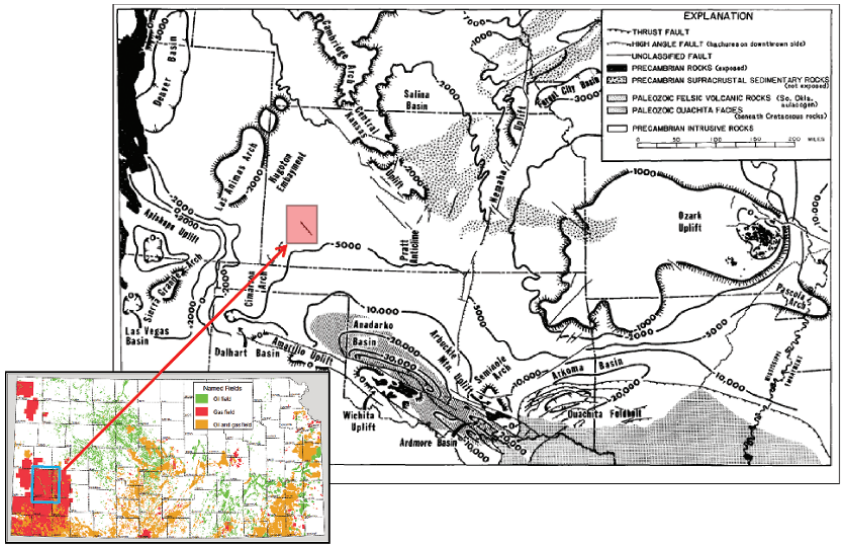

Figure 10.3 Locator map for North Hugoton Storage Complex (red-shaded box) showing Pre-Cambrian basement configuration [4]. Inset map illustrates the oil and gas fields in Kansas in 2009 (http://www.kgs.ku.edu/PRS/petro/ogSheetMap.html).

oil pools, Patterson, Heinitz, and Hartland, aligned on a geologic structure (Figure 10.4) and is one of the four geologic sites in the NHSC. The four NHSC geologic sites are similar in that they have approximately 100 ft of structural closure, are located on a prominent northwest-southeast structural trend, have the same geologic history, and have the same saline aquifer reservoirs beneath them.

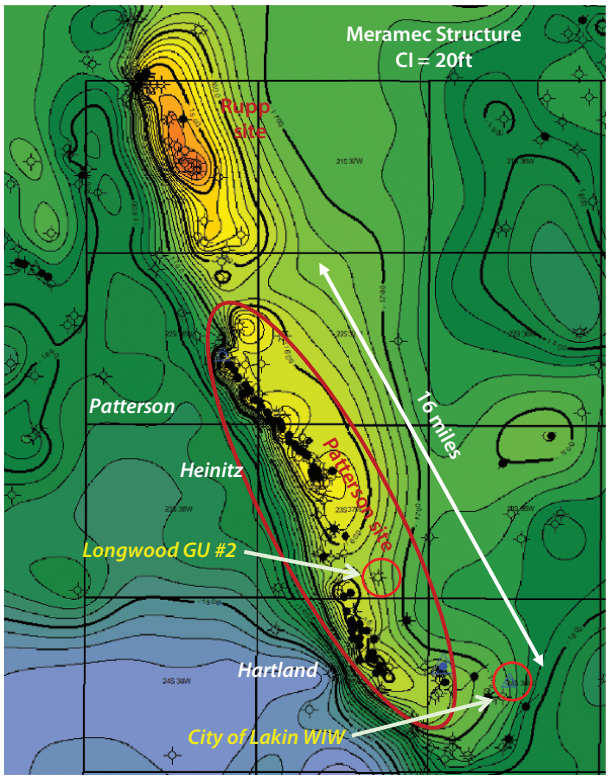

Figure 10.4 Structure map on top of the Meramec (Mississippi) covering the area modeled for the Rupp and Patterson geologic sites. Contour interval = 20 feet. Patterson site is outlined by the red dashed line.

Three stratigraphic intervals are considered for CO_2 storage—the Mississippian Osage, Middle-Ordovician Viola, and Cambrian-Ordovician Arbuckle—shown in stratigraphic charts in Figures 10.5 and 10.6. All three have regional lateral extent and appear to be separated by vertical barriers to fluid migration (Meramec, Kinderhook, and Simpson dense carbonate and thin shales). The Morrow shale (Pennsylvanian) on top of the Meramec (Mississippian) is a regional top seal for the oil and gas accumulations in the Mississippian, Morrow sandstone and Chester sandstone.

The Mississippi stratigraphy deserves additional discussion and explanation of how we have treated it for mapping and modeling purposes. The Mississippi-aged Chester Stage unconformably overlies the Meramec Stage. There is a major unconformity atop the Mississippi upon which the Morrow was deposited. The Chester thins atop structures throughout the NHSC due to erosions and in some areas has been completely eroded

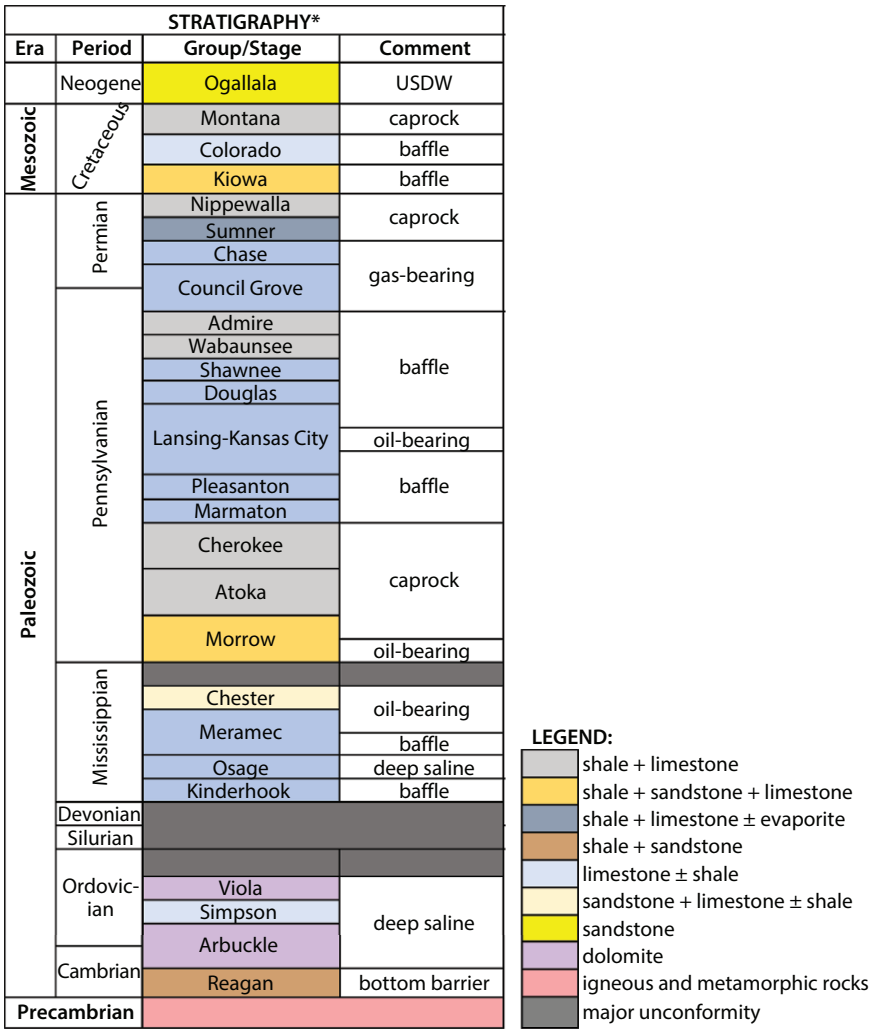

Figure 10.5 Generalized stratigraphic chart for the NHSC in southwest Kansas. Comments column shows oil and gas producing intervals in the area and regional barriers, caprock and baffles to vertical fluid flow. USDW = underground source of drinking water.

and Morrow rests directly on Meramec. The lower Morrow section and the Chester similarly comprise interbedded limestone and shale making it difficult to correlate the contact between them when complicated by an unconformity. For mapping and modeling purposes, the Morrow and Chester have been lumped. The Mississippian-aged Meramec Stage comprises the Ste. Genevieve, St. Louis, Spergen (Salem), and Warsaw

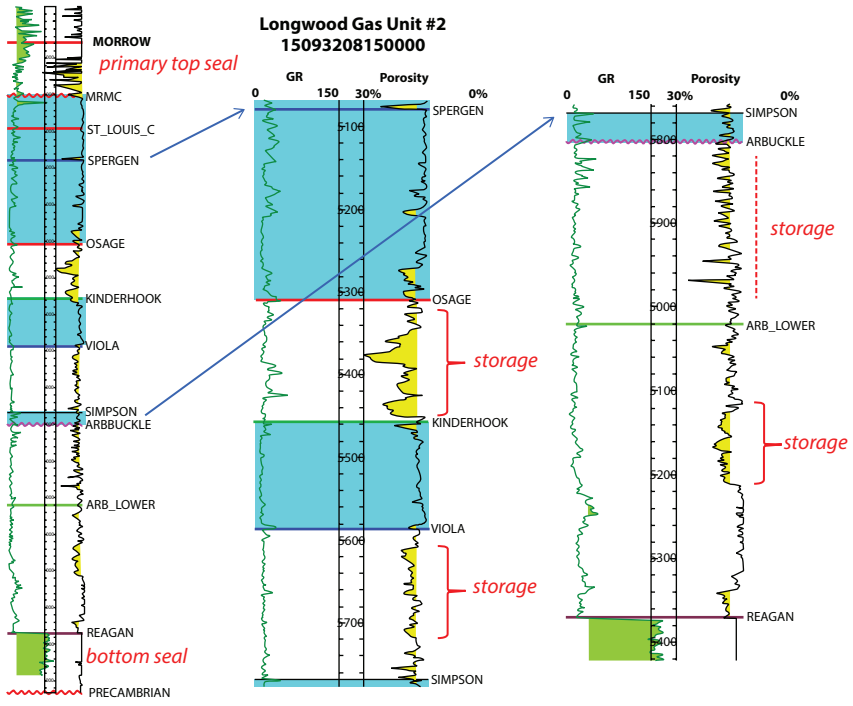

Figure 10.6 Stratigraphy of the Lower Paleozoic and proposed storage zones illustrated by a wireline log from a key well in the Patterson site, the Longwood Gas Unit #2 well. Tight carbonate baffles separate storage units from one another (shaded blue). Porous intervals (>7% porosity) are shaded yellow and shale intervals are shaded green.

limestones. Because of an unconformity atop the Meramec and the major unconformity atop the Mississippian, it is not always clear whether the Ste. Genevieve or the St. Louis is the subcropping unit, so we chose to pick that top as the Meramec, rather than differentiate. The St. Louis C, the main producing zone in the Pleasant Prairie field, top was also picked but not used as a horizon in modeling.

Saline aquifer reservoirs in the Osage and Viola consist of thick (>100 ft), vertically continuous, laterally extensive porous carbonate, primarily medium-crystalline sucrosic dolomite with good intercrystalline porosity and varying amounts of chert. The Arbuckle storage reservoir consists of stacked thin beds of porous dolomite over the 570-foot-thick Arbuckle, separated by thin intervals of tight carbonate. Although they do not appear to be well-connected vertically, drill stem tests in the Arbuckle, albeit limited in number, prove otherwise with fluid recoveries averaging more than 2,000 feet of saltwater in one-hour flow tests.

10.3 Oil Production History and CO_2 Enhanced Oil Recovery Potential in the Region

Oil has been produced in the Patterson site since 1966 with the discovery of the Patterson oil pool. A total of 7.3 million barrels of oil have been produced from the three pools through August 2018, most of it from the Morrow sandstone (Table A in Figure 10.7). The Morrow sandstone reservoir in the Patterson-Heinitz Unit (two fields unitized in 2010) has responded well to a waterflood installed in 2010 (Figure 10.7B and 10.7C). In all, 5.5 million barrels of oil have been produced from the combined Patterson and Heinitz before and after unitization, and an additional 1.2 million barrels of oil are expected from the waterflood (6.7 million barrels ultimate recovery). Because of the oil volume, reservoir conditions, solution-gas drive mechanism and being a successful waterflood, the Patterson-Heinitz Morrow reservoir is a candidate for CO_2 enhanced oil recovery (EOR).

In addition to the Patterson-Heinitz Unit, there are many other CO_2 EOR opportunities in southwest Kansas, four of which were part of a DOE-funded study (DE-FE0002056) conducted by the Kansas Geological Survey

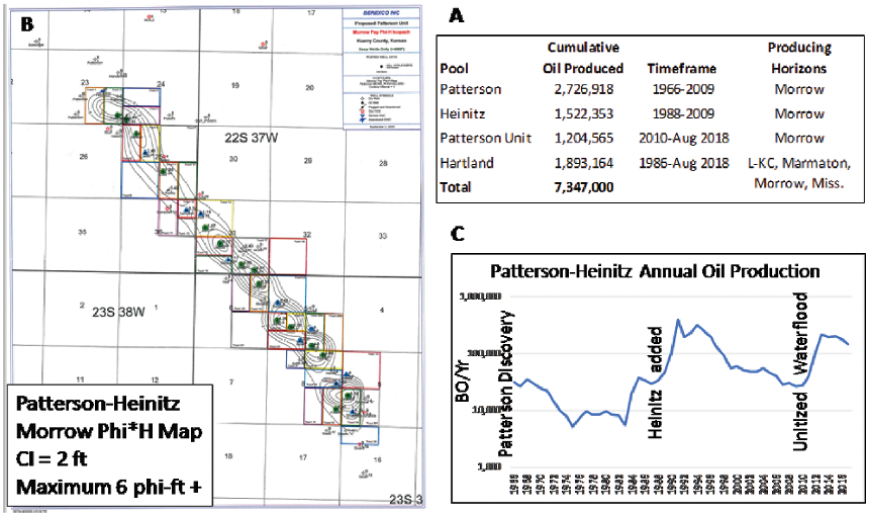

Figure 10.7 A — Table of oil produced and producing horizons at the Patterson site. B — Porosity (fraction) * thickness (H) map of the Morrow sandstone in the Patterson-Heinitz Unit. Map is courtesy of Berexco LLC, operator of the Unit. C — Annual oil production for the combined Patterson, Heinitz and Patterson-Heinitz Unit.

(1) and located within fifty miles of the Patterson site. The CO_2 EOR market for CO_2 could help the economics of transporting CO_2 to the Patterson site through economies of scale and the reduction of market risk. There would be the added benefit of concurrent CO_2 storage in the EOR projects. The four fields—Pleasant Prairie South (part of the Pleasant Prairie site), Eubank North Unit, Shuck, and Cutter—are similar in size and reservoir as the Patterson-Heinitz Unit, having produced a combined 23.6 million barrels of oil through 2014 from the Morrow and Chester (Mississippian) sandstones. Dubois *et al.* [5] estimated the ultimate recovery by primary and secondary (waterflood) of 25.4 million barrels and the potential CO_2 EOR recovery at 13 million barrels of oil. Their reservoir simulations estimate 5 Mt CO_2 would be stored in the oil reservoir in the process.

10.4 Estimating CO_2 Storage Volume—Building the Static Model

Storage volume was estimated by building a static geologic model on the basis of mainly public, but some well data from our industry partner, Berexco LLC, and then performing dynamic simulations of CO_2 injection into targeted reservoirs.

10.4.1 Workflow for Building 3-D Static Model

A simple, un-faulted 3-D static model was built for a 920 mi^2 (2,400 km^2) area and then a smaller area was cut out of the model for simulation (Figure 10.7). A large area with relatively coarse XY cells was required to capture enough data to model the reservoirs. Few wells in the region penetrate the target saline storage intervals because they do not produce hydrocarbons and the oil and gas reservoirs are at shallower depths. A smaller area was cut out from a larger modeled area for simulating the Patterson and the Rupp structures in separate simulation exercises. The Lakin had been modeled and simulated separately, but data from the few useful wells in that area were incorporated in the Patterson and Rupp static model.

A conventional workflow (Figure 10.8) for building a 3-D static model was deployed: 1) gather, prepare and analyze well-scale well data from public sources and operator-partner data, 2) build thirteen 2-D structure and isopach maps (grids) with Geoplus Petra™, 3) develop petrophysical relationships to estimate permeability knowing porosity, 4) import well headers, tops and digital well logs into Petrel™ for static model building, 5) build wireframe model using the imported 2-D grids as horizons

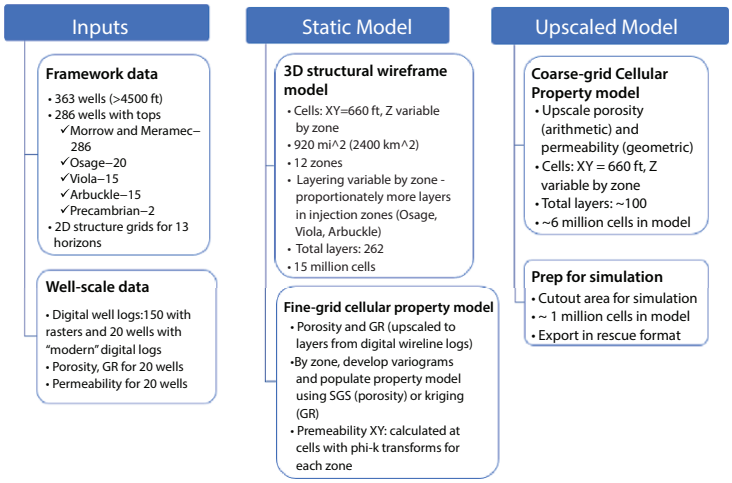

Figure 10.8 General workflow used for building the Patterson static model and preparing it for export for simulation.

making 12 zones and layering, and with 660 ft xy cells, 6) upscale porosity and GR to layer scale, 7) develop porosity variograms for 10 of the 12 zones, excluding the Morrow and Reagan, and GR for the Arbuckle, and model porosity for the 10 zones using sequential Gaussian simulation and simple kriging for the GR in the Arbuckle, 8) calculate permeability at the upscale model by zone to reduce cell count, porosity—arithmetically, permeability—geometrically, 9) cut a smaller area around the Patterson and Rupp sites for simulation, and 10) export in rescue format.

10.4.2 Well Data

There are 363 wells deeper than 4,500 ft in the model area and 1,952 shallow wells (<4,500 ft). The vast majority are shallow gas wells that have depths of less than 3,200 feet, that were completed in the Permian Chase and Council Grove Groups, and that are part of the shallow Hugoton-Panoma gas field. Of the 363 wells, 361 penetrate the top of the Meramec, but relatively few penetrate the prospective saline storage zones—Osage, Viola, and Arbuckle—because there is no production below the upper 150 feet of the Meramec. Raster log images were available for most wells in the immediate vicinity of the simulation model. Formation tops were picked for all wells with logs available having penetrations below the Meramec. Only 21 wells penetrated the Osage, 20 cut the Viola, and 14 penetrated the Arbuckle. Modern logs, having a minimum neutron

and density porosity and gamma ray, were digitized for 20 wells yielding porosity coverage for the Osage (12 wells), Viola, (9 wells) and Arbuckle (8 wells). Although the data are sparse, porous intervals in the three candidate injection zones are laterally extensive. Because of porosity modeling difficulties in the immediate Patterson-Heinitz-Hartland area due to disparate data, especially in the Arbuckle, we needed to place a pseudo well halfway between the Longwood GU-2 well and the next well with Arbuckle data 10 miles to the northwest. The pseudo well is essentially a copy of the Longwood GU-2 with minor adjustments due to changes in thickness in some of the zones.

10.4.3 Petrophysics

Porosity input for the geomodel was the average of neutron and density porosity and gamma ray at the half-foot scale for the 20 wells with modern logs and the pseudo well from the Morrow to total depth. Permeability was calculated in the geomodel using porosity-permeability transform equations derived from available empirical data.

Empirical data used in petrophysical analysis at the Patterson site include limited core data from the Longwood GU-2 well, engineering injection/falloff test in the City of Lakin WIW, both within the bounds of the reservoir simulation and extensive core and NMR log data from Berexco KGS-Cutter 1 well [1], located 30 miles south of the Patterson site. Conventional core analysis for plugs and whole core in the Longwood well provide nearly full coverage in the Osage, but limited coverage in the Viola and Arbuckle. Initial porosity-permeability transform equations for the Osage were based on core from the Longwood well while transforms for all other zones (Meramec, Spergen, Warsaw, Kinderhook, Viola, Simpson and Arbuckle) were based on KGS-Cutter 1 data. Although the Arbuckle was split into two zones, upper and lower and porosity modeled separately, only one porosity-permeability transform was used to calculate permeability. No transform was derived for the Morrow and Reagan. The Morrow exhibits high vertical heterogeneity including shale (caprock) tight limestone and sandstone, and localized porous sandstone. For this simulation, the Morrow interval was generically treated as a caprock with very low permeability. There is only one penetration through the Reagan, and little else is known of this interval in the region. It was treated as a no-flow boundary in these simulations.

Porosity-permeability transform equations for six zones derived by cross-plotting porosity and Coates-based permeability from NMR digital log in the KGS-Cutter #1 [1]. In the KGS-Cutter #1, the Coates-based

NMR permeability was closely correlated with core permeability, validating the methodology. Coates-based permeability from NMR in the KGS Cutter #1 well is an order of magnitude higher than core permeability in the Longwood GU-2 well for the same porosity value. Longwood GU-2 cross plot is core-derived permeability and log-derived porosity, while the KGS-Cutter #1 cross plot uses Coates-derived NMR permeability based on log porosity.

Adjustments (increases) to permeability were made in the simulation model for the Osage and Arbuckle. The adjustments are justified by reservoir performance data demonstrating that reservoir-scale permeability data are significantly greater than matrix permeability at the core scale. Six miles east of the southernmost simulated CO_2 injection well, the maximum injection rate in the City of Lakin Class I well injection/falloff test in the Arbuckle was 4,831 barrels of water per day on a vacuum. The calculated average permeability is 1.43 Darcy over a 690 ft interval, a thousand times the average permeability using the geology specific transform. The permeability transform based on core data for the Osage is less than $1/10^{th}$ that of a transform based on the KGS-Cutter #1 data, both likely to be significantly lower than reservoir-scale data. Merit Energy obtains >2,000 barrels of water per day per well from the Osage water supply wells for its Victory field area just southeast of the NHSC area, requiring much greater permeability than the average of 1.34 mD for core data from the Longwood #2 well.

10.4.4 Three-Dimensional Static Model

A single 3-D cellular model covering both the Rupp and Patterson geologic sites was constructed using the workflow discussed in detail above. Figure 10.9 is a view from the southeast of the fine-grid permeability model before upscaling. There is a known fault with nearly vertical offset, down to the southwest, that bounds the structure to the southwest. The exact location of the fault is not known because of the lack of seismic data. Discussion of faulting is covered later in this report. In this phase, the mapping and modeling was performed without inserting the fault or faults. The 3-D model and cross section illustrate the continuous nature of the permeable intervals in the proposed injection zones, Osage, Viola, and Arbuckle. It also shows the low permeability in the Meramec, Spergen and Warsaw intervals above the Osage.

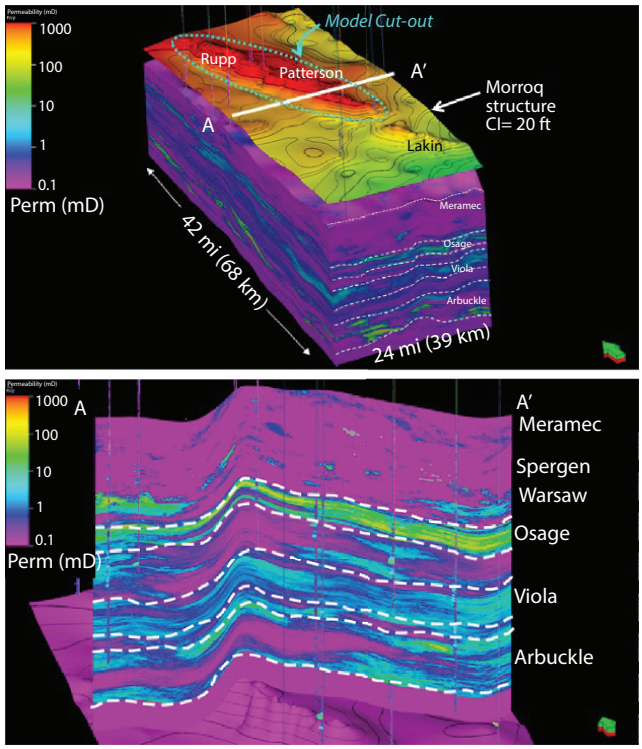

Figure 10.9 Upper figure—3-D volume of permeability from the top of the Meramec to basement. The map above the cube is the top of the Morrow; its color does not reflect permeability. Area of model cut out for the Patterson simulation is indicated by the dashed ellipse. Lower figure—A-A' cross section through the permeability model in the upper figure. Map at the base of the cross section is the top of the basement.

10.5 Estimating CO_2 Storage Volume—Running the Dynamic Model

The key objectives of the dynamic modeling were to determine the volume of CO_2 stored, resulting rise in pore pressure and the extent of CO_2 plume migration in the Patterson field structure. Simulations were conducted using the Computer Modeling Group (CMG) GEM simulator, a full equation of state compositional reservoir simulator with advanced features for modeling the flow of three-phase, multi-component fluids that has been used to conduct numerous CO_2 studies [6, 7].

10.5.1 Initial Reservoir Conditions and Simulation Constraints

The initial conditions specified in the reservoir model are specified in Table 10.2. The simulations were conducted assuming isothermal conditions. Although isothermal conditions were assumed, a thermal gradient of 0.008 °C/ft was considered for specifying petrophysical properties that vary with layer depth and temperature such as CO_2 relative permeability, CO_2 dissolution in formation water, etc. The original static pressure in the injection zone was set to reported field test pressures and the Arbuckle pressure gradient of 0.48 psi/ft was assumed for specifying petrophysical properties. Perforation zone was set at top 35 ft in all three injection intervals: Osage, Viola, and Arbuckle. Injection rate was assigned according to maximum calculated based on well tests and reservoir properties. Boundary conditions were selected as open Carter-Tracy aquifer with leakage allowed.

Four wells were completed in the main part of the Patterson structure and were "perforated" in the Mississippi Osage, Viola, and Arbuckle. No flow boundary conditions were specified above and below the injection zones as indicated by brine chemistry. CO_2 was injected at rates determined by the petrophysical conditions at each injection site and within

Table 10.2 Model input specification and CO_2 injection rates.

Injection Interval	**Osage**	**Viola**	**Arbuckle**
Temperature	60 °C (140 °F)	61 °C (142 °F)	62 °C (144 °F)
Pressure	1,650 psi (11.38 MPa)	1,700 psi (11.5 MPa)	1,800 psi (11.72 MPa)
Max. BHP	2250 psi ()	2300 psi	2400 psi
TDS	100 g/l	140 g/l	180 g/l
Formation Top	5,260 ft	5,500 ft	5,740 ft
Formation Base	5,400 ft	5,700 ft	6,340 ft
Perforation Zone	110 ft	200 ft	150 ft
Injection Period	30 years	30 years	30 years
Number of wells	4	4	4
Injection Rate	3,050 T/day	1,400 T/day	1,080 T/day
Total CO_2 injected	33.5 MT	15.3 MT	11.8 MT

each perforated interval. The lateral boundary conditions were set as an infinite-acting Carter-Tracy aquifer [8, 9] with leakage.

10.5.2 Simulation Results

Figure 10.10 shows the maximum lateral migration of the CO_2 plume approximately 100 years after cessation of CO_2 injection activities at Patterson Field. The plume grows rapidly during the injection phase and is largely stabilized 20–30 years after the end of injection period. CO_2 travels throughout the reservoir for an additional several years and enters stabilization phase after several years post injection commencement. A significant amount of CO_2 (~30%) is dissolved in water over the period of 50 years past injection commencement.

Figure 10.11 presents the distribution of reservoir pore-pressure at the maximum point of CO_2 injection. The pressure increases are estimated to be below 500 psi on commencement of injection and then pressure gradually drops after the commencement of the injection as the capillary effects are overcome. The pressure decreases to almost pre-injection levels after approximately 15–20 years, as illustrated in Figure 10.12.

Figure 10.13 illustrates modeled cumulative injection volumes obtained via injection by four injection wells completed at Osage, Viola, and Arbuckle intervals. Maximum combined injection rate for four wells modeled for the Patterson site is 5,800 metric tonnes/day. The cumulative injected CO_2 estimate for the Patterson site is 60.7 M metric tonnes; however, the injection strategy could be optimized to inject even higher amount of CO_2 at this site.

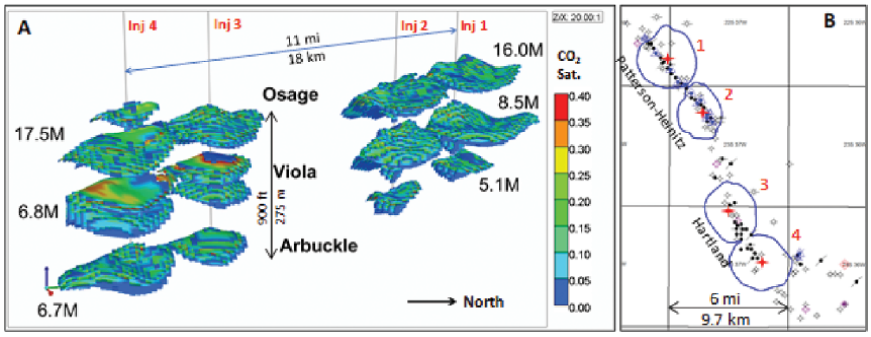

Figure 10.10 Dynamic simulation results showing CO_2 plumes after vertically stacked injection in the Arbuckle, Viola, and Osage. A. 3-D view of CO_2 plumes in stacked saline aquifers with CO_2 volume stored for each plume (million tonnes). B. Plate showing aerial extent of plumes for the four injectors and 132 wells that penetrate the Morrow caprock (~4,800 ft).

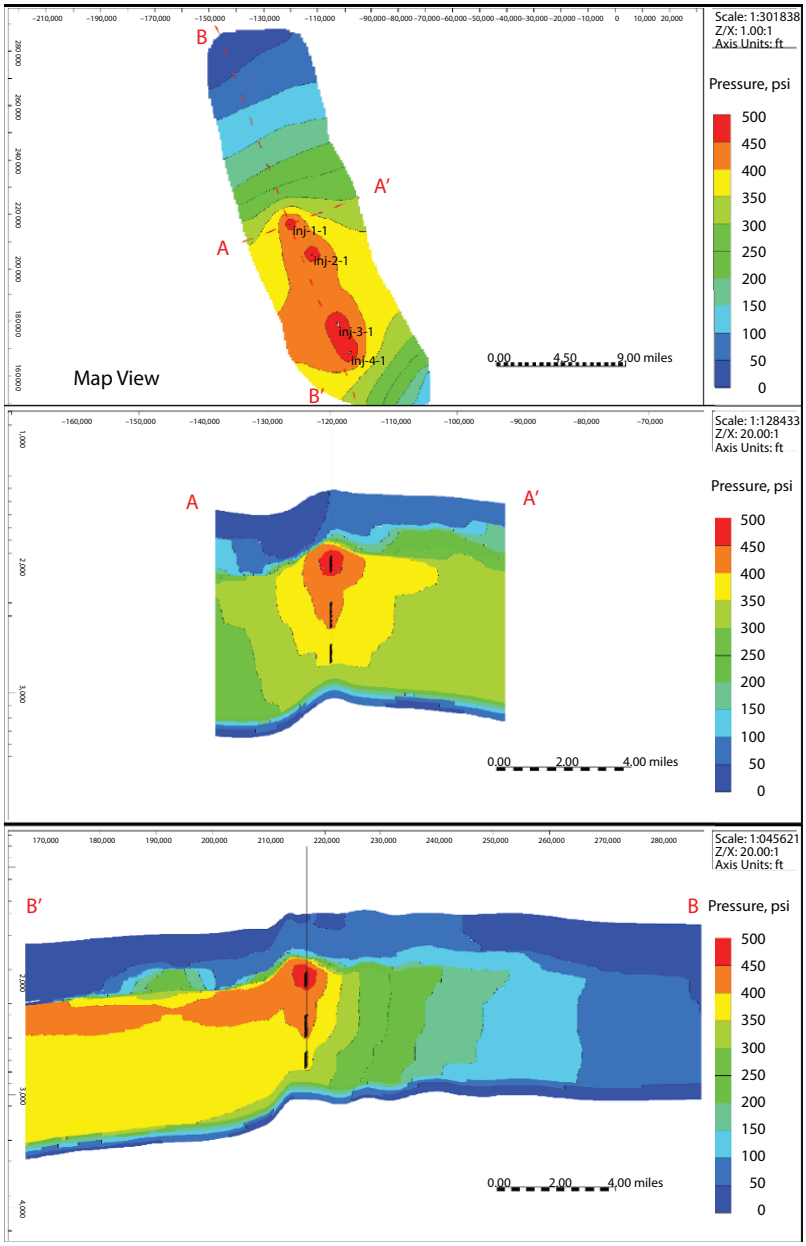

Figure 10.11 Maximum reservoir pressure increases as a result of CO_2 injection.

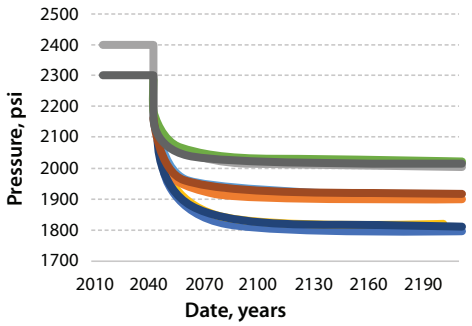

Figure 10.12 Bottom-hole pressure profiles for CO_2 injection in four wells and three injection intervals.

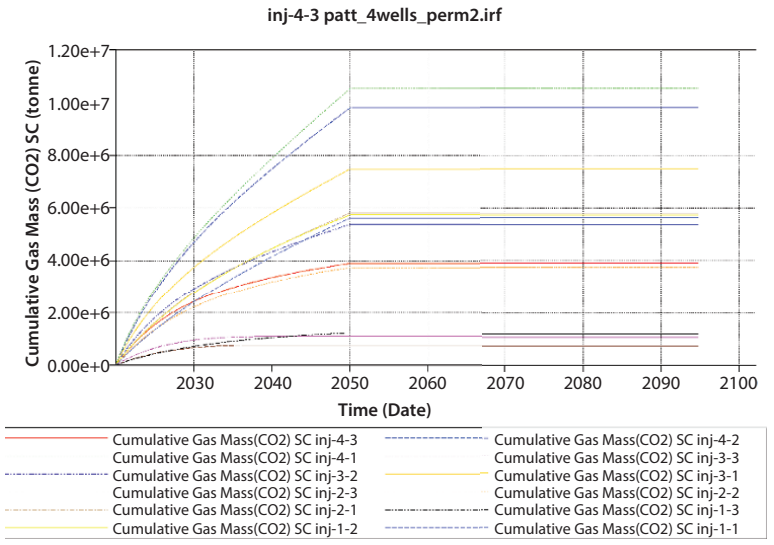

Figure 10.13 Cumulative CO_2 injection volumes in four wells and three injection intervals.

10.6 Summary/Discussion

For CO_2 injection simulations at the Patterson site, four wells were placed in close proximity to the apex of the linear closed structure where there was higher porosity and permeability indicated in the 3-D static model in the three storage zones, the Osage, Viola, and Arbuckle. A fully compositional simulation using CMG Gem software was performed. Injection was restricted to a delta P of 600 psi above reservoir pressure and a maximum

of 2,400 psi in the Arbuckle, approximately equal to hydrostatic pressure and 2,100 psi under fracture pressure (assuming 0.75 psi/ft). Daily injection rates were 1.6, 1.3, 1.5, and 1.4 kilotonnes/day for 30 years, storing 60.7 million tonnes. Maximum plume diameter averages 2.9 miles (4.6 km) 100 years after injection ceased.

This presented scenario is a conservative estimate and the performance of the dynamic model could be further improved. For example, it is possible to optimize well locations and increase the number of injectors; perforations could also be placed more strategically and perforated intervals could be extended to decrease injection pressures; and delta injection pressure could be increased to 600 psi. Stated measures would allow injecting much larger volumes of CO_2 in a safe manner without increasing potential risks.

References

1. Watney, W.L. *et al.*, Modeling CO_2 sequestration in saline aquifer and depleted oil reservoir to evaluate regional CO_2 sequestration potential of Ozark Plateau aquifer system, south-central Kansas, final report, Award Number: DE-FE0002056, submitted October 2, 2015, 4, 867 p, 2015.
2. Holubnyak, Y., Watney, W., Hollenbach, J., Birdie, B., Hollenbach, J., Bidgoli, T., Rush, J., Doveton, J., Fazelalavi, M., Victorine, J., Newell, D., Jackson, C., Lessons Learned from Small Scale Field Test Demonstrating CO_2 EOR and Geologic Storage at Wellington Field in Southern Kansas. *14th Greenhouse Gas Control Technologies Conference*, Melbourne, 21-26 October 2018, (GHGT-14). Available at SSRN: https://ssrn.com/abstract = 3365741.
3. Watney, W.L. *et al.*, Integrated CCS for Kansas (ICKan) SF 424 R&R, application for federal assistance, Phase I—Integrated CCS pre-feasibility study activity under CarbonSAFE, DOE-NETL FOA 1584, 2016.
4. Rascoe, B., Jr. and Adler, F.J., Permo-Carboniferous hydrocarbon accumulations, Mid-Continent, U.S.A. *AAPG Bull.*, 67, 979–1, 001, 1983.
5. Dubois, M.K., Williams, E.T., Youle, J.C., Hedke, D.E., Potential for CO_2 storage and enhanced oil recovery in four southwest Kansas oil fields, an extended abstract; in W. L. Watney, PI, Final Report for DOE Award Number: DE-FE0002056, Modeling CO_2 Sequestration in Saline Aquifer and Depleted Oil Reservoir to Evaluate Regional CO_2 Sequestration Potential of Ozark Plateau Aquifer System, South-Central Kansas. IV1–IV19, 2015c.
6. Chang, K.W., Minkoff, S.E., Bryant, S.L., Simplified model for CO_2 leakage and its attenuation due to geological structures. *Energy Procedia*, 1, 3, 453–3, 460, 2009.
7. Bui, L.H., Tsau, J.S., Willhite, G.P., Laboratory investigations of CO_2 near-miscible application in Arbuckle Reservoir. *SPE Improved Oil Recovery*

Symposium held in Tulsa, Oklahoma, 24–28 April 2010, SPE Publication 129710, 2010.
8. Dake, L.P., Chapter 9, in: *Fundamentals of Reservoir Engineering*, Elsevier Scientific Publishing Co., 1978.
9. Carter, R.D. and Tracy, G.W., An improved method for calculating water influx. *Petroleum Transactions, AIME*, 219, 415–417, 1960.

11

Salt Precipitation at an Active CO_2 Injection Site

Stephen Talman[1]*, Alireza Rangriz Shokri[1], Rick Chalaturnyk[1] and Erik Nickel[2]

[1]Civil and Environmental Engineering Dept., University of Alberta, Edmonton, AB
[2]Petroleum Technology Research Centre, Regina, SK

Abstract

The Aquistore research program is part of SaskPower's Boundary Dam Integrated Carbon Capture and Storage (CCS) Demonstration project. In this project carbon dioxide is injected into a 3400 m deep injection-well drilled specifically for CO_2 injection. The target aquifer is highly saline (TDS 330 g/L) with injection through four distinct perforation zones extending over about 200 m.

Drying-induced salt precipitation within the target reservoir has been identified as having the potential to cause formation damage in CO_2 injection operations. Key parameters in assessing the possible severity are the initial salinity of the formation water and the residual water saturation under drainage. However, a second mechanism for reducing CO_2 injectivity was observed at the Aquistore site. Downhole images from the injection well, together with recovered samples reveal that scales of simple salts have formed on the inside of a CO_2 injection well. These are developed by evaporation of formation water to near complete dryness in the CO_2 dominated wellbore fluids. The timing of the water backflow into the well and the mechanism driving it are uncertain, but the very high salinity of the formation water means that the total volume of scale observed could be due to minor volumes of flow back fluid. Since large salt build-ups are associated with what is very likely small volumes of inflow, the salts precipitated in the wellbore may threaten CO_2 injectivity. This observation suggests that an effort should be made prior to the onset of CO_2 injection to reduce the likelihood of such a scale development. This requires a better understanding of the conditions responsible for any flowback of water into the injection well.

Images and other descriptions of the salt deposits will be presented along with an interpretation of their mechanisms of formation.

**Corresponding author*: stalman@ualberta.ca

Ying Wu, John J. Carroll, Mingqiang Hao and Weiyao Zhu (eds.) Gas Injection into Geological Formations and Related Topics, (183–200) © 2020 Scrivener Publishing LLC

Keywords: Salt precipitation, injectivity, aquistore, CO_2 injection, downhole image, geological CO_2 storage

11.1 Introduction

The Aquistore research project managed by the Petroleum Technology Research Centre is part of SaskPower's Boundary Dam Integrated Carbon Capture and Storage (CCS) Demonstration project [10]. Carbon dioxide, captured from the flue gas of Unit Three of the Boundary Dam coal-fired power generation station, is injected into a 3400 m deep injection well drilled specifically for CO_2 injection. Carbon dioxide injection rates of 400 tonnes/day are routinely achieved, and a net injected mass of 240 thousand tonnes injected as of August 2019. The target aquifer is highly saline (TDS 330 g/L) with injection through four distinct perforation zones extending over about 200 m.

Saline aquifers can be susceptible to porosity and permeability reductions near the injection well, known as near-wellbore formation damage, due to salt precipitation driven by formation dry-out. Formation damage, caused by salt precipitation was studied by Lorenz and Muller [4], and later by Pruess and Muller [8] for gas storage systems in saline aquifers. Both studies identify that the initial salinity and the residual water saturation are critical properties in defining the potential for salt-induced damage. A comprehensive review paper of the salt precipitation literature was recently published [5], and more recent work is noted in Piao *et al.* [7]. The focus of these works is restricted to processes that occur within the aquifer; there is no consideration of salt migration back into the wellbore. A recent report by Berntsen *et al.* [2] is notable in that salt formation was detected within gas saturated portion (essentially the wellbore) of their bench-scale CO_2 injector model.

As discussed in Miri and Hellevang [5], the eventual mass, and spatial distribution, of salts precipitated in the drying aquifer are controlled by multiple factors. These are: the initial salt content of the brine; the efficiency of brine displacement by the injected CO_2; the solubility of water in the CO_2 stream; the kinetics of water uptake into the injected CO_2 (see also [9]); capillary forces which can pull brine in towards drier zones; diffusion of salts away down the concentration gradient induced by evaporation; and large scale flows associated with gravity override induced by the buoyancy of CO_2. Although each of these factors will be important in controlling the formation damage, each of these processes will only allow salts to form in

previously water wet locations. As such they cannot be responsible for salts found within the wellbore.

Mineral precipitation, or scale formation, within producing wellbores is well known. Commonly, the precipitates are minerals which are less soluble at surface conditions than downhole [11] so their formation is driven by temperature and pressure changes during production. However, precipitation of salts induced by water evaporation has also been observed in gas producers [3]. Furthermore, there is a short report dealing with the recovery of both halite and calcium chloride salts ($CaCl_2 \cdot 6H_2O$ and $CaCl_2 \cdot 4H_2O$) in a CO_2 injection well associated with a CO_2 sequestration project [12]. The recovery of $CaCl_2$ salts, which are strongly deliquescent, is of especial interest. It can only form in very dry conditions, and it will eventually dissolve by drawing water out of ambient air. As such, this salt may be lost, or at least transformed post-recovery so its presence and phase are likely to represent storage, rather than formation, conditions. We will refer here the calcium chloride salts by the generic $CaCl_2$ rather than as a specific phase.

The material described by Sminchak *et al.* [12] was recovered as part of a well workover to clear a suspected blockage from within the injection tubing. It was formed at the placement depth of a packer which was used to isolate the injection zone. The injection zone immediately under this packer was reported to be scale free [12]. Calcium chloride rich annular fluid and formation brines were proposed as the primary source of the precipitated components with evaporation enhanced by the injection of dry CO_2. Sminchak *et al.* [12] presented several strategies for preventing formation of scale associated with the packer.

In this paper, we present downhole photographic evidence of extensive evaporite scales within the CO_2 injection well at Aquistore along with mineralogical details of solid recovered from the well. The predominant mineral in the recovered scale is halite, with lesser amounts of sylvite. A video taken within the injection well shows extensive salt formation extending downwards from some, but not all, perforations. Some scale formation was associated with each perforation zone, but the most extensive scale formation was observed in a zone which was determined not to be actively receiving CO_2 based on downhole spinner logs.

Formation of salts in previously dry environments may occur *via* a final mechanism mentioned by Miri and Hellevang [5]. This "salt self-enhancing mechanism" was described by Miri *et al.* [6] as:

> … salt crystals preferentially nucleate and grow close to the interface between CO_2 and water owing to the locally increased salt concentration.

> These crystals are largely immersed in the aqueous phase, but partly protrude into the CO_2 stream. This protruding surface is covered with a thin layer of water due to surface energy effects (i.e. hydrophilic nature). As a result of evaporation, this hydration layer rapidly becomes highly super-saturated, leading to further crystallization and surface roughening. In turn, this results in the formation of nucleation points on the surface of crystal which promote further nucleation and lead to the growth of a massive aggregate of salt micro-grains.

Their experimental results showed salt crystals growing out away from the brine/gas interface; this phenomenon may also be responsible for the features observed in the Aquistore injection well. Furthermore, repeated cycling of injection rates and pressures may lead to the repeated cycling of formation water into previously dried regions near the wellbore, which can increase the extent of formation damage and/or the flux of salts into the wellbore itself.

11.2 Laboratory and Field Data

11.2.1 Data Sources

The 3396 m injection well for the Aquistore project was drilled in the summer of 2012 [10]. Carbon dioxide injection through perforations that are distributed through 4 zones in the 4.5" diameter well began in April 2015. Formation water was collected during the drilling at several depths, with two samples taken from the CO_2 injection horizon. This water was analyzed by a commercial lab (Isobrine Solutions).

In May 2017, a video camera was deployed down the injection well in order to evaluate the integrity of the injection tubing. The obtained images were black and white in medium resolution. Downward-viewing axial images were continuously collected as the camera descended while some horizontal images were taken in instances where the camera was stopped. While the upper portions of the well showed little or no abnormalities; significant deposits of light coloured scale were present from 3170 m and below.

During a subsequent well-workover, samples of this material were from the well. Sub-samples of the material were studied in a commercial X-Ray Diffraction (XRD) laboratory under a contract with PTRC.

11.2.2 Chemical Composition of Formation Water

The chemical composition of the formation water is presented in Table 11.1. The formation water is a very saline (TDS 330 g/L) Na^+, Ca^{2+}, Cl^- rich brine. Chloride is far and away the dominate anion; it represents >99.8 mole% of

Table 11.1 Composition of formation water recovered at a depth of 3334 m at the Aquistore injection well. Only the dominant cations (> 0.1 moles/L) and anions (> 0.0005 moles/L) are reported. An estimate of the type and amount of each precipitate that would form from the complete evaporation of a litre of the formation water is given in the fourth through sixth columns. The phases were chosen based on their stability in the pure salt/water system at downhole conditions (e.g., $MgCl_2 \cdot 6H_2O$ would precipitate in the Mg-Cl-H_2O system at 100 °C).

Solution composition		**Precipitates**			
	g/L		**mmoles/L**	**g/L**	**cc/L**
Na^+	87.7	Halite	3815.0	222.95	102.7
K^+	4.96	Sylvite	124.0	9.24	4.6
Ca^{2+}	32.5	$CaCl_2 \cdot 2H_2O$	809.3	118.98	64.3
Mg^+	1.70	$MgCl_2 \cdot 6H_2O$	70.0	14.23	9.1
Cl^-	203.0	Anhydrite	1.6	0.22	0.1
SO_4^{2-}	0.15	Calcite	0.4	0.04	< 0.1
HCO_3^-	0.05	Total			180.9
Br^-	0.71				

anions in solution. Mineral stability calculations performed with PHREEQC (using the [1], 2015 Pitzer activity model database) suggest that the water is at, or near, saturation with halite and anhydrite at reservoir conditions; anhydrite stability is achieved despite the near absence of SO_4^{2-} in the formation water through the very high Ca^{2+} activity. The dissolved silica concentration (not reported here) is close to that expected from equilibrium with amorphous silica at near surface conditions. This suggests that some silica was lost from the solution *via* precipitation during, or subsequent to, sampling.

Evaporation of this water will precipitate trace amounts of anhydrite, barite and other metal sulphates, together with calcite and other metal carbonates. However, since the chloride so completely dominates the other anions, the bulk of the precipitates formed will be chlorides, as shown in the fourth column of Table 11.1.

11.2.3 X-Ray Diffraction Analysis of Recovered Salt Samples

Material recovered from the Aquistore injection well was undertaken by Calgary Rock and Materials Services Inc. (Holderness, pers. comm.) on

Table 11.2 XRD analysis of recovered salt.

	Weight %	
	A	**B**
Halite (NaCl)	96.6	54.8
Sylvite(KCl)	3.4	3.2
Siderite ($FeCO_3$)	0	42.0

two samples, identified here as A and B. Both samples were predominantly halite (see Table 11.2), with minor amounts of sylvite. Sample B also contained a significant amount of siderite which is likely a reaction product between the tubing and injected CO_2. No other minerals were identified in either sample.

11.2.4 Downhole Video Analysis and Image Sizing

Two cameras, one oriented with a downhole view and the other horizontally, were run down the injection well. Although the images may be somewhat distorted, a sense of the size of the observed features can be estimated. For the axial images a reference dimension is the diameter of the wellbore (11.4 cm) and the illuminated zone extends some 80-100 cm downhole. The specifications for the perforation job were that the perforations define a helix, with a vertical offset between perforations of about 60 mm and 72° angular separation and the diameter of the holes is 1.1". Figure 11.1-(a) is an image, taken perpendicular to the wellbore axis, showing two perforations in the wellbore. The vertical distance between the perforation centers is about 40% of the total image height, meaning that the field of view is about 150 mm. An axial image, clearly showing three perforations, is illustrated in Figure 11.1-(b).

11.2.4.1 Material Fixed to the Wellbore

Significant quantities of a stalactite-like scale have developed in the wellbore. The scale is closely associated with the perforated zones, and it is non-uniformly distributed both within a particular perforated zone and between perforated zones. The upper two zones are much less affected than the lower two, with the most extensive deposition in the third zone. The scale is generally absent in the unperforated zones, although there is a pillar of scale extending from the third to the fourth perforated zone.

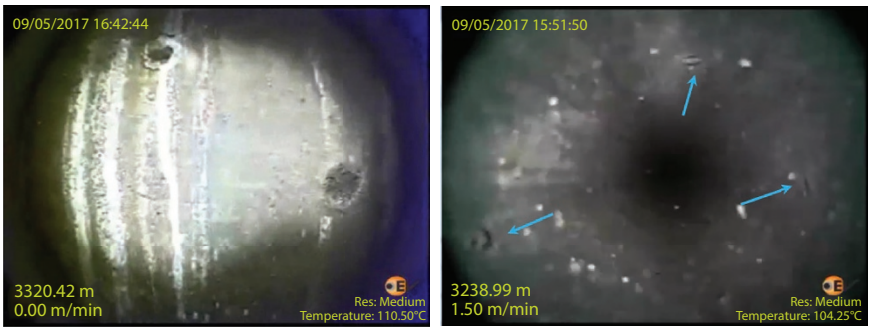

(**a**) (**b**)

Figure 11.1 (a) a horizontal view of two perforations in the injection well, (b) a vertical view of the well with three clearly visible perforations which are indicated by arrows. The white specks in this, and most of the following, images are due to material that is falling past the camera after being dislodged by it.

Several images of the perforations and associated scale are shown in Figure 11.1.

The perforations shown in Figure 11.1 appear to be clean. In contrast, many others are associated with a light coloured scale (e.g., Figure 11.2). This scale, and its adherence to the perforation pattern, is evident in the very uppermost perforations (Figure 11.2-a), and to a greater or lesser extent, throughout most of the perforated zones. The three axial images are all from the upper 2.5 m of the perforation zone; over this distance the amount of scale deposited ranges from extensive (Figure 11.2-b) to virtually absent (Figure 11.2-c). A close-up, horizontal image of two of these deposits show that they are highly porous.

The volume of each scale buildup shown in Figure 11.2-(a) is not large – on the order of 30 cc. The material itself is very porous (see Figure 11.2-d) so that its mass should be on the order of tens of grams. This mass of solid will form from the evaporation of roughly 100 cc of formation fluid meaning that only a minor flow of formation water back into the well is required in order to create these features. Slightly further downhole (Figure 11.2-b) the deposits are larger so that some of the scale from vertically stacked perforations merge; however, their volume remains on the scale of a few litres.

The third perforated zone is much more heavily impacted by scale formation. Typical wellbore views within this zone, as well as directly underneath it, are shown in Figure 11.3. In this region, the total volume of scale formed reaches an appreciable proportion of the total volume of the injector. In particular, one body of scale extends some 50 m in length, much of it through the unperforated zone, separating the lowest two perforation zones.

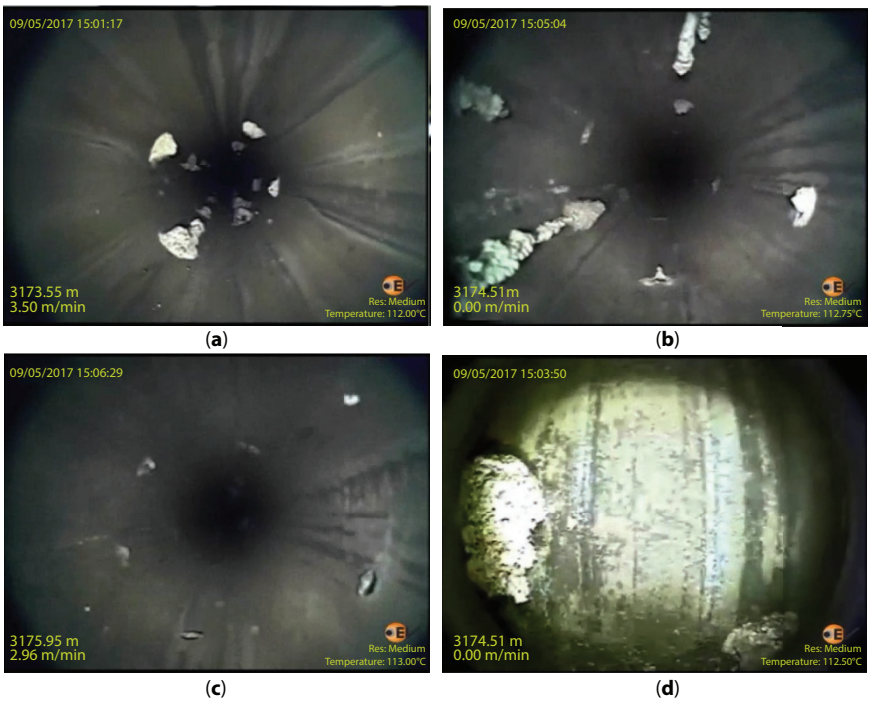

Figure 11.2 (a) axial view showing a region at the top of the first perforated zone indicating the formation of a scale at regular intervals, (b) transition from an extensively scaled zone to a relatively clean zone, (c) two clean perforations, with some less-well focused although also apparently clean ones below, (d) an axial view showing the scale and its highly porous nature.

11.2.4.2 Lowest Reaches of the Well

At 3346 m depth, which is 29 m from plug back total depth of 3375 m [10] the appearance of the wellbore scale changes dramatically. Here, the scale is less massive, and seemingly unrelated to the location of the perforations. The form of the scale suggests that it formed in place by the drying of a surface which had been coated by a highly saline solution. These deposits are shown in (Figure 11.4-a and -b). Figure 11.4-(c) was obtained from slightly below this level, at 3351 m, and it shows both some dislodged material (the bottom half of the Figure 11.4) as well as a few thicker particles with an ice-like appearance growing on the wall (upper half). The coherence of these crystals with the tubing wall suggests that they have grown from evaporation of a film of saline solution, presumably following a drop of the water level in the sump.

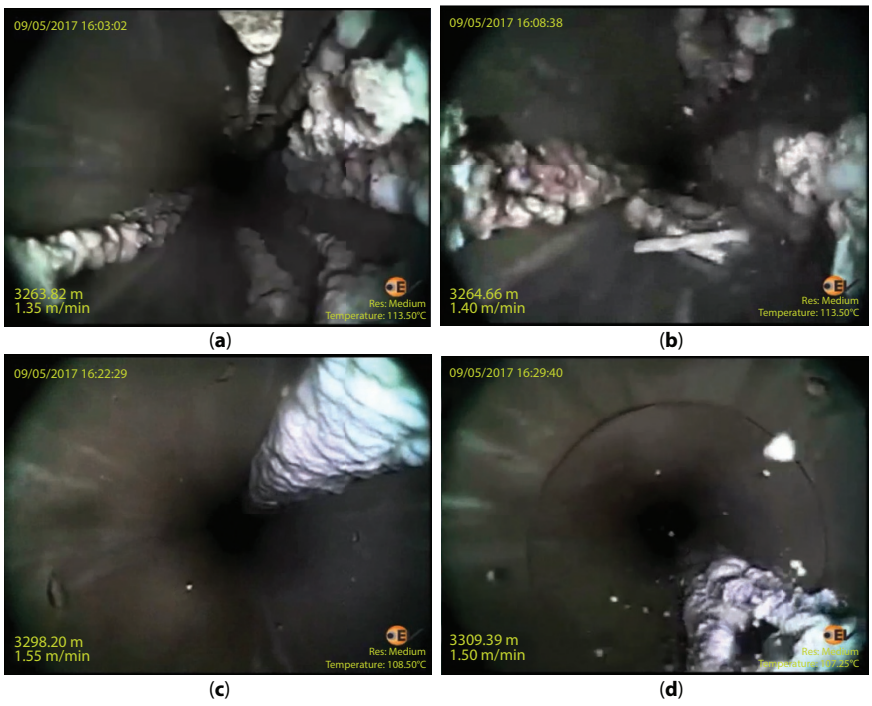

Figure 11.3 (a) axial view showing extensive scaling observed in the third perforated zone (b) large deposits near the bottom of the third perforated zone. Some of the material, visible in the central portion of the picture, was dislodged from above, (c) clean perforations at the top of the fourth perforated zone together with an extensive scale deposit sourced from above. This body is contiguous with the rightmost sample in the previous picture and it extends further to a depth of 3319 m. (d) continuation of the previous feature showing that, at least in this section, it is seemingly hollow.

11.2.4.3 Dislodged Materials

During visual scanning operation, a considerable amount of scale was dislodged. Some of this was caught up in the wellbore on other obstructions while other pieces could be observed in the downhole video as they were falling. These displaced pieces give a further sense of the shape and internal structure of the scale than the undamaged pieces stuck to the wellbore. Three examples are seen in Figure 11.5. Figure 11.5-(a) shows a tubular piece that fills much of the field of view, making it a piece of a few cm length, while Figure 11.5-(b) shows a much blockier piece. Both are highly porous, although for Figure 11.5-(b) this is much more evident in other pictures taken when the camera is closer to it. The rounded shape in further

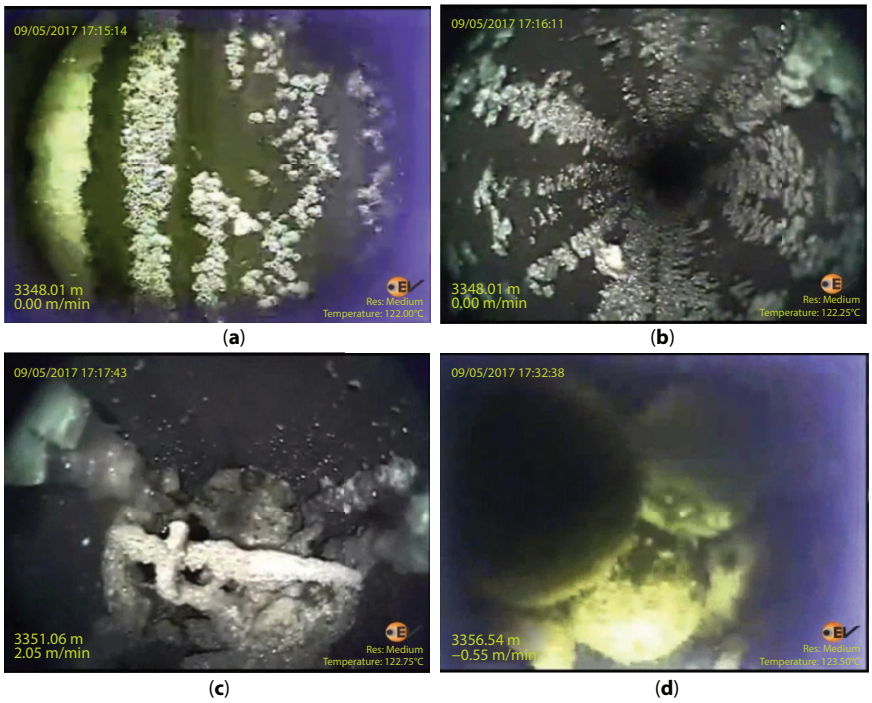

Figure 11.4 (a) a horizontal view of a more uniformly distributed scale that is present near the well bottom, (b) as the image to the left except as from the axial view. These images (a-b) show a scale that is more evenly distributed around the wellbore, and thinner than those seen in the previous Figure 11.3. (c) an image showing a precipitate (top-left quadrant) that is smoother, and with a different surface finish than that seen elsewhere in the well. (d) spherical forms than are floating, presumably in a water flooded zone at a depth 9 m above the last perforation and 20 m above the plug back total depth of 3375 m [10].

Figure 11.5 (a) and (b) Images of material falling down the well after having, presumably, dislodged by the camera and associated cabling.

downhole in Figure 11.5-(b) is a distinct piece that is attached to the wellbore which can be seen more clearly in the lowest image in Figure 11.6.

11.3 Implication and Interpretation

Figure 11.6 is an overview of where the salt forms and it provides some measure of total volume of precipitated salt. Clearly, the second perforated zone has the least scale formed. Based on the well-logs, this perforation

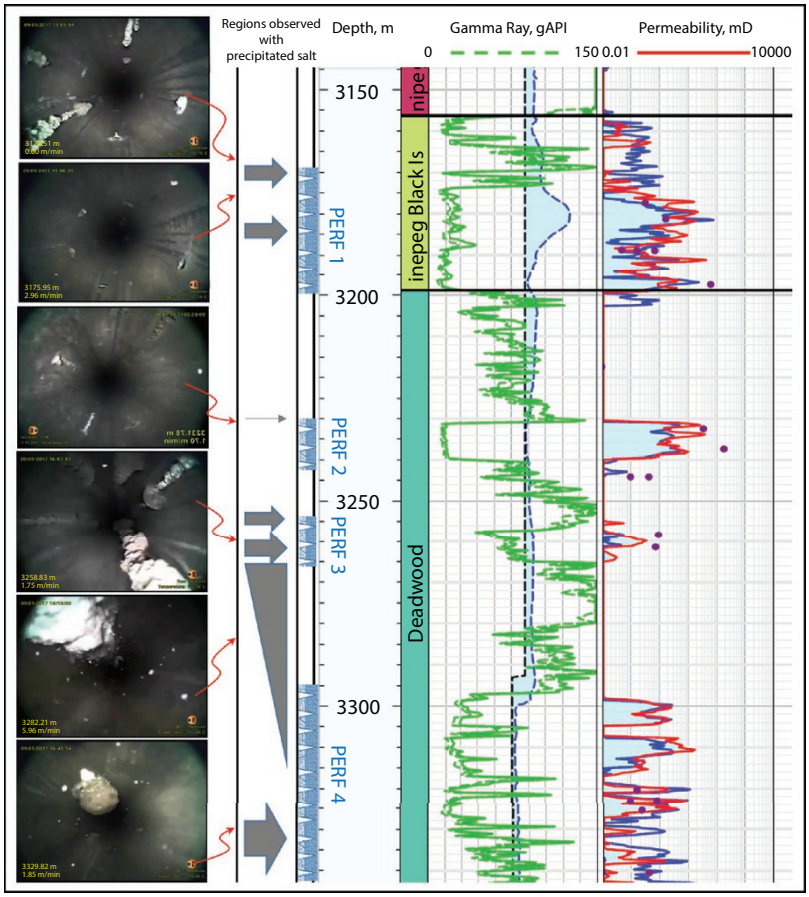

Figure 11.6 An overview of the aquifer physical properties and regions associated with salt scale. Images from different depths are shown at the left with the red arrows indicating their location. The grey shapes indicate general locations where there is salt buildup. An indication of the volume of the deposits is given by the size of these forms.

zone is associated with relatively homogeneous, high permeability, strata in the aquifer. The most scale is associated with the lowest injectivity, third perforation zone. Scale, when present in the first and fourth perforation zones, seems to be formed at the same depth as some of the less permeable strata in the perforated zone. This observation suggests that back-flow into the wellbore is related to permeability variations in the near-wellbore region, although the exact mechanisms, driving the process, are not obvious. From previous work dealing with salt formation in the aquifer, it is clear that a number of processes may contribute to such a flow. The proposed flows arise from complex interactions between mechanical responses, capillary forces, and chemical potential gradients; however, with two exceptions, the salt formed will be associated with either a stationary or receding (away from the CO_2 source) water/CO_2 interface. Self-enhanced salt formation has the potential to draw water into an advancing precipitation front [6]. Similarly, pressure driven flow back into the well, during low injection-rate episodes, can provide a source of brine into the wellbore. Detailed modelling of these flows is outside the scope of this observational study; however, these conceptual models are further discussed below.

During the early stages of injection there will be both a pressure gradient driving the injected CO_2 into the aquifer, and a chemical potential gradient drawing water into the dry injected CO_2 at the wellbore-formation interface. Assuming that the aquifer is preferentially wetted by water rather than CO_2, an overpressure will be required before the defending water phase will be displaced by the invading CO_2 phase. In the event that two perforations near each other are backed by materials that have appreciably different entry pressures, CO_2 will invade one perforation while its neighbour may remain water saturated. Salt will precipitate at this static CO_2/water interface. Enhanced capillary suction from this precipitate will continue to draw brine inwards which may lead to deposits growing within the wellbore. The ever-expanding salt deposit will lead to a continually increasing evaporative flux which will, eventually, reduce the local water pressure at the perforation. This reduced pressure in the defending phase will facilitate CO_2 invasion and eventually deplete the brine source from the salt scale. The relative rates of evaporation into the wellbore and capillary suction will determine the amount of salt that can be transported by such a process. This process is further complicated by the fact that the brine will precipitate both NaCl and $CaCl_2$ within the very dry CO_2 region; however, the brine itself will dissolve $CaCl_2$. Consequently, the precipitated salts may be repeatedly dissolving and recrystallizing within the wellbore and surrounding rocks. This means that the suction forces may also vary considerably

through pore structure reorganization due to ongoing dissolution/re-precipitation reactions.

Modelling of the flow field which develops around a CO_2 injection well reveals that inward flows can develop near the lower perforations in response to the general upward drift of the buoyancy of the injected fluid (e.g. [7]). Under continuous injection, the modelling results indicate that this flow does not push fluids back into the wellbore; there seems always to be enough drive from the CO_2 injection to keep the CO_2 plume expanding albeit at different rates depending on depth. However, the lift that drives this inward flow will continue irrespective of the rate of CO_2 injection. During extended shut-ins, it is conceivable that this counter-current flow will drive the bottom of the CO_2 plume above some of the lower perforations in the wellbore. Should this occur, brine will flow out of the perforations back into the wellbore until the wellbore becomes filled to the level of the wet perforations, or the CO_2 injection starts up to such an extent that the perforation can be invaded. Were this to occur, the potential to form salt is limited by the capacity of the presumably near stagnant CO2 column to absorb water.

Lacking information on when the salt deposits formed, it is not possible to ascribe a mechanism to the formation of any of the observed salts. However, it is possible to estimate the volume of water required to transport the precipitated salt. From Table 11.1, every litre of brine entering the wellbore carries solutes capable of depositing 180 cc of salt on complete drying. Brine seepage through these precipitates will preferentially dissolve the most soluble salts (presumably $CaCl_2$ > $MgCl_2$ > KCl), which will re-precipitate further from the brine source. Halite, once formed, is expected to be essentially inert as the invading brine is at or near halite saturation. However, irrespective of the eventual distribution of the particular salt types, the minimum amount of brine required to deposit the observed salt will be around six times the volume of salt that is observed. As an aside note, the total volume of the bottom 500 m of the injector is about 5000 L (or 10 L/m). CO_2 injection rates at Aquistore can exceed 10,000 kg/hr; such a stream has the potential to dry some 60 kg of water per hour which would deposit around 8-10 L of salt per hour. Since the wellbore did not fill up with salt within the first month of operation, it means that the rate of salt deposition is limited by the rate of water ingress.

An accurate estimate of the mass of salt deposited in the wellbore cannot be obtained from the available images. However, the total volume of precipitate is likely on the order of 25 L. This estimate is obtained by assuming that the bulk of the salt is found between 3365 m and 3410 m

(with a total volume of 450 L) and that in this region, the salt fills about 10% of the available volume in the tubing. The porosity of the scale was arbitrarily assigned a value of 50%. Thus, some 150-200 L of formation brine leakage will provide sufficient fluid to deposit the salts observed within the wellbore.

The solubility of pure water in CO_2 at downhole conditions, assumed to be 100 ^{0}C and 35 MPa, is about 2.3 mole% [13]. At reservoir conditions, each metre of tubing will contain 160 moles of CO_2 meaning that, under stagnant conditions, 3.6 moles of water can evaporate per metre of tubing. This is equivalent to 65 g H_2O. Since the brine is both denser than water, and relatively water poor, some 90 mL of formation water, which would precipitate 15 mL of salt, can be evaporated to dryness by each meter of a standing column of dry CO_2, assuming a density of 1300 kg/m^3 for the brine. Presumably, solvation of water in the standing CO_2 column will result in a density change in the CO_2 rich phase; this could generate some density gradients that would initiate mixing, and consequently would increase the efficiency of evaporation.

A value of 15 mL of precipitated salt/m is lower than what observed in most locations where there is salt, but it is of the right order of magnitude for some of the more tubular deposits detected around individual perforations (e.g., Figure 11.2-a). These deposits could have formed shortly after CO_2 injection, possibly during commissioning tests, by a process much like the self-enhanced growth described by Miri *et al.* [6]. The more brine required to form the massive deposit observed beginning in the third perforated zone (e.g., Figure 11.3-c), are likely due to a different driving flow. Additionally, the surface crust (Figure 11.4-a and -b) almost certainly is derived from evaporation of surface film left behind by a dropping column of brine.

11.4 Conclusions and Remarks

Open perforations are demonstrated here to be a source allowing formation fluids back into CO_2 injectors. The water in this backflow will rapidly evaporate into the dry CO_2 rich fluids in the injector, and any associated salts will eventually precipitate. Since the formation water is saturated with respect to halite, salt precipitation will occur very near to the inflow site, and will continue until either the water detaches from the wall or evaporates to dryness. For the highly saline formation fluids at the Aquistore injection site, the volume of salts precipitated at total dryness will be on the order of 20% of the original fluid volume. Consequently, salt precipitation

associated with any significant flux of water has the potential to disrupt CO_2 injection in perforated zones below this water inflow.

A number of operational problems can be anticipated to arise due to the drying of any inflow and the associated salt precipitation. Firstly, many of the perforations in the injection well appear to be, at least, partially plugged by precipitated salts. Although these currently plugged perforations were likely never amongst those which received the greatest CO_2 flux, continued salt deposition will result in the well underperforming in the long term. Such deposits may grow to eventually cover productive lower perforations. Additionally, scale which is dislodged will fall further clogging the lower reaches of the injection well. A final consideration is that the falling debris cause any water at the bottom of the well to become very saline, and highly corrosive.

Based on their analysis of a similar halide rich scale, Sminchak *et al.* [12] made several suggestions for minimizing the risk of scale buildup near the top of the injection zone. These include using of annular fluids that are unlikely to precipitate minerals in a dry (CO_2) environment, and keeping the volume of fluids introduced into the well during well workover events low. Such measures will be effective when the source of the scale is the introduced water, but the results presented in this paper show that backflow of formation water into the injection well has the potential to also add significant volumes of scale into the injection well. Periodic injections of water would effectively remove the scale in the injector at the Aquistore site, although, unless sufficient water is used, the mobilized salts will remain in near wellbore pore spaces where they may end up re-precipitating *via* formation dry-out.

Given that the mechanisms driving the backflow of water into the CO_2 injector at Aquistore are not yet fully understood, minimizing injection interruptions and injection variations would likely be beneficial in reducing the scale production, as at least some of the backflow into the injector will be driven by local pressure reductions. Most modelling studies of CO_2 sequestration assume a constant injection rate (e.g., [7]), but this ideal will not be easily realized in practice. The observations presented in this study suggest that the consistent radial displacement of water away from the wellbore, predicted by these models, is not achieved in the field. Understanding behaviours, associated with transients in the injection rate, may also be critical in understanding flows in and around the wellbore during operations of actual CO_2 injectors. Finally, the distribution of most of the salt in the Aquistore injector is associated with perforations in a zone with low injectivity. Scale formation in, and below, these zones may make the perforation of zones with only marginal injectivity counterproductive.

11.5 Acknowledgments

This research is a part of Carbon Capture, Utilization & Storage theme, partially funded by the Future Energy Systems, at the University of Alberta. The third author (RJC) is the principal investigator of the project, titled "Advancing Containment, Conformance and Injectivity Technologies for Effective Geological Storage of CO2". We gratefully acknowledge the Petroleum Technology Research Centre, Regina, Saskatchewan, for additional funding, recommendations, and access to data.

References

1. Appelo, C.A.J., Principles, caveats and improvements in databases for calculating hydrogeochemical reactions in saline waters from 0 to 200°C and 1 to 1000 atm. *Appl. Geochem.*, 55, 62–71, 2015.
2. Berntsen, A., Todorovic, J., Raphaug, M., Torsæter, M., Chavez Panduro, E.A., Gawel, K., Salt clogging during supercritical CO_2 injection into a downscaled borehole model. *Int. J. Greenhouse Gas Control*, 86, 201–210, 2019.
3. Kleinitz, W., Dietzsch, G., Köhler, M., Halite Scale Formation in Gas-Producing Wells. *Trans. IChemE, Part A*, 81, 352–358, 2003.
4. Lorenz, S. and Muller, W., Modelling of halite formation in natural gas storage aquifers, Proceedings, TOUGH Symposium, Lawrence Berkeley National Laboratory, Berkeley, California, May 12–14, 2003.
5. Miri, R. and Hellevang, H., Salt precipitation during CO2 storage—A review. *Int. J. Greenhouse Gas Control*, 51, 136–147, 2016.
6. Miri, R., van Noort, R., Aagaard, P., Hellevang, H., New insights on the physics of salt precipitation during injection of CO2 into saline aquifers. *Int. J. Greenhouse Gas Control*, 43, 10–21, 2015.
7. Piao, J., Shik Han, W., Choung, S., Kim, K., Dynamic Behavior of CO2 in a Wellbore and Storage Formation: Wellbore-Coupled and Salt-Precipitation Processes during Geologic CO2 Sequestration. *Geofluids*, 2018, Article ID 1789278, 20, 2018.
8. Pruess, K. and Müller, N., Formation dry-out from CO2 injection into saline aquifers: 1. effects of solids precipitation and their mitigation. *Water Resour. Res.*, 45, 3, Article ID W03402, 2009.
9. Roels, S.M., Ott, H., Zitha, P.L.J., μ-CT analysis and numerical simulation of drying effects of CO2 injection into brine-saturated porous media. *Int. J. Greenhouse Gas Control*, 27, 146–154, 2014.
10. Rostron, B., White, D., Hawkes, C., Chalaturnyk, R., Characterization of the Aquistore CO2 project storage site, Saskatchewan, Canada. *Energy Procedia*, 63, 2977–2984, 2014.

11. Shen, J. and Crosby, C.C., Insight into Strontium and Calcium Sulfate, Scaling Mechanisms in a Wet Producer. *J. Pet. Technol.*, 35, 1249–1255, 1983.
12. Sminchak, J., Zeller, E., Bhattacharya, I., Analysis of unusual scale build-up in a CO_2 injection well for a pilot-scale CO2 storage demonstration project. *Greenhouse Gases Sci. Technol.*, 4, 357–366, 2014.
13. Spycher, N., Pruess, K., Ennis-King, J., CO2–H2O mixtures in the geological sequestration of CO2. I. Assessment and calculation of mutual solubilities from 12 to 100°C and up to 600 bar. *Geochim. Cosmochim. Acta*, 67, 3015–3031, 2003.

12

The Development Features and Cost Analysis of CCUS Industry in China

Hao Mingqiang[1]*, Hu Yongle[1], Wang Shiyu[2] and Song Lina[3]

[1]Research Institute of Petroleum Exploration and Development, Beijing, China
[2]China University of Geosciences, Beijing, China
[3]China University of Petroleum, Beijing, China

Abstract

The carbon capture and storage (CCS) industry is developing rapidly worldwide, and projects are gradually turning from single-section items to whole-industry ones. The target of capture has expanded from power plants and natural gas processing to steel, cement, kerosene, fertilizers, and hydrogen production. Among China's CCS demonstration programs, use of carbon capture, utilization, and storage (CCUS) takes a main role. The scale of projects in operation and under construction is relatively small, but the scale of projects being planned is larger. High emission reduction cost has become the bottleneck in applications of CCS. Since the industry will develop from demonstration stage to industrial application in the future, national policies and carbon trading will be the main driving factors in the operation of CCS industrial chain, so for developing countries, in order to exploit the CCS techniques, it is more urgent to obtain technology and funds through market mechanism. Costs of CO_2 sources are comprised of three main parts: capture, compression and transportation, all of which are affected by the scale of capture. The cost of capture is also related to the concentration of emission source. For the type of high CO_2 concentration, the expense of compression takes the lead in accounting, and for the low CO_2 concentration type is capture cost. Considering the tolerance of CO_2 is lower than source cost for most oil fields, it is necessary to seek ways including technology, policies, markets, and so on to fill the gap and promote sustainable development.

Keywords: Carbon capture storage and utilization, cost analysis, China

**Corresponding author*: haomingq@petrochina.com.cn

Ying Wu, John J. Carroll, Mingqiang Hao and Weiyao Zhu (eds.) Gas Injection into Geological Formations and Related Topics, (201–216) © 2020 Scrivener Publishing LLC

12.1 Introduction

As one of the technical approaches in the global fight against climate change, Carbon capture and sequestration (CCS) has received extensive attention all over the world. According to the IEA, by 2050, among all the emission reduction technologies used to limit greenhouse gas concentration to 450ppm, carbon capture, utilization, and storage (CCUS) will account for 20%. Nowadays, several main energy research institutes in the world, including the IEA, IEF and OPEC, as well as some organizations which actively advocate carbon reduction, have all agreed that CCUS technology will be the main carbon reduction technology in the future [1, 2]. Among the numerous carbon reduction technologies, CCUS has the following features: (1) It has a huge potential for emission reduction; (2) It will be well combined with fossil fuels; (3) CO_2 could be utilized as a resource; (4) Costs for long-term emission reduction are relatively low. As a new industry, CCUS is still in the stage of research and demonstration in terms of the whole industry chain [3, 4].

12.2 Characteristics of CCUS Project

12.2.1 Distribution and Characteristics of CCUS Project

According to the statistics of GCCUSI, by May 2012, there were more than 300 CCUS projects in the world, of which 74 were massive integrated items, 14 were in operation and 52 were in planning. Figure 12.1 shows the distribution of the world's large-scale integrated CCUS projects. It shows that most large-scale integrated items and the big amount of captured CO_2 are mainly concentrated in North America and Europe, with 62%, followed by Canada, Australia and China [5, 6].

12.2.2 Types and Scales of CCUS Emission Sources

Emission sources of large-scale integrated projects in the world cover several categories, including power plants, natural gas treatment, syngas, coal liquefaction, fertilizer, hydrogen production, steel, refining and chemical industries (see Figure 12.2). Among them, the power plant has the largest amount of carbon capture (52%), followed by natural gas treatment (20%) and syngas (14%) [7].

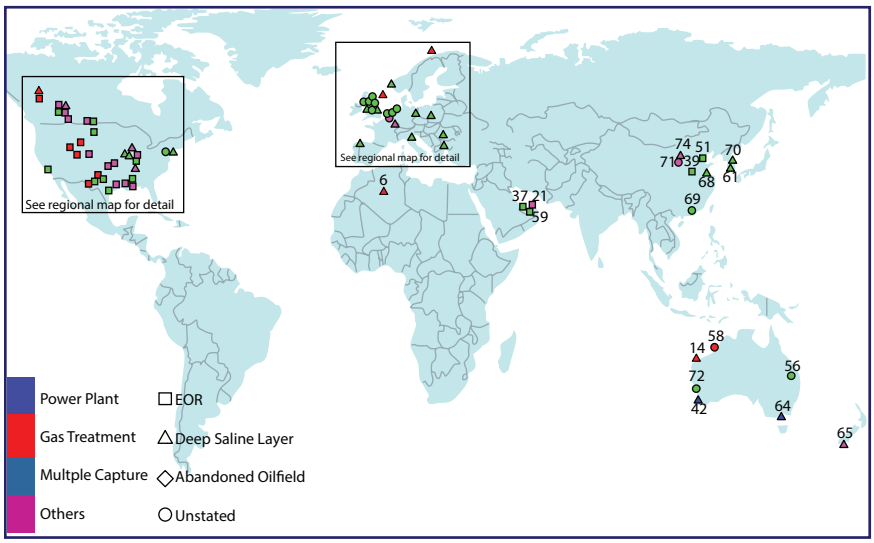

Figure 12.1 Distribution of the world's large-scale integrated CCUS projects.

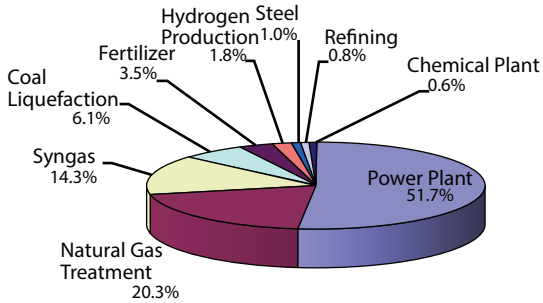

Figure 12.2 Pie chart of the carbon capture amount constitution of the world's large-scale integrated CCUS projects.

Considering the capture amount of an item on average, CO_2 capture scale in the natural gas treatment, syngas, coal liquefaction and power plants is very large, up to 5.0~8.5 million tons per year, and the average capture amount of a single project is 2.0~3.7 million tons per year. The scale of fertilizer, hydrogen production, steel, oil refining and chemical industries is relatively small, ranging from 0.6~2.5 million tons per year, with an average of 0.9~1.2 million tons per year [8].

12.2.3 Emission Scales and Composition of CO_2 Emission Enterprises in China

Main types of emission sources in China are power plants, cement, steel, and coal chemical industry, accounting for 92% of the total, while the other 4 categories account for only 8% (see Figure 12.3).

Among the emission sources collected, CO_2 emissions from coal and electric power are about 10 million tons per year, while the CO_2 emissions from companies like calcium carbide, refining, synthetic ammonia and polystyrene are relatively small, ranging from hundreds of thousands of tons to several million tons, mostly within 5 million tons per year (see Figure 12.4). CO_2 emissions from coal chemical, steel and cement industries vary considerably, mostly from 1~30 million tons per year [9].

12.2.4 Distributions of CO_2 Sources in China

The distribution of carbon emission enterprises of the eight major industries is consistent with the population and economic development of China, mainly in eastern China, and relatively few in the west (see Figure 12.5). Most of them are power plants, cement, steel and chemical industries of low concentration. The sources of high concentration, including coal chemical industries, synthetic ammonia, calcium carbide and moderate concentration like polyethylene, are relatively small. Overall, abundant CO_2 emission sources are all found near several main oilfields of PetroChina, such as Xinjiang Oilfield and Changqing Oilfield, which are surrounded by emission sources of relatively high concentrations, including enterprises of coal

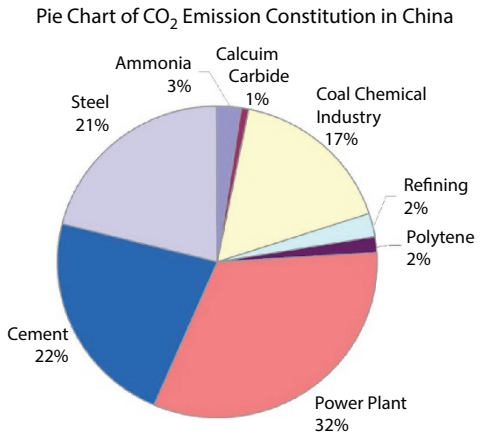

Figure 12.3 Pie chart of CO_2 emission constitution in China.

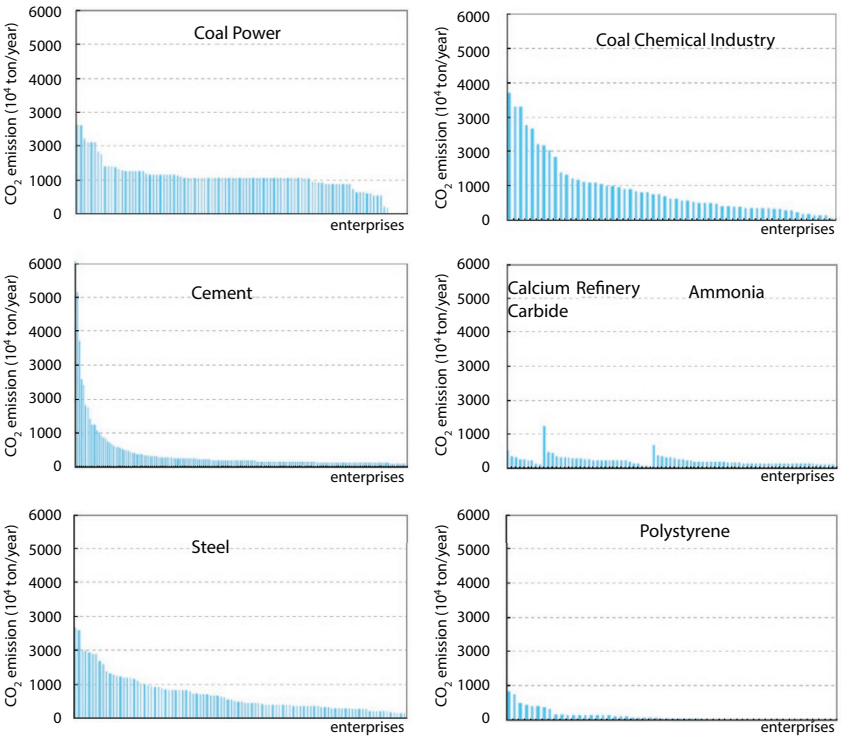

Figure 12.4 Distributions of CO_2 Emissions of eight kinds of enterprises in China.

chemical, synthetic ammonia and calcium carbide. For Huabei Oilfield, Jidong Oilfield, and Dagang Oilfield, there are more medium concentration sources like polyethylene and low concentration sources like cement and electric power enterprises, while Daqing Oilfield and Jilin Oilfield in northeastern China are mainly surrounded by emission sources of low concentration, including thermal power plants, refineries and iron and steel enterprises [10].

12.2.5 Characteristic Comparison Between Projects in China and Abroad

Among the world's large-scale comprehensive CCUS projects in operation and implementation (under construction) in recent years, all the emission sources of the items in operation are high concentration industries like natural gas treatment, chemical fertilizer production and syngas. For the execution items, CO_2 are captured from power plants and

Figure 12.5 Distributions of carbon sources in China.

hydrogen production. For planning projects, capture targets extended to steel, cement, kerosene, chemical and other industries. The project scale is 0.4-8.5 million tons per year, mostly more than one million tons per year. The distance of transportation is 0-315 kilometers, and most of which are more than 100 kilometers. As for the sequestration type, 62.5% of the projects in operation and execution are EOR projects, while the proportion of CO_2-EOR items in planning projects is smaller, accounting for 46%. The number of saline layer sequestration projects has increased [11].

Compared with international items (see Table 12.1), there are less whole-industry-chain CCUS projects which are in operation and execution in China. Their scales are smaller, while the capture targets are relatively monotonous. Pipeline transportation of long distance is hardly used. CO_2 captured is mainly from the food and chemical industry and saline layer sequestration items are less.

Table 12.1 Characteristic comparison between foreign and Chinese projects.

Type	Abroad	China
Whole-Industrial-Chain Project	More whole-industrial-chain projects	More single-section projects
Scale of Project	Most are more than 10^6 ton/year.	• The scales of projects in operation and under construction are relatively small (3,000-120,000ton/year). • Scales of the planning projects would reach to 1-5*106 ton/year.
Captured Object	• Emission sources of projects in operation and under construction are from natural gas treatment, fertilizer production and syngas which are high concentration. • For executing projects are from power plants and hydrogen production companies. • For the planning projects, categories of captured objects expanded to steel, cement, kerosene and chemical industry.	• Captured objects of projects in operation and under construction come from power plants and separated natural gas. • For the planning projects are from power plants and coal liquefaction.

(*Continued*)

Table 12.1 Characteristic comparison between foreign and Chinese projects. (*Continued*)

Type	Abroad	China
Transportation	Most items are greater than 100 km, and the longer one is up to 315km.	• Pipeline transport only are used in Jilin among all projects in operation and under construction. The distance is 25km. • In the planning projects, the long distance of pipeline transport could reach 100-200km.
Type of Sequestration	• The sequestration of projects in operation and under construction is EOR method (62.5%). • For the planning items, projects sequestration by saltwater layers increase (54%).	• For projects in operation and under construction, most of which are food and chemical utilization. EOR and saltwater layer sequestration are also adopted in an item separately. • For the planning projects, sequestrations of saltwater layers and abandoned oil reservoirs are considered.

12.3 Industry Patterns & Driving Modes

12.3.1 CCUS Industry Patterns at Home and Aboard

According to the combinations of capture, transportation, utilization and sequestration in the CCUS industry, three industry patterns at home and abroad can be divided. We can find the following features of each combination:

1. CU type: the capture - utilization combination, means that the captured CO_2 is directly used in the chemical, refrigeration and beverages. For instance, the 120,000-ton flue gas capture project in the Shanghai Shidongkou power plant, which is supported by the Huaneng Group, is used for the food industry.
2. CTUS type: the capture - transport - utilization - sequestration combination, such as the Enid fertilizer project in Oklahoma, US. The captured gas, amount of which is 68 million tons per year, transported by land-land pipeline used for CO_2 drive in oil reservoirs.
3. CTS type: the capture - transport - sequestration combination, like Norway's Sleipner project, undertaking in the North Sea, and captured CO_2 will be injected into saline layers.

On the part of the world's large-scale comprehensive projects, the United States, Canada and the Middle East are dominated by the CTUS-EOR industry pattern, while in Europe and Australia-New Zealand, CTS- saline layer and abandoned oilfields are the most. Among the 74 large-scale integrated projects, CTUS (CO_2-EOR) projects exceeded both in the number of items and capture amount in the projects in operation and execution. For planning ones, however, the number of CTS projects (sequestration of saline layers or abandoned oilfields) is in a dominant position.

In China, more attention is paid to the utilization of CO_2 for projects in operation and construction. Therefore, the CU model becomes the main industry pattern, while there are less whole-industry-chain projects with CUS or CTUS patterns. Among the planning of large-scale projects, the whole-industry-chain and permanent-sequestration items with CTUS or CTS patterns have increased [12, 13].

12.3.2 Driving Modes of CCUS Industry

Basically, public funds, national incentive policies, tax (carbon tax), mandatory emission reduction and carbon trading are five driving modes to the development of CCUS industry at present. The progress of CCUS technology will also bring about a lower cost, and further promote the development of the industry [14].

Incentive policy: investment and subsidy from government

Incentives include investments and subsidies from government or organizations, tax breaks for mining royalties, CO_2 price guarantees as well as government guarantees for investment loans and low-interest loans.

Financial support: developed countries have funded CCUS projects with $26-36 billion, most of which was provided to power systems. And CCUS industry projects in Canada, Australia and Europe are also eligible for funds. Several other agencies have also funded the CCUS programs.

Tax breaks for royalties: the 2008 Emergency Rescue Act in the US amended the tax credit for investment in advanced coal and coal gasification projects. For advanced coal capture and sequestration projects with emission reduction of more than 65%, the tax credit of $1.25 billon could be increased, up to 30% of its cost, while for coal gasification projects that reduce emissions by more than 75%, the number is $250 million.

CO_2 price guarantee: the Contracts for Difference (CFD), introduced in the draft of the UK Energy Act is a long-term transitional mechanism, used for different arrangements for CCUS, renewable energy and nuclear energy. In order to provide energy, a project always needs to receive a constant price model (also known as "exercise price") effectively through the protocol of CFD. If the exercise price is higher than the wholesale price of power market, the generator will receive funding for the difference; on the contrary, if the price in the power market is higher than the exercise price, the generator will compensate for the difference. Exercise price will be set at a level sufficient to support different types of technology.

Government guarantees for investment loans and low-interest loans are also incentives.

Improvement of carbon pricing mechanism

The improvement of carbon pricing mechanism includes carbon tax and carbon trading market.

Concerning the increase of global carbon dioxide emissions and the pressure on carbon taxation, the carbon tax system has become the main policy for developed countries to promote the emission reduction of

domestic enterprises. A carbon tax system is established to control greenhouse gas emissions, and on the other hand, carbon tax can provide a price signal for carbon emissions externalities.

The carbon tax system was first introduced in 1990 in Finland, followed by other countries like Sweden, Norway, the Netherlands, Denmark, Slovenia, Italy, Germany, Britain and Switzerland. In 2010, the National Development and Reform Commission (NDRC) and the Ministry of Finance jointly issued a special report on the Framework Design of China's carbon tax system and put forward a proposal for the levy of carbon tax.

Carbon trading, or greenhouse gas emissions trading, means a party of the contract can obtain a reduction amount of greenhouse gas emission by paying the other. Carbon trading can be divided into two sorts: one is quota-based trading, where buyers buy emission-reduction quotas under a "cap-and-trade" system. The other is project-based trading, where buyers buy emissions reductions from projects that prove to reduce greenhouse gas emissions like the clean development mechanism (CDM).

At present, many CCUS projects are in the stage of research and demonstration, the main drivers of which are the government's financial support and national incentive policies, as well as taxation or other factors. Mandatory emission reduction and carbon trading market might become the main driving factors when the industry moves from the stage of demonstration to commercial operation.

The progress of CCUS technology: a lower cost

The progress of CCUS technology itself can bring about a lower cost, and further promote the development of industry. The development of CCUS technology includes expansions of transport and sequestration, reduced capital costs and technological improvements. Early estimates of the experimental costs for small-scale projects are lower than those observed costs in subsequent large-scale applications. Due to the changes in design and improvements in the early state of commercial production, the cost always increases; but then will decrease with the more mature technology and the gained experience.

Measures to reduce the cost of CO_2 emission reduction include: expanding the scale of transport and sequestration, increasing the utilization; enhancing the financial capacity of CCUS chain, reducing investment risks, enhancing investors' confidence for projects; improving the capture technology and expanding the capture capacity, as well as improving the engineering design and performance of projects. Capture cost is the main component in cost of emission reduction. The study shows that the capture cost is 24% lower in the early stage of commercialization than in the stage of demonstration, and 34% lower in the stage of mature commercialization (see Table 12.2).

Table 12.2 Capture costs in each stage of development ($/tCO2).

Stage of development	PC-Coal	PC-Gas	Oxy	IGCC	Average	Rate of cost reduction
Demonstration (2013-2015)	107	84	105	82	95	
Early commercialization (2020)	79	61	77	70	72	24%
Mature commercialization (2030)	70	51	67	61	62	34%

12.4 Composition & Factors of CO_2 Source Cost

The CO_2 source cost mainly includes capture cost, compression cost and transportation cost. At present, there are three kinds of estimation of CO_2 capture investment in power plants and industrial enterprises: engineering quantity, regression and scale index (scale factor). The method of scale index was used in this article, when the compression and transportation costs were calculated through the method studied by David L. McCollum and Joan M. Ogden at the University of California, Davis, USA [15].

Factors influencing CO_2 source cost include CO_2 flow, emission concentration and transportation distance.

For capture cost, the main factors are emission concentration and flow rate. When the concentration is at a high level, the capture cost is low, and vice versa. At the same concentration, the capture cost decreases with the increase of CO_2 flow rate. The influence degree, however, varies with the concentration. The effect of flow rate is more obvious when CO_2 concentration is low. This is shown in Figure 12.6a.

As for compression cost, the main factors are CO_2 flow and transportation distance (which is at a limit of 50 km). The trend that CO_2 flow affects the cost appears as: in some flow range, the compression cost decreases with the rise of CO_2 flow. When the flow reaches a certain scale, the compression chains need to be increased because of the rise of the compression power, which improve costs of investment and operation, thus cause a jump of the curve. This is shown in Figure 12.6b.

For transportation cost, the main influence factors are transportation distance and CO_2 flow. Transportation cost increases in power function with the rise of distance and decreases in power function with the increase of CO_2 flow. The longer the distance is, the faster the decreasing speed is. Transportation costs are shown in Figure 12.7.

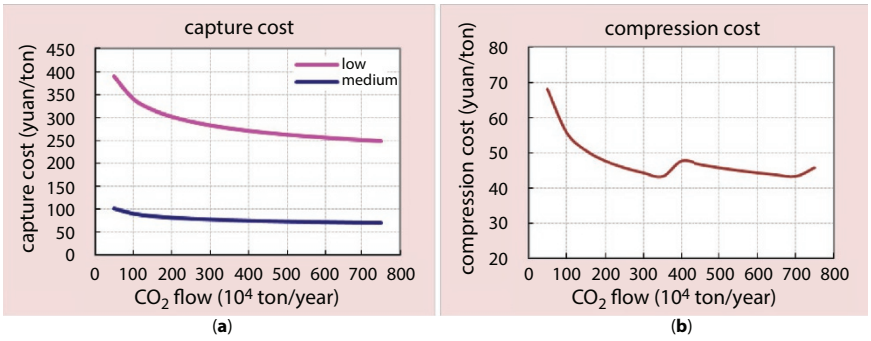

Figure 12.6 Relationship between (a) capture cost, (b) compression cost and CO_2 flow.

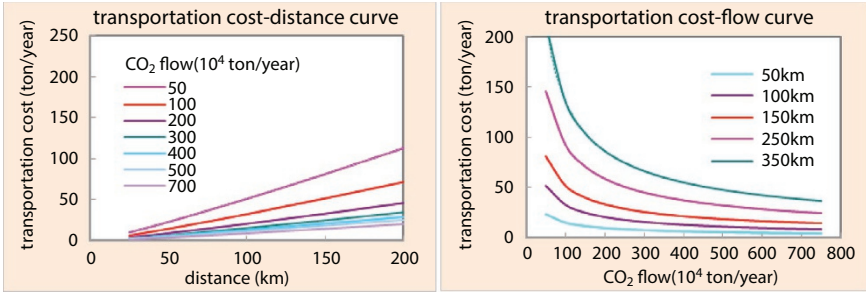

Figure 12.7 Relationship between transportation cost and distance, CO_2 flow.

For CO_2 sources of high concentration, compression cost has a dominant place of 90%, with the cost about 54~83 yuan per ton; for medium CO_2 concentration the main part is capture cost, accounting for about 60%, and compression costs accounted for about 35%, while most of the cost at 125~227 yuan per ton. As for CO_2 source of low concentration, capture cost is accounted for 80%, while the source cost is 300~400 yuan per ton (see Figure 12.8).

The bearing capability for CO_2 is lower than the source cost in most oilfields, thus the gap between them needs to seek technology, policies, market and other ways to fill in order to forge ahead and continuously develop. According to the above results, two means could be considered to improve the situation gradually [16, 17].

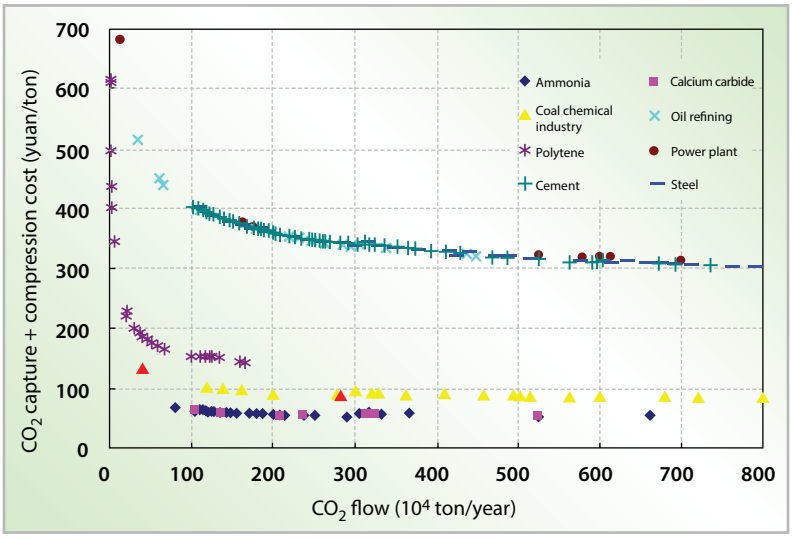

Figure 12.8 Estimated costs of different kinds of emission sources.

On the one hand, the CO_2 source could be taken into account for the tendency of the future cost reduction to fill the cost blank. The CO_2 source cost reduction mainly refers to the capture cost of the origin, thus for the supply source which owns origins of low concentration and high capture cost, the effect on increasing the financially feasible projects of oil areas is obvious. If the cost of CO_2 source is reduced by 20% ~30% or even lower, the number of financially feasible oilfields could be greatly increased.

On the other hand, policy benefits could be considered throughout the links of sequestration in reservoirs, including reducing resource tax or granting certain sequestration subsidies. Then the development scales of CCUS projects of enterprises could be expanded in a great way, especially at low oil price. For some oil areas, it is necessary to rely on policy support. The CO_2 bearing capacity of each oil field is evaluated with the assumption that resource tax exemption and granting sequestration subsidies respectively.

If the CO_2 source cost is reduced, and the preferential policies such as exemption of resource tax or the granting of sequestration subsidies are adopted, the supply cost could be decreased from sources; meanwhile the capacity cost in sequestration is also able to be improved, so that the number of financially feasible oilfields can be greatly increased.

12.5 Conclusions

1. The types, distributions, scales and features of CCUS projects in China and abroad are compared and analyzed. The target of capture has expanded from power plants and natural gas processing to steel, cement, kerosene, fertilizers, and hydrogen production. CCUS projects are gradually turning from single-section items to whole-industry ones, of which scales become larger and larger with a broad prospect.
2. According to the combination of capture, transportation, utilization and sequestration of CCUS industry, the CCUS industry models at home and abroad can be divided into three types: CU, CTUS, and CTS. The five industry driving modes include government and public funds, state incentives, taxes (carbon tax), mandatory emission reduction and carbon trading.
3. Cost of CO_2 sources is comprised of three main parts: capture, compression and transportation, all of which are affected by the scale of capture. The cost of capture is also

related to the concentration of emission source. For the type of high CO_2 concentration, the expense of compression takes the lead in accounting, and for the low CO_2 concentration type is capture cost. For most oil fields, the tolerance of CO_2 is lower than source cost, and ways like technology, policies and markets are needed to fill the gap.

References

1. CCUS in China: Towards Market Transformation, The Climate Group, 2011.
2. Technology Roadmap - Carbon Capture and Sequestration in Industrial Applications, International Energy Agency (IEA), 2011.
3. CCUS in China: 18 Hot Issues, The Climate Group, 2011-04.
4. Cost and Performance Baseline for Fossil Energy Plants, DOE/NETL, November 2010.
5. Cost and Performance of Carbon Dioxide Capture from Power Generation, Work Report, IEA, 2011.
6. The Global Status of CCS, Global CCS Institute, 2013.
7. Carbon Capture & Sequestration: Assessing the Economics, McKinsey & Company, September 2008.
8. Raveendran, S.P., The Role of CCS as a Mitigation Technology and Challenges to its Commercialization, MIT Technology and Policy Program, 2013.
9. Piessens, K. and Laenen, B., Policy Support System for Carbon Capture and Sequestration, Belgian Science Policy, September 2008.
10. Kemp, A.G. and Kasim, S., The Economics of CO2-EOR Cluster Developments in the UK Central North Sea/Outer Moray Firth, North Sea Study Occasional Paper, No. 123, January, 2012.
11. Carbon Dioxide Enhanced Oil Recovery, NETL, March 2010.
12. CCS Cost Reduction Taskforce, The UK Carbon Capture and Sequestration Cost Reduction Task Force, 2013.
13. Technology Roadmap-Carbon capture and sequestration, IEA, 2013.
14. Carbon capture and sequestration in industry application-technology synthetic working report, UNIDO, November 2012.
15. McCollum, D.L. and Ogden, J.M., Techno-Economic Models for Carbon Dioxide Compression, Transport, and Sequestration & Correlations for Estimating Carbon Dioxide Density and Viscosity, UCD-ITS-RR-06-14, 2006.
16. Wang, Y., *Carbon finance: Global vision and distribution in China*, China Economic Publishing House, 2010-08-04.
17. De Boer, D. and Kater, H., Carbon Price Research in China, China Carbon Forum, 2013.10.

13

CO_2 Movement Monitoring and Verification in a Fractured Mississippian Carbonate Reservoir during EOR at Wellington Field in South Kansas

Yevhen Holubnyak[1,2]*, Eric Mackay[2], Oleg Ishkov[2] and Willard Watney[1]

[1]Kansas Geological Survey, Lawrance, KS, USA
[2]Heriot-Watt University, Edinburgh, Scotland, UK

Abstract

This study benefits from the availability of unique field data on tracking of injected CO_2 plume movement in the reservoir using results of reservoir fluid chemical composition monitoring, CO_2 plume and injection impact delineation, and studying effects of faults and naturally occurring fractures on fluid movement gathered from a field located in Kansas, USA. Approximately 20,000 metric tons of CO_2 were injected in the top sequence of the Mississippian age carbonate reservoir at Wellington Field in South Central Kansas to evaluate potential for CO_2 Enhanced Oil Recovery (EOR) and to estimate potential of transitioning to geologic CO_2 storage through EOR. This paper focuses on tracking of CO_2 plume movement in the reservoir using results of reservoir fluid chemical composition monitoring, CO_2 plume and injection impact delineation, and studying effects of faults and naturally occurring fractures on fluid movement at the Wellington Field. We found that one of the identified and mapped faults worked as a partial barrier to CO_2 movement and the associated damage zone and fracture network performed as a flow conduit, determining CO_2 flow paths.

Keywords: CO_2 EOR, CO_2 geologic storage, CO_2 plume delineation, reservoir fluids movement, carbonate reservoirs, MVA, mid-Continent USA

**Corresponding author*: eugene@kgs.ku.edu

Ying Wu, John J. Carroll, Mingqiang Hao and Weiyao Zhu (eds.) Gas Injection into Geological Formations and Related Topics, (217–226) © 2020 Scrivener Publishing LLC

13.1 Introduction

Carbonate reservoirs are notoriously complex and very difficult to characterize and study. The main objectives of this study are: to determine whether or not geochemical interactions of injected carbon dioxide (CO_2) gas with formation minerals and brine have any effect on fluid flow in the reservoir and Enhanced Oil Recovery (EOR) performance in general; to investigate whether or not brine geochemistry signatures can be used to identify potential field compartmentalization; and to evaluate potential impact of mineralization on CO_2 storage.

This study benefits from the availability of unique field data on tracking of injected CO_2 plume movement in the reservoir using results of reservoir fluid chemical composition monitoring, CO_2 plume and injection impact delineation, and studying effects of faults and naturally occurring fractures on fluid movement gathered from a field located in Kansas, USA.

Approximately 20,000 metric tons of CO_2 were injected in the top sequence of the Mississippian age carbonate reservoir at Wellington Field in South Central Kansas to evaluate potential for CO_2 Enhanced Oil Recovery (EOR) and to estimate potential of transitioning to geologic CO_2 storage through EOR.

Collected organic and inorganic components measured concentration data from the field will be organized and compared to existing laboratory and field results; geochemical modelling will be performed at various scales, including equilibrium, kinetic rate, and field scale reservoir modelling; results will be compared with existing data from several other carbonate reservoirs, including Weyburn CO_2 EOR, Permian Basin floods, and others; and core flood experimental results from the Wellington field and other projects will be compared with field observations and modelling. Once geochemical data are analyzed, it will be important to compare field performance and flow patterns with observed geochemical changes and attempt to find correlations and quantify impact of geochemical reactions on field performance.

Recent studies [1–3] and indications from industry [4] verify the importance of Kansas as a central region for a future of Carbon Capture and Storage (CCUS) in Midwest USA. When a source of CO_2 becomes available in the region, many other reservoirs that are very similar to the Wellington Field with 250-350 million barrels of oil to be recovered [1] will benefit from current research findings.

13.2 Wellington Field Faults and Fractures

Based on core observations, Formation Micro Imaging (FMI), dipole-dipole sonic logs, and regional earthquake focal mechanism analysis, the fracture intensity for a selected upper 35 m (115 ft) of Mississippian reservoir was present but estimated as low. Additional well test analysis and 3D seismic analysis reveal at least 12 vertical faults with NNE orientation in the Wellington Field reservoir and adjacent Anson Bates Field [5].

Previous investigations by [6] and [7] mapped reservoir thickness and porosity distribution at Wellington field. Later, 3D P-wave reflection seismic quantification of azimuthal anisotropy in the Mississippian cherty dolomite was performed, using Amplitude Variation with Azimuth (AVAZ) pre-stack method, which is linked to the subsurface stress field, it was possible to map fracture density and orientation in the Mississippian reservoir (Figure 13.1) [8].

Azimuthal analysis of the 3D P-P wave data collected in Wellington provides a sense of the anisotropy in the top of the Mississippian and Arbuckle. A defining feature observed in both is a fault that trends northeast through the injector/producers pattern between KGS 2-32 CO_2 injector and producer well #62 (Figure 13.1). The fault is associated with discrete facies changes across the field described in [6, 7]. The perceived fracture pattern surrounding the fault in the Arbuckle is also within the range of σ_H and

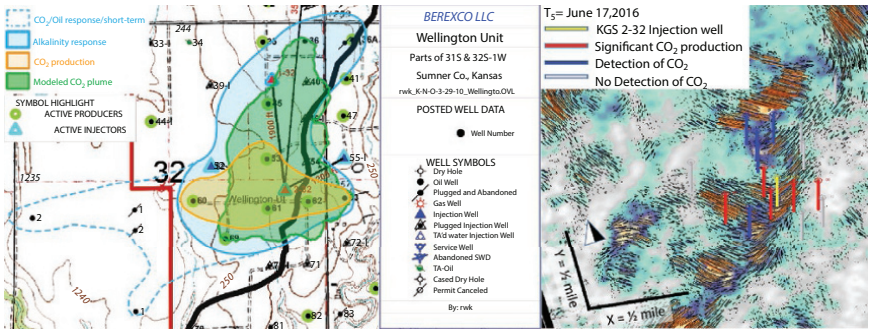

Figure 13.1 (Left) Wellington field maps (left) showing well locations and active CO_2 production (orange outline) versus observed alkalinity increase (blue outline) and anecdotal evidence of short-term CO_2 breakthrough (dashed blue line) versus predicted by simulations CO_2 plume (green outline), the solid black line outlines mapped fault; (Right) discrete fracture network model [8] illustrating faults and associated damage zone/fractures at Wellington Field.

fracture orientations as determined from [8]. Results are consistent with observed rock properties known to cause detectable variations in seismic data; fracture and maximum horizontal stress direction. Large-scale features such as faults are indirectly observed by its effect on the surrounding material. Fractures observed in FMI logs are consistent with patterns observed in the Wellington field seismic azimuthal analysis.

13.3 EOR Field Operations and Production/ Injection History

The CO_2 was transported to the site in trucks in liquid state at a pressure of approximately 17 bar and temperature of -24°C in a liquid state with each truck delivering 20 tons of CO_2. Surface facilities consisted of: seven portable tanks that could hold up to 70 tonnes of cooled and pressurized CO_2 delivered by tracks; pump system; programmable logic controller that can manipulate the control valve in order to not exceed the maximum specified flow rate and to ensure that the bottom hole pressure in the injection well does not exceed the maximum allowable pressure. Total of 1,101 truckloads, 19,803 metric tons, average of 120 tonnes per day were delivered over the course of injection that lasted from January 9 to June 21, 2016.

After cessation of CO_2 injection, KGS 2-32 well was converted to a water injector and it currently continues to operate as such. CO_2 EOR progression in the field was monitored weekly with fluid level, temperature, and production recording, and formation fluid geochemical composition sampling. As a result of CO_2 injection, the observed incremental average oil production increase was about 68% (Figure 13.2), with only about 18% of injected CO_2 produced back.

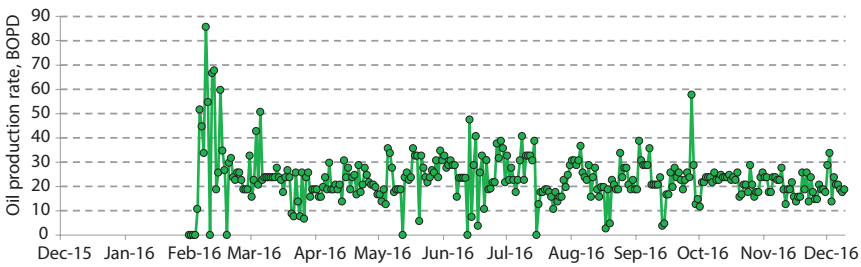

Figure 13.2 Oil production history for a CO_2 EOR flood period of December 2015 to December 2016 at relevant tank battery.

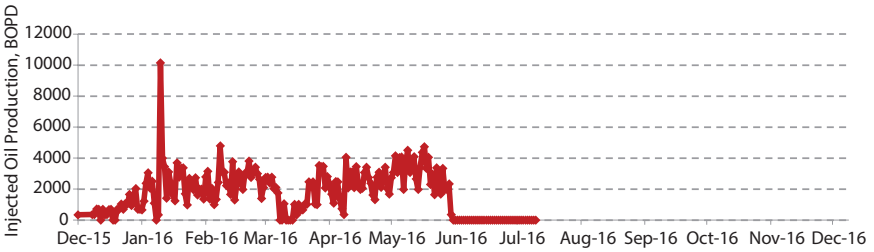

Figure 13.3 CO_2 injection schedule for a CO_2 EOR flood period of December 2015 to December 2016.

[9] explain field operations in more details. The CO_2 injection schedule is provided in (Figure 13.3). Note that the first CO_2 injection test was performed in mid-December, 2015, where a few hundred tonnes of CO_2 were injected. On January 9, 2016, regular operations started. In mid-March, 2016, CO_2 injection stopped for field maintenance for several days and resumed until full stop on June 21, 2016.

13.4 Geochemical Monitoring Survey Setup

Geochemical water analysis of organic and inorganic components was performed in order to understand if this method could be used as an early CO_2 detection system, as a plume location and containment method, and in order to understand a degree of impact of CO_2 on mineral composition, detect changes in water and rock geochemistry as a result of injection. Along with geochemical survey, pressure and production data was recorded at wells and tank batteries.

Wellington Field reservoir does not have gaseous component in production. Gas separating units are not installed normally on wells and gas pressure is negligible. Therefore, the CO_2 breakthrough could be easily detected and recorded by installing gas separating units on each well where CO_2 breakthrough was anticipated and on tank batteries.

Baseline data for chemical composition of reservoir brine was recorded on several occasions prior to CO_2 injection: in 2011 and 2012 during well drilling operations at the start of a project (characterization phase), in 2015 as a part of background geochemical survey and as a part of KGS 2-32 CO_2 injector drilling operations, and in 2016 as a repeat background survey. In total, 52 wells and two tank batteries were sampled as a part of baseline survey. The range for baseline pH was recorded on May 12, 2015, and on January 20, 2016, as 4.9 min and 6.5 max with 5.5 median. The range for

baseline alkalinity was recorded on May 12, 2015, and on January 20, 2016, as 31 mg/l min and 152 mg/l max with 75 mg/l median.

Based on reservoir simulations, wells surrounding CO_2 injector were grouped in three areas: two inner circles with the radiuses of 182 m and 460 m. Wells within first radius were sampled weekly during the course of CO_2 injection and after injection commenced in June 2016 until January 2017 were tested semi-monthly until mid-2017. Wells within radius of 1 km around KGS 2-32 were sampled after initial breakthrough at the wells of the first inner circle; however, sampling interval for these wells was chosen according to flood performance and was not strictly set from the beginning of the injection. In total, sampling and water chemistry analysis of 17 wells surrounding CO_2 injector well were performed.

Additional water chemistry analysis on 17 selected for sampling wells was performed by contracting Baker and Hughes Oilfield Services in order to check for possible errors and to compare results from two separate laboratories.

Total dissolved solids and pH measurements were analyzed in the field and alkalinity analysis was performed in the lab shortly after sample arrival (within 2-3 days). These results were used as an early detection for CO_2 arrival at well locations. The geochemical survey design and methodologies were outlined in more detail in [9].

13.5 Geochemical Monitoring Survey Observations

The CO_2 gas production registered by gas separating units was recorded at only 5 wells (Figures 13.1 and 13.4). Well proximity also did not assure CO_2 breakthrough: wells to the west of the injector and to the west of the described fault produced CO_2 and experienced oil production improvement within weeks since the start of injection. Wells to the west of the injector and across the mapped fault experienced CO_2 breakthrough only several months after the start of injection and oil production improvements were marginal.

Continuous geochemical monitoring showed that the alkalinity has noticeably increased (Figure 13.5) and pH has decreased in 17 of the continuously monitored wells and some randomly sampled wells around the CO_2 injector. The alkalinity increase was most noticeable at 5 wells with CO_2 breakthrough and recorded production: well 53 recorded a maximum of 622 mg/l, while other wells had maximums at 583, 580, 307, and 229 mg/l (Figure 13.5). Alkalinity increases correlated with produced CO_2 volume. Wells to the west of a fault had higher production volumes and alkalinity increases.

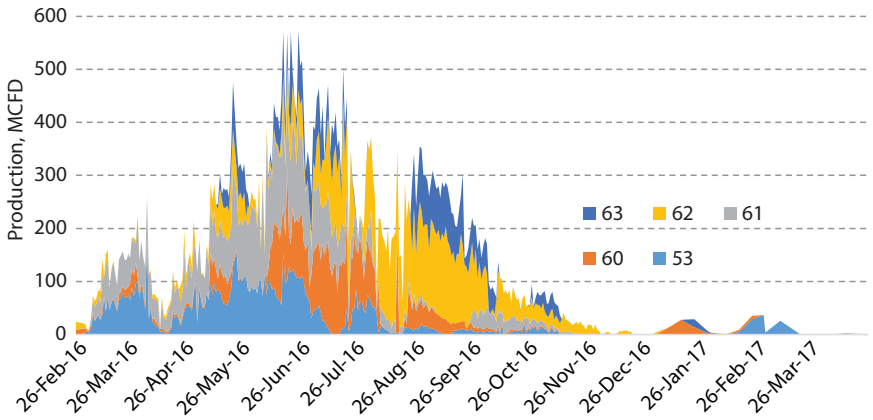

Figure 13.4 Stacked area plot of metered CO_2 production at installed gas separators through time.

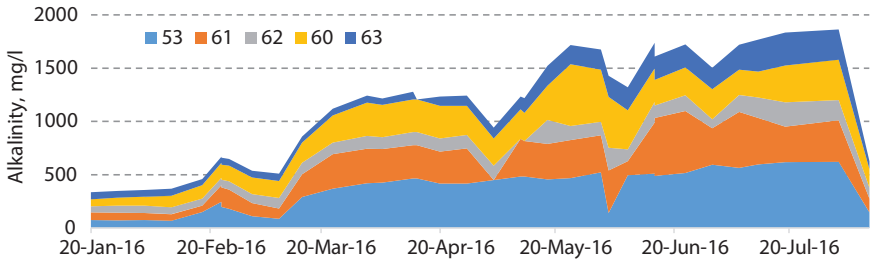

Figure 13.5 Stacked area plot of alkalinity response at wells with CO_2 breakthrough and active long-term production.

Alkalinity increases and pH decreases were also recorded at other wells beyond the zone with CO_2 production (Figure 13.6). Wells 45 and 69 observed the most noticeable increase in alkalinity: 165 and 109 mg/l respectively. Alkalinity departures from a baseline and CO_2 gas detections were recorded as far away as well 136A to the north of CO_2 injector. Wells 1 and 2 to the South and South-West of CO_2 injector recorded a CO_2 pressure for a brief period of one or two days and were reported by a neighboring operator (Figure 13.1). After this initial breakthrough at wells 1 and on in mid-March, wells were monitored but no indications of CO_2 pressure nor alkalinity increases were detected; however, these wells did report oil production increase. Alkalinity increase could be observed on tank batteries as well and it is correlated with oil production increase.

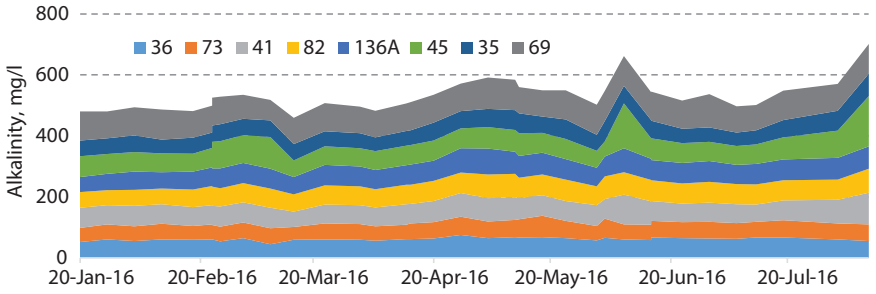

Figure 13.6 Stacked area plot of alkalinity response at wells without CO_2 breakthrough and without active long-term production.

Although the statistical modeling is yet to be completed, it is safe to assume that alkalinity increase in produced brine is correlated with CO_2 injection and movement in the reservoir; however, pH decrease patterns require statistical modeling to be used as indicators. In addition, alkalinity increases seem to correlate with oil production increases (Figures 13.7 and 13.8); however, statistical modeling will better verify this hypothesis.

Based on this preliminary analysis the CO_2 plume was delineated. The reservoir modeling forecast [9] could be interpreted as in agreement with field data; however, more analysis on CO_2 concentrations in the reservoir is desirable.

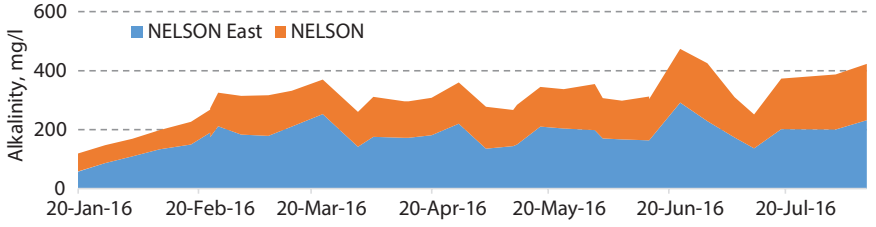

Figure 13.7 Stacked area plot of alkalinity response at relevant field batteries.

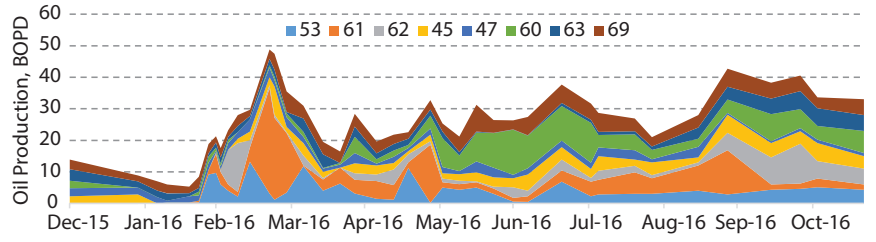

Figure 13.8 Stacked area plot of oil production at individual wells.

13.6 Conclusions

CO_2 movement seem to correlate with mapped faults and discrete fracture network (Figure 13.1). Based on presented observations, it is hypothesized that CO_2 movement in the reservoir was affected by (1) major structural elements and associated depositional and other changes in reservoir properties, and (2) fluid movement in the fracture network. The first phenomenon explains fluid delivery across the fault and the second phenomenon explains the discrepancy between actual CO_2 production and observed elevated alkalinity and decreased pH in the produced brine.

The major fault that is mapped in between CO_2 injector and producer 62 to the East acts as a partial barrier to fluid flow and associated fracture network enhances fluid flow and helped to deliver CO_2 to the wells along and to the West of a fault. Fractures, acting as conduits to CO_2 flow, could not, however, deliver large volumes of CO_2 to the wells beyond the "inner circle" of wells. Therefore, the fracture flow could not be directly translated into matrix flow. The preliminary volumetric calculations support this explanation of CO_2 movement and concentrations at Wellington carbonate reservoir.

13.7 Acknowledgments

The work was supported by the U.S. Department of Energy (DOE) National Energy Technology Laboratory (NETL) under Grant DE-FE0006821, W. L. Watney, J. Rush, and Y. Holubnyak Joint PIs. Project is managed and administered by the Kansas Geological Survey/KUCR at the University of Kansas and funded by DOE/NETL and cost-sharing partners.

13.8 Disclaimer

or favoring by the United States Government or any agency thereof. The views and opinions of authors expressed herein do not necessarily state or reflect those of the United States Government or any agency thereof.

References

1. Crabtree, B. and Christensen, J., CO_2-EOR Potential in the MGA Region, Great Plains Institute for Sustainable Development Report, 2012.
2. Edwards, R. and Celia, M., Infrastructure to enable deployment of carbon capture, utilization, and storage in the United States. *Proc. Nat. Acad. Sci.*, 115, 38, E8815–E8824, Sep 2018, doi: 10.1073/pnas.1806504115.
3. Dubois, M. and McFarlane, D., Economics for CO_2 capture, compression, and transportation in the Mid-Continent. *Second CCUS for Kansas forum, co-sponsors: Kansas Geological Survey and State CO_2-EOR Work Group*, University of Kansas, Lawrence, Kansas, July 26, 2018, 2018.
4. Nemec, R., *Oxy, White Energy Assessing Two West Texas CO_2 Projects, Natural Gas Intelligence (NGI) Daily*, June 21, 2018, https://www.naturalgasintel.com/articles/114802-oxy-white-energy-assessing-two-west-texas-CO_2-projects.
5. Schwab, D.R., Bidgoli, T.S., Taylor, M.H., Characterizing the potential for injection-induced fault reactivation through subsurface structural mapping and stress field analysis, Wellington Field, Sumner County. *J. Geophys. Res.: Solid Earth*, 2017.
6. Fadolalkarem, Y., Pre-Stack Seismic Attribute Analysis of the Mississippian Chert and the Arbuckle Group at the Wellington Field, south-central Kansas. University of Kansas master's thesis, 2015.
7. Sirazhiev, A., Seismic Attribute Analysis of the Mississippian Chert at the Wellington Field, south-central Kansas. University of Kansas master's thesis, 2012.
8. Graham, B.L., Haga, L.N., Nolte, K.A., Tsoflias, G.P., Watney, W.L., Fracture Mapping and Feasibility of Monitoring CO_2 in situ From Seismic Data at the Mississippian Carbonate Reservoir, Wellington Oil Field, South-Central Kansas, in: *DOE NETL Mastering the Subsurface Through Technology Innovation, Partnerships and Collaboration: Carbon Storage and Oil and Natural Gas Technologies Review Meeting*, Pittsburgh, PA, August 1-3, 2017, 2017.
9. Holubnyak, Y., Watney, W., Hollenbach, J., Rush, J., Fazelalavi, M., Bidgoli, T., Wreath, D., Pilot Scale CO_2 EOR at Wellington Field in South Central Kansas. *Soc. Pet. Eng.*, April 14, 2018, doi: 10.2118/190308-MS.

14

Simulation Study On Carbon Dioxide Enhanced Oil Recovery

Maojie Chai* and Zhangxin Chen

Department of Chemical and Petroleum Engineering, The University of Calgary, Calgary, Alberta

Abstract

Carbon dioxide injection, with the development of carbon dioxide capture technology, is regarded as a promising method for enhanced oil recovery (EOR). Miscible flooding of carbon dioxide EOR theoretically provides a high recovery factor. However, there exists a minimum pressure requirement to achieve miscible flooding, which is minimal miscible pressure (MMP).

The study in this paper investigates the carbon dioxide flooding based on simulation. The feasibility of reducing minimal miscible pressure by enriching the injected carbon dioxide is first analyzed through phase behavior simulation. Then, a carbon dioxide flooding test has been simulated and compared with real laboratory data. The sensitive parameters in carbon dioxide flooding were ranked in sensitivity analysis and updated through inverse history matching. The updated relative permeability curves not only reflect a residual oil saturation reduction due to the carbon dioxide interacting with a fluid but also reduce the uncertainty of measurement in laboratory tests.

Keywords: Carbon dioxide flooding, minimal miscible pressure, sensitivity analysis, history match

14.1 Introduction

After conventional primary and secondary oil recovery processes of reservoir fluids, there is usually a large amount of oil trapped and unrecovered in a reservoir. This residual oil is a target for enhanced oil recovery (EOR) techniques that contribute and help overcome the ever-increasing energy

**Corresponding author*: maojie.chai@ucalgary.ca

Ying Wu, John J. Carroll, Mingqiang Hao and Weiyao Zhu (eds.) Gas Injection into Geological Formations and Related Topics, (227–244) © 2020 Scrivener Publishing LLC

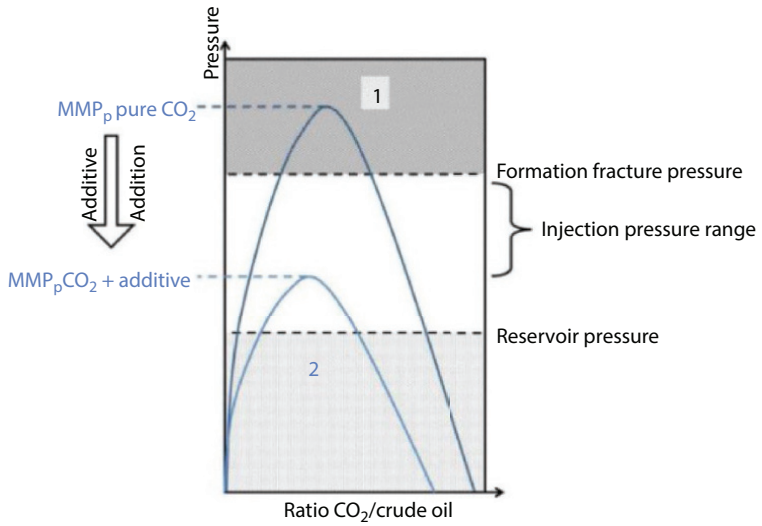

Figure 14.1 Schematic view of the miscibility gap of the system CO_2/crude oil and the influence of additive addition on the miscibility gas, with the MMP [3].

demand in the future. Secondary recovery, water flooding, for example, can only reach a 50% recovery factor; then production comes to tertiary oil recovery or enhanced oil recovery [1]. Some EOR methods are conducted by injecting solvent or gas, among which CO2 EOR is one possible method of the tertiary oil recovery. Carbon dioxide, as a greenhouse gas, has always aroused public attention and requires treatments like carbon dioxide storage. Owing to carbon dioxide's physical properties, carbon dioxide can form miscible flooding with crude oil underground under certain conditions. In this way, carbon dioxide has been proven and utilized as a good solvent for CO2 miscible flooding. With miscible flooding, an interface force is approximately zero and thus the recovery factor can be dramatically increased and reach over 90% [2]. One limitation of the CO2 EOR process is pressure; the CO2 miscible flooding can only be feasible when the reservoir pressure is above the minimal miscible pressure which is also called MMP (see Figure 14.1). The MMP can be experimentally estimated or simulated. For those reservoirs whose pressure is below MMP, the CO2 EOR process may not promise a high recovery rate and economic production.

Also, in most reservoirs, the minimum miscible pressure when injecting pure carbon dioxide is above the formation fracture pressure, which is not preferred in a real case. The idea is to look for a possible and economical method for reducing the system minimal miscible pressure and, finally, reaching the miscible flooding.

Based on a simulation method, this paper studies reducing the miscible pressure of carbon dioxide injection and updating the sensitive parameters through inverse history matching during the carbon dioxide injection.

14.2 Phase Behavior Study

Common miscible flooding includes first contact miscible and multiple contact miscible. Related phase diagrams are illustrated below.

Figure 14.2 (a) illustrates the first contact miscible flooding phase behavior. The oil sample lies closer to the side of the lighter components (C1-6). The line contact with pure carbon dioxide and the oil sample illustrates the mixture of these two fluids. From the phase diagram, a two-phase envelope lies on the left side of the triangle envelope. In case a), the mixture of carbon dioxide and the oil sample will not separate into two phases. This condition is called first contact miscible. However, the pressure required for first contact miscible is usually too high to reach or greatly above the formation fracture pressure. In a real case, it is rare to achieve carbon dioxide first contact miscible flooding.

In Figure 14.2 (b), the oil sample lies between the light components (C1-6) and heavy component (C7+). The mixture of carbon dioxide and the oil sample will fall into the separate process. However, when mixing, the fluids will be separated into gas and liquid. The gas including injected carbon dioxide and intermediate component (C2-6) always moves faster than the separated liquid in a reservoir. The enriched gas will contact with the original oil and finally become miscible. This process is called a vaporized and condensate process or multiple contact miscible [4]. The multiple contact miscible pressure is less than the first contact miscible pressure.

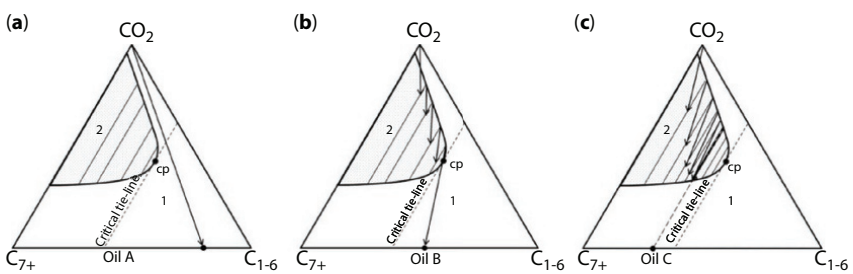

Figure 14.2 Schematic view of the phase triangles of CO_2 flooding process at constant temperature and pressure. (a) First contact miscible, (b) multiple contact miscible, and (c) immiscible [3].

However, the multiple contact miscible pressure is still not easy to reach for many reservoirs or the MMP is greater than the formation fracture pressure [5]. Thus, a reduction in multiple miscible pressure is necessary to promise the feasibility of carbon dioxide flooding projects.

In Figure 14.2 (c), more heavy components exist in the oil sample compared with the previous two samples. The mixture of carbon dioxide always lies into the two-phase zone. Even when the vaporization occurs and injected carbon dioxide is enriched, the mixture still lies in the two-phase envelope. This implies that the carbon dioxide miscible flooding is not feasible for heavy oil. However, the vaporization characterization of carbon dioxide has been applied for some heavy oil or bitumen recovery (VAPEX).

14.3 Simulation Study

14.3.1 Fluid Sample Properties

The fluid sample composition and related PVT lab data in this study is provided by CMG. Fluid sample components and mole fractions are shown below.

PVT properties are general terms to express the phase behavior of a reservoir fluid as a function of pressure and temperature. Basic fluid PVT tests include saturation pressure, separator, constant composition expansion, differential liberation, and swelling tests.

In the simulation study, the components of the reservoir fluid are first lumped into several pseudo components and the difference between the lumped fluid phase envelop and unlumped fluid phase behavior is minimized [6, 13]. Then an equation of state will be tuned by regression of different PVT test results to reflect the phase properties of this fluid.

14.3.2 Phase Behavior Simulation

In the simulation study, CMG-Winprop is used to characterize the reservoir fluid by using lab data. The purpose of this part is to use lab data to characterize reservoir data by using the CMG-Winprop phase simulator.

Winprop is an equation of state-based fluid behavior and PVT modelling package. In Winprop, laboratory data for fluids can be imported and an equation of state can be tuned to match its physical behavior [7]. The supplied data for reservoir oil contains a description of associated single carbon numbers and their fractions, and saturation pressure, separator,

Table 14.1 Fluid sample components and mole fractions.

Components	Mole fractions	Components	Mole fractions
CO2	0.011829992	C14	0.014488207
N2	0.001609801	C15	0.013373729
CH4	0.115410332	C16	0.010649451
C2H6	0.060057952	C17	0.00903965
C3H8	0.064763523	C18	0.009658805
IC4	0.022165718	C19	0.008172835
NC4	0.047551038	C20	0.005324726
IC5	0.032815169	C21	0.003962586
NC5	0.037025418	C22	0.003219602
FC6	0.065135016	C23	0.002352786
C7	0.084204963	C24	0.001981293
C8	0.098940832	C25	0.001857462
C9	0.078384914	C26	0.001857462
C10	0.051513624	C27	0.001981293
C11	0.031329199	C28	0.002105124
C12	0.021298902	C29	0.002105124

constant composition expansion, differential liberation and swelling test results. The full composition is given in Table 14.1.

Due to the complexity of numerical simulation methods, it is not feasible to run models with 30 components. As such, a method for combating long run time is to lump similar components together into pseudo components, as shown below in Table 14.2. However, when lumping, the interaction between those components in one lump is not considered. Thus, the next step in a simulation study is to use regression to tune the equations of state to match the laboratory data.

In the regression part, properties of lumped compositions are tuned, such as critical pressure and temperature, interaction coefficient exponents and volume shift parameters, in order to match the provided lab data

Table 14.2 Lumped pseudo components.

1st pseudo component	CO2
2nd pseudo component	N2-CH4
3rd pseudo component	C2H6-NC4
4th pseudo component	IC5-C07
5th pseudo component	C08-C12
6th pseudo component	C13-C19
7th pseudo component	C20-C30+

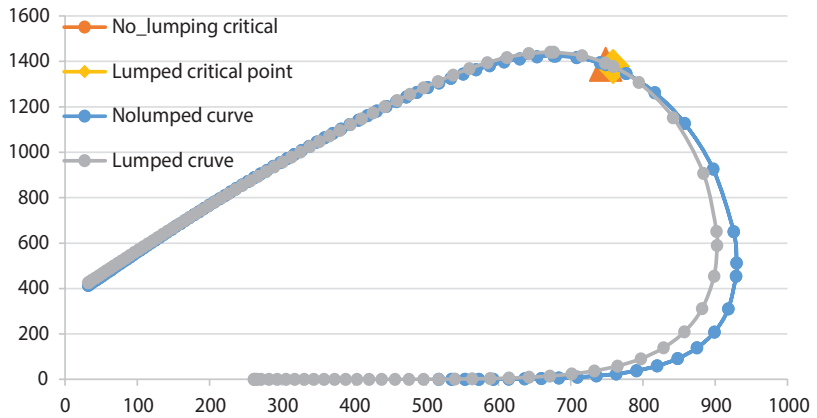

Figure 14.3 P-T phase envelope diagram.

(CCE, swelling, and separator and differential liberation tests) to reflect a reasonable equation of state (EOS) to describe the characterized oil sample.

The above regression curves show (Figure 14.3, 14.4, 14.5, and 14.6) a good match with saturation pressure and lab data illustrating that the tuned equations of state have a reasonable physical description of the characterized reservoir fluid. In addition, from the simulation output result in Figure 14.7, the error as shown above has been reduced less than one present. The triangle phase diagrams generated by CMG-Winprop of the given fluid sample under different operated pressure (1000 psia, 2000 psia, 3000 psia and 3500 psia) are listed in Figure 14.8.

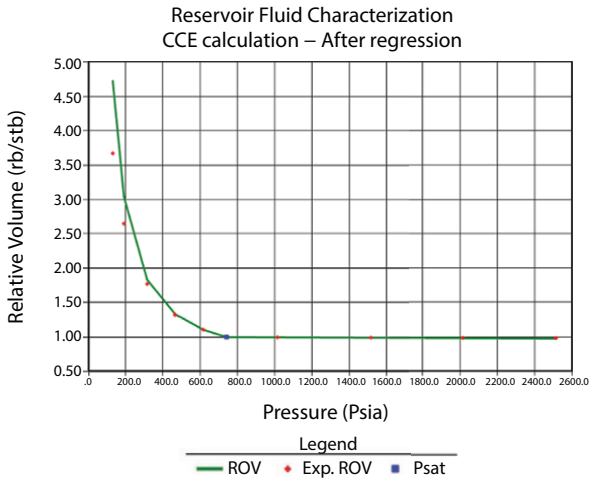

Figure 14.4 CCE test lab and regression results.

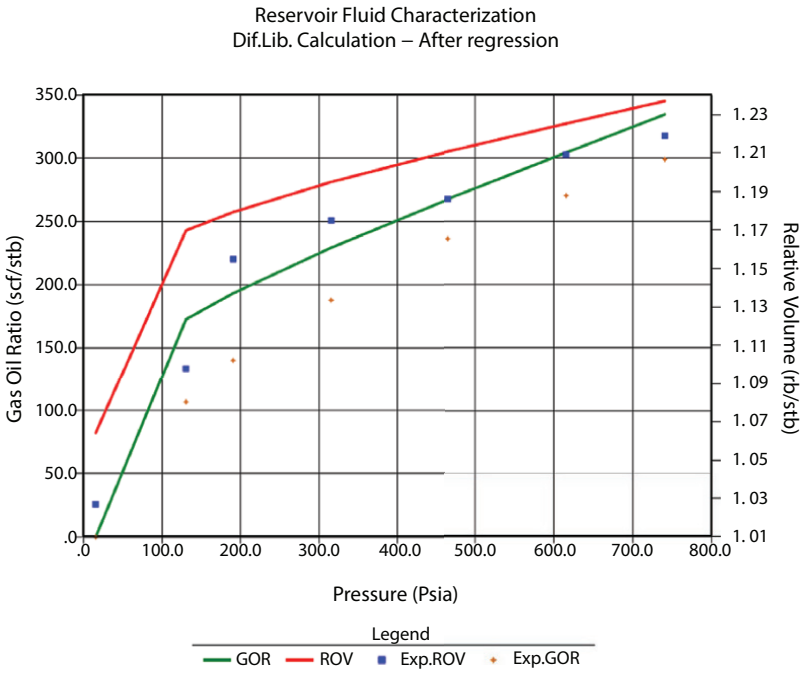

Figure 14.5 Differential liberation lab test and regression results.

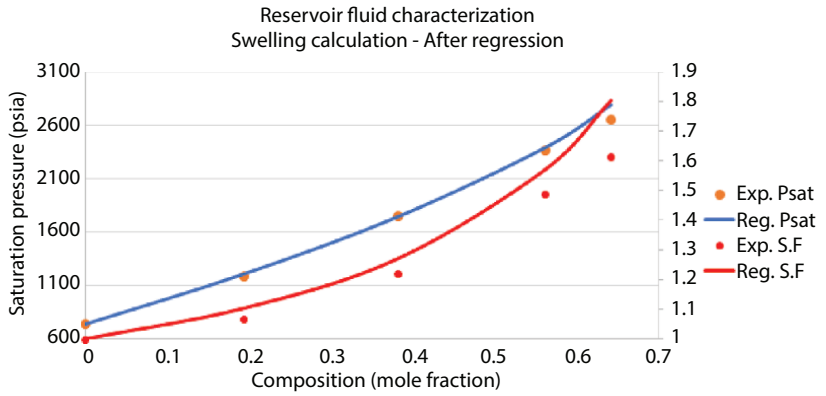

Figure 14.6 Swelling test lab result and regression results.

Calculation option	Date type	Pressure (MF-SWELL)	Experimental data	Before regression	After regression	ERROR reduction	ERROR after	Weight factor
5 PRESSAT								
20 SEPAR	PSAT		7.4000E+02	7.3756E+02	7.3826E+02	9.4656E–04	2.3556E–03	8.0000E+02
	GOR		2.4700E+02	2.4939E+02	2.4291E+02	–6.8592E–03	1.6543E–02	3.0000E+01
	FVF		1.1800E+00	1.1875E+00	1.1614E+00	–9.3957E–03	1.5767E–02	1.0000E+00
	API		4.0000E+01	3.4267E+01	3.4676E+01	1.0228E–02	1.3309E–01	1.0000E+01

Figure 14.7 Simulation regression result output.

The phase simulation results have been shown above. Theoretically, the two-phase zone is shrunk when increasing the operated pressure, and thus miscible flooding is easier to achieve under higher pressure. Also, when the injected carbon dioxide is enriched with intermediate components, the injection point shifts towards the intermediate component. The mixture of crude oil and injected gas shifts towards the intermediate component in the triangle phase diagram. As a result, the system does not require such a small two-phase region compared with injecting pure carbon dioxide, which means that the required miscible pressure decreases and releases the limitation of a high-pressure requirement.

Minimal miscible pressure can either be predicted in the laboratory or by using a tuned equation of state [8]. Owing to expensive laboratory tests, simulation is an economic and fast method to calculate the minimal miscible pressure when carbon dioxide flooding is used.

For validation, minimal miscible pressure was simulated under different concentrations of solvent (C2-C5) co-injected with carbon dioxide.

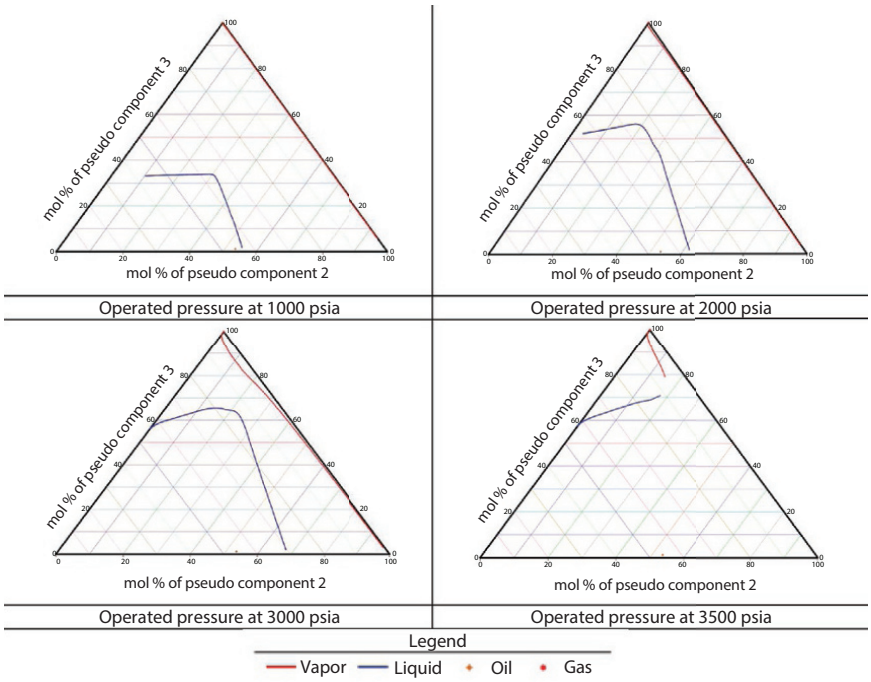

Figure 14.8 Phase envelope under different operated pressures.

The simulated results of different concentrations of intermediate components (0%, 5%, 10%, and 15%) in co-injection are shown in Figure 14.9.

The result has a same trend with Voon's lab result, where the minimal miscible pressure increases inversely after a critical concentration of solvent [9]. Thus, there exists an optimum value of solvent concentration to achieve the minimum MMP. The mechanism of the later inverse part where minimal miscible pressure is increasing while increasing the solvent concentration above 10% has not been studied clearly. As Voon also illustrated, this mechanism may be a relationship between polarity and a reduction in MMP.

14.3.3 Lab Scale Core Flooding Simulation

The purpose of this core flooding simulation is to create a simulation which models a linear core flood done in the lab. Core floods are often used for determining interactions between fluids in rock samples and for further predicting field performance. In particular, relative permeabilities

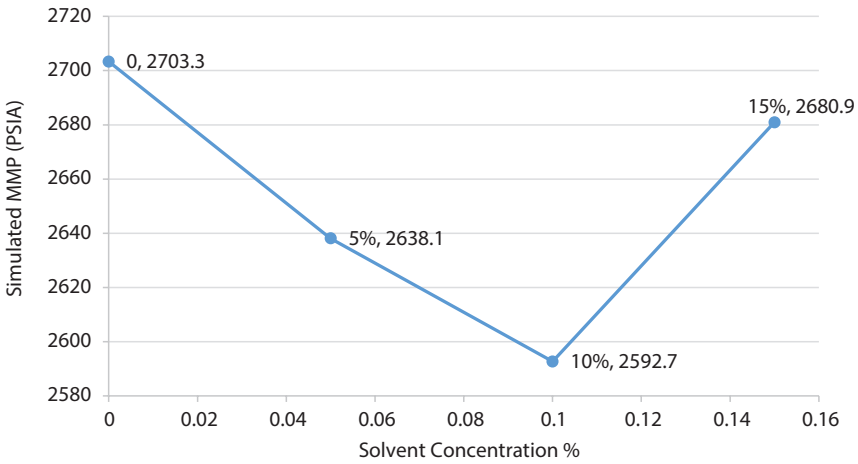

Figure 14.9 Simulated minimal miscible pressure under different solvent concentrations.

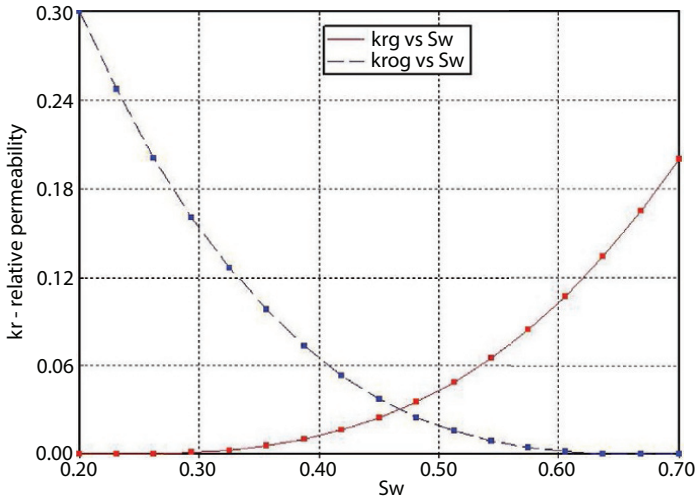

Figure 14.10 Relative permeability vs water saturation.

are often obtained as well as displacement mechanisms, such as the addition of miscibility.

The experimented core sample is 2.86614 ft in length and 0.122867454 ft in diameter. The core is homogenous with 0.2439 in porosity, 11.43 md in absolute permeability and 4×10^{-6} psi^{-1} in rock compressibility. For

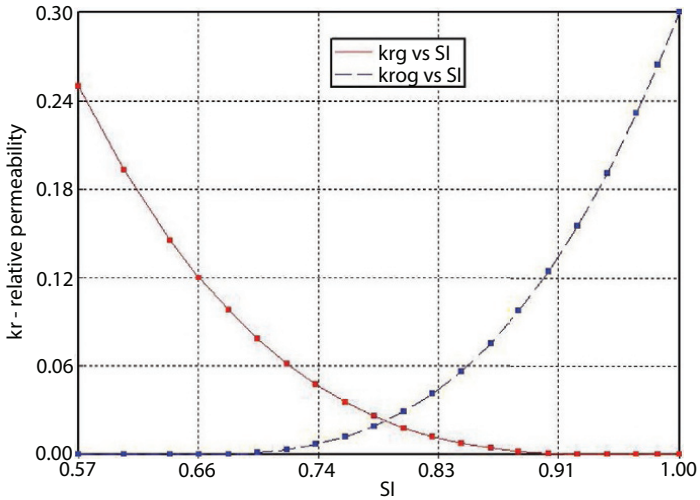

Figure 14.11 Relative permeability vs liquid saturation.

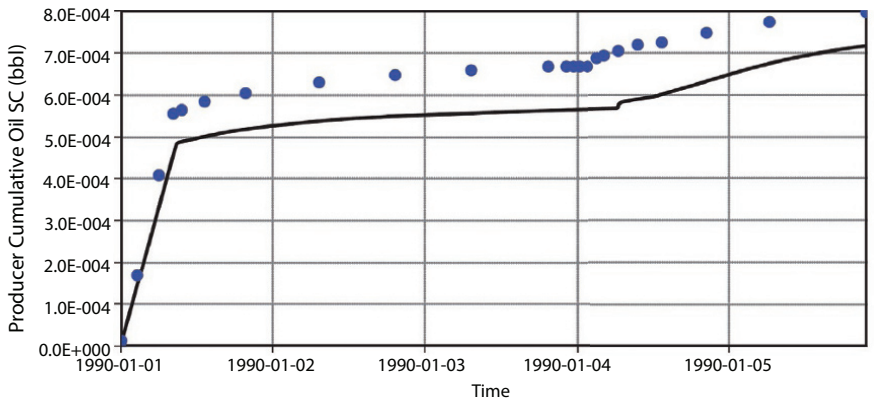

Figure 14.12 Simulated cumulated oil production and lab data.

solubility of components, Henry`s constant value is applied with 8.1646×10^4 psi and infinity is set as 3.5391×10^{-2} m^3/kgmole as default for carbon dioxide component and assumed zero solubility for other carbon components.

Relative permeability curves shown in Figs. 14.10 and 14.11 are created from the analytical Corey equation based on laboratory-determined end points.

In the lab core flooding experiment, the core sample is first produced by water injection at 10 cm^3/hr for 2.932 days, then CO_2 injection at

Table 14.3 Parameterization of uncertain parameters.

Relative permeability parameters	Observed value from lab	Initial guess	
		Min	Max
SWCON - Endpoint Saturation: Connate Water	0.2	0.01	0.25
SWCRIT - Endpoint Saturation: Critical Water	0.2	0.06	0.4
SOIRW - Endpoint Saturation: Irreducible Oil for Water-Oil Table	0.2993	0.05	0.4
SORW - Endpoint Saturation: Residual Oil for Water-Oil Table	0.2993	0.05	0.4
SOIRG - Endpoint Saturation: Irreducible Oil for Gas-Liquid Table	0.3702	0.01	0.45
SORG - Endpoint Saturation: Residual Oil for Gas-Liquid Table	0.43461	0.01	0.45
KROCW - Kro at Connate Water	0.3	0.1	1
KRWIRO - Krw at Irreducible Oil	0.2	0.1	0.7
Nw-Exponent for calculating Krw from KRWIRO	3	2	4
No-Exponent for calculating Krow from KROCW	3	2	5
Nog-Exponent for calculating Krog from KROGCG	3	1	4
Ng-Exponent for calculating Krg from KRGCL	3	1	4

10 cm^3 hr for 0.098 days and, finally, chasing water injection at 10 cm^3/hr for 1.876 days.

Owing to the small volume carbon dioxide injection, this is like a carbon dioxide slug displacement. Additional production has been observed on the cumulative production curve in the final stage. The additional production during the chasing water injection is due to the carbon dioxide slug interaction with the oil and causing swelling (for example, a density

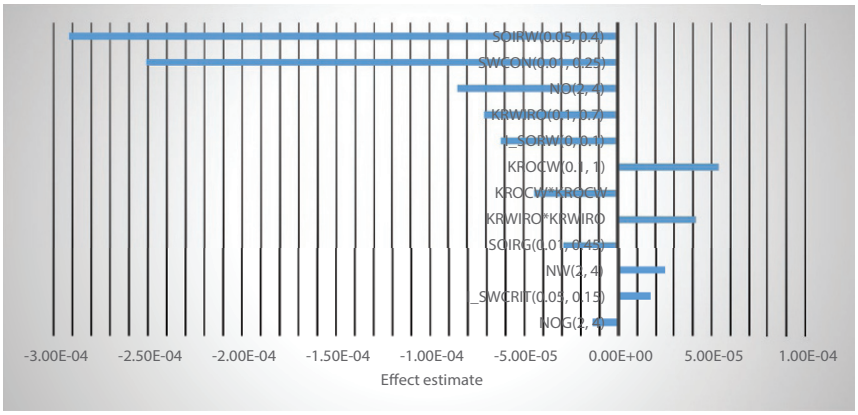

Figure 14.13 Parameter effect estimation from sensitivity analysis.

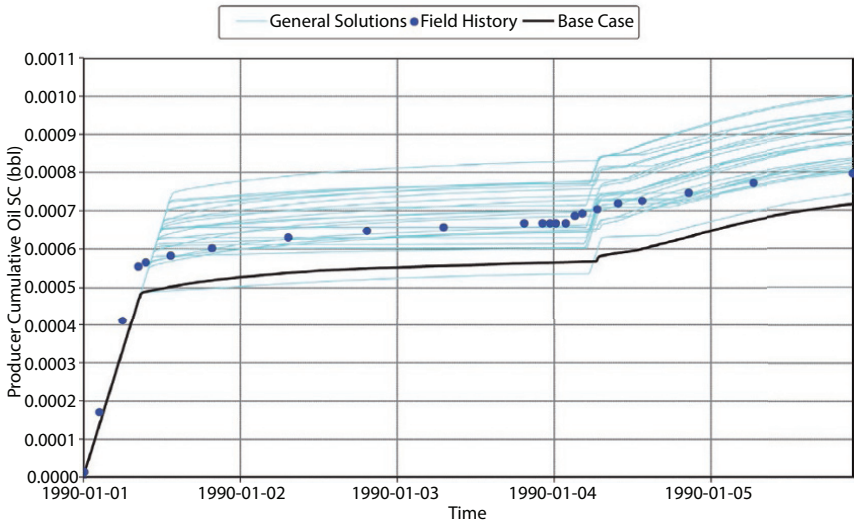

Figure 14.14 Sensitivity analysis result.

and viscosity decrease) and relative permeability changes such as a Sorw reduction.

The simulation result has a same trend with the experimental test result. However, it can be observed that the simulation model does not perfectly match the lab data. The difference between them will be discussed and updated by history match.

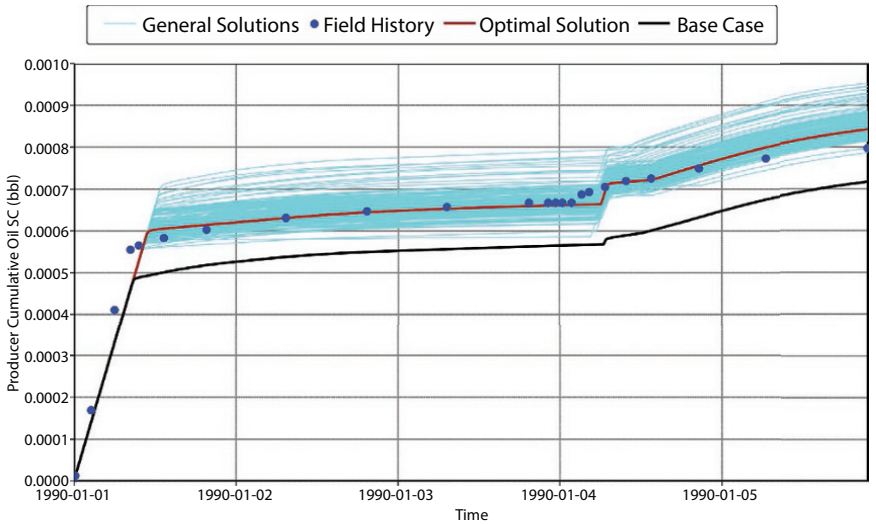

Figure 14.15 History match cumulative oil production result.

14.3.4 Sensitivity Analysis of Uncertain Parameters

Based on the previous simulation and lab results, it can be seen that the oil production in the simulation model did not match that from the laboratory perfectly. When analyzing the sensitive parameters, relative permeability data is typically placed at the top of uncertain parameters [10] (see Figure 14.13).

The most commonly used relative permeability model is a functional model, which determines a relative permeability curve by the endpoints and exponential factors. Thus, the most uncertain parameters in which we are interested in sensitive analysis are those endpoints and exponential factors in relative permeability curves [11].

The relative permeability end points were measured in the laboratory for a core sample. These values are measured as the entire core length, while a simulation model incorporates absolute values. As such, the relative permeability curves need to be adjusted in order to obtain an appropriate match over the length of the core.

Before updating a relative permeability curve, sensitivity analysis is carried out to determine the sensitivity of uncertain parameters and their interaction with the simulation result. Uncertain parameters are first needed to be parameterized within an initial guess range. The result from sensitivity analysis should give an indication of which parameters should be investigated further in order to obtain a history match between the simulation model and laboratory result.

In the sensitivity analysis, CMG's CMOST is used automatically handling numerous simulation models based on various parameters set within a range instead of carrying them manually. The uncertain parameters related to a relative permeability curve are plotted in a tornado plot illustrating how sensitive a parameter is to the cumulative oil production.

From the effect estimation chart, parameters with higher values in the plot can be considered to be more sensitive to the cumulative oil production.

The parameters of an oil-water table are more sensitive to the production performance. The parameters of the gas phase, as ranked in the above effect estimation (Table14.3), do not have much effect on the result. Based on the sensitivity analysis result, it can be observed that the laboratory data falls within the range we set, which means that the optimal values of each parameter also fall within the set range. Thus, those high sensitive parameters are needed to be refined within a defined range in history match in order to match the laboratory data and describe the physical properties along the core length with more accuracy.

14.3.5 Updated Relative Permeability Through History Match

From the previous sensitivity analysis, the objective function falls within the range we set. High sensitive parameters as ranked in the effect estimation table are refined to minimize the discrepancy between the simulated production data and lab observation data. Once the discrepancy is minimized, the corresponding relative permeability curves are regarded as approximations of real permeability curves [12].

In the history match part, owing to the refined sensitive parameters, the case number is increased to one thousand. The simulation result is showed in Figure 14.12.

The measured cumulative oil production in the lab is represented by blue dots. The black line represents the base case. Other grey lines represent individual cases, while the red line represents the optimal case by adjusting the uncertain parameters.

The optimal case, which is high light in red, has decreased the error to 2.81% compared with the lab measured cumulative oil production. The adjusted parameters in the optimal case are plotted in Figs. 14.16 and 14.17 compared with the base case. As mentioned in the sensitivity analysis, the parameters of gas saturation are not much sensitive to the result, and the endpoints of the gas relative permeability and saturation are kept as the measured values in the laboratory in the adjustment process.

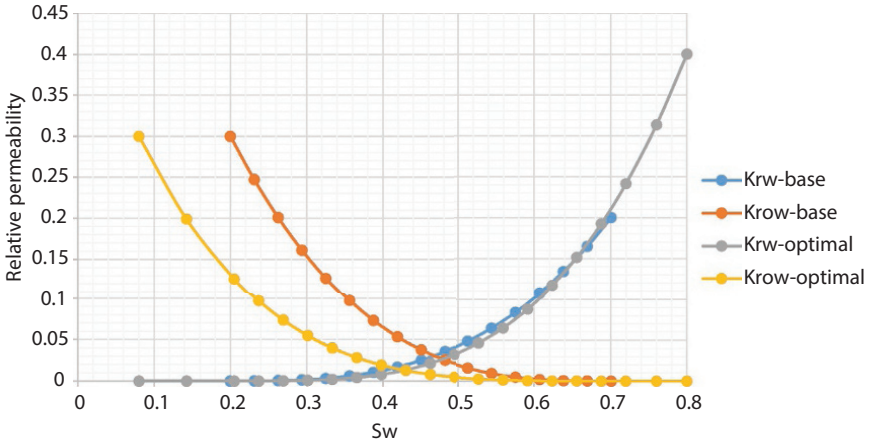

Figure 14.16 Adjusted water-oil table and base case.

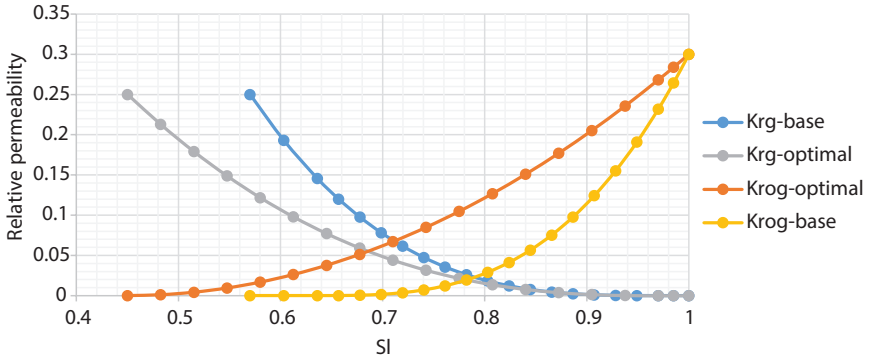

Figure 14.17 Adjusted liquid-gas table and base case.

The shift of the endpoints in the relative permeability curves, on one hand, reflects the extra oil production owing to a carbon dioxide slug interacting with oil, causing swelling (a density and viscous decrease) and reducing the residual oil saturation; it, on the other hand, reduces the uncertain parameters measured in lab experiments.

The updated relative permeability curves have been obtained inversely by history matching the production data from displacement measurement. Owing to the minimum discrepancy compared with the observed data, the updated relative permeabilities are regarded as an optimal case describing the fluid-core properties with the minimum uncertainties and can be utilized for further field scale prediction.

14.4 Conclusions

In this simulation study, slim tube simulation is conducted as a fast method to determine the minimal miscible pressure of carbon dioxide injection with different concentrations of intermediate solvents. The simulation results show that it is possible to enrich the injected carbon dioxide by co-injection with intermediate components and decrease the minimal miscible pressure for miscible flooding. The limitation of pressure required for carbon dioxide EOR is released to some extent.

Also, based on a minimal miscible pressure curve, there exists an optimal concentration of an intermediate component when reducing the MMP during carbon dioxide flooding, and thus optimization analysis is needed for planning carbon dioxide flooding projects.

Sensitivity analysis and history match are conducted by CMG's CMOST. Based on the sensitivity analysis, the sensitive parameters are plotted in a tornado plot. The sensitive properties of relative permeability curves are updated inversely from history match and can be used for predicting further field scale prediction.

Carbon dioxide injection has been developed for over fifty years. Owing to the limitation of a gas source, few projects were successful. Under such a low oil price background, carbon dioxide flooding with booming of the carbon dioxide capture technology is regarded as an economic production method and is more attractive than other conventional methods. Economically, this study makes it easier and more economic to get CO_2 miscible flooding and highly improve the recovery factor. In addition, environmentally, CO_2 EOR can also decrease the CO_2 emission in the atmosphere. For further research it is possible to continue CO_2 storage if a reservoir has a good storage capacity and seal rock over itself.

References

1. Lake, L., *Enhanced oil recovery*, Austin, TX, University Co-op, 2011.
2. Stalkup, F., Carbon Dioxide Miscible Flooding: Past, Present, And Outlook for the Future. *J. Petrol. Technol.*, 30, 08, 1102–1112, 1978. Available: 10.2118/7042-pa.
3. R. R. and N. P., Reducing the Miscibility Pressure in Gas Injection Oil Recovery Processes. *Soc. Petrol. Eng.*, 2016.
4. Brannan, G. and Whitington, H., Enriched-Gas Miscible Flooding: A Case History of the Levelland Unit Secondary Miscible Project. *J. Petrol. Technol.*, 29, 08, 919–924, 1977. Available: 10.2118/5826-pa.

5. Perera, M., Gamage, R., Rathnaweera, T., Ranathunga, A., Koay, A., Choi, X., A Review of CO_2-Enhanced Oil Recovery with a Simulated Sensitivity Analysis. *Energies*, 9, 7, 481, 2016. Available: 10.3390/en9070481.
6. Schlijper, A., Simulation of Compositional Processes: The Use of Pseudocomponents in Equation-of-State Calculations. *SPE Reserv. Eng.*, 1, 05, 441–452, 1986. Available: 10.2118/12633-pa.
7. Alfarge, D., Wei, M., Bai, B., Numerical simulation study on miscible EOR techniques for improving oil recovery in shale oil reservoirs. *J. Petrol. Explor. Prod. Technol.*, 8, 3, 901–916, 2017. Available: 10.1007/s13202-017-0382-7.
8. Fazlali, A., Nikookar, M., Agha-Aminiha, A., Mohammadi, A., Prediction of minimum miscibility pressure in oil reservoirs using a modified SAFT equation of state. *Fuel*, 108, 675–681, 2013. Available: 10.1016/j.fuel.2012.12.091.
9. Voon, C.L. and Awang, M.K., Reduction of MMP Using Oleophilic Chemicals C, 2014.
10. Bu, T. and Damsleth, E., Errors and Uncertainties in Reservoir Performance Predictions. *SPE Formation Eval.*, 11, 03, 194–200, 1996. Available: 10.2118/30604-pa.
11. Parvazdavani, M., Masihi, M., Ghazanfari, M., Gas–oil relative permeability at near miscible conditions: An experimental and modeling approach. *Sci. Iran.*, 2012. Available: 10.1016/j.scient.2012.11.007.
12. Li, H., Chen, S., Yang, D., Tontiwachwuthikul, P., Estimation of Relative Permeability by Assisted History Matching Using the Ensemble Kalman Filter Method. *J. Can. Petrol. Technol.*, 51, 03, 205–214, 2012. Available: 10.2118/156027-pa.
13. Chen, Z., Huan, G., Ma, Y., Computational Methods for Multiphase Flows in Porous Media. *Comp. Sci. Eng. Ser.*, 2, 2006.

15

Blowout Recovery for Acid Gas Injection Wells

Ray Mireault

Independent Consultant, Calgary, AB, Canada

Abstract

How does the industry develop specialized recovery equipment and procedures *a priori*, to quickly stop a blowout from an acid gas injection (AGI) well while protecting health, safety and the environment? This paper presents an ongoing process to address the challenge.

A key first step was recognizing that the composition of the acid gas would result in very different plume behaviour compared to a conventional sour gas blowout, making some aspects of conventional blowout recovery operations impossible or too dangerous to attempt. With a high likelihood that escaping acid gas cannot be ignited or will not achieve sufficiently high combustion temperatures to reduce ground level concentrations of H_2S, SO_2 and CO_2 to relatively safe (ppm) concentrations:

- The atmosphere at the wellsite may be too dangerous for personnel to manually assess the extent of wellsite damage through an initial reconnaissance, or to be at the wellsite during recovery operations.
- The industry cannot count on ignition of the plume to protect the public and environment from the lethal effects of H_2S, SO_2 and CO_2. Monitoring ppm air-quality trends to determine when to evacuate the public does not work if the first reading could be 30% H_2S.
- The industry does not currently have electrically powered heavy equipment with remote power generation; capable of operating in an oxygen deficient environment.

Email: ray.mireault.peng@gmail.com

Ying Wu, John J. Carroll, Mingqiang Hao and Weiyao Zhu (eds.) Gas Injection into Geological Formations and Related Topics, (245–258) © 2020 Scrivener Publishing LLC

The next key realization was that no single person or organization could have the scope of expertise to "solve" the problem. Thus, the search was on for individuals/organizations with:

- The knowledge and experience to better define particular aspects and,
- The enthusiasm and creativity to collaboratively develop an overall solution.

An early finding is that the required areas of expertise do exist but in isolated pockets. The next challenge is bringing everyone together.

Keywords: Acid gas, well, blowout, blowout recovery

15.1 Introduction

In the event of an uncontrolled release of acid gas, how would the industry effect recovery operations? Collaboration with international acid gas processing experts, emails and meetings with blowout recovery experts (Wild Well, Capstone Well Servicing and Safety Boss), and searches of well safety and regulatory websites indicate research is needed to inform safe and effective well control methods involving acid gas release.

While there is published literature on acid gas system surface design and reservoir/aquifer considerations for acid gas injection, papers on acid gas wells are extremely limited and until 2018 did not address the thermodynamic behaviour of acid gas during an uncontrolled release. To illustrate:

1. Lynch *et al.* (1985) describe a dynamic kill of an underground blowout while drilling a well for a naturally occurring CO_2 deposit [1].
2. Galic *et al.* (2009) present an initial attempt at modelling a conceptual CO_2 capture and storage system, comprising an onshore power plant CO_2 source, a transport/distribution pipeline and multiple offshore wells injecting into one or more depleted gas reservoirs in the North Sea [2].
3. Mireault *et al.* (2010) present some wellbore dynamics for acid gas injection well operation [3].
4. Mireault *et al.* (2010) present some wellbore dynamics for CO_2 sequestration well operation [4].
5. Mireault (2018) presents the wellbore thermodynamics of an acid gas release [5].

The rarity of such incidents is encouraging but the worldwide lack of knowledge to regain control is concerning.

15.2 Methodology

In the absence of industry experience, a collaborative, non-linear approach was adopted to brainstorm and evaluate potential well control measures that address the unique conditions and risks associated with an acid gas release. The study objectives included:

- Increasing the understanding of the unique thermodynamic aspects of acid gas releases and associated challenges of safe mitigation.
- Identifying potentially effective acid gas release control methods and equipment for two release scenarios (low rate and medium-high rate) for further discussion and evaluation.

Investigations proceeded simultaneously and iteratively on several levels as questions and challenges were uncovered. The primary means of communication were phone calls, emails and face-to-face meetings with individuals and companies with the experience and expertise to provide insights. The investigation topics can be roughly grouped as follows:

1. Acid Gas Wellbore Behaviour During a Blowout
2. Acid Gas Flammability and Toxicity
3. Acid Gas Escape Plume Behaviour
4. Acid Gas Blowout Recovery Operations

A summary of the findings to date follows:

15.3 Wellbore Behaviour

At the 7th AGIS, Mireault [5] presented wellbore thermodynamics that demonstrate the escaping fluid temperature could be extremely cold, in the order of -50 to -80°C, over a wide range of acid gas compositions when acid gas is a dense phase fluid or 2-phase liquid in a reasonably pressured reservoir. However, by late 2018 it was realized that an uncontrolled release from a low pressure, depleted reservoir, where acid gas is in a gaseous

phase at reservoir conditions, might yield a markedly warmer escape gas temperature. Such a situation could be encountered early in the life history of a disposal well.

The depleted reservoir case was modelled using the VMG Symmetry software platform, which encompasses the VMGThermo property package and Pipe, the multiphase flow modelling software. The VMG Symmetry suite was selected because of its proven track record in accurately modelling acid gas properties and phase behaviour, as well as multiphase flow. While the industry more commonly uses the Pipe software to model multiphase flow in pipelines, particularly those with significant elevation changes, in the hands of an experienced user it proved quite capable of modelling acid gas wellbore behaviour.

As an example, a 2700 m deep injection well was modelled with:

- Reservoir temperature of 85° C and depleted reservoir pressures of 828 and 2280 kPaa.
- Acid gas composition of 78/20/2% $H_2S/CO_2/C_1$
- 73 mm tubing and 178 mm production casing
- An AOF of 3.41 and 24.01 $10^3m^3/d$ at reservoir pressures of 828 and 2280 kPaa, respectively.

Operating points for the 4 blowout scenarios are visually presented by overlaying the tubing/casing performance curves against the IPR curves (Figure 15.1). The simulations confirm that escape gas temperature is in the range of 48 to 58°C.

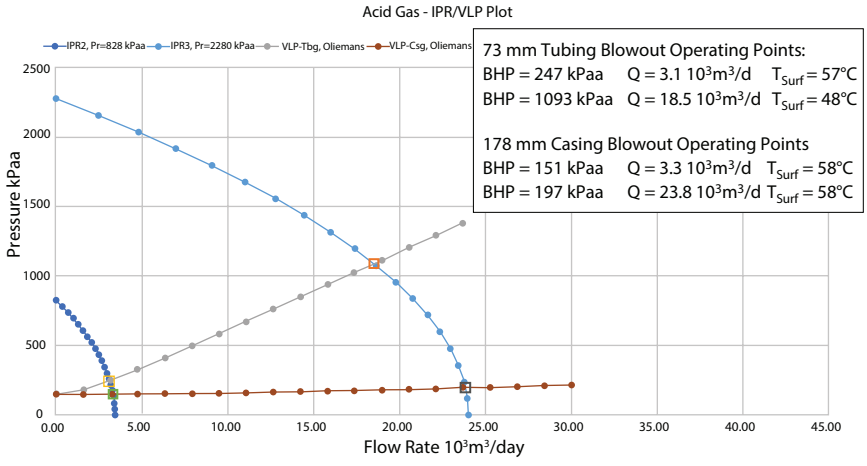

Figure 15.1 Depleted Reservoir Low Blowout Rate Example.

15.4 Acid Gas Flammability and Toxicity

Ignition is the cornerstone of emergency response planning and blowout recovery operations for sour gas blowouts. However, discussions with Alberta Sulphur Research and Questor Technology Inc. (CAN) personnel quickly ruled it out as a solution for an acid gas blowout because:

- The CO_2 concentration of the acid gas may be such that it can't be ignited.
- The flammable limits for H_2S are 4 to 44% by volume in air. Thus, an escaping acid gas cloud may be too lean or too rich to ignite, or perhaps only isolated "pockets" within the cloud can be ignited.
- Although H_2S may initially be ignited (with a -60°C boiling point it vaporizes readily), it may be unable to heat the area around the flame enough to sustain the fire. The auto ignition temperature of H_2S is 232°C. (https://en.wikipedia.org/wiki/Hydrogen_sulfide)
- Even if the fire can be sustained, insufficient heat may be generated to dilute and dissipate CO_2, SO_2 and unburnt H_2S to safe ground level concentrations. The low heating value of H_2S is why incinerators require supplemental fuel gas to meet emission standards – the heating value of H_2S is 6545 Btu/lb vs 21,537 Btu/lb for methane.

Conventional air quality monitoring and emergency response evacuation procedures for sour gas blowouts also rely on ignition of the escaping gas. After ignition, ground level concentrations of H_2S, CO_2 and SO_2 are continuously monitored and the sizes of the evacuation area adjusted as needed to protect the public. It's a proven response procedure when ground level concentrations change gradually and consistently remain within the ppm range.

However, conventional monitoring procedures are not a solution if ground level concentrations can suddenly become lethal. The alarm-to-evacuation response time may not be fast enough for a toxic gas cloud with a rapid rate of travel. Exposure to 100 ppm of SO_2 or H_2S is considered immediately dangerous to life and health. https://www.atsdr.cdc.gov/toxfaqs/tf.asp?id=252&tid=46

High CO_2 concentrations are also a concern. According to one safety data sheet, a 10% CO_2 concentration can cause unconsciousness in 1 minute or less. (http://www.generalair.com/pdf/Safety%20Topics/Carbon%20Dioxide%20Asphyxiation.pdf

15.5 Escape Plume Behaviour

If acid gas toxicity cannot be addressed through ignition, then a detailed understanding of the escape plume behaviour is critical to developing effective emergency response and blowout recovery procedures. Proximity to population centres will be a key factor in determining the appropriate response times and recovery measures for a given situation.

Plume modeling experience suggests that at -50 to -80°C the cold escaping gas would have essentially no loft such that the industry would be faced with an advancing ground level blanket of lethal, heavier-than-air acid gas; a blowout scenario the industry has no experience with. Anecdotal evidence is consistent with the wellbore and plume modelling predictions:

- Lynch *et al.* [1] report frozen chokelines and casing valves and "softball size chunks of solid CO_2 spewing hundreds of feet into the air" out of surface fissures that resulted from an underground blowout while drilling a CO_2 reservoir in the Sheep Mountain Unit, Huerfano County, Colorado.
- An informal presentation [6] on a blowout from a CO_2 injection well that was part of an EOR scheme at a temperate latitude in Eastern Europe showed photos of a stable blanket of CO_2 that reached from ground level to the tops of the deciduous trees (perhaps 10 to 12 m) in hilly, rolling farmland.
- The 1986 CO_2 limnic release from Lake Nyos, Cameroon, created a white cloud of gas up to 100 m tall over the lake. A river of gas up to 50 m tall then flowed down the valley, killing more than 1,700 people and 3,500 livestock within 25 km of the lake. http://volcano.oregonstate.edu/silent-deadly, https://en.wikipedia.org/wiki/Lake_Nyos_disaster. Although it is not a perfect analogy to an acid gas release† it does confirm the stability of a heavier-than-air cloud travelling at ground level over long distances.

How quickly the blanket expands depends on the release rate, while the thickness and geometry of the blanket and its direction of travel are likely

†From Wikipedia, the release volume was estimated at 100,000 to 300,000 (metric) tons; (51–153 10^9 m3 or 1.8 to 5.4 TCF at STP).

influenced by factors that include air temperature, wind conditions, topography and vegetation. For example:

- Mountainous terrain may tend to create a very thick blanket, with gravity directing expansion and travel down to lower elevations and along the length of a valley.
- Treed terrain may trap the blanket and reduce or delay any dilution and dissipation from the wind and sun.
- Open prairie or an offshore blowout might reduce the depth of the blanket but allow it to spread more quickly over a larger area.

A ground level blanket of toxic gas over the wellsite, plant and access roads further presents unique challenges for blowout recovery operations that include:

- Personal protection for recovery personnel working in a toxic atmosphere.
  - Standard supplied air (SCBA) units are good for approximately 30 minutes, which is too short a time period for isolation and repair efforts. Diving bell or NASA style "space" suites with long umbilical cords would be too bulky.
  - Visibility could be limited by "fog" within the blanketed area, particularly at very cold acid gas exit temperatures. The cold temperatures would also cause water vapour to condense, which creates the potential for sulphuric acid formation.
- Protection of off-site support crew, as well as first responders and the public, from sudden shifts in the advancing cloud's direction.
- Operation of reconnaissance and heavy equipment in an oxygen deficient atmosphere.
- The safe conduct of operations when wellsite steels (e.g., pipeline, wellhead, valves, tubulars) are susceptible to brittle failure at temperatures below -20°C.

Plume escape modelling for a depleted, low release rate reservoir has yet to be undertaken. A depleted, low pressure reservoir implies a warmer exit gas temperature with a lower exit gas velocity and smaller release volume for a given time period. However, the impact on cloud height and dispersion behaviour is unknown and requires further investigation.

15.6 Blowout Recovery Operations

From discussions with Capstone Well Servicing and Safety Boss Inc. the steps in conventional blowout recovery operations can be broadly categorized as follows:

1. Initial wellsite reconnaissance and assessment.
2. Recovery Plan Development and Equipment/Material/Personnel Logistics
3. Site Equipment Preparation, Fabrication and Testing – (e.g., heat shields, water supply/storage, fire hoses, pumps, etc.)
4. Preparation for and Removal of Damaged Wellsite Equipment and Piping
5. Fire Extinguishing (temporary) and Installation of New Well Control Equipment (typically BOP stack)
6. Testing of the newly installed pressure control equipment leading to shut-in of gas flow.

The same sequence was assumed as a starting point to develop recovery procedures for an acid gas blowout. However, points to consider in developing acid gas recovery procedures include:

- Acid gas blowouts from the initial injecting well(s) should only be cased hole blowouts that occur during injection or well servicing operations, since well drilling occurs prior to the start of injection. The exception is if subsequent wells are deliberately or unknowingly drilled into an existing acid gas reservoir plume.
- An initial reconnaissance and damage assessment are essential first steps in any recovery operation.
- Ultimately, a well has to be accessed in order to replace damaged valving to secure the well.
- Explosion-proof electric or hydraulic motors can operate in an oxygen deficient atmosphere. The challenge is providing an adequate power supply.
- Although erosional velocity damage would still be a concern, if there isn't a fire at the wellsite there may be less damage to above ground BOP /wellhead valves and piping, as well as any service equipment on location at the time of the blowout; unless the loss of wellbore integrity is below the casing flange.

- Procedures to protect recovery support personnel and the general public from a ground level blanket of immediately toxic gas will be different from conventional procedures.

15.6.1 Initial Reconnaissance

Initial reconnaissance is conventionally done by donning an air pack and walking through the wellsite lease. With an acid gas environment, a better approach might be a combination of:

- A camera-equipped drone for an initial fly-over of the wellsite and for real-time monitoring of the escape cloud's location, direction and rate of advance.
- A remotely operated "bomb" squad style robot for "up-close" assessment and possibly light duty recovery operations (e.g., rotate valve handle).

The power requirements for reconnaissance work are low enough to be supplied by batteries; creating mobile, self-contained units. If successful, remotely operated units could avoid or at least minimize exposure of recovery personnel to the acid gas blanket.

15.6.2 Heavy Equipment for AG Recovery Operations

The large power requirements for heavy equipment including bulldozers, cranes, and water pumps can, in theory, be supplied by electric motors connected (with very long cables) to a power generating system located a safe distance from the wellsite. TransAlta uses electric shovels/excavators to mine coal for power generating plants near Edmonton (https://www.transalta.com/facilities/mines-operation/highvale-mine/), so the technology might be adapted for wellsite blowout recovery operations.

Another potential technology might be the hydraulic motors/options used for undersea work, which provide the benefit that there is no possible source of spark ignition.

While service rigs that are on the well at the time of a sour gas blowout are invariably destroyed by the resulting fire, an on-site service rig during an acid gas blowout may not suffer the same fate. An electric drive rig connected to remote power generation might still be operational for subsequent recovery operations.

Another area for investigation is the degree to which heavy equipment (including the rig) could be automated. While 100% remote operation may

not be achievable, the minimum objective would be to prevent personnel from being simultaneously exposed to the hazards of moving equipment and rotating machinery in a toxic atmosphere.

15.7 Recommendations for Further Investigation

The following areas require further investigation to develop recovery procedures for an acid gas blowout:

- Acid Gas Escape Cloud Modelling, including behaviour under attempted ignition.
- Personnel Training
- Blowout Recovery Procedure Development and Testing
- Blowout Equipment Development and Testing

15.7.1 Acid Gas Escape Cloud Modelling

Further insight on the behaviour of an escaping cloud of acid gas is required for emergency planning to protect the public and personnel, and develop wellsite blowout recovery procedures. Questions for simulation modelling include:

- The behaviour of an escaping cloud in different terrains and at different well locations within a given terrain. What shape is the cloud likely to take; long and narrow, round or irregular? What might be the height of the cloud? What factors significantly influence cloud shape and travel over the area? Is there an advantage to locating the well at the base of the valley, near the crest or on a high plateau?
- Does acid gas composition significantly affect cloud behaviour?
- Can the escaping effluent be ignited under any conditions? What is the impact of ignition? At what concentration of CO_2 is ignition no longer possible?
- By what mechanism(s) and how quickly could an acid gas cloud be diluted to safe concentrations?
- What are the concentration gradients between the edge and core of an acid gas cloud? How much time / distance is there between the first reading of an advancing cloud and a lethal concentration reading?

- How quickly does a cloud travel and what are the important factors that determine travel speed?
- How quickly can a cloud change direction and what are the significant affecting factors?
- Should acid gas wellsites have 2 different access/escape routes pre-built, to deal with the variability in cloud formation and migration? Should there be a minimum arc radius between the routes? How will evacuation of residents or tenure holders be handled?

Questor Technology Inc. (CAN) has confirmed their willingness to be involved in researching these questions. Questor is a well-established incinerator manufacturer with proven expertise in modelling emission concentrations from acid gas sources. Questor has developed proprietary software to quantify emission concentrations from a source such as an incinerator, flare stack, or damaged wellhead. Incinerators in acid gas and tail gas clean-up service achieve >99.99% combustion efficiency and successfully maintain emissions within the prescribed limits for regulatory compliance.

15.7.2 Personnel Training

Two (2) levels of training are recommended as follows:

1. For those who work around the wells on any kind of basis BEFORE a catastrophic event, including operators, field foremen and well maintenance and rig service personnel. Training would be centered around personal safety, leak detection, best operating practices, example situations that could result in a loss of well control, and the basics on how to recognize a problem, who to call and exactly how deadly problems can be.
2. The second level would be geared toward the recovery team and those who would have input/participation of any kind in a recovery operation including operator company office and field emergency response personnel, and regulatory personnel. Training for this level would include the level 1 subjects plus:
   a) Wellsite initial reconnaissance and assessment – equipment and procedures
   b) Damaged wellsite equipment and material removal procedures

c) Specialized on-site recovery equipment and operating procedures
d) Well blowout control equipment and installation procedures

It is envisioned that training would be delivered via a combination of classroom instruction and field exercises, with rental of 3rd-party facilities for the field component of the course(s).

A third course or seminar may also be appropriate for municipal/regional first responders (police, ambulance crews, fire departments, hospital staff), and other non-industry personnel who would become involved in the event of an emergency.

15.7.3 Development of Recovery Equipment and Procedures

Once funding arrangements are in-place, Safety Boss has indicated their willingness to lead/be involved with the development and testing of specialized blowout recovery equipment and procedures, as well as Level 2 training for emergency response personnel.

Prototype development and testing would necessarily go hand-in-hand with course development for the level 2 training, and would similarly require rental of 3rd-party facilities. One possibility is the Energy Safety Canada Training facility at Genesee, which normally provides hands-on safety training in the controlled ignition and extinguishing of hydrocarbon plumes.

Ultimately, development of test objectives and detailed test procedures should lead to a full-scale test exercise of the equipment and procedures.

15.8 Acknowledgments

The following individuals (listed in no particular order) graciously provided their time and expertise to this study:

Dr. Robert Marriott and Paul Davis - Alberta Sulphur Research
Rob Graefer - Capstone Oilfield Services Ltd.
Dr. John Carroll, P. Eng. - Gas Liquids Engineering
Cam Murray P. Eng. - Murray Technical Ventures Ltd.
Chris Mamen P. Eng., Nick Battocletti, Audrey Mascarenhas P. Eng. and John Sutherland P. Eng. Questor Technology Inc. (CAN)

Nelson Hertz and Monty Mason - Safety Boss Inc.
Gordon Slemko P. Eng. and Dr. James Van der Lee P. Eng. - Virtual Materials Group, a Schlumberger Technology
Research funding was provided by the B.C. Oil and Gas Research and Innovation Society (OGRIS), with the technical support and assistance of the B.C. Oil and Gas Commission.

References

1. Lynch, R.D., McBride, E.J., Perkins, T.K., Wiley, M.E., Dynamic Kill of an Uncontrolled CO_2 Well. SPE 11378. *J. Petrol. Technol.*, 1267– 1276, July 1985.
2. Galic, H., Cawley, S.J., Bishop, S.R., Gas, F., Todman, S., CO_2 Injection into Depleted Gas Reservoirs. *SPE Paper 123788 - MS presented at the Offshore Europe Oil & Gas Conference*, Aberdeen, UK, 8-11 September 2009.
3. Mireault, R., Stocker, R., Dunn, D., Pooladi-Darvish, M., Wellbore Dynamics of Acid Gas Injection Well Operation. *CSUG/SPE Paper 135455 presented at the Canadian Unconventional Resources & International Petroleum Conference*, Calgary, Alberta, Canada, 19-21 October 2010.
4. Mireault, R., Stocker, R., Dunn, D., Pooladi-Darvish, M., Wellbore Dynamics of Carbon-Sequestration Injection Well Operation. *SPE Paper 135485 presented at the SPE International Conference on CO_2 Capture, Storage, and Utilization held in New Orleans*, Louisiana, USA, 10-12 November 2010.
5. Mireault, R. Emergency Response Planning for Acid Gas injection Wells, from The Three Sisters, pages 333–346 by Wu, Ying, Carroll, J.J. and Hu, Yongle. Published by Scrivener Publishing LLC and distributed by John Wiley & Sons (2019).
6. *Informal presentation made during the SPE International Conference on CO_2 Capture, Storage, and Utilization*, New Orleans, Louisiana, USA, 10–12 November 2010.

16

The Comprehensive Considerations of Leak Detection Solutions for Acid Gas Injection Pipelines

Shouxi Wang[1,2*], John Carroll[3], Fan Ye[4], Lirong Yao[4], Jianqiang Teng[4] and Haifeng Qiu[4]

[1]Xi'an Shiyou University, Xi'an, China
[2]Xi'an PipePlus Technology Ltd., Xi'an, China
[3]Gas Liquids Engineering Ltd., Calgary, AB, Canada
[4]Sinopec Northwest Company, China

Abstract

Despite their variations in length, pipelines are required to move acid gas from gas processing facilities to injection wells in an acid gas injection project. Effective and reliable acid gas pipeline leakage awareness and alarms are key due to common concerns regarding the toxicity, hazardous effects and high pressure inside the pipeline. Up to now, there are many different leak detection methods and systems available for gas/liquid pipelines, such as different CPM methods defined by API 1130, acoustic and fabric leak detection system, and distributed or fix point [1] H_2S sensor [2] along the pipeline. What is the best and most proper leak detection solution for specific acid gas pipelines, which may be short or long, in gas or liquid phase, through a high consequence area, and etc.? Detailed considerations are discussed here, regarding features and behaviors of acid gas flows with/without leakage, the selection and expected performances of leak detection systems (LDS) over different acid gas pipeline scenarios, and the implementation and operation of LDS.

Keywords: H_2S, acid gas, pipeline, leak detection

**Corresponding author*: wangsx@yahoo.com

Ying Wu, John J. Carroll, Mingqiang Hao and Weiyao Zhu (eds.) Gas Injection into Geological Formations and Related Topics, (259–282) © 2020 Scrivener Publishing LLC

16.1 Introduction

The economic and environmental benefits of acid gas injection (AGI) are obvious and well known by the government, scholarship, industry and public. But the development and implementation of AGI facilities and projects are not as quick as expected. The worries and concerns regarding operation safety may be one of the key reasons that are slowing down the development, because safety is as important as its technology for an AGI project. Among the worries and concerns is the potential leak occurrence [3] of toxic acid gas from pipelines that move the acid gas from gas processing facilities to injection wells.

The best response to the leak occurrence of pipelines is to discover the leak early and quickly, alarm the leak reliably and locate the leak accurately, so that the impact and loss from unexpected leak accidents can be controlled and limited to acceptable ranges. Quick awareness and accurate location of the leak event are important to reduce losses and avoid disaster.

Up to now, there are many different leak detection methods and systems available for gas/liquid pipelines, such as different Computational Pipeline Monitoring (CPM) methods defined by API 1130 [4], acoustic and fabric leak detection system, and distributed or fix point H_2S sensor along the pipelines. Acid gas pipelines of an AGI project are very different from the normal oil/gas pipelines. What are the features of their flow and layout, leak detection requirements, the implementation and operation regarding the leak detection and safety operations of acid gas pipelines?

Detailed consideration are discussed here, regarding the features and behaviors of acid gas flows with/without leakage, the selection and expected performances of leak detection systems (LDS) over different acid gas pipeline scenarios, and the implementation and operation of LDS.

16.2 Flowing and Layout Features, Leak Detection Strategies of the Acid Gas Pipelines

Flow and layout features of the pipeline are key factors for the decision making of the systems, methods, data requirements, expectations, and strategies of its leak detection. Compared to normal oil and gas pipelines, acid gas pipelines from AGI projects have the following common flow and layout features:

1. Short in length and small in size: the length of acid gas pipelines of an AGI project is usually short due to the requirements

of the AGI project. For short acid gas pipelines, the location of the leak is not as important as the long-distance pipeline, because leakage can be tracked easily and quickly after a reliable leak alarm is issued. The length of the pipeline is an important factor for choosing the LDS method: MB method may be good enough for a short pipeline, but PPA and RTM methods should be selected for a long pipeline;

2. High pressure and supercritical flow: most of AGI pipeline flows are small, stable and in high pressure and supercritical state. In high-density states, the thermodynamic properties of acid gas are closer to liquid than gas. Thus, all the CPM leak detection methods are suitable to be applied to acid gas pipeline even it is in high pressure gas phase. The fluid phase inside the pipeline, gas or liquid, has a determining impact on the performance and effectiveness of LDS system. For example, the PPA method will not work properly for most of the gas pipeline;
3. Toxic fluid and high consequences: the fluid inside is extremely detrimental and may result in serious consequences. The LDS system must be responsive to small leaks to avoid these outcomes. The alarms should be reliable by installing and setting up different alarm methods in the affected areas, such as H_2S sensors in the lower sites along the pipelines. Whether it is a high consequence area is a key consideration for selecting the reliability and available LDS system;
4. Short of variations: most of the pipelines in AGI projects are short of variations, such as their relatively stable flow, simple composition, predictable phases and thermodynamic behaviors. This feature will enhance the performance of their pipeline LDS.

16.3 The Behavior of the Acid Gas Flows with Leakages

16.3.1 Leak Experiments on Liquid Pipeline

A series of experiments was conducted on the measurement responses at two ends of a water pipeline to leaks of different sizes and locations. The water pipeline system, which used 3 pump stations to drive water from one tank to another through the DN40 mm and 1210 m long pipelines,

was designed specially for online simulation and leak detection and set up in Xi'an Shiyou University, as shown in Figure 16.1. The online simulation was conducted for 876 m trunk pipelines with upstream and downstream pressures set by real-time measured data from SCADA.

There are 6 valves allocated along the pipeline for the test of pipeline leak location (PLL) of any sizes. Table 16.1 lists the measurement response tests of the water pipeline to leaks of different sizes and locations.

Figure 16.2 presents the responses of pipeline measurements to the leaks of different locations and sizes. The measurements and changes of pressures and flow rates are stamped with leak sizes and locations, which are significant to be used to diagnose the occurrence of a leak with a sufficient size.

16.3.2 Leak Experiments on Gas Pipeline

Figure 16.3(a) is a sample copy of the gas leak detection system and Figure 16.3(b) shows its process. In the system, air is compressed and goes through the pipeline with a normal flow-rate of approximately 45 L/min. The monitored pipeline, from PT-1 to PT-2, is 300 meters long with 2 leak test points at 100 meters and 200 meters from the upstream PT-1. The real-time measurement data are collected by the computer to apply the predefined leak detection procedures. The 2 leak test points are used to

Figure 16.1 Lab of online simulation and LDS.

Table 16.1 Matrix of the leak measurement response tests of liquid pipeline.

PLL valve	Location from upstream (m)	Control	Leak size (kg/h)				
PPL1	213.061	Auto/Remote	13	158	534	833	976
PPL2	460.785	Auto/Remote	109	275	586	770	858
PPL3	709.2	Auto/Remote	48	287	549	675	725
PPL4	121.839	Manual	0	314.928	383.067	610.884	1094.544
PPL5	368.959	Manual	0	296.5	531.06	822.94	931.51
PPL6	616.743	Manual	0	120.725	241.218	433.155	899.21

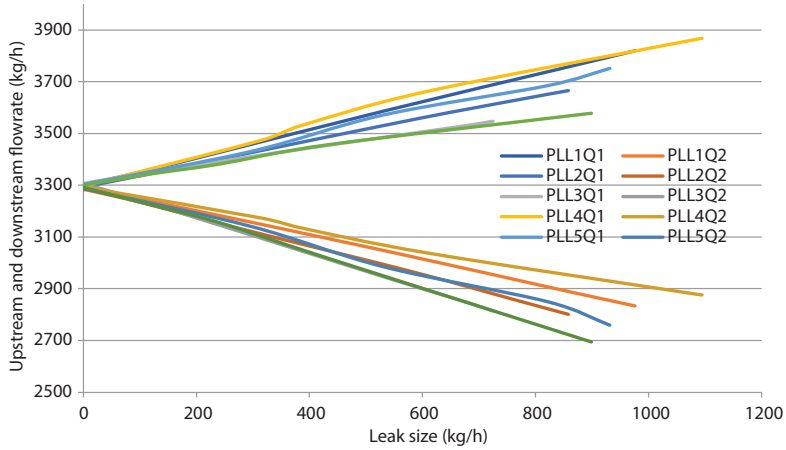

(**a**) Changes of up and down stream flow-rate with leak sizes

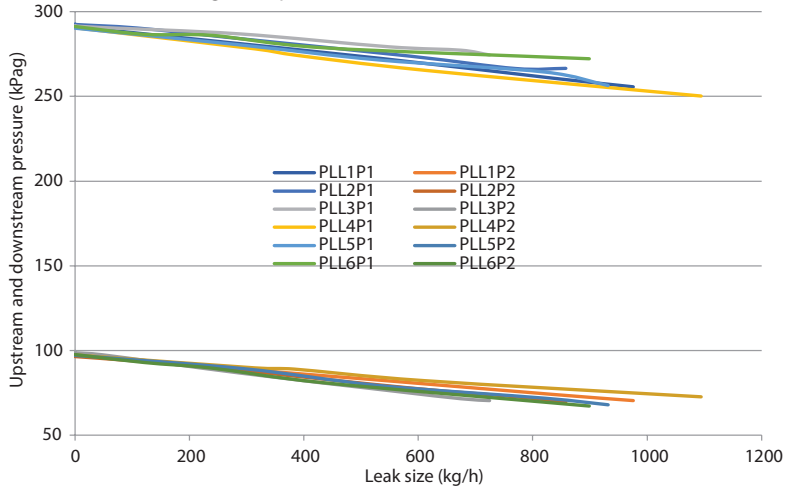

(**b**) Changes of up and down stream pressures with leak sizes

Figure 16.2 Measurement responses of water pipeline to leaks.

test the performances of LDS and check the behaviors and response of the real-time data to leaks of different sizes and locations.

With this LDS system shown as Figure 16.3, 6 sets of leak experiments were conducted on each leak test point to obtain a total of 12 sets of measurement behaviors and responses, shown in Figure 16.4. Here, P1_1-5L indicates pressure readings from upstream PT-1 when there was a leak of 5 L/min at test position Leak1, Q2_2-25L indicates flow readings from upstream FT-2 when there was a leak of 25 L/min at test position Leak 2.

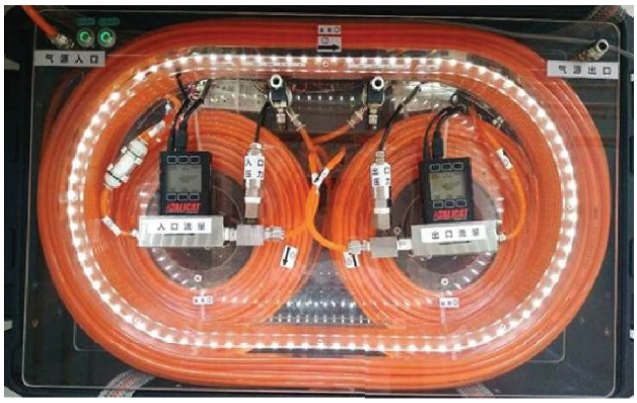

(**a**) Test box of gas leak detection system

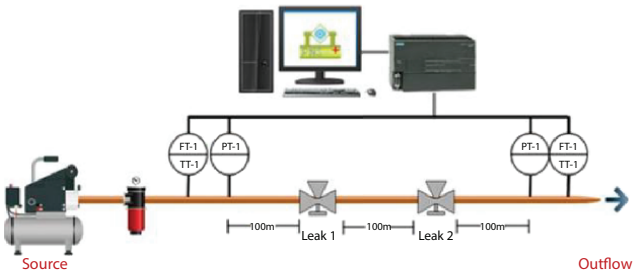

(**b**) Process of the gas leak detection system

Figure 16.3 Sample copy of the gas leak detection system.

The measurement behaviors are presented in Figure 16.4 in response to leaks of different sizes and 2 locations of the air pipeline. Each curve in Figure 16.4(a) shows the over time upstream inlet pressure (P1) changes, recorded by PT-1, while there was a leak occurrence at Leak1 or Leak2 with a leak size from 5 L/min to 30 L/min. The over time downstream outlet pressure (P2) changes were recorded by PT-2 and shown in Figure 16.4(b). The upstream inlet flow-rate (Q1) and downstream outlet flow-rate (Q2) were measured by FT-1 and FT-2 respectively. Figure 16.4(c) gives the trends and compares of inlet and outlet flow due to leaks at Leak1, and same as Figure 16.4(d) at Leak 2.

16.3.3 Summary of Leak Responses

The leak experiment data, shown in Figure 16.2 and Figure 16.4, reveal the measurement responses to leak occurrences, locations and sizes, and these flow behaviors and features are important symptoms of pipeline leaks that can be used to detect and diagnose the leaks. According to Figure 16.2

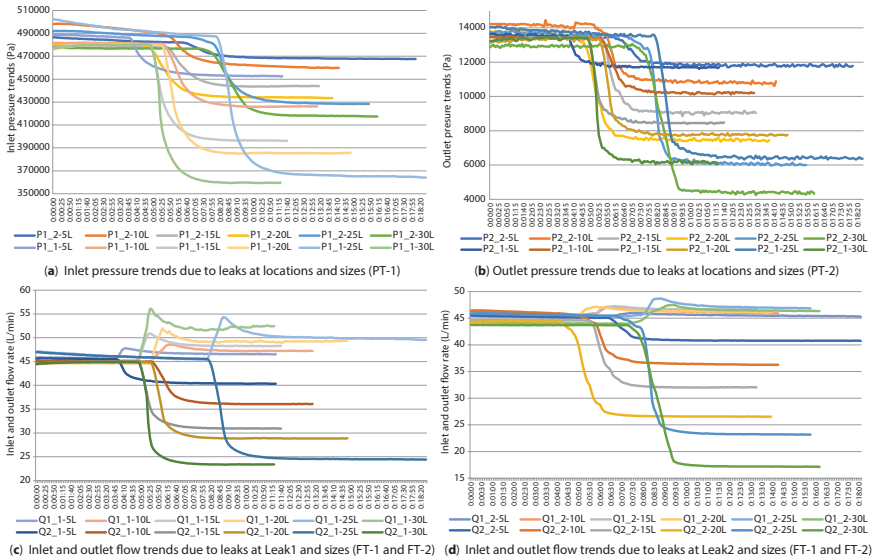

Figure 16.4 Measurement responses to leaks at different sizes and locations of the gas pipeline.

and Figure 16.4, the pipelines' measurement responses to leak occurrences have the following common features:

1. The pressure at both ends will drop drastically if a leak occurs in the pipeline. The bigger the leak size, the more the pressures will decrease. At the same leak size, the closer the leak to the measurement point (up or down stream), the bigger the drop at the point. The pressure dropping rate of gas pipeline is not as significant as liquid pipeline's;
2. The time of the leak occurrence impact on the measurement point depends on the distance between the leak and measurement point. The impact of the leak will initiate from the leak location and develop along the pipeline to both ends at an acoustic speed. The closer the leak to the measurement point, the earlier the readings at the measurement point will be flooded. The pressure and flow-rate measurement readings, excluding temperature, are to be affected quickly;
3. The upstream flowrate will increase and downstream flowrate will decrease in response to the leak occurrences. The bigger the leak size, the more the flowrate will change. At the

same leak size, the closer the leak to the upstream, the higher the upstream flowrate will increase.

16.4 Specification, Measurement Requirements and Features of the Available Pipeline Leak Detection Methods

There are many different leak detection methods available for the AGI pipelines [5]. The CPM methods, which relied upon the SCADA system with the minimum measurement requirements at only the two pipeline ends, are the most effective, economical and easy to be implemented [6].

16.4.1 Mass Balance (MB)

MB method is the most reliable leak detection method which checks the pipeline leak size and status by balance analysis of the inlet/outlet flow measurements and line pack variation over time (Equation 16.1).

$$M_0(t) = \sum M_{in} - \sum M_{out} - \sum_{lines} \frac{\partial}{\partial t}\left[\int_0^L \rho A\, dx\right] = \begin{cases} = 0, \text{no leak} \\ > 0, \text{leak} \end{cases} \tag{16.1}$$

Here, M_{in} *and* M_{out} are the flow measurements at the inlet and outlet of the pipeline, kg/s; M_0 is the estimated leak size; line pack change is considered by integration along the pipeline which is very important when the fluid inside has high compressibility.

Stochastic process should be applied to ensure the reliability of the leak alarm, such as the SPRT (Sequential Probability Ratio Test) algorithm based on Neyman-Pearson's probability ratio.

The MB method issues leak alarm by leak size without leak location. It suffices when the pipeline is not too long and leak location can be easily tracked which is the most common case of the AGI pipelines. Besides the alarm reliability, MB method can discover small leakage over longer times by accumulative impact of the leakage.

But MB method is sensitive and reliable for both gas and liquids pipeline systems, as long as the flow measurements at the two pipeline ends are accurate and effective.

16.4.2 Pressure Point Analysis (PPA)

The PPA method issues leak messages by leak location without size, which is caught by the combination of the wave transfer speed along the pipeline and the time differential of the first pressure sudden changes at the two pipeline ends (Figure 16.5, Equation 16.2).

$$\begin{aligned} x_0 &= \frac{C-V}{2C}\left[L+\left(t_1-t_2\right)\cdot(C+V)\right] \\ &= \frac{C-V}{2C}[L+\delta t\cdot(C+V)] \approx \frac{1}{2}(L-C\cdot\Delta t) \end{aligned} \tag{16.2}$$

Here, x_0 is the leak location estimated, m; C is the acoustic speed, m/s; V is the average flowing speed, m/s; L is the length of the pipeline, m; t_1 and t_2 is the time the leak wave reach the upstream and downstream measurements.

The PPA method obtains the fastest response to the occurrence of leakages and is easy to be implemented. It is very effective to the leak detection for acid gas pipelines of liquid or high density phases, but not for gas phase where no sudden pressure change will occur due to small leakages because of the compressibility. The key process is the discovery of the times from which the pressures at the two pipeline ends begin to drop suddenly.

Despite its immediate response and less measurement requirement, PPA provides lower reliability of leak alarm because 1) there is only one chance to locate the leaks and no update and correction are available after the occurrence; 2) the pressure trends at pipeline ends are also affected by up/down stream connections, fluid inside, and etc.

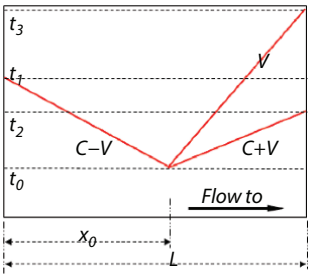

Figure 16.5 Transfer of leak wave along the pipeline.

16.4.3 Real-Time Model (RTM)

The RTM method issues both leak size and location based on the flow rate discrepancy analysis of measured and simulated which comes from the real-time transient models driven by online data and setting [7] (Figure 16.6, Figure 16.7, and Equation 16.3).

$$\begin{cases} Leaksize: M_L^j = E\left(e_1^j\right) - E\left(e_2^j\right) \\ Leaklocation: x_L^j = \dfrac{L}{1 - E\left(e_1^j\right) / E\left(e_2^j\right)} \end{cases} \tag{16.3}$$

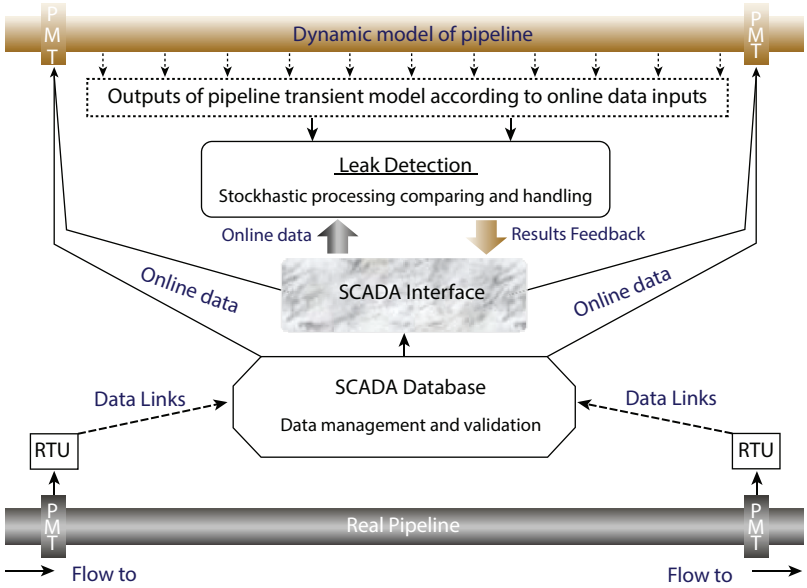

Figure 16.6 System and structure of RTM leak detection.

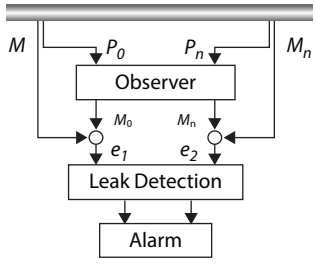

Figure 16.7 Process of RTM leak detection.

where, $e^j = \{e_i(j), i = 1,2\}^t = \begin{Bmatrix} e_1(j) \\ e_2(j) \end{Bmatrix} = \begin{Bmatrix} M_0^j - \overline{M}_0^j \\ M_n^j - \overline{M}_n^j \end{Bmatrix}$, M is the flow rate measured and simulated, kg/s; subscript 0 for upstream, n for downstream and L for leak.

The RTM method is suitable for acid gas pipeline flow in gas, liquid and high-density phases. The correlations for leakage locating and quantity diagnosing are derived on the basis of the online real-time observation and the readings of pressure, temperature, and flow rate at both ends of the pipeline. As an online real-time system, great attention has been paid to the stochastic processing and noise filtering of the meter readings and the models to reduce the impact of signal noise. It is also essential for the robust real-time pipeline observer to have the self-study and adjustment abilities that are needed to respond to the large varieties and uncertainness of pipeline configuration, pipeline operation conditions, and fluid properties.

16.4.4 Data Requirements of the CPM Leak Detection Methods

One of the important advantages of the internal CPM methods over external methods is their complete compatibility of measurement and online data requirements with the ordinary pipeline managements and operations. The real-time flow rates, pressures and temperatures at both pipeline ends can be easily collected and gathered to control centers by SCADA systems which are the standard option of modern pipeline projects.

Each CPM method has its own leak detection measurement requirements and alarm message. Table 16.2 shows the measurement required and alarm message available for the leak detection methods mentioned above.

Table 16.2 Data requirement and solution of CPM leak detection.

		Leak detection methods		
		MB	**PPA**	**RTM**
Measurements required at line ends	Pressure	√	√	√
	Flow rate	√		√
	Temperature	√		√
Leak detection and alarm	Leak Size	√		√
	Leak Location		√	√

Obviously, PPA has the minimum real-time data requirement and is easiest to be implemented.

16.4.5 Matrix Features of the Pipeline LDS

In addition to the internal CPM methods, external LDS methods become more and more popular and provide some featured functions to pipeline leak detection and invasion monitoring. Special consideration must be taken when selecting external methods due to their extra installation and long term maintenance costs. The detailed features of each LDS method are shown in Table 16.3.

16.5 Evaluation of the Erhaolian AGI LDS System

16.5.1 Erhaolian AGI System

Figure 16.8 shows the process and PNS model of Erhaolian AGI system of Sinopec Northwest Company. The pipeline, 3/4" Sch-STD from Inlet_Pipe to Outlet_Pipe, is 2.5 km long with 3 inline pipeline leak locations (PLL) for testing purpose: PLL1 at 0.6 km, PLL2 at 1.25 km and PLL3 at 1.9 km. The injection well, ID 76 mm, is 6040 m long and 5547 m deep. The acid gas to be injected has the following components (mole percentage): 0.440044 of H_2O, 49.4649 of H_2S, 49.785 of CO_2, 0.240024 of C1, 0.040004 of C2 and 0.010001 of N_2.

Figure 16.9 gives the pressure and flow profiles of the system. 11861.2 m^3/d(0.2273 kg/s) of acid gas will be injected through the 6040 m well-bore to the well bottom at 5547 m deep. The well head injection pressure is 7.852 MPa and the well bottom pressure is 60.07 MPa.

16.5.2 Measurement Responses to Different Leak Size and Location

For the pipeline of Erhaolian AGI system, two different leak sizes (0.02 kg/s and 0.03 kg/s) are used for each of the 3 leak testing points (PLL1, PLL2 and PLL3) to do the experiments on measurement responses. Figure 16.10 shows measurement responses to leaks at different sizes (8.8% and 13.2% of the normal flow) and locations (600 m, 1250 m and 1900 m from the upstream).

Table 16.3 Features of pipeline LDS.

	Internal CPM LDS method			**External LDS Method**	
	MB	**PPA**	**RTM**	**Acoustic**	**Fiber optic**
LDS Principle	Statistical analysis (SPRT) of mass balance	Analysis of the pressure drop generated by a leak	Compare between measured and calculated values	Analysis of the infrasonic wave caused by leak	Distributed sensing of temperature, noise/ vibration or hydrocarbons
Application Requirements	Measurements of the mass flow; SCADA and communication	Measurements of pressure, dedicated data acquisition equipment and communication	Measurements of flow, pressure, temperature; SCADA and communication	Measurements of infrasonic wave, dedicated infrasonic sensors and data acquisition equipment and communication	Installation of proprietary fiber optic sensing cable, equipment

(*Continued*)

Table 16.3 Features of pipeline LDS. (*Continued*)

	Internal CPM LDS method			**External LDS method**	
	MB	**PPA**	**RTM**	**Acoustic**	**Fiber optic**
Fluid Application	For gas, liquid and multiphase pipelines, onshore and offshore	For liquid pipelines, onshore and offshore	For gas and liquid pipelines, onshore and offshore	For gas, liquid and multiphase pipelines, onshore and offshore	For gas, liquid and multiphase pipelines, mostly onshore
Reliability	High, designed to minimize false alarms	Low to medium, depending on tuning and system	Medium, depending on model performance	High, once per year was announced	Low to medium, depending on environmental factor and leak effect
Sensitivity	Medium	High, detecting small leaks and thefts quickly	Low to medium due to difficulty in maintaining high accuracy models	High	Very high, detecting small leaks quickly

(*Continued*)

Table 16.3 Features of pipeline LDS. (*Continued*)

	Internal CPM LDS method			**External LDS method**	
	MB	**PPA**	**RTM**	**Acoustic**	**Fiber optic**
Robustness	High, can still detect leaks even if some instruments fail. Works under steady state, transient and shut in conditions	Medium, loss of function if pressure sensors are not available. Works under steady state, transient and shut in conditions	Medium, loss of function due to missing data, slack flow or transient operations	Low	Low, may not detect leaks if cable is cut or if the hole is not located near the cable. Works under steady state, transient and shut in conditions
Leak Location Accuracy	No	High, down to 100's of meters, depending on scanning rate	Low to medium, depending on model performance	Very high, down to 10's of meters	Very high, down to 10's of meters

(*Continued*)

Table 16.3 Features of pipeline LDS. (*Continued*)

	Internal CPM LDS method			External LDS method	
	MB	**PPA**	**RTM**	**Acoustic**	**Fiber optic**
Calculation of Leak Size	Yes	No	Yes	No	No
Installation Cost*	Medium	Low	High	Very high if cable is to be installed	Very high if cable is to be installed
Maintenance Cost	Medium	Medium	Medium, expert tuning required	Very high, special team required	Very high, special team required
Remarks	Good track record on both gas and liquid pipelines. Suitable for existing and new pipelines.	Requires pressure sensors only. Suitable for existing and new pipelines.	Suitable for existing and new gas/liquid pipelines if flow, pressure, temperature measurements are available.	Dedicated infrasonic sensors and data acquisition equipment and communication required, suitable for existing and new pipelines.	DAS/DVS can be used for intruder detection. Difficult to test the performance. Difficult to retrofit.

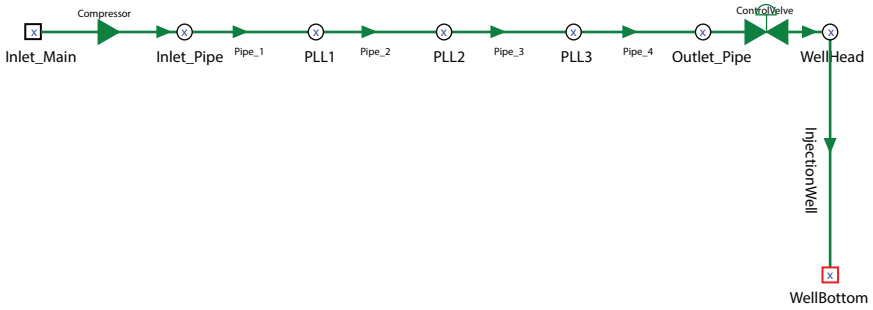

Figure 16.8 Process and PNS model for Erhaolian AGI system.

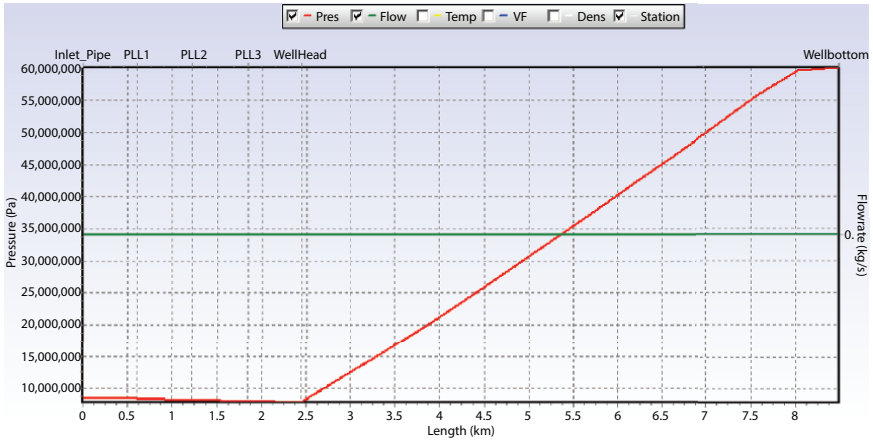

Figure 16.9 Normal pressure and flow profiles of Erhaolian AGI system.

1. Each curve in Figure 16.10(a) gives the trends and compares of inlet and outlet flows due to leaks at different sizes and locations. With the occurrence of leaks, the differentials between the upstream and downstream flows increase from zero at normal status to leak sizes at leak status. The bigger the leak size, the more the differential of the up and down stream flows. While there is a leak at any location, the upstream flow rate will go little bit higher and the downstream flow rate will go much lower than the flow without leaks;
2. Figure 16.10(b) shows the upstream pressure changes over time. With the occurrence of leaks, the upstream pressure

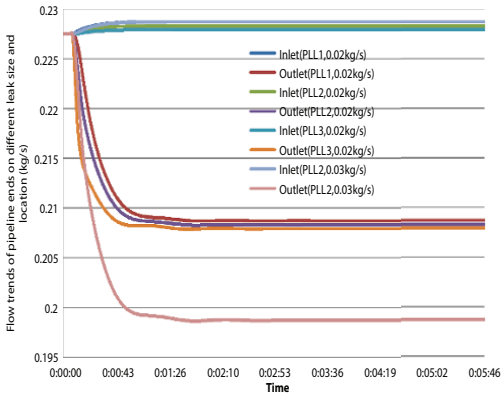

(**a**) Flow trends of pipeline ends on different leak size and location

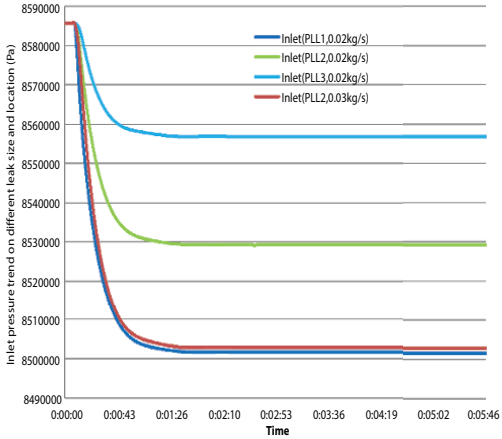

(**b**) Inlet pressure trend on different leak size and location

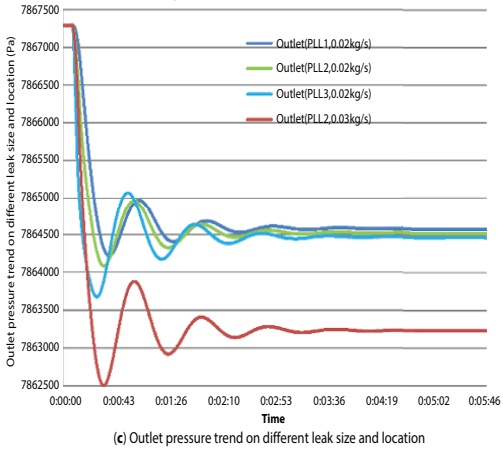

(**c**) Outlet pressure trend on different leak size and location

Figure 16.10 Measurement responses due to leaks of Erhaolian AGI pipeline.

drops quickly and significantly, depending on both the leak sizes and locations;

3. The overtime downstream pressure changes are shown in Figure 16.10(c). With the occurrence of leaks, the downstream pressure drops quickly but not as significantly as the upstream pressure. The leak size has more impact than the leak location on the pressure drops, such as a drop of 2.8 kPa on a leak of 0.02 kg/s and a drop of 4.06 kPa on a leak of 0.03 kg/s. In this case, the PPA method will not work properly for the small leaks because the pressure measurements are insensitive to insignificant pressure drop.

Comparing Figure 16.2 and Figure 16.4 with Figure 16.10, the measurement responses of an AGI pipeline are very close to and similar with the experiments done in labs, although the AGI pipeline system differentiates greatly from the pipeline systems in lab.

16.5.3 The Performances of CPM Leak Detection Methods

A series of leak detection experiments was conducted to check the performances of the CPM leak methods by the virtual AGI system shown in Figure 16.8. Five different leak sizes (0.01 kg/s, 0.02 kg/s, 0.03 kg/s, 0.05 kg/s and 0.08 kg/s) are applied to each of the 3 leak testing points (PLL1, PLL2 and PLL3).

The architecture of virtual LDS for Erhaolian AGI system consists of the virtual AGI system and the virtual LDS model for the AGI pipeline, as shown in Figure 16.11. The virtual LDS model is driven by the real-time

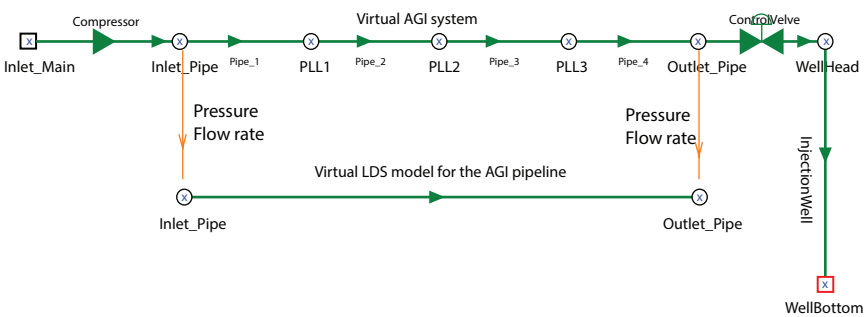

Figure 16.11 Architecture of virtual LDS for Erhaolian AGI pipeline.

pressure, flowrate and temperature from Inlet_Pipe and Outlet_Pipe to do the following processes at given time interval:

1. Online RTM simulation driven by up and downstream pressures;
2. Line-pack calculation based on the simulated pressure and temperature profiles;
3. Mass balance leak detection according to up/down stream flow readings, line-pack variations, and stochastic diagnosing;
4. RTM leak sizing and locating by correlation analysis of the differential between simulated and measured flow rates at the pipeline ends.

Figure 16.12 shows the screen shots of leak detection procedures by PNS^{TM} 4.2, including the leak locating by RTM and the leak sizing by MB.

Figures 16.13 and 16.14 demonstrate the overall performances and procedures of leak locating and sizing. Figure 16.13 shows the diagnosing procedures of leak size by MB method for different leak sizes and locations.

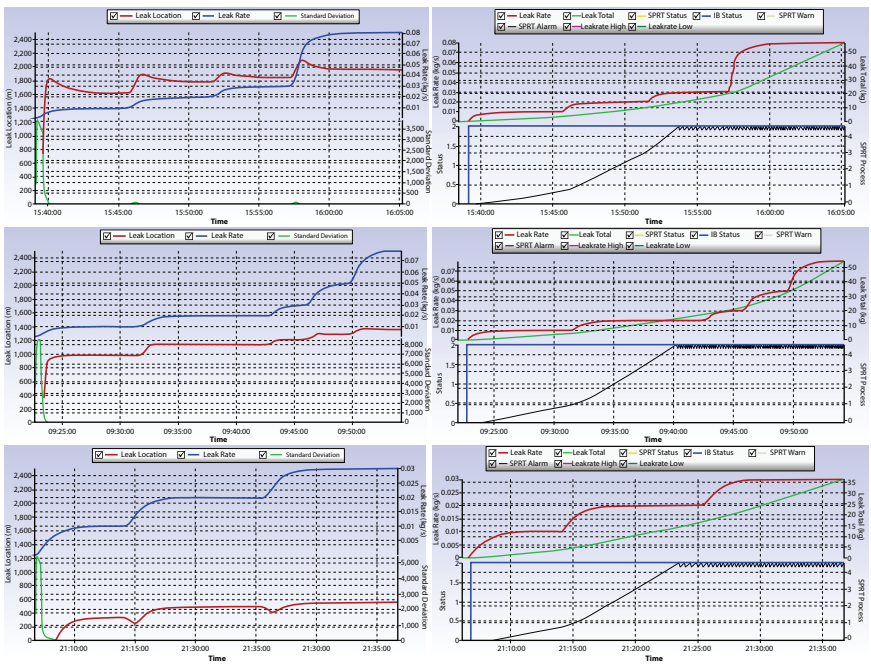

Figure 16.12 Performances of PNS leak detection on Erhaolian AGI pipeline.

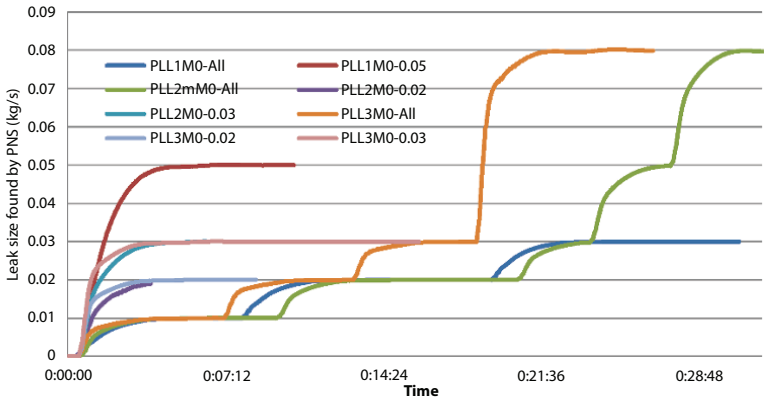

Figure 16.13 Procedures to find leak size by MB for different leak sizes and locations.

Figure 16.14 shows the leak locating procedures by RTM method for different leak sizes and locations. The following phenomena can be observed from the procedures:

1. As long as a leak occurs and continues, the sizing procedure by MB and locating and sizing procedures by RTM will work and update continuously and target at the better solution;

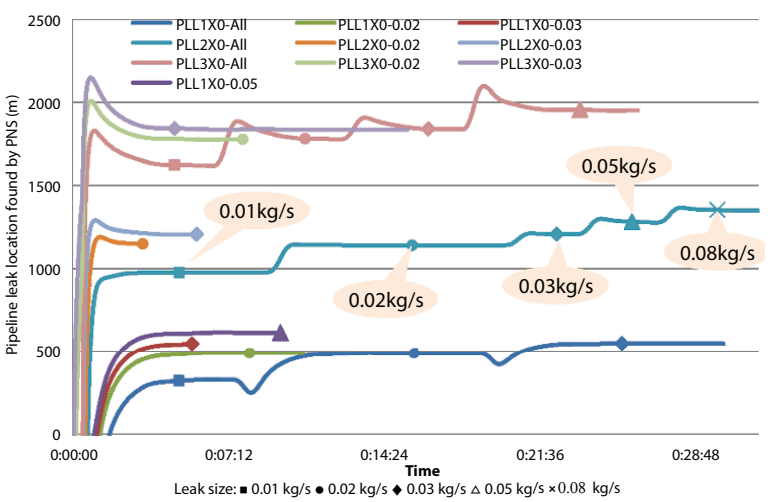

Figure 16.14 Procedures to find leak size by RTM for different leak sizes and locations.

2. The estimation procedures of leak size by MB are mainly affected by the leak size, despite where the leak occurs. Alarms will be issued faster if the leak size is larger;
3. The locating and sizing procedures of leaks by RTM are effective in response to the occurrence and development of leaks. The estimated leak location and size will approach eventually to its best solution over time. The bigger the leak, the faster and closer the estimation will approach the correct values.

16.6 Conclusion

1. Every AGI system is different. Special considerations should be taken into whenever selecting the LDS for an AGI pipeline, such as the composition, lengths, phases, high consequences, measurements and SCADA, and etc.;
2. For a short acid gas pipeline, more attention should be paid to increasing the sensitivity and reliability of the LDS than locating the leak. In this case, MB method may suffice;
3. The CPM leak detection methods, based on the internal flow of the pipelines defined by API 1130, should be the first option when selecting the LDS system because it is easy, effective, efficient, and economical to be implemented, installed, and operated. The CPM methods should provide acceptable leak detection performances because the AGI pipeline is short of variations;
4. For high consequence areas of an AGI project, multiple leak detection systems should be considered. For example, in addition to the MB and RTM methods that monitor the pipeline leak status systematically, H_2S sensors should be installed at sensitive points, such as well head, lower points that are close to the AGI facilities in the high consequence areas.

16.7 Acknowledgments

This paper is sponsored by National Natural Science Foundation of China (NSFC:51274166), Sinopec (G86YJ-12-ZS-0006) and Shaanxi Science and Technology Coordinating innovation project (2016KTZDGY07-05).

References

1. Bouchet, S., Kasprzycki, S., Lepine, N. *et al.*, Evaluation of fixed point H2S gas detectors intended for use in industrial safety applications, 2010.
2. Ali, F.I.M., Awwad, F., Greish, Y.E., Mahmoud, S.T., "Hydrogen Sulfide (H_2S) Gas Sensor: A Review," in. *IEEE Sens. J.*, 19, 7, 2394–2407, 1 April, 2019.
3. Wikipedia, List of pipeline accidents in the United States in the 21st century. https://en.wikipedia.org/wiki/List_of_pipeline_accidents_in_the_United_States_in_the_21st_century, Feb.18, 2017.
4. API 1130, Computational Pipeline Monitoring for Liquids Pipeline, American Petroleum Institute, 2007.
5. Zhang, J., Hoffman, A., Murphy, K., Lewis, J., Twomey, M., Review of Pipeline Leak Detection Technologies, PSIG 1303, Prague, Czech Republic, 16–19 April 2013.
6. Shaw, D., Phillips, M., Baker, R., Munoz, E., Rehman, H., Gibson, C., Mayernik, C., Leak Detection Study – DTPH56-11-D000001, U.S. Department of Transportation Pipeline and Hazardous Materials Safety Administration, Dec. 10 2012.
7. Wang, S. and Carroll, J.J., Leak Detection for Gas and Liquid Pipelines by Online Modeling, SPE104133, SPE Projects, Facilities & Construction, 2007.

17

Injection of Non-Condensable Gas in SAGD Using Modified Well Configurations - A Simulation Study

Yushuo Zhang* and Brij Maini

Chemical and Petroleum Engineering Department, University of Calgary, Calgary, AB, Canada

Abstract

The objective of this research is to examine the feasibility of NCG co-injection with steam in SAGD using modified well configurations using numerical simulation. The NCG used in this project is methane. The aim is to form a more stable insulating layer just below the top of formation, which results in lowered overburden heat loss and cSOR. To place the NCG directly below the overburden rock, vertical steam injectors with dual completions are implemented in this study. Simulation runs are created using CMG STARS (Thermal and Advanced Process Simulator). These simulation results demonstrated substantial improvement in cSOR by injecting NCG separately from steam using the dual completed vertical injectors.

The producer operational constraint is a combination of maximum live steam rate and minimum bottom-hole pressure (BHP). The base case covers production from May 2011 to January 2020 in steam only SAGD operation. The base case of non-flowing boundary condition showed approximately 157,000 m3 oil production in about 10 years, with a cumulative Steam Oil Ratio (cSOR) of 9.0.

The simulation results show that injecting the non-condensable gas improved cSOR but maintained similar cumulative oil production compared to conventional SAGD process. As expected, non-condensable gas reduces the gas mobility and stabilizes the insulating blanket formed by high gas saturation at the top of the steam chamber. The optimized simulation case with three vertical wells enabled the cSOR to be as low as 2.27.

Keywords: SAGD, NCG, modified well configuration, heat loss

**Corresponding author*: yus.zhang@hotmail.com

Ying Wu, John J. Carroll, Mingqiang Hao and Weiyao Zhu (eds.) Gas Injection into Geological Formations and Related Topics, (283–308) © 2020 Scrivener Publishing LLC

17.1 Introduction

17.1.1 Background

Canada has one of the world's third-largest oil reserves, and 97% of the reserves are Alberta's oil sands. Alberta's oil sands can be found in three deposits: Athabasca, Cold Lake, and Peace River [1]. Due to the high viscosity of bitumen, additional treatments are required to produce oil. About 20% of the oil sands are close enough to the surface to be mined. The rest of the oil sands are too deep to be mined. For those *in situ* oil sands, steam assisted gravity drainage (SAGD) and cyclic steam stimulation (CSS) are commonly used technologies to produce oil.

This project focused on the Long Lake type reservoirs. In a SAGD operation, two horizontal wells are drilled – namely the injector and the producer. Steam is injected through the injector to lower the viscosity of the bitumen. The producer is normally placed five meters below the injector. Bitumen is drained to the producer primarily due to the gravitational force.

17.1.2 Project Objectives

The proposed NCG (non-condensable gas) injection project takes place at the fourth well pair of Pad 11 (Injector: 04/04-01-086-07W4/0, Producer: 10/04-01-086-07W4/0). The main objective of the project is to assess the effects of co-injection of NCG with steam on reservoir performance that includes production and steam losses to top water/high water saturation zones [2].

In this project, methane is used as the NCG to be co-injected with steam at rate of 1 vol% to 3 vol% [3]. The Long Lake SAGD project is an *in situ* oil extraction project 40km southeast of Fort McMurray in the Athabasca oil sands region of Alberta. The proposed NCG (non-condensable gas) injection project will take place at the fourth well pair of Pad 11 (Injector: 04/04-01-086-07W4/0, Producer: 10/04-01-086-07W4/0).

Steam circulation at Pad 11 began in December 2009 and SAGD production commenced 5 months later. As of May 2015, Pad 11P04 had recovered approximately 23.3% (90254.0 m^3) of the estimated bitumen in place (386630.2 m^3).

17.2 Relevant Field History

17.2.1 Depositional History

The Long Lake SAGD project is focused on the oil sands reservoir within the lower McMurray Formation, the basal unit of the Lower Cretaceous Mannville Group. The McMurray formation directly overlies the sub-Cretaceous uniformly that is developed on the Paleozoic carbonates of the Beaverhill Lake Group (4). Directly overlying the McMurray Formation are the Wabiskaw, Clearwater and Grand Rapids formation of the Beaverhill Lake Group.

17.3 Reservoir Characterization

17.3.1 Geology Overview

The characterization of the McMurray formation was examined through the use of logs, core data and literature [5]. Six Observation and Abandoned wells within Pad 11 were investigated. Well logs provide the insight of the formations and conditions in the subsurface, and primarily aim at detection and evaluation of possibly productive horizons.

17.3.1.1 Core Analysis

In general, the laboratory works on a core sample that may yield permeability, porosity, pore size distribution, grain size and density. Core analysis data for OB and AB wells in Pad 11 are obtained [5]. Core porosity was compared with values read from the log interpretation. The average core horizontal and vertical permeability data can be also obtained.

17.3.1.2 Log Analysis

Open-hole well logs of six observation and abandoned wells were interpreted. Gamma ray, density and neutron porosity, and formation resistivity logs were interpreted at a one-meter interval. From all the log reading, the cumulative shale volumes, the effective porosity, net pay, water saturations and oil saturations were calculated.

17.3.1.3 Shale Volume Calculations

Shale has great impact on porosity, permeability and fluid distribution. The Gamma Ray log was used to estimate the shale content of Sandstone. The shale volume (V_{sh}) was determined by using the following equations [6].

Let,

$$X = \frac{\text{GR ss} - \text{GR clean}}{\text{GR shale} - \text{GR clean}} \tag{17.1}$$

$$\text{Vsh} = 1.7 - [3.38 - (X + 0.7)^2]^{0.5} \tag{17.2}$$

Values of GR shale = 110 and GR clean = 20 were used in our calculation.

17.3.1.4 Porosity Calculations

The estimated average porosity of the formation was calculated using the neutron and density porosities obtained from the logs using the following equations [6]:

$$\phi_{total} = \frac{\phi_{D+}\phi_N}{2} \tag{17.3}$$

The presence of shale content requires further correction in order to calculate the effective porosity [6]:

$$\Phi_{eff} = (1 - \text{Vsh})^{*}\phi_{total} \tag{17.4}$$

The effective porosity for Pad 11 was calculated to be 32% by using the best log representation.

17.3.1.5 Water and Oil Saturation

Water saturation (S_w) determination is the most challenging of petrophysical calculations and is used to derive the hydrocarbon saturation ($1\text{-}S_w$). Because of the content of shale affecting the resistivity responses in the formation, Simandoux method is used when $V_{sh} > 0.20$ and $R_{sh} < 8.0$. Therefore, the Simandoux expression for shaly sands was used to calculate the water saturation [7].

From log interpretation, only the best well logging data were used for the water saturation calculation. This resulted in average water saturation from Pad11 observation and abandoned wells to be 26.3%.

17.3.2 Permeability Data

A linear relationship between logarithm permeability and porosity was developed in order to get more reliable data [8]. K_{max} values were obtained from AccuMap, and the correlation of K_{max} and porosity was created. The data points of K_{max} and porosity are scattered around and could not obtain a linear line from the plot.

Clayton V Deutsch and his team developed a core and FMI image-based hierarchical permeability modeling approach that applied to several Long Lake wells in 2011 [9]. Since the correlation is not obvious from our permeability data, the permeability modeling approach will be used to calculate permeability values at each pay depth according to porosity data. Equation listed below were used to calculate horizontal permeability and vertical permeability:

$$K_H = 92121^* \varnothing^{2.7193} \tag{17.5}$$

$$K_V = 0.8848^* K_H - 137.02 \tag{17.6}$$

The calculated average vertical permeability is 2915.9 mD and calculated average horizontal permeability is 4671.24 mD, respectively.

17.3.3 PVT Data

Athabasca bitumen viscosity differs over a temperature range from 20 to 300°C [10]. Viscosity vs. Temperature curves for Long Lake bitumen were obtained [11].

Based on STARS User Guide (2017), the distribution of solution gas between liquid and gas phases is determined by the temperature and pressure dependent K-value correlation. Therefore, Gas-Liquid K values coefficients for methane were used in simulation for flash calculation, and K values can be calculated using the equation [12]:

$$K = \frac{KV1}{P} * \exp\left(\frac{KV4}{T - KV5}\right) \tag{17.7}$$

where KV1, KV4 and KV5 correspond to the units of P and T. Specifically, K values of methane are calculated using the following equation.

$$K = \frac{545470}{P\ (kPa)} * \exp\left(\frac{-879.84}{T(°C) + 265.99}\right) \tag{17.8}$$

17.3.4 Reservoir Values

From the log analysis, the reservoir characterization results are listed in Table 17.1.

17.4 Analytical Production Forecast

17.4.1 Butler Model

The Butler model is based on a quasi-steady state approximation, and it treated an ideal situation where heat lost by condensed steam occurs uniformly along a two-dimensional, symmetric steam chamber-bitumen interface [13].

Thermal diffusivity and bitumen kinetic viscosity values listed in the reservoir property were used in the Butler model. Butler's model assumes a homogenous reservoir, and therefore, uses an average effective permeability for the calculations. Average vertical permeability is used in the Butler

Table 17.1 Reservoir characterization results.

Formation properties	Average values
Gross Pay (m)	40-50
Net Pay (m)	20-32
Porosity (%)	32
Water Saturation (%)	26.3
Oil Saturation (%)	73.7
Horizontal Permeability (mD)	4671.24
Vertical Permeability (mD)	2915.9

model since vertical permeability plays the most important role in Gravity Drainage. Therefore, the average vertical permeability is used as initial permeability input in the Butler model.

Figure 17.1 shows the bitumen rate in the field and the rate obtained from Butler's model for well 11P05 after tuning input parameters. A decent history match to field data is obtained, and it plays an important role for production forecasting. In this analytical model, permeability decreases

Table 17.2 Average reservoir properties used in the history matched Butler's model.

Steam Pressure (kPa)	1860
Permeability (Darcy)	0.5
Porosity	0.32
Initial Oil Saturation	0.737
Change in Oil Saturation	0.637
Viscosity "m" Value	4
Reservoir Width (m)	39
Reservoir Length (m)	440
Reservoir Height (m)	28

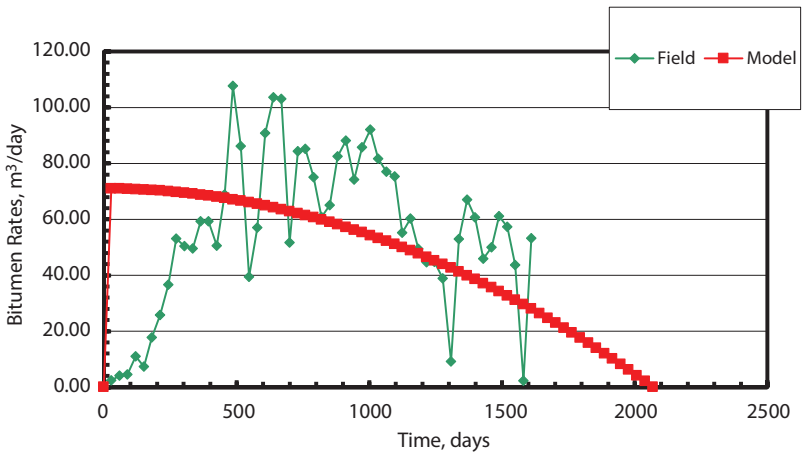

Figure 17.1 Production rates forecast for 11P04 based on optimized history match model.

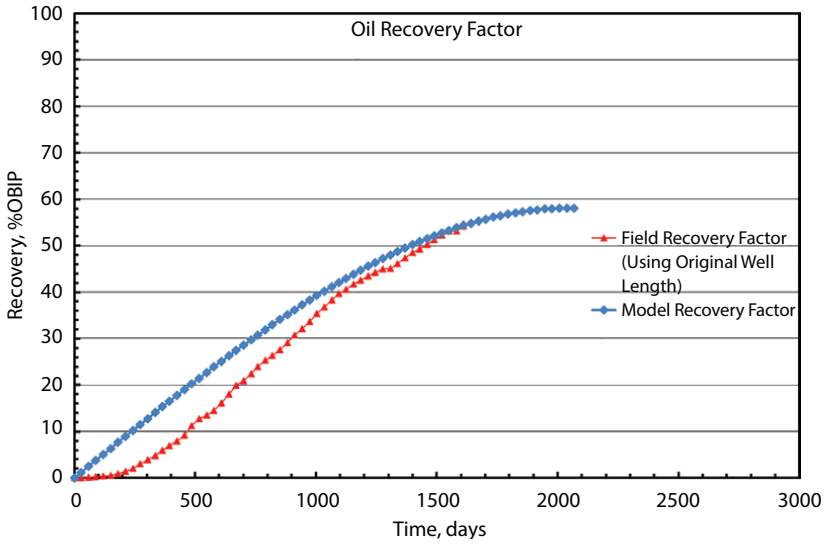

Figure 17.2 Recovery factors for field and model for 11P04.

from 3.996 Darcy to 0.5 Darcy, and reservoir length shrinks from 647 meters to 440 meters. Moreover, the residual oil saturation also decreases from 0.2 to 0.1, which corresponds to a changeable oil saturation of 0.637. Overall, the analytical model over predicts the amount of bitumen produced. Table 17.2 lists average reservoir properties used in the history

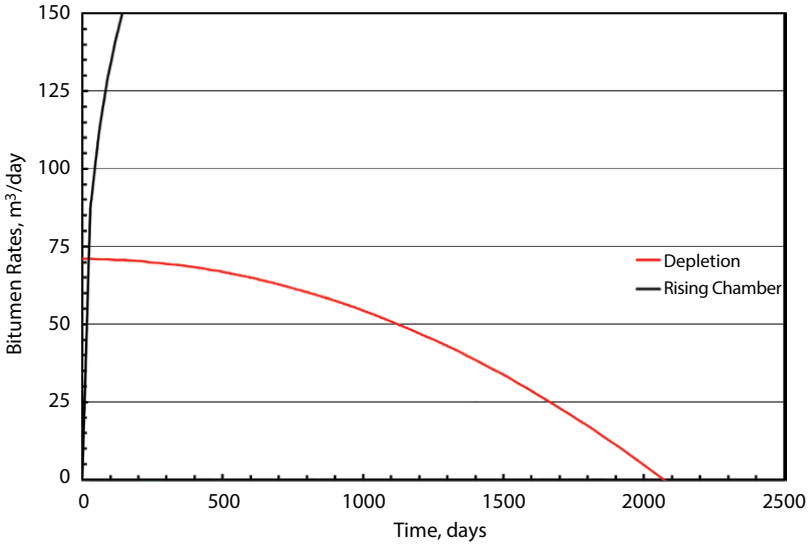

Figure 17.3 Depletion and rising chamber bitumen rates.

matched Butler's model. The field cumulative production for 11P04 after 1611 days of operation is 90169 m^3. At this time, Butler's model predicts 90597.6 m^3 of bitumen produced, resulting in a % error of 0.48%. At the end of field operation, the recovery factor is about 54% but the recovery factor using Butler's model is 58.10% due to a decrease in reservoir length. Butler's model shows the life of the well is around 5.67 years.

Figure 17.2 shows the comparison between the model recovery factor (using effective reservoir length) and the field recovery factor (using initial reservoir length). Depletion and rising chamber oil rates are plotted in Figure 17.3. In the end of production using the Butler model, the cumulative oil production is about 96855.2m^3, and the overall recovery factor is about 58.10%.

17.4.2 Reservoir Performance with NCG Co-Injection

The main goal for this project is assessing the potential benefits of non-condensable gas (NCG) co-injection with steam using a modified well configuration. NCG at the top of the steam chamber improves SOR by reducing heat loss to the overburden. From reservoir interpretation, top water is identified above the net pay formation.

NCG forms a stable isolation below top formation and prevents direct contact between hot steam chamber and formation. Therefore, methane provides further insulation and reduction of overburden heat loss, which contributes to reduction of injecting steam [14].

17.5 Reservoir Simulation

17.5.1 Geological Model

The model was constructed with lateral homogeneity (i and j direction) and vertical heterogeneity (k direction). Since the SAGD process depends on growth of the steam chamber, which is predominantly influenced by the vertical reservoir properties, therefore a vertical heterogeneous reservoir was deemed adequate for this simulation model.

The geological model consists of 68 layers in the vertical direction (k direction), 43 x 1m layers perpendicular to the horizontal well direction (i direction), and 25 x 50m layers along the horizontal well direction (j direction). The zone of interest for grid top is from depth of 185m (top of the gas cap) to 228m (2m below the producer). Because of the model is

laterally homogeneous in the horizontal direction, this will improve the simulation run time.

Initially, the grid top structural map and gross pay map for the Pad 11P04 area were digitized. Maps were originally obtained and contour map interpretations were obtained [5]. The model consists of several uniform reservoir parameters but it does not accurately represent the complexity of this reservoir. The actual geostatistical model accounts for lateral and vertical heterogeneity. Due to the available data on AccuMap, the current model is built vertical heterogeneously and lateral homogeneously.

17.5.2 Reservoir Property

The gross pay and net pay of the reservoir were determined through the log interpretation and volumetric calculation. The grid top, top gas and cut off depths were also determined. This reservoir is a live-oil reservoir. The gas zone is located from 185m to 190m. In the gas zone, each component of saturations (S_w=0, S_o=0.30, S_g=0.70) is specified. Top water zone (S_w=0.70, S_o=0.30, S_g=0) is located from 190m to197.5m. The oil saturation and water saturation in the bitumen zone, porosity and permeability were also determined from reservoir interpretation.

The properties were calculated from the log analysis from all observation wells located within Pad 11, which was closest to 10/04-01-086-07W4/0. In order to improve maps prior to simulation, the grid top contour map and gross pay contour map were retrieved again (5). The porosity, water saturation and oil saturation were determined at each 1-meter interval.

Given that Pad 11 is an unconventional reservoir, the vertical permeability is most imperative to fluid flow for SAGD. The horizontal permeability is laterally homogenous in the model. The vertical permeability is calculated using correlation ratio (K_v/K_H). The calculated average vertical permeability is 2915.9 mD and calculated average horizontal permeability is 4671.24 mD, respectively.

17.5.3 Well Location

The surface-hole UTM Easting (501532.74m) and the UTM Northing (6252105.33m) is used as surface reference point for the CMG model. The surface reference point is located 687 m west and 200.6 m south of the wellhead of 11P04. It defines the origin point (0, 0) for the CMG model on the i-j grid. The surface UTM coordinates and true vertical depth (TVD)

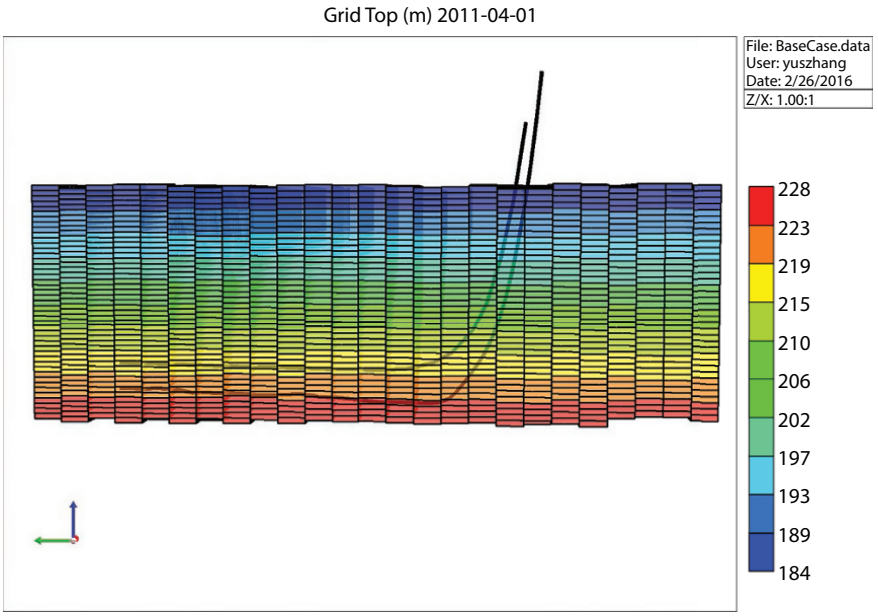

Figure 17.4 Well trajectory side view.

for the 11P04 were also obtained and were corrected to the reference point to obtain CMG model coordinates [5]. This allows the exact well trajectories to be generated in the CMG model. The coordinates for horizontal well pair were obtained from the AccuMap. Figure 17.4 illustrates the well trajectory side view in reservoir simulation model.

17.5.4 Initial Reservoir Simulation Inputs

Reservoir simulation inputs were required to initialize the reservoir model. Initial reservoir temperature for the model is 7°C [15]. Initial pressure is set to be 1100 kPa at reference depth of 228 m. The initial GOR of reservoir is 10 SCF/1 STB, which converts to oil mole fraction at reservoir condition. Therefore, the calculated oil mole fraction for bitumen is 0.9548, and oil mole fraction for methane is 0.0452, respectively.

17.5.5 Relative Permeability Data

The oil-water and the gas-liquid relative permeability curves are shown in Figures 17.5 and 17.6. The end-point relative permeability data were from a generic Athabasca oil sands reservoir [16]. The relative end-points of the curves were adjustable parameters for history matching production from 11P04.

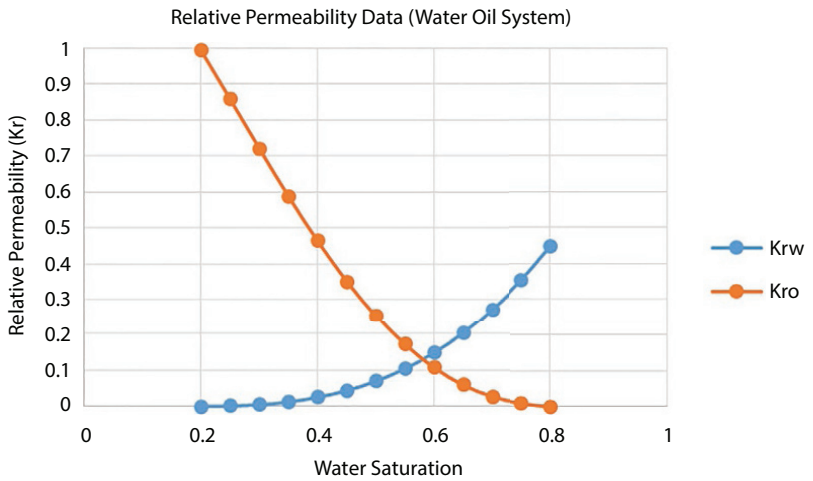

Figure 17.5 Relative permeability curve for oil-water system.

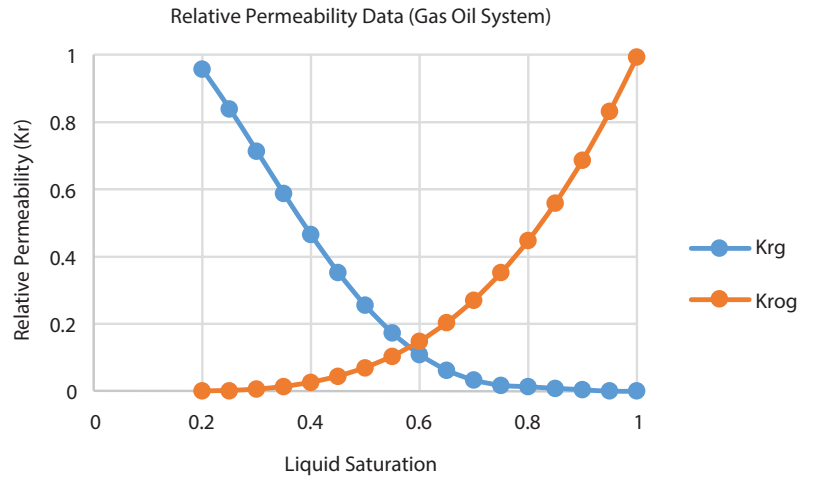

Figure 17.6 Relative permeability curve for gas-oil system.

17.5.6 Well Operational Parameters

It is essential that well communication to be established during the SAGD pre-heating stage. This is accomplished in the circulation period by increasing the temperature of the reservoir in between the injector and producer, resulting in lower bitumen viscosity and increased mobility. The circulation stage model was simulated using heaters. Heater Wells were used for

injector and producer to model the heat transfer that occurs before beginning SAGD operations.

The SAGD mode was initiated after two months of circulation from April 2011 to May 2011. Well operational constraints were specified for the initial simulation run. The primary constraint for the injectors was the surface water rate obtained from field data. The injected steam was set to a temperature of 208°C with 90% saturated steam. The producer's constraint was initially set to surface oil rate from field data and then changed to surface liquid rate in history matching. In order to prevent excess steam production, the steam constraint for the producer was set to a maximum value of 5 m^3/day.

17.5.7 History Match

The preliminary simulation results were plotted on a graph and compared to the field production history exported from AccuMap [5].

The objective of the history match is to calibrate oil and water production rates and steam chamber development from the model to compare with actual field data. Therefore, reservoir parameters were adjusted in order to obtain an adequate match. The key parameters are relative oil permeability at connate water saturation (K_{ro}), relative water permeability at irreducible oil saturation (K_{rw}), relative gas permeability at connate liquid saturation (K_{rg}), critical water saturation, irreducible oil saturation, residual oil saturation, and vertical permeability to horizontal permeability ratio (K_V/K_H). The non-flowing boundary and the flowing boundary production history matching were conducted throughout the semester.

17.5.7.1 Flowing Boundary Condition

The simulation with flowing boundary is created to obtain better history matching results. We add total 30 vertical producers at the sides of the grid block shown in Figure 17.7. Each edged well has three meter well spacing. The reservoir pressure for the producer is 1100 kPa, which is close to initial reservoir pressure of 1043 kPa. The main objective of adding the flowing boundary for our model is to drop the water production when preforms history matching and to prevent pressure build-up in the reservoir. With the flowing boundary, the fluid flow is more realistic.

17.5.7.2 Final History Match Results

Based on the results from the above changes, it was determined that a sufficient history match was obtained using the following relative permeability data.

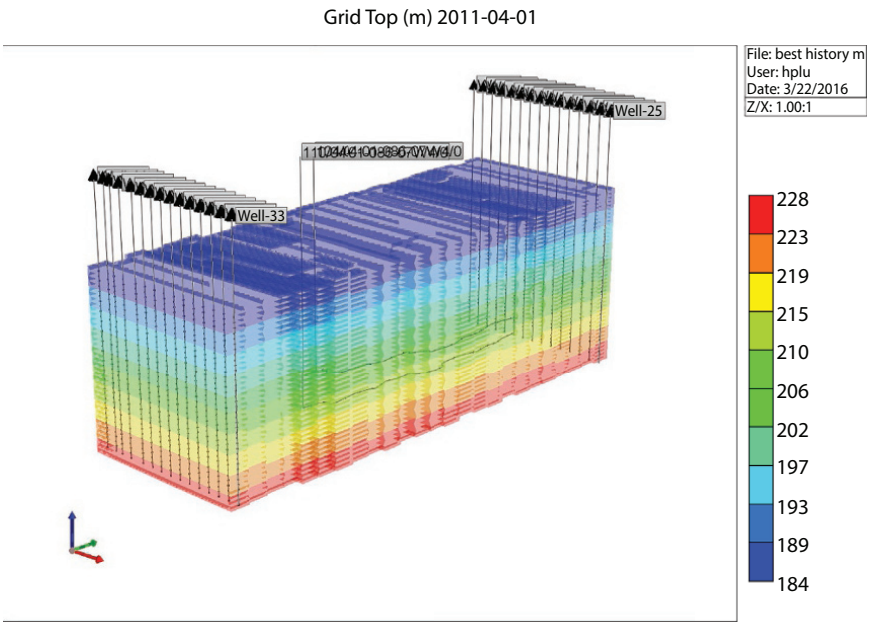

Figure 17.7 Simulation 3D model with flowing boundary.

The simulation cumulative oil production was almost overlapped of the field production data as seen in Figure 17.8. It was the best history match case using above parameters.

The surface liquid rate was exactly history matched because the total surface liquid is set to be an operational constraint. The cumulative oil production for the model is 96, 000 m^3, and the recovery factor is 24% for the entire field in 2016.

Literature research was conducted to determine how to further calibrate the water production and oil production from the simulation. Once the lean zones are accurately identified, the critical water saturation of different regions is adjusted to obtain a better history match. The produced water from our simulation matches up almost perfectly with the field result; the oil appears to have an accurate history match. Various changes to simulation parameters were attempted to improve produced oil, but this final run presented was the most representative of overall field production and pressures. Due to limited data and time constraints, the final history match presented is deemed acceptable to run forecasts and evaluate the modified well performance. Table 17.3 lists input parameters for best history matching in reservoir simulation studies.

Table 17.3 Input parameters for best history matching.

SWCON - Endpoint Saturation: Connate Water	0.2
SWCRIT - Endpoint Saturation: Critical Water	0.3
SOIRW - Endpoint Saturation: Irreducible Oil for Water-Oil Table	0.1
SORW - Endpoint Saturation: Residual Oil for Water-Oil Table	0.1
SOIRG - Endpoint Saturation: Irreducible Oil for Gas-Liquid Table	0.1
SORG - Endpoint Saturation: Residual Oil for Gas-Liquid Table	0.1
SGCON - Endpoint Saturation: Connate Gas	0
SGCRIT - Endpoint Saturation: Critical Gas	0
KROCW - Kro at Connate Water	1
KRWIRO - Krw at Irreducible Oil	0.4
KRGCL - Krg at Connate Liquid	0.4
Kv/Kh Ratio	0.4
Steam Quality	0.95

17.5.8 SAGD Production Forecasts

Production forecasting provides insight into the longevity of a well. Indicators such as recovery factor, production rates, SOR's and energy lost to all boundaries can be used to estimate future performance. A base case production forecast was completed using the achieved history match to observe future reservoir performance of well pair 11P04 until 2020.

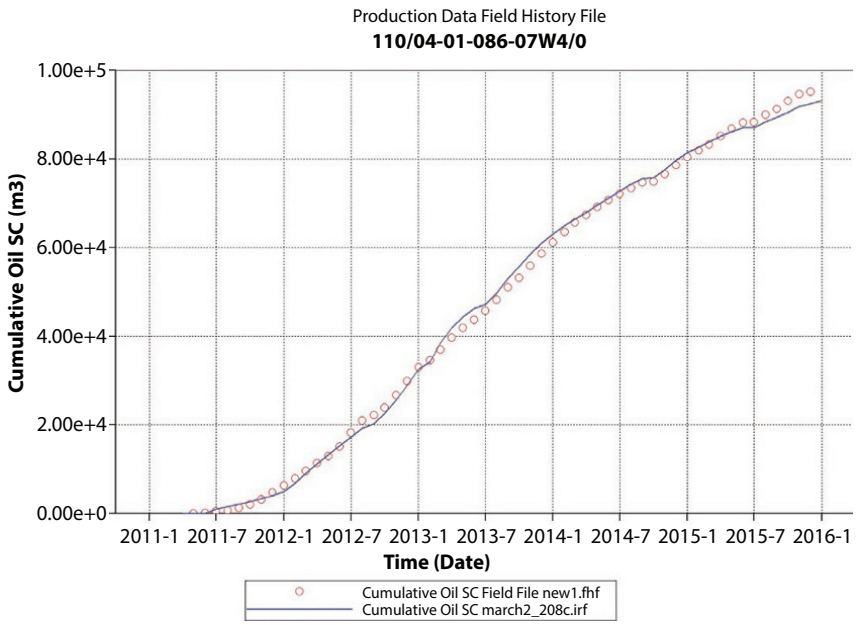

Figure 17.8 Final run cumulative oil volume.

17.5.8.1 Base Case HZ Well Production with Steam Only (Flowing Boundary)

Production forecasting were applied to the model in order to obtain a forecast. Models were run based on their operational constraints which were the bottom-hole pressure (BHP) and maximum steam injection rates. A series of production forecasts at different operational constraints and were run for comparison. The following is the traditional horizontal production forecast model with steam as a base case.

Well ran on since May 2011. The production data forecast to January 2020. The operational constraints were changed from surface water rate to bottom-hole pressure 3000 kPa for injector in January 2016. The primary operational constraint for producer changed from liquid rate to minimum bottom-hole pressure 1073.72 kPa in January 2016. The secondary operational constraint for producer was set the maximum steam rate to 5 m^3/day.

The cumulative oil production for the model is 104, 000 m^3, and the recovery factor is 29% for the entire field in 2020.

17.5.8.2 Forecast Results: Production Rate

Based on the current operational constraints, the daily oil production forecast for 11P04 is also analyzed. From 2011 to 2016, the simulation has a very good history match to actual field data. But from 2016 to 2020, the model experienced significant production drops due to reservoir depletion. Detailed production forecast of oil rate is illustrated in Figure 17.9. The average oil drops to below 20 m^3/day. The peak oil rate is 132 m^3/day. Cumulative oil production forecast is shown in Figure 17.10.

17.5.8.3 Forecast Results: Steam-to-Oil Ratio

The field SOR performance is shown in Figure 17.11. The current cSOR is around 4.80. The steam oil ratio increases dramatically when it produces less oil with same injection rate. The SOR reaches to 9.0 by 2020 in our following forecast.

17.5.9 Modified Well Simulation Forecast

17.5.9.1 Modified Well Configuration with Non-Flowing Boundary

The traditional horizontal injector was modified to three vertical injectors. NCG would inject below the top formation or below the top water zone. The following tables indicate the operational constraints for the steam injector and NCG injector using modified well configuration with non-flowing boundary condition. The minimum bottom-hole pressure is set to 1073.75 kPa and maximum steam rate for producer is 5 m^3/day. The steam injector operational constraint is maximum 100 m^3/day of surface water rate and 3000 kPa of bottom-hole pressure. The NCG injector operational constraint is maximum 1348 m^3/day of surface gas (methane) rate.

17.5.9.2 Perforating Below Top Water Zone

The well spacing between each vertical well remains at 250 m. The vertical injectors were perforated right below the top water zone. This allowed the non-condensable gas to form an insulation layer just right below the top

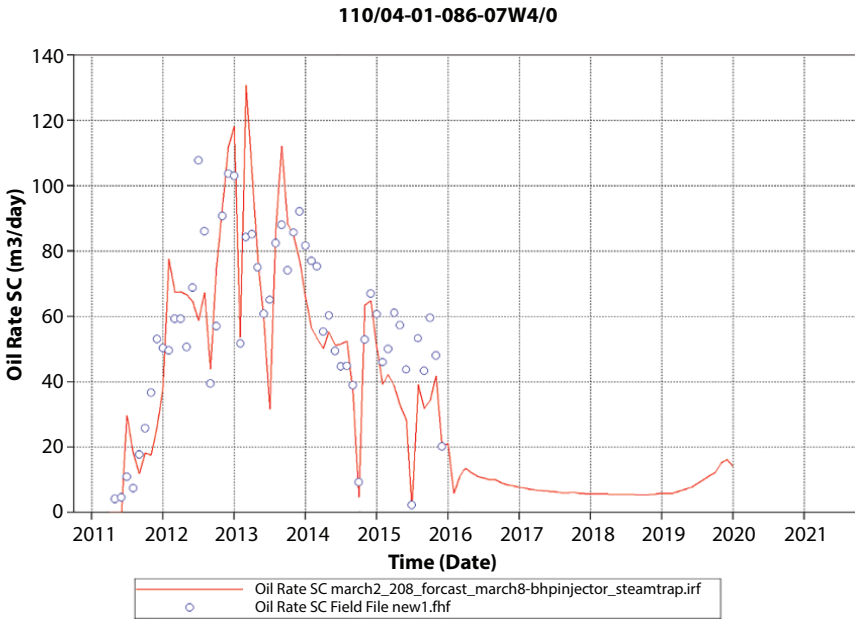

Figure 17.9 Oil rate production forecast.

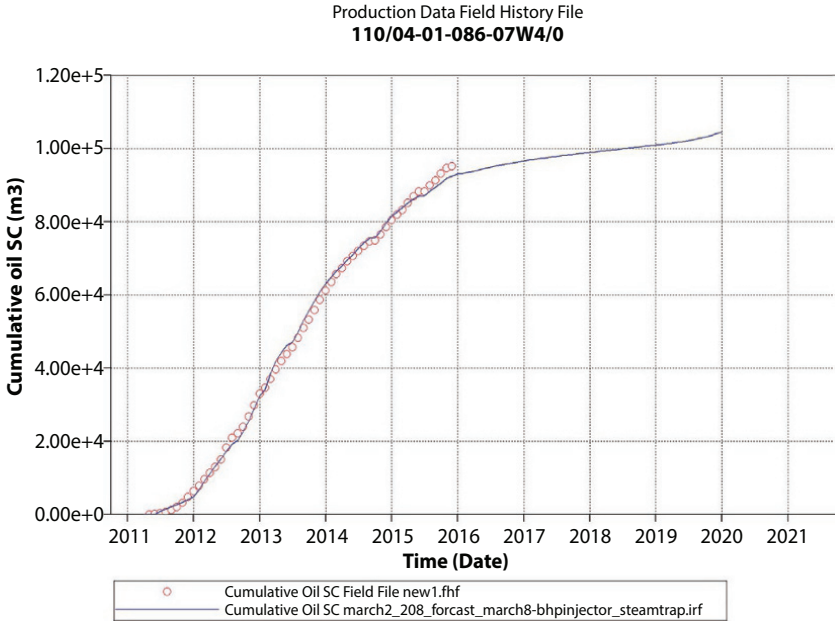

Figure 17.10 Cumulative oil production forecast.

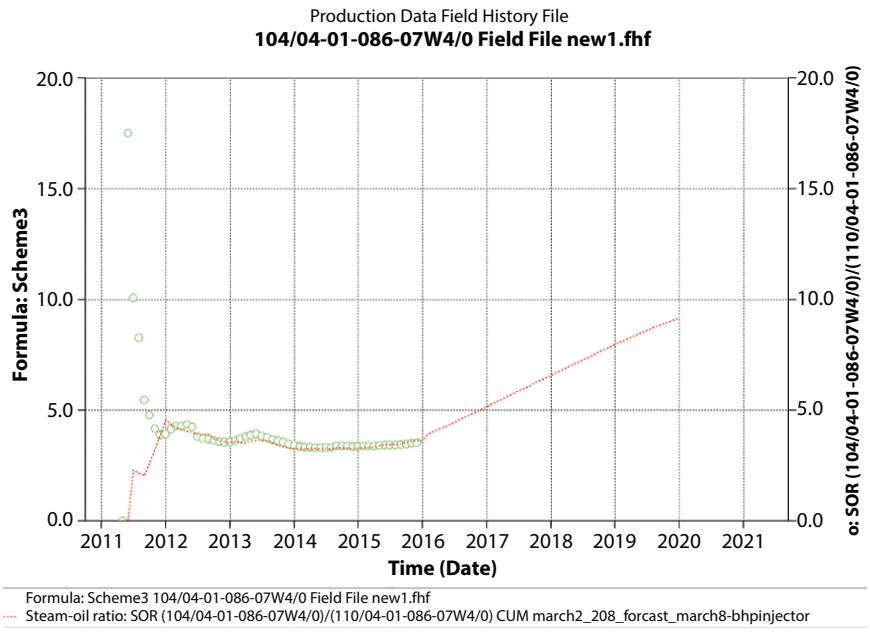

Figure 17.11 Cumulative SOR performance and forecast.

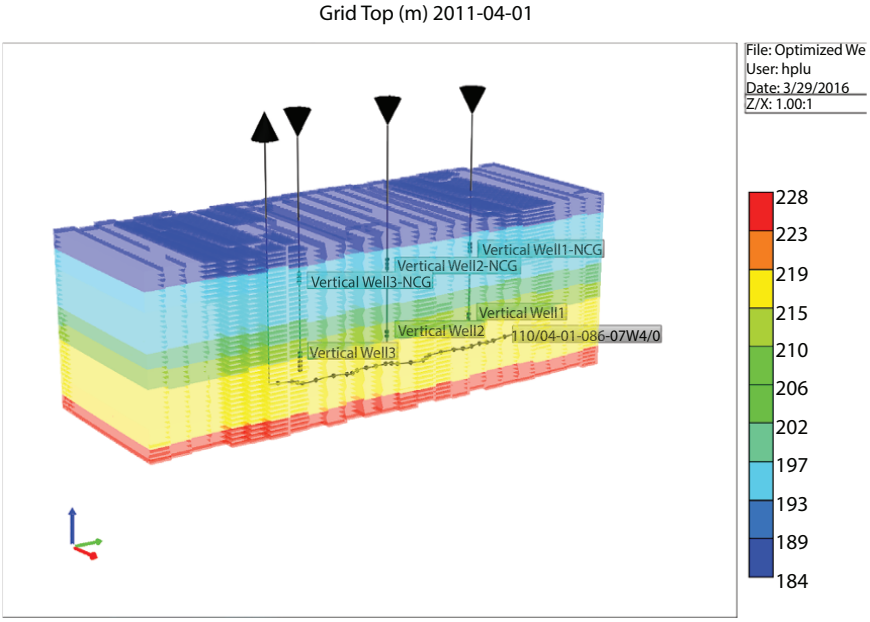

Figure 17.12 Grid top structure when perforates below top water.

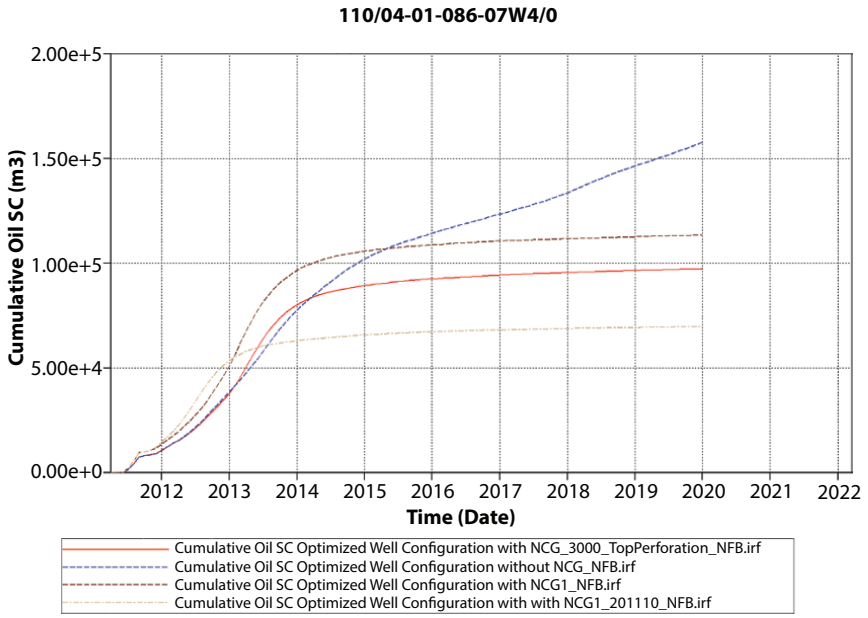

Figure 17.13 Cumulative oil with NFB using modified well configuration.

water zone. Grid top structure is shown in Figure 17.12 when perforations located below top water.

17.5.9.3 Forecast Results: Production Rate

Figure 17.13 shows the cumulative oil production is less comparing to the modified well configuration without NCG case. The cumulative oil drops from 157,000 m^3 to 113,000 m^3 when perforations are shot below water zone. The cumulative oil drops to 97,000 m^3 when perforations are shot below top formation. In the last test case, the NCG was injected when the steam chamber reaches the top formation in October 2011 but the cumulative oil rate is the lowest compared to other three cases. Therefore, the NCG should be injected at the beginning of SAGD process and right below the top water zone due to a larger oil production. This conclusion applies to the next few test cases.

17.5.9.4 Forecast Results: Steam-to-Oil Ratio

It clearly shows a decrease in SOR from 2.94 to 1.87 when adding NCG to the modified well configuration model. SOR for both cases (NCG

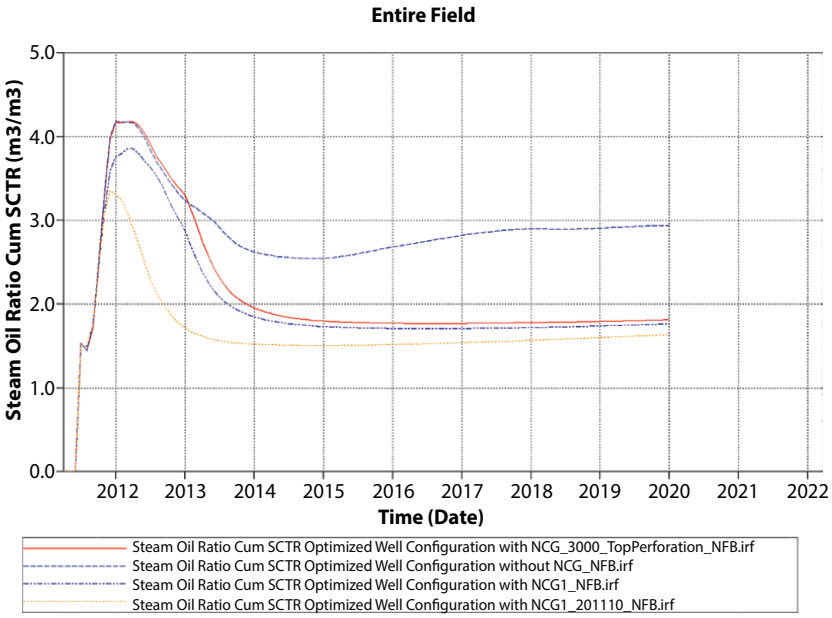

Figure 17.14 SOR performance in NFB.

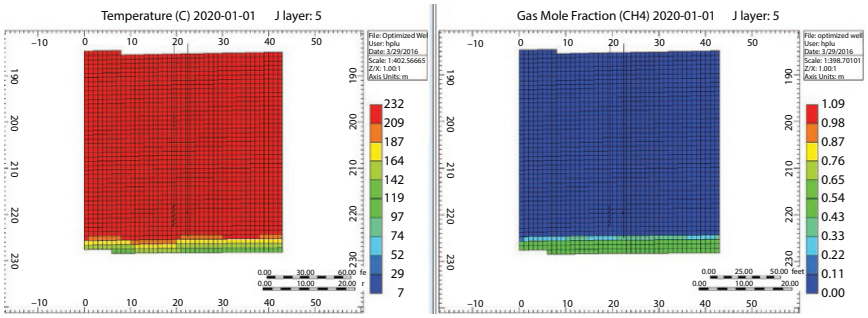

Figure 17.15 Temperature and gas mole fraction in 2020.

below formation and NCG below water zone) are almost identical. In Figure 17.14, the SOR was improved when co-inject steam with NCG.

17.5.9.5 Steam Chamber Development without NCG

These are the figures of steam chamber development without non-condensable gas. Without forming an insulation layer, the temperature is extremely

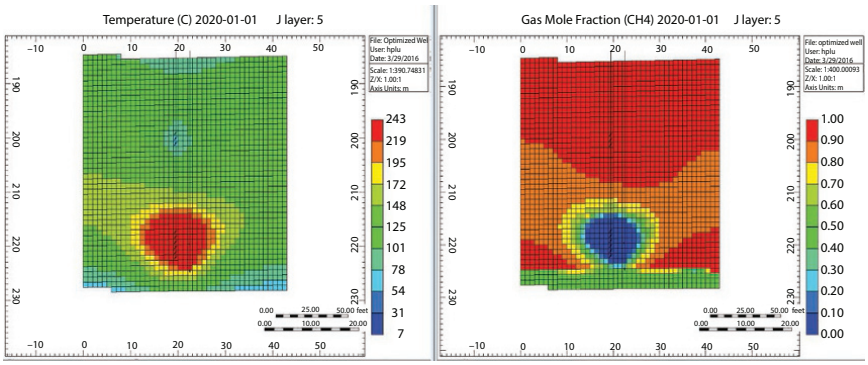

Figure 17.16 Temperature and gas mole fraction in 2020.

high at the top of the formation, such as is shown in Figure 17.15. This is the main reason that a large amount of heat will be directly lost to overburden.

17.5.9.6 Steam Chamber Development with NCG

In the tests above, the best result is from the case with NCG that injected at the beginning of SAGD process. This simulation run includes 1 mole % of NCG in the total injected fluid (Steam and NCG). The steam chamber development is observed in the following figures. The NCG injector constraint for each well is injecting 1348 m^3 of NCG per day. Even though the NCG layer will protect heat loss to the overburden, the excess injection of NCG will greatly influence steam chamber development. In this case, the steam chamber could not reach to the top bitumen zone, shown in Figure 17.16. In order to determine the acceptable mole fraction of NCG that needs to be injected, a sensitivity analysis with different mole fraction of NCG is conducted.

17.5.9.7 Simulation Sensitivity Analysis in Non-Flowing Boundary

The SOR comparison with various moles of NCG is shown in Figure 17.17. The highest NCG mole fraction (1.5%) results lowest steam oil ratio. This is due to the reason that it minimized the overburden heat loss. Overall, SOR 2.27 is acceptable and cumulative oil is relatively large for 0.25 mole % NCG case. Cumulative oil rate is illustrated in Figure 17.18.

The temperature profile figures are illustrated in Figure 17.19. They explains that why the 0.25 mole % NCG case is the most optimized case

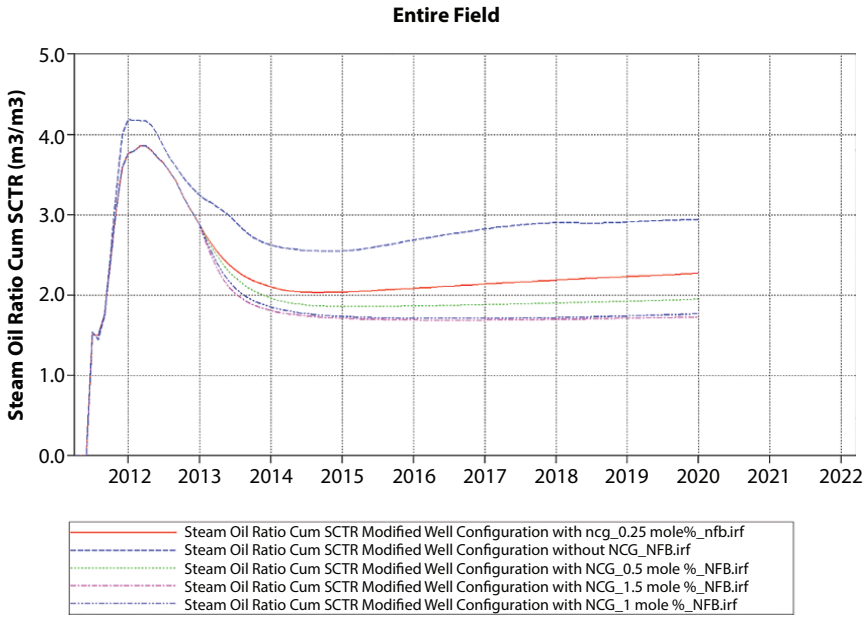

Figure 17.17 SOR comparison.

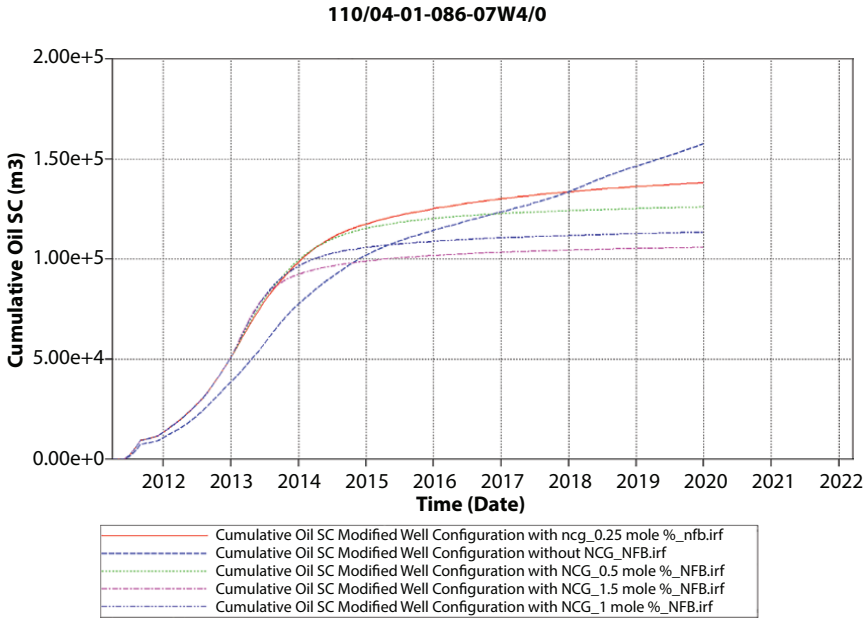

Figure 17.18 Cumulative oil comparison with specified moles of NCG.

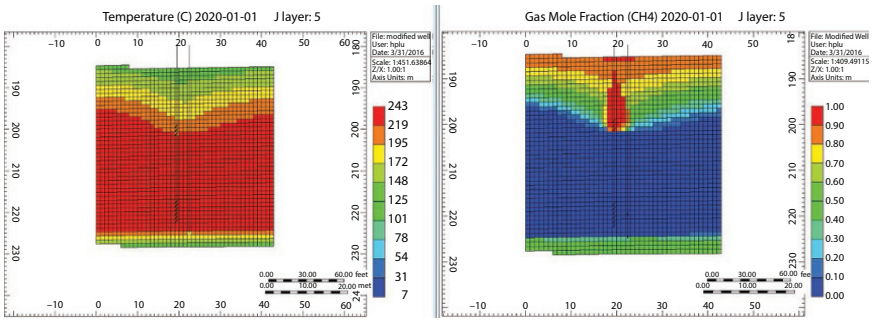

Figure 17.19 Temperature and gas mole fraction profile in 2020.

since the high temperature steam chamber reaches to the top of bitumen zone. In this situation, there is less overburden heat loss and the bitumen zone is mostly depleted at the high temperature condition.

17.5.9.8 Summary of Simulation Results

For simulation cases with non-flowing boundary condition, results are listed in Table 17.4. The base case SAGD shows a cumulative oil production of 157,000 m^3 and SOR of 9.0. The optimized NCG case would consider both cumulative oil rate and SOR. The cumulative oil production should not be too low compared to the base SAGD case. Therefore, the optimized case has cumulative oil production of 145,000 m^3 and SOR of 2.27 for the 0.25 mole % of NCG case.

17.6 Conclusion

The overburden heat loss is less when adding NCG due to the effect of isolating NCG layer below cap rock. It has been expected to attain the objectives of this project through a series of goals. These goals include reservoir characterization, recovery and production forecasting, preliminary drilling and completions, and facilities design followed by the economic evaluation.

The conventional SAGD well configuration cases showed little improvement in SOR no matter NCG was injected. The modified well configuration cases showed clearly improvement in SOR. In the end, the NCG mole % sensitivity analysis was conducted. The results demonstrated the case with 0.25 mole % NCG have better cumulative oil rate and improved SOR.

Table 17.4 Summary of Simulation Results (Non-Flowing Boundary Condition).

Injected fluid	Type of injection well(s)	Injector BHP constraint (kPa)	Cumulative oil production (m^3)	Cumulative SOR
Steam only	Horizontal well	3,000	157,000	9.00
Steam with 1.0 mole % NCG	Horizontal well	3,000	145,000	6.00
Steam & 1.5 mole% NCG (segregated injection)	3 Vertical wells	3,000	155,000	1.75
Steam & 1.0 mole% NCG (segregated injection)	3 Vertical wells	3,000	113,000	1.87
Steam & 0.5 mole% NCG (segregated injection)	3 Vertical wells	3,000	125,000	1.98
Steam & 0.25 mole% NCG (segregated injection)	3 Vertical wells	3,000	145,000	2.27
Steam only (segregated injection)	3 Vertical wells	3,000	160,000	2.94

The modified well configurations allow the injection of steam and NCG separately at different perforations. This is achieved by replacing the horizontal injector with three vertical injectors. The total drilling and completion costs for modified well configurations is $1,709,487.00.

According to the economics analysis, the total project cost is around $3.9 billion for base case. Sensitivity analysis is conducted on the fixed capital investment (FCI), oil production, and Western Texas Intermediate (WTI). From the sensitivity analysis, it is found that the project is most sensitive on the oil price change. NPV for base case is $-580.9 million, and for NCG case is $-704.6 million. Rate of return for base case is 17.3%, and for NCG case is 16.5%. Payout period for base case is 4.1 years, and for NCG case is 4.3 years. NCG injection does reduce cost associated with steam generation and lower carbon intensity of the plant; however, it reduces the production by 12%. It is concluded that NCG injection is not economically beneficial under current oil price and carbon tax regulation.

References

1. Alberta Energy Regulator, Crude bitumen production, 2015. http://oilsands.alberta.ca/about.html.
2. Considerations for the addition of non-condensable gases to steam in the SAGD process, Nexen Inc, 2014.
3. Hangingstone Demonstration Project, Thermal *in-situ* scheme progress report, Approval No. 8788I, Japan Canada Oil Sands Limited (JACOS), 2011, February 9, 2012.
4. Becker, D.L., Hamilton, C., Villegas, F., Nexen/OPTI Long Lake pilot project - SAGD drilling experience. *Paper 2004-300 presented at Petroleum Society's 5th Canadian International Petroleum Conference*, Calgary, Alberta, June, 2004.
5. Markit, I.H.S., AccuMap (Version 25.03), October, 2015.
6. Baker, R., Yarranton, H., Jensen, J., *Practical Reservoir Engineering and Characterization*, Gulf Professional Publishing, 2015.
7. Crain, E.R., *The log analysis handbook*, Pennwell Books.
8. Donnelly, J.K. and Hitchner, J., Determining Oil Sand Reservoir Properties from Logs and Core –The Controversy Continues. *Soc. Petrol. Eng.*, January, 2002, doi: 10.2118/79034-MS.
9. Zhang, X.K., Feizabadi, S.A., Yang, P., An Integrated Approach to Building History-Matched Geomodels to Understand Complex Long Lake Oil Sands Reservoirs, Part 1: Geomodeling. *Soc. Petrol. Eng.*, June 10, 2014, doi: 10.2118/170027-MS.
10. Ashrafi, M., Souraki, Y., Karimaiek, H., Torsaeter, O., Bjorkvikb, B.J.A., Experimental PVT property analyses for Athabasca bitumen, *SPE 147064-MS presented at the Canadian Unconventional Resources Conference*, Calgary, Alberta, Canada, November, 2011.

11. Ahmadloo, F. and Yang, P., Solvent-assisted Start-up of SAGD Wells in Long Lake Project, *SPE 170052-MS presented at the SPE Heavy Oil Conference*, Canada, Calgary, Alberta, Canada, June, 2014.
12. Reid, R., Prausnitz, J., Sherwood, T, T., *The properties of gases and liquids*, McGraw-Hill, 1977.
13. Gates, I., *Unconventional Oil Exploration Course Notes*, 2014.
14. Alturki, A.A., Gates, I.D., Maini, B.B., Co-injection of noncondensable gas improves ES-SAGD Performance in shallow oil sands reservoir with a small top water zone, SPE 137092-MS. *presented at Canadian Unconventional Resources and International Petroleum Conference*, Calgary, Alberta, October, 2010.
15. Long lake annual performance presentation in accordance with AER directive 054, Nexen Inc, 2015.
16. Law, D.H.-S., Nasr, T.N., Good, W.K., Field-Scale Numerical Simulation of SAGD Process With Top-Water Thief Zone. *Soc. Petrol. Eng.*, January, 2000, doi: 10.2118/65522-MS.

18

The Study on the Gas Override Phenomenon in Condensate Gas Reservoir

Kun Huang[1], Weiyao Zhu[1]*, Qitao Zhang[1], Jing Xia[2] and Kai Luo[2]

[1]Institute of Applied Mechanics, University of Science and Technology Beijing, Beijing China,
[2]China Petroleum Exploration and Development Research Institute, Beijing China,

Abstract

The cyclic gas injection technique is commonly used in the development of condensate gas reservoir. However, the override of injected gas induces severe gravity segregation in formation, greatly limits the application of this technique, and relevant studies are rarely found in literatures. This paper studied the phase behavior of the mixture composed of injected dry gas and condensate gas during the process of dry gas injection. The visual PVT cell exhibits a combination of dry gas - condensate gas - condensate oil for pressure fluctuate around dew pressure and a combination of dry gas - condensate gas for pressure above dew pressure. Considering the main influencing factors, a corresponding theoretical model is established to portray the formation and development of injected gas override in condensate gas reservoir. The case study indicates that the injected dry gas would surpass the original condensate gas and break through from the top of the reservoir. In addition, a transition zone is formed between the injected gas and condensate gas, and the transition zone would evolve over time.

Keywords: Condensate gas, cyclic injection, phase behavior, numerical simulation

18.1 Introduction

The depletion of a condensate gas reservoir results in low recovery efficiency of condensate oil due to retrograde condensation under a

**Corresponding author*: weiyaook@sina.com

Ying Wu, John J. Carroll, Mingqiang Hao and Weiyao Zhu (eds.) Gas Injection into Geological Formations and Related Topics, (311–320)

pressure lower than dew point pressure. Development based on maintaining pressure production through gas injection can inhibit the precipitation of condensate oil and increase recovery efficiency [1, 2]. At present, gas injection is considered a good method for mining a condensate gas reservoir that is rich of condensate oil. Maintaining pressure production through gas injection is mainly divided into full and partly maintaining pressure production, on the basis of global mining practices concerning condensate gas reservoirs. Appropriate maintenance of pressure production through gas injection is applied in light of the content of condensate oil, the ground-dew point pressure difference and air source condition. Dry gas, nitrogen, air, and CO2 are the main gaseous media of injection [3, 4]. Dry gas is considered an injection medium for condensate gas reservoirs. It is categorized among hydrocarbon gases and can be used to extract heavy components in wet gas effectively after being mixed with wet gas in the formation, thereby realizing phase equilibrium. As a result, the gaseous condensate oil content in formation decreases, which results in the reduction of retrograde condensate oil saturation in formation. The recovered wet gas is processed into dry gas and then injected in formation for cyclic use [5]. Therefore, compared to other nonhydrocarbon gases, dry gas can effectively increase the recovery rate of condensate oil.

The dry gas overlying on condensate gas is found to greatly affect the recovery efficiency, although the effects of gravity difference and thermodynamics during the migration of reservoir components under high temperature and pressure on the component migration law are unknown. This paper uses PVT tests to demonstrate the phase behavior of the condensate gas in the dry gas injection process. In addition, the gravity segregation in the PVT tube is measured by chromatographic instrument.

18.2 Experimental

18.2.1 Pressure-Volume-Temperature Tests

The PVT apparatus is used to study the phase behavior of the oil and gas hydrocarbon mixtures. The core component of the system is a fully visual PVT cell, and mixtures of oil and gas are transferred into the cell for tests. The visual cell gives a vivid presentation of the changes in the volumetric properties of mixtures during the testing process. The schematic diagram for the apparatus is given in Figure 18.1.

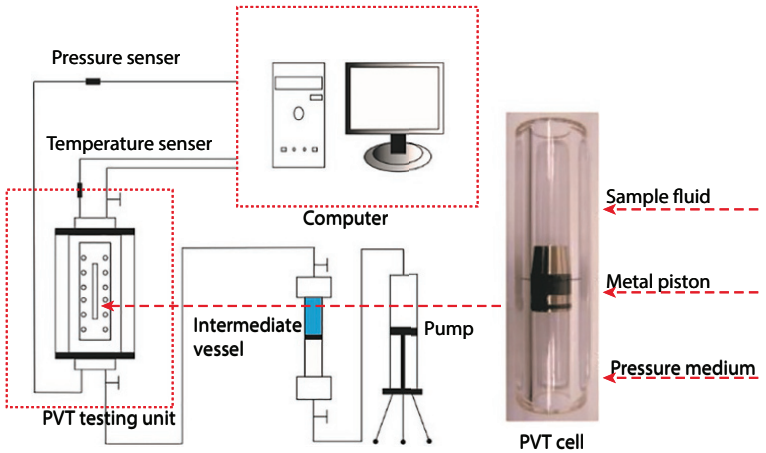

Figure 18.1 Schematic diagram of the PVT experiment.

18.2.2 Pressure-Volume-Temperature Tests Design

1. The dry gas is injected from the top of the PVT cylinder in a slow and continuous manner, and the phase behavior of the two pseudo phases is recorded. The testing conditions are set as: (1) testing pressure (49MPa) is a little lower than the dew point pressure (49.98MPa) to simulate a reservoir condition that near the critical area; (2) testing pressure (53MPa) is higher than dew point pressure (49.98MPa) to simulate a reservoir condition far from the critical area. This step stops when the injected gas volume equals the volume of the original condensate gas.
2. After the first step, the fluid in the PVT cylinder is kept stable for a certain period of time to monitor the phase behavior of the mixture under the influence of mass transfer.
3. After the second step is completed, the mixture is made to stand still for 8 hours, and then the mixture is slowly removed from the PVT cylinder to test the composition at different vertical sections.

18.3 Results and Discussion

18.3.1 Phase Behavior During the Injection Process

Figure 18.2 shows the phase behavior of the mixture composed of the original condensate gas and the injected dry gas. The first run was carried out

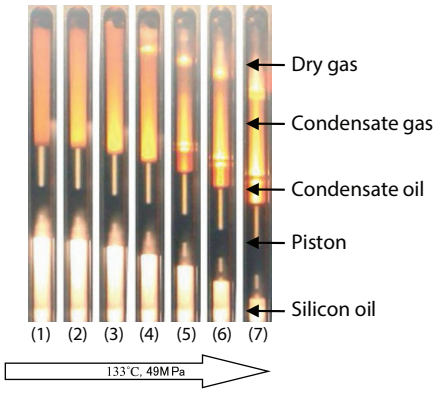

Figure 18.2 Phase behavior of the mixture (133°C, 49MPa).

under conditions (133°C, 49MPa) which lay in the adjacent area of the dew point, and with the second one (133°C, 52MPa) a little far from the dew point. The dry gas was injected from the top of the visual cylinder, and the testing process was recorded by camera.

The image (1) in Figure 18.2 was taken when there was only condensate gas in the PVT cylinder. This image was used as a reference photo to compare with other photos, and in this image, the condensate gas is dark red. At this stage, the condensate gas is under the conditions which lay in the vicinity of the dew point, and the condensate gas demonstrated uniform fluid phase with no obvious interfaces.

Images (2) through (3) were taken at the initial injecting stage. At this time, the injected gas at the top of the visual cylinder show a bright yellow color and is very different from the color of the condensate gas at the bottom. It implies that there is a significant difference in the physical properties between the dry gas and condensate gas at 133 °C and 49 MPa.

With the continuous injection of dry gas, the PVT tube presents the upper dry gas phase and the lower condensate gas phase with a clear interface between the two pseudo phases (Figure 18.2. image (4)). The dry gas is transparent and the condensate gas is yellow.

The volume of the upper dry gas phase continues to increase with the injection of dry gas. Due to the fact that the testing pressure is close to the dew point, the injected gas easily leads to the instability of the system. Consequently, the condensate liquid emerges. In that case, the dry gas, condensate gas and condensate oil coexist in the PVT cylinder with two obvious interfaces.

The upper gas phase continues to increase with time. In image (7), the interface between dry gas and condensate gas thickens as a result of mass transfer process, and the boundary between the two pseudo phases

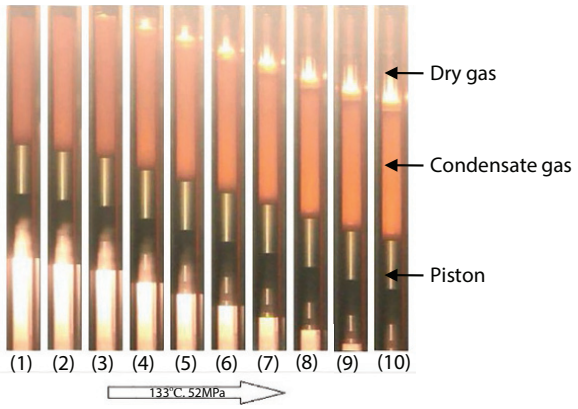

Figure 18.3 Phase behavior of the mixture (133°C, 53MPa).

gradually becomes blurry. This test stops when the injected gas volume equals the volume of original condensate gas in the PVT cylinder.

Figure 18.3 shows the phase behavior of the mixture when the test is carried out under a higher pressure. For the run with the higher pressure, the change of the phase behavior is close to the one with lower pressure. The primary difference is that the condensate liquid phase was no longer witnessed during the process.

In general, the results exhibited a lighter dry gas phase at the upper part, an intermediate gas phase (mixture of dry gas and condensate gas) in the middle, and in some cases, a heavier condensate oil phase (the oil phase is prone to emerge when the testing condition lay in the vicinity of the critic areas) in the lower part. Besides, due to the mass transfer process, the boundaries of the three pseudo phases would maintain a certain amount of time before they became blurred and vanished.

18.3.2 The Effect of Mass Transfer on the Phase Behavior

Figure 18.4 presents the change of interfaces over time for the test with the lower pressure. For the 16 images in Figure 18.4, the time interval between every two images is 30 minutes. The image shows that the "pseudo phase interface" between the dry gas and the condensate gas would remain stable for a certain period of time, and the condensate gas-condensation liquid interface exhibits a stronger stability. In addition, the dry gas-condensation gas "pseudo interface" gradually thickens and becomes blurred, and barely exists in the end. However, the condensate gas-condensation liquid phase interface remains through the whole testing process and clearly separates the upper yellow transparent condensate gas and the lower red condensate gas.

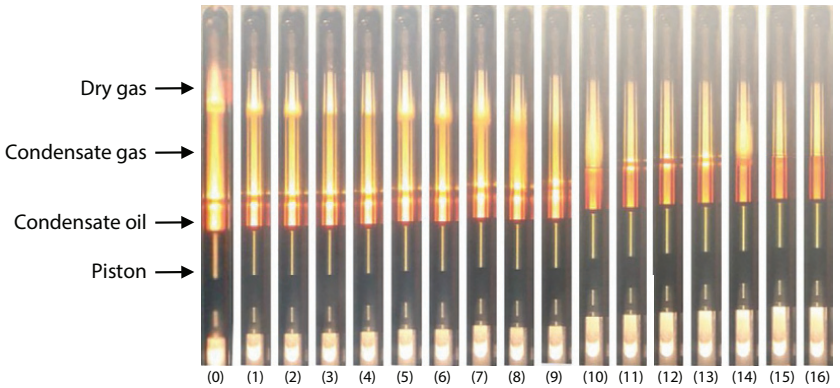

Figure 18.4 The vertical diffusion process (133°C, 49MPa).

It indicates a stronger diffusion process between the dry gas and the condensate gas, as well as a weaker diffusion process between the condensate gas and the condensate liquids in the PVT cylinder. As a result, it takes even longer for the interface between condensate gas and condensate liquid to vanish.

The images in Figure 18.5 were taken every hour. The image shows that the interface becomes more and more blurred with the extension of time. The dry gas is getting darker and darker, which is mainly caused by the diffusion the condensate gas into the dry gas. In this process, the dry gas become heavier, and the volume of the dry gas phase gradually increases, indicating the extraction of the condensate gas by the dry gas. Yet it still takes a long time to witness the disappearance of the interface. The PVT tests verifies the existence of the gravity segregation in the development of condensate gas reservoir by cyclic injection technique.

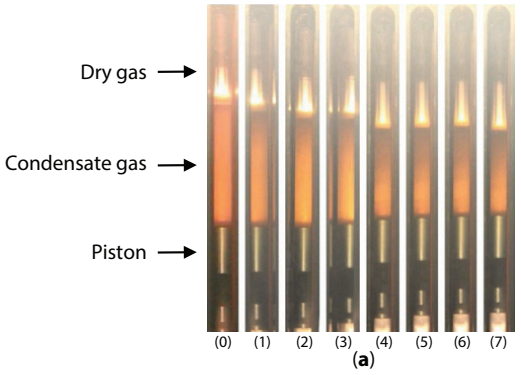

Figure 18.5 (a) The vertical diffusion process (133°C, 53MPa).

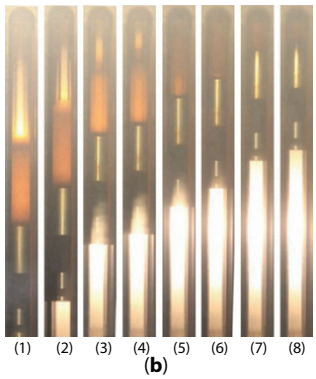

Figure 18.5 (b) The remove of the mixture from the top of the cylinder.

18.3.3 Composition of the Mixture in the Cylinder

Chromatographic composition tests were performed on different sections in the PVT tube. The images were taken every 0.75 cm the piston moves up. It can be seen from Figure 18.6 and Table 18.1 that as the depth increases, the content of C_2 to C_6 increases gradually except the decrease of methane.

The equilibrium state between the condensate gas and dry gas widely exists in the condensate gas reservoir developed by cyclic injection

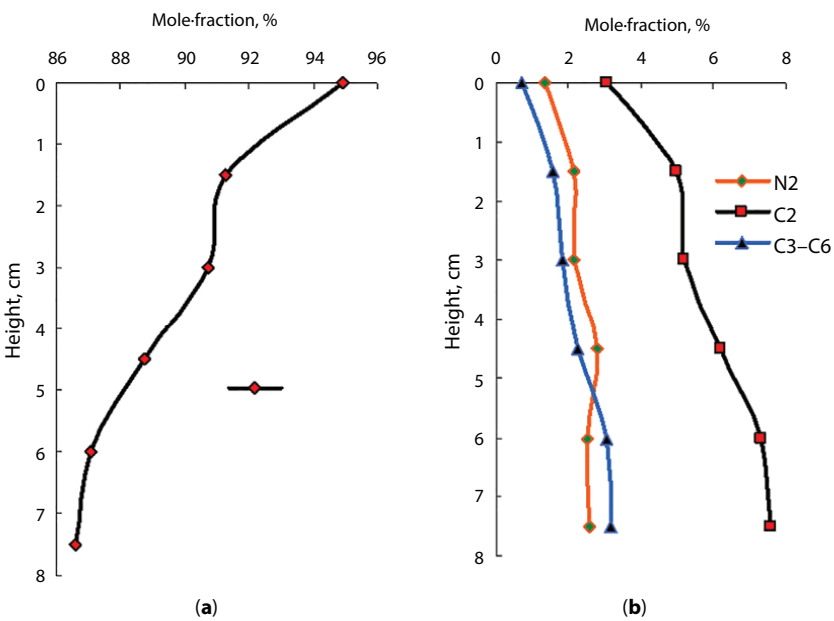

Figure 18.6 The composition of the mixture at different sections (133°C, 53MPa).

Table 18.1 The composition of the mixture at different vertical sections (133°C, 53MPa).

Depth	CO_2 mol%	N_2 mol%	C_1 mol%	C_2 mol%	C_3 mol%	iC_4 mol%	nC_4 mol%	iC_5 mol%	nC_5 mol%	C_6 mol%
0 cm	0.000	1.358	94.949	3.061	0.492	0.067	0.114	0.026	0.040	0.007
1.5 cm	0.000	2.161	91.266	4.990	0.882	0.167	0.191	0.120	0.091	0.132
3 cm	0.000	2.191	90.752	5.184	1.005	0.191	0.225	0.142	0.097	0.212
4.5 cm	0.000	2.801	88.732	6.188	1.259	0.243	0.294	0.190	0.125	0.169
6cm	0.000	2.537	87.102	7.312	1.584	0.317	0.398	0.287	0.199	0.265
7.5cm	0.000	2.607	86.614	7.576	1.662	0.334	0.424	0.298	0.198	0.286

technique. The development process shows a binary system when the formation pressure is above the dew point pressure, and a ternary system when the formation pressure is lower than the dew point pressure. Generally, the top of the reservoir is segregated by the gas phase composed of dry gas and condensate gas, and the higher the elevation is, the lighter the gas will become. Similarly, the gas gradually becomes heavier with the increase of depth, specifically, the gas-oil ratio is getting smaller and smaller, and the density is getting larger and larger.

18.4 Conclusions

When the injection pressure is near the dew point during the gas injection process, the pressure fluctuations will lead to the formation of three phases in the PVT tube, and the dry gas, the condensate gas, and the condensate phase are witnessed from the top to the bottom of the PVT tube.

The dry gas-condensate gas interface gradually becomes blurred with time, but the gas-liquid interface is obvious and stable.

When the gas injection pressure is higher than the dew point pressure, the pseudo phase boundary is stable and barely disappears.

As the depth increases, the methane content decreases with the increase of the intermediate component and the heavy component.

References

1. Jessen, K. and Orr, F.M., Gas cycling and the development of miscibility in condensate reservoirs. *SPE Reserv. Eval. Eng.*, 7, 05, 334–341, 2004.
2. Sadooni, M. and Zonnouri, A., The effect of nitrogen injection on production improvement in an Iranian rich gas condensate reservoir. *Petrol. Sci. Technol.*, 33, 4, 422–429, 2015.
3. Nasiri Ghiri, M., Nasriani, H.R., Sinaei, M. *et al.*, Gas injection for enhancement of condensate recovery in a gas condensate reservoir. *Energ. Source Part A: Recovery, Utilization, and Environmental Effects*, 37, 8, 799–806, 2015.
4. Linderman, J.T., Al-Jenaibi, F.S., Ghori, S.G. *et al.*, Feasibility study of substituting nitrogen for hydrocarbon in a gas recycle condensate reservoir[C]// Abu Dhabi International Petroleum Exhibition and Conference. *Soc. Petrol. Eng.*, 2008.
5. Yuguan, L., Adjustment measures of circulating gas injection in kekeya condensate gas field in xinjiang province and its development effectiveness. *Nat. Gas Ind.*, 20, 4, 61–62, 2000.

19

Study on Characteristics of Water-Gas Flow in Tight Gas Reservoir with High Water Saturation

Qitao Zhang[1], Weiyao Zhu[1]*, Wenchao Liu[1], Yunqing Shi[2] and Jin Yan[2]

[1]Institute of Applied Mechanics, University of Science and Technology Beijing, Beijing China
[2]SINOPEC Exploration and Development Research Institute, Beijing China

Abstract

Aiming at the characteristics of tight gas reservoirs with low gas saturation, based on the experimental results, a new mathematical model of gas-water two-phase flow in tight reservoirs is presented. For multi-scale flow characteristics of tight reservoir fluids, a dynamic cross-scale relative permeability curve system for gas and water is presented, which corresponds to distinct relative permeability curves for different flow condition. The gas-water problem has a high degree of nonlinearity, and has high requirements for wellbore processing and matrix calculation. In order to ensure the stability of the solution, the full implicit finite difference method and the full implicit well processing method have been adopted for calculation. The model is verified and a series of influence factors have been analyzed. The results show that the TPG has a significant impact on gas well productivity. It has a relatively shorter stable production period and the gas production in the later stage of production is significantly reduced when TPG is taken into account.

Keywords: Tight gas, low gas saturation, confined water, relative permeability, numerical simulation

**Corresponding author*: weiyaook@sina.com

Ying Wu, John J. Carroll, Mingqiang Hao and Weiyao Zhu (eds.) Gas Injection into Geological Formations and Related Topics, (321–332) © 2019 Scrivener Publishing LLC

19.1 Introduction

As is known, liquid flow in the low or ultra-low permeability reservoirs is low-velocity non-Darcy flow, namely, flow with a threshold pressure gradient (TPG) [1]. The model was presented first by Soviet Union scholars in 1951 and further studied by many scholars [2–4].

However, gas flow with TPG in porous media is a controversial issue. There is the slippage effect with gas flow in porous media without irreducible water, which was first presented by Klinkenberg in 1941. The result of laboratory cores containing water tested by Rose in 1948 indicated that the higher the water saturation, the weaker the slippage effect. The same conclusion was obtained by Estes and Rushing in 1956. The slippage effect is positive for the development of gas reservoirs, but the flow behavior of fluids in many water-bearing gas reservoirs developed was shown as low-velocity non-Darcy flow, which is a negative effect. The view that gas flow, similar to liquid in porous media, could be the low-velocity non-Darcy flow was first proposed in 1986. In recent years, some researchers tried to verify the view and find the conditions of low-velocity non-Darcy gas flow by experimental measurements and theoretical analysis [5–16].

The study is organized as follow. First, we conducted the gas-flooding experiments with different flooding pressure. Then the NMR measurements were used to analyse the water occurrence in the core samples after the experiments. After that, a mathematical model was established to consider the gas-water interaction behavior under different pore and production pressure. Finally, a reservoir simulator was presented to study the characteristics of two-phase flow in the duration of reservoir exploitation.

19.2 Experiments

19.2.1 Materials

The core samples in this paper originate from Sulige gas field, China, which is a typical sandstone reservoir. The properties of the cores are shown in Table 19.1.

The characteristics of the formation water content are shown in Table 19.2. From the analysis results, it can be known that formation water in this reservoir is type of $CaCl_2$.

Table 19.1 Properties of cores from Sulige gas field.

Core number	Diameter, cm	Length, cm	Porosity, %	Permeability, mD
GA110-1	2.55	3.60	15.0	7.41
GA110-1	2.55	3.60	14.2	4.71
GA110-1	2.56	3.61	10.9	0.628
GA110-1	2.55	3.61	5.1	0.048

Table 19.2 Properties of formation water in Sulige gas field.

Ion type	Ca^{2+}	Na^{+}	K^{+}	Mg^{2+}	Cl^{-}	HCO^{3-}	$\mathbf{SO_4^{2-}}$
Ion concentration, mg/L	2528	13793	2414	270	29703	337	734

19.2.2 Experimental Procedure

It can be known that NMR technology can measure parameters like the content of mobile water and remaining water saturation in a core sample precisely. When the core is fully saturated with water, T_2 map manifests the pore distribution in the core. By comparing with the T_2 map after gas flooding, it is accessible to study the pore characteristics of pore which contain great amount of remaining water.

1. Drill the plunger rock sample with a diameter of 2.5 cm and align the ends. Then use solvent (alcohol + benzene) extraction method to wash the core. The rock sample is then dried in a vacuum oven at 105 °C until it maintains a constant weight. Weigh the core sample.
2. Evacuate the core, saturate it with formation water. Weight the core sample after saturating. Measure the NMR T_2 curve in fully saturated condition. Calculated the water saturation, and the mobile water saturation.
3. Put the core into the gripper. Check the connection of apparatus. Start the gas flooding experiment at a certain flooding pressure. Continue the experiment until there is

no water flow out the core and the gas rate reaches a constant state.

4. After the gas flooding process in one flooding pressure. Weigh the core again and conduct the NMR measurement again.
5. Increase the flooding pressure. Repeat steps 3 and 4, until the whole experiment ends.

19.2.3 Experimental Results and Analysis

According to a large number of experimental experiences, it is determined that the boundary T_2 value of the mobile water and residual water in the sandstone core pores is between 12ms and 16ms. The part larger than the boundary value indicates the mobile water in the large pores, and the part smaller than the boundary value indicates the water in the small pores. Hence, according to the core magnetic test T_2 spectrum, the existence of water in the core of different pore types could be identified.

Representative experimental results are presented in Figure 19.1. It can be seen from the figures that in the low-pressure gas flooding stage, as the gas-flooding pressure gradually increases, the signal larger than the boundary value gradually weakens, and the signal less than the boundary value remains generally unchanged. When the gas-flooding pressure increases to a certain extent, the signal drop which is greater than the boundary value is very low and remains generally unchanged. This indicates that the water in the macropores is mainly in the form of mobile water, the water in the small pores is mainly in the form of residual water. At the same time, the smaller the pore, the less the mobile water in the pores, and the residual water occupied a larger ratio.

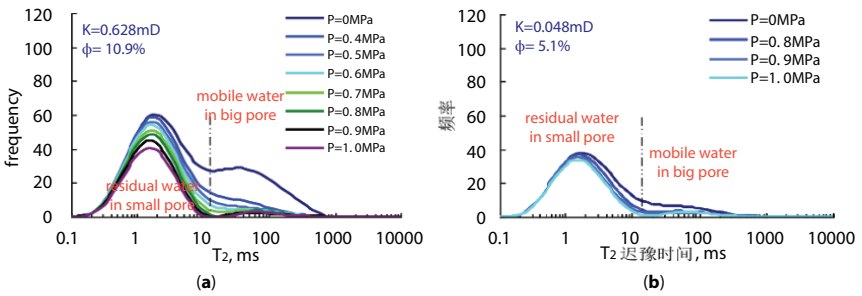

Figure 19.1 NMR experimental results.

To further analyze the characteristic of water distribution in tight reservoir and its effect, we discussed the relationship between mobile water saturation, the gas-flooding pressure and core physical properties as shown in Figure 19.2.

After that we can conclude that: (1) The residual water saturation in the small pores is also related to the permeability K and the gas flooding pressure (production pressure) ΔP. For a tight gas reservoir, when the production pressure is less than the critical driving pressure, the residual water saturation approximately keeps constant and high; when the production pressure is higher, the residual water saturation decreases linearly:

$$S_{\text{w约束水}}(K, \Delta P) = \begin{cases} S_{\text{w\_constant1}}(K) & \Delta P \le \Delta P_1(K) \\ A(K)\Delta P + B(K) & \Delta P_1(K) \le \Delta P \le \Delta P_{1\text{wc}}(K) \end{cases} \tag{19.1}$$

$$S_{\text{w\_constant1}}(K) = -0.076\ln(K) + 0.6472 \tag{19.2}$$

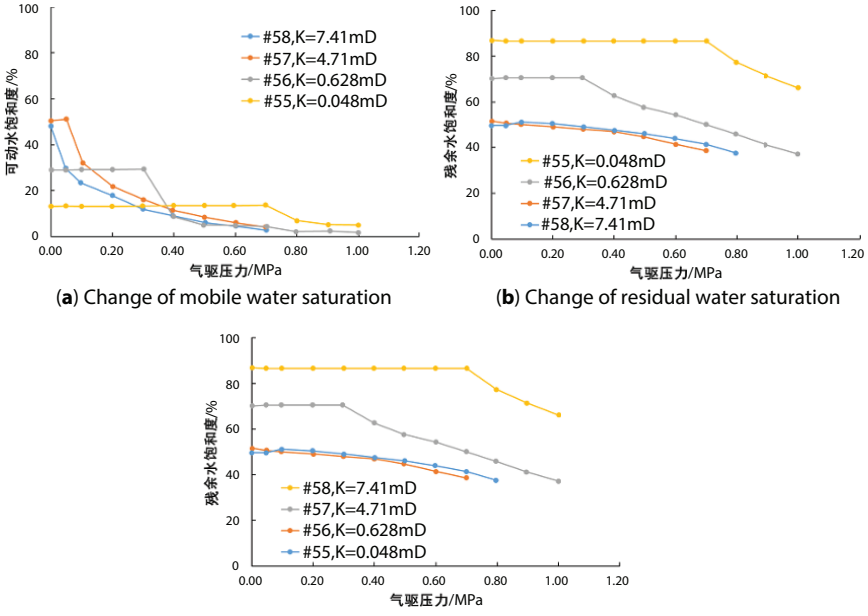

(**a**) Change of mobile water saturation

(**b**) Change of residual water saturation

(**c**) Change of total water saturation with gas flooding pressure

Figure 19.2 Analysis of NMR results.

$$\Delta P_1(K) = 0.282K^{-0.289} \tag{19.3}$$

$$\Delta P_{1wc}(K) = -0.043\ln(K) + 1.22 \tag{19.4}$$

$$A(K) = -0.0097K^2 + 0.1085K - 0.5255 \tag{19.5}$$

$$B(K) = 0.0185K^2 - 0.206K + 1.085 \tag{19.6}$$

(2) The residual water saturation in the large pores is also related to the permeability K and the gas flooding pressure (production pressure) ΔP. For a tight gas reservoir, when the production pressure is less than the critical driving pressure, the residual water saturation approximately keeps constant and high; when the production pressure is higher, the residual water saturation decreases logarithmically:

$$S_{w可动水}(K, \Delta P) = \begin{cases} S_{w\_constant0}(K) & \Delta P \le \Delta P_0(K) \\ A(K)\ln(\Delta P) + B(K) & \Delta P > \Delta P_0(K) \end{cases} \tag{19.7}$$

$$S_{w\_constant0}(K) = 0.0748\ln(K) + 0.3498 \tag{19.8}$$

$$\Delta P_0(K) = 0.568e^{-0.539K} \tag{19.9}$$

$$A(K) = 0.0035K^2 - 0.0309K - 0.0717 \tag{19.10}$$

$$B(K) = 0.0023K^2 - 0.0232K + 0.0392 \tag{19.11}$$

After we get the residual water saturation in different production pressure and pores with different permeability, a new relative permeability curve could be obtained which varied a lot in different place and time of calculation. In the numerical simulation, we added this mobile relative permeability curve for calculation.

19.3 Numerical Simulation for Tight Gas Reservoir with Low Gas Saturation

19.3.1 Model Description

To simplify the gas-water two-phase flow modeling while honoring nonlinear flow behavior, the following assumptions are made in the model construction and percolation simulation:

(1) The simulation process is gas-water two-phase flow with capillary force taken into account.
(2) Gas and water are mutually immiscible and water phase is incompressible.
(3) Stress effect to the formation porosity is neglected.
(4) Fluid flow happens under constant temperature.
(5) Gravity force is ignored.

1. Motion equation:
In order to consider the multi-scale flow effects of gas, the Knudsen number is added here to carry out gas-water two-phase multi-scale numerical simulation. The Knudsen number is assigned to each grid in the form of matrix.

$$\vec{v}_g = -\frac{KK_{rg}}{\mu_g}\left(1+\alpha K_n\right)\left(1+\frac{4K_n}{1-bK_n}\right)\frac{dp_g}{dx} \tag{19.12}$$

$$\vec{v}_w = -\frac{KK_{rw}}{\mu_w}\left(\frac{dp_w}{dx}-\lambda\right) \tag{19.13}$$

2. continuity equation:
In gas-water two-phase percolation, the continuity equations are as follows:
Gas-phase:

$$-\left(\frac{\partial\left(\rho_g v_{gx}\right)}{\partial x}+\frac{\partial\left(\rho_g v_{gx}\right)}{\partial y}+\frac{\partial\left(\rho_g v_{gx}\right)}{\partial z}\right)+q_g=\frac{\partial\left(\phi\rho_g S_g\right)}{\partial t} \tag{19.14}$$

Water-phase:

$$-\left(\frac{\partial\left(\rho_w v_{wx}\right)}{\partial x}+\frac{\partial\left(\rho_w v_{wx}\right)}{\partial y}+\frac{\partial\left(\rho_w v_{wx}\right)}{\partial z}\right)+q_w=\frac{\partial\left(\phi\rho_w S_w\right)}{\partial t} \quad (19.15)$$

3. Fundamental Differential Equation:
From all the aforementioned equations together, we can get the fundamental differential equation as follows:

Gas-phase:

$$\nabla\cdot\left(\rho_g\frac{KK_{rg}}{\mu_g}\left(1+\alpha K_n\right)\left(1+\frac{4K_n}{1-bK_n}\right)\frac{dp_g}{dx}\right)+q_g=\frac{\partial\left(\phi\rho_g S_g\right)}{\partial t} \quad (19.16)$$

Water-phase:

$$\nabla\cdot\left(\rho_w\frac{kk_{rw}}{\mu_w}\left(\nabla p_g-\nabla p_{cgw}-\lambda\right)\right)+q_w=\frac{\partial\left(\phi\rho_w S_w\right)}{\partial t} \quad (19.17)$$

Numerical simulator was established utilizing finite difference method based on a fully implicit approach. The interface of the simulator is shown in Figure 19.3.

19.3.2 Model Validation

In order to verify the correctness of the calculation model, this paper compares the model with the CMG calculation model. Since the CMG is temporarily unable to effectively deal with the threshold pressure gradient function, we degenerate into an ideal reservoir for comparison, regardless of the threshold pressure gradient. The calculation parameters are: reservoir permeability of 0.5 mD, reservoir porosity of 0.08, fluid density of 1000 kg/m^3, fluid viscosity of 1.023 mPa.s. The reservoir thickness is 10 m, the half-length of fracture is 100 m, and the initial water saturation is 0.6. The calculation results are shown as follows:

The numerical model is validated by comparing with the CMG results. The results of comparison are shown in Figure 19.4. We can see from Figure 19.4 that the numerical model runs according to the CMG results strictly.

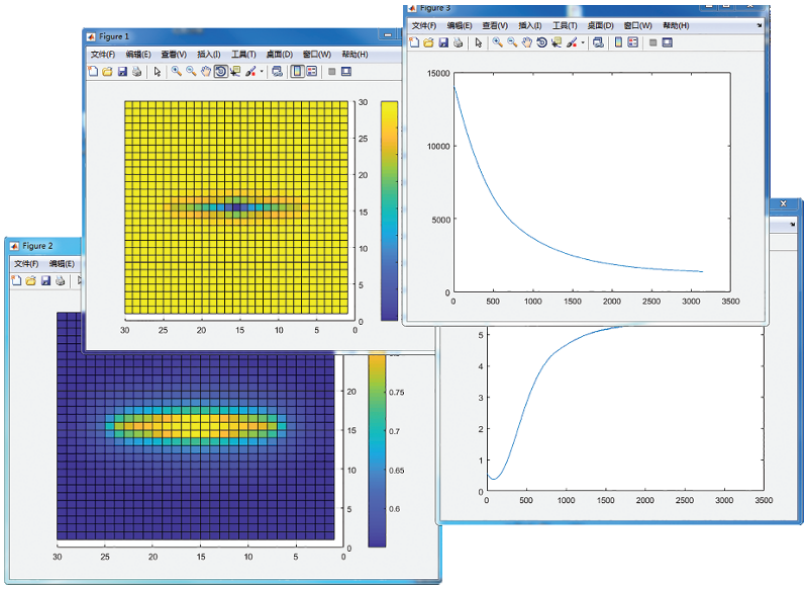

Figure 19.3 Interface of the reservoir simulator.

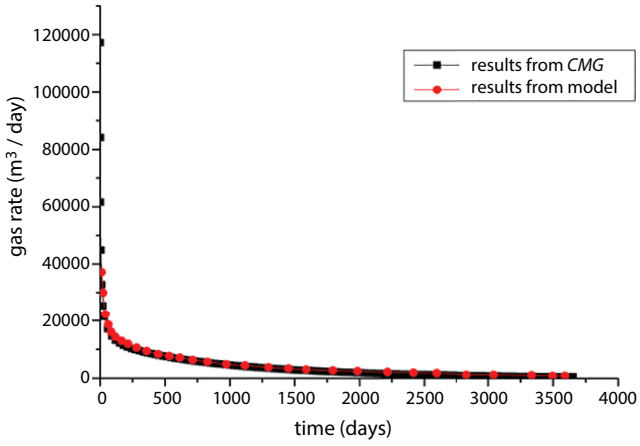

Figure 19.4 Comparison between CMG and model results.

19.3.3 Effect of Threshold Pressure Gradient

After model validation, threshold pressure gradient of water phase was added into the model to considering its effect. The calculation parameters in the numerical model was from an actual reservoir in China which are shown as follow:

Table 19.3 Calculation parameters in the numerical model.

Parameter	Value	Unit
Reservoir initial pressure	25	MPa
Reservoir average porosity	9.8	%
Reservoir average permeability	0.5	mD
Initial water saturation	62	%
Reservoir height	5	m
Fluid viscosity	0.1	mPa·s
Half-length of hydraulic fracture	100	m
Fracture conductivity	15	D·cm

In the numerical model, we regulated that the production well (vertical well) should operate at a constant gas rate (15000 m^3/d) at first. When the production rate cannot reach that level gradually, the well would operate at a fixed well- bottom hole pressure (15 MPa). The effect of the water phase TPG is shown as follow:

In terms of gas rate, the productivity curves of the two situations have similar decline patterns. However, under the conditions of TPG effect, the stable production period is relatively shorter (approximately 20%). In the later stage of production, both of situations have a rapid decline in daily gas production, of which the value is close to zero. In terms of water rate,

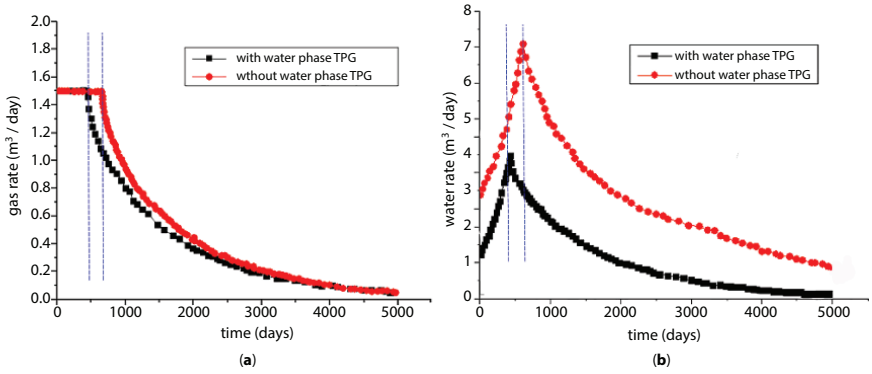

Figure 19.5 Effect of water phase threshold pressure gradient on water rate and gas rate: (a) gas rate with and without TPG effect; (b) water rate with and without TPG.

daily water rate gradually increases at first, and after conversion to constant bottom-hole pressure conditions, the amount of water produced gradually decreases. It could be seen from the figure that the TPG effect has a significant influence on the water production. In the case of the TPG effect, the water production is significantly reduced, the peak production of water is reduced by 40%, and the final production of water is reduced by 90%.

19.4 Conclusions

(1) The occurrence of water and its mobility in different core sample are various, which is mainly related to the pore structure and flooding pressure.
(2) Residual water saturation in different part of reservoir may be distinctive due to different production pressure and reservoir properties. Thus, a mathematical description of the residual water saturation was presented and a mobile relative permeability curve was added into the numerical model.
(3) Through the numerical simulation, it could be seen that TPG has a significant effect on gas rate and water rate. Under the situation of TPG, the stable production period was 20% shorter and water rate was 40% smaller.

References

1. Song, H.Q., Zhu, W.Y., Wang, M. *et al.*, A Study of Effective Deployment in Ultra-Low-Permeability Reservoirs with Non-Darcy Flow. *Liq. Fuels Technol.*, 28, 16, 1700–1711, 2010.
2. Behzadi, H. and Alvarado, V., Impact of three-phase relative permeability model on recovery in mixed media: Miscibility, ift, and hysteresis issues. *Energy Fuels*, 24, 10, 5765–5772, 2010.
3. Babchin, A.J. and Nasr, T.N., Analytical model for the capillary pressure gradient in oil–water–rock system. *Transport Porous Med.*, 65, 2, 359–362, 2006.
4. Prada, A. and Civan, F., Modification of Darcy's law for the threshold pressure gradient. *J. Petrol. Sci. Eng.*, 22, 4, 237–240, 1999.
5. Estes, R.K. and Fulton, P.F., Gas slippage and permeability measurements. *J. Petrol. Technol.*, 8, 10, 69–73, 1956.
6. Rushing, J.A., Newsham, K.E., Van Fraassen, K.C., *Proceedings of the Society of Petroleum Engineers (SPE) Annual Technical Conference and Exhibition*, Denver, CO, Oct 5-8, 2003.

7. Pascal, H., Nonsteady flow through porous media in the presence of a threshold gradient. *Acta Mech.*, 39, 207–24, 1981.
8. Lu, J., Pressure behavior of a hydraulically fractured well in tight gas formation with threshold pressure gradient. *SPE Middle East Unconventional Gas Conference and Exhibition*, 2012, SPE-152158-MS.
9. Wang, X. and Sheng, J.J., Effect of low-velocity non-Darcy flow on well production per- formance in shale and tight oil reservoirs. *Fuel*, 1, 90, 41–6, 2017.
10. Dou, H., Ma, S., Zou, C. *et al.*, Threshold pressure gradient of fluid flow through multi- porous media in low and extra-low permeability reservoirs. *Sci. China: Earth Sci.*, 57, 11, 2808–18, 2014.
11. Yan, Q., He, Q., Wei, L. *et al.*, A laboratory study on percolation characteristics of single-phase flow in low-permeability reservoirs. *J. Xi'an Pet. Inst.*, 5, 2, 1–6, 1990.
12. Li, A., Zhang, S., Liu, M. *et al.*, A new method of measuring starting pressure for low permeability reservoir. *J. China Univ. Pet.*, 32, 1, 68–72, 2008.
13. Yang, Z., Li, X., Liu, S. *et al.*, Threshold pressure effect of low permeability tight gas reservoirs in Sulige gas field. *Acta Pet. Sin.*, 36, 3, 347–55, 2015.
14. Wu, J., Cheng, L., Li, C. *et al.*, Experimental study of nonlinear flow in micropores under low pressure gradient. *Transport Porous Med.*, 119, 247–65, 2017.
15. Xiong, Y., Yu, J., Sun, H. *et al.*, A new non-Darcy flow model for low-velocity multi- phase flow in tight reservoirs. *Transport Porous Med.*, 117, 367–83, 2017.
16. Song, F., Wang, J., Lui, H., Static threshold pressure gradient characteristics of liquid influenced by boundary wettability. *Chin. Phys. Lett.*, 27, 2, 024704, 2010.

20

The Description and Modeling of Gas Override in Condensate Gas Reservoir

Weiyao Zhu*, Kun Huang, Yan Sun and Qitao Zhang

Institute of Applied Mechanics, University of Science and Technology Beijing, Beijing, China

Abstract

The override of injected gas in condensate gas reservoir leads to poor displacement efficiency, and research that presents a specific description of gas overburden encountered in condensate gas reservoir is rare. This paper presents a mathematical model to describe the override of injected gas, and finite element method is performed on a two-dimensional (2D) cross-section to achieve the results. The paper studies the effects of several key factors involved in the development of gas overburden, including the densities of injected gases and other factors related to reservoir properties as well as exploitation methods. The results demonstrate that the density difference between injected gas and condensate gas plays a vital role in the overburden phenomenon, and injected dry gas would surpass the condensate gas with injected CO2 flowing along the bottom of the condensate gas. A further case study exhibits that perforation position and dip angle are two other dominant factors in the development of gas overburden.

Keywords: Gas override, condensate gas, mathematical model, orthogonal experiment

20.1 Introduction

As one of the unconventional gas reservoirs, condensate gas reservoir has very important economic value. During the development of condensate gas reservoirs, the pressure drop leads to the occurrence of retrograde

**Corresponding author*: weiyaook@sina.com

Ying Wu, John J. Carroll, Mingqiang Hao and Weiyao Zhu (eds.) Gas Injection into Geological Formations and Related Topics, (333–342) © 2020 Scrivener Publishing LLC

condensate phenomenon, the formed condensate oil would block the gas seepage channels and hamper the gas production process. Therefore, the condensate gas reservoirs are usually developed by cyclic gas injection technique. The main function of the procedure is to maintain the formation pressure and prevent the occurrence of condensate oil. However, in the process of gas injection, gravity overburden of different degrees is likely to occur, during which the injected gas breaks through from the upper part of the reservoir and forms a secondary "gas cap," greatly decreasjng the recovery efficiency.

Yet most studies regarding the gas override phenomena were focused on those taking place during steam flooding processes and gas-liquid displacements. In the course of steam flooding, premature breakthrough of steam results in unfavorable sweeping areas and poor displacement efficiencies [1, 2].

Nzekwu [3] studied the effect of density difference on the override of injected agent. They observed the gravity overburden in liquid – liquid displacement even with low density differences. They also reported the override and underride with different density combinations of injected fluid and the in – place liquid during simultaneous injection of gas and liquid. There were also studies that took advantage of gas's own density to displace the bottom oil and achieved good results, especially in the dipping reservoirs, which has exhibited significant effect [4].

Rossen [5] and Shi [6] the gravity number to measure the degrees of gravity overburden. The gravity number is related to the pressure difference between the gaseous and liquid phases. Rossen argued that the larger mobility and gravity would induce a more obvious gravity overburden, and in continuous injection mode, a larger injectivity would result in a higher speed and pressure, and the consequently smaller gravity number can mitigate the influence of gravity overburden.

Based on their study, Boeije [7] studied the influence of injection speeds on gravity overburden, and Boeije suggested different injection strategies for the injected foam with different mobilities to reduce the influence of overburden. Shi [8] confirmed with numerical simulation that the attainable maximum injection pressure at the maximum injection rate brought the most favorable result in the continuous foam injection process, and at the same time, led to the least development of the gravity overburden.

Taking into consideration the viscosity-gravity ratio, Stone [9] and Jenkins [10] studied the starting point where gravity overburden took place for gas-water mixing zones in rectangular and radial reservoirs. They divided the reservoir into gas phase zone, gas-water mixing zone and water phase

zone, and they established a theoretical model for the gas-water mixed-phase displacement at steady-state.

Generally, most research regarding the override phenomenon was concentrated on gas – water phases, and only rarely has it focused on the override in the gas phase alone. The major differences lie in that the diffusion process is of great importance for the emergence of this phenomenon.

In this paper, the injector-producer model is established according to the actual well spacing. A mathematical model is established on the basis of the Darcy flow theory and the concentrated matter transfer theory to predict the formation and development of injected gas override. The effects of different injection strategies and reservoir properties on the development of gravity overburden were also studied. The results show that the gravity overburden is mainly affected by the density difference between injected gas and condensate gas, and the dry gas demonstrates the greatest degree of overburden, and the carbon dioxide can greatly mitigate the unfavorable effects caused by overburden. In addition, studies have shown that reservoir thickness, sedimentation pattern, well spacing, and injection-pressure differential also have different impacts on gravity overburden.

20.2 Mathematical Formulation

This study aims to solve the problem of override of injected gas during the cyclic gas injection process for condensate gas reservoirs. In this paper, a two-dimensional porous medium was constructed with width b and height h. The porous medium was considered to be saturated with condensate gas in the first place.

Generally, the mass transfer easily takes place during the development of condensate gas reservoirs. Considering the density difference between the injected gas and the condensate gas, and in the same time, to simplify the calculation process, the fluid involved in this study are divided into three pseudo phases: dry gas phase, condensate gas phase, condensate liquid phase, the formation fluid are categorized in three pseudo components: C_1 (CH_4), C_2~C_4 (C_2H_6~ C_4H_8), C_{5+} (C_5H_{10}~C_{7+}).

The conservation equations for injected gas and condensate gas in this study is:

$$\frac{\partial W_i}{\partial t} + \nabla \cdot \left(\mathbf{F}_i + \mathbf{D}_i + \mathbf{J}_i \right) = R_i, \qquad i = 1,2,3 \tag{20.1}$$

In the above equation, W_i, $\mathbf{F}_i$, $\mathbf{D}_i$, $\mathbf{J}_i$ represent the mass concentration, the convection flux, the diffusion flux, and the override flux. Their definitions are given as:

$$W_i = \phi \sum_{j=1}^{3} \rho_j S_j c_{ij} \tag{20.2}$$

Where ϕ, j, ρ_j, S_j and c_{ij} are the porosity, the phase identification, the density of phase j, the saturation of phase j, and the mass concentration of component i in phase j.

$$\mathbf{F_i} = \sum_{j=1}^{3} \rho_j \mathbf{v_j} c_{ij} \tag{20.3}$$

The subscripts c, d, L represent the condensate gas phase, the dry gas phase and the condensate liquid phase. Similarly, the subscripts 1, 2, 3 represent the three pseudo-components: CH_4, C_2H_6~C_4H_8 and C_5H_{10}~C_{7+}

$$\mathbf{D_i} = -\sum_{j=1}^{3} \rho_j \phi S_j D_{ij} \nabla c_{ij} \tag{20.4}$$

Where D_{ij} is the Maxwell-Stefan diffusion coefficient of component i in phase j.

$$\mathbf{J_i} = \phi \boldsymbol{v}_{gs} \rho_d c_{id} \tag{20.5}$$

In this part, we constructed a term $\boldsymbol{v}_{gs}$ to describe the vertical overburden velocity. $\boldsymbol{v}_{gs}$ is related with the vertical velocity and a function f affected by permeability, their definitions are given as:

$$\boldsymbol{v}_{gs} = \mathrm{f}(N_g, K)\boldsymbol{v}_z \tag{20.6}$$

Where K_z, K_x are the vertical permeability and horizontal permeability of the formation, and a, b are regression coefficients. N_g is a parameter related to the pressure gradient, the density difference between phases and the formation thickness.

Flux generated by chemical reaction

$$R_i = \sum_{j=1}^{3} \phi \rho_j S_j r_{ij} \tag{20.7}$$

The velocity is described by Darcy's Law

$$v_d = -\frac{KK_{rg}}{\mu_d} \nabla \left(p_g - \rho_i g H \right) \tag{20.8}$$

$$\boldsymbol{v_c} = -\frac{KK_{rg}}{\mu_c} \nabla \left(p_g - \rho_c g H \right) \tag{20.9}$$

$$\boldsymbol{v_L} = -\frac{KK_{rL}}{\mu_L} \nabla \left(p_g - \rho_L g H \right) \tag{20.10}$$

Where K, μ, ρ, g, and H are the permeability, the viscosity, the density, the gravity acceleration, and the formation height.

20.2.1 Numerical Scheme

This study adopted the Crank-Nicolson implicit difference method, which is a second–order implicit scheme and can generate numerically stable results. The differentially processed equations feature strong nonlinearity, and in this paper, the modified Newton-Raphson iterative method was used to solve the nonlinear equations.

20.3 Results and Discussion

20.3.1 The Development and Assessment of Gas Override

In Figure 20.1, one can observe the occurrence of gas override, specifically, the methane surpasses the condensate gas and breaks through from the top of the reservoir. In order to gain an intuitive understand of the overburden phenomenon, in this section, we adopt the concepts of override angel and

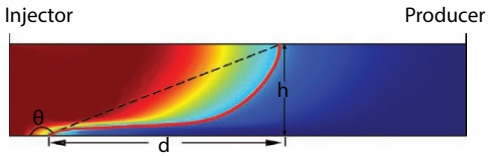

Figure 20.1 The shape of the injected gas override.

horizontal override distance to assess the degree of gas overburden, and their definitions are depicted in Figure 20.1. In Figure 20.1, the d represents the horizontal overburden distance and θ represents the overburden angle.

$$\theta=\pi-\text{arctg}\left(\frac{h}{d}\right) \tag{20.11}$$

Notably, the θ is proportional to the degree of gas overburden. That is to say, when θ is 90°, it means that the dry gas does not flow over the condensate gas, and when θ is greater than 90°, the dry gas exceeds the condensate gas. The larger θ implies a heavier development of gas overburden.

It can be seen from Figure 20.2 that from day 0 to day 700, the horizontal overburden distance and the overburden angle experience an increase of 158m and 68° respectively. The override angle exhibits a drastic increase in the early stage and a moderate one afterwards.

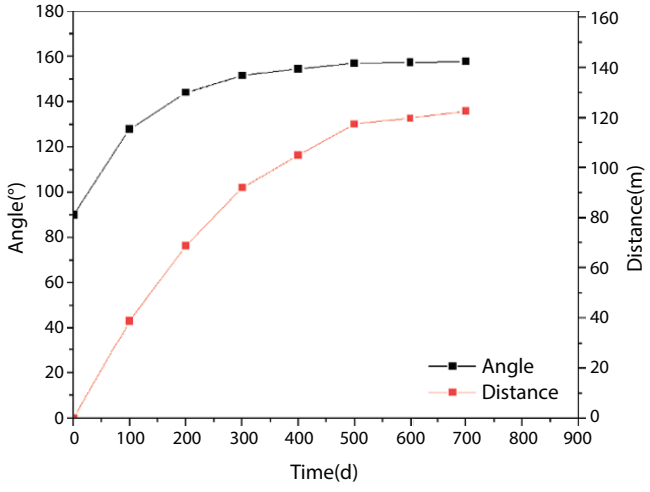

Figure 20.2 Overburden angle and horizontal overburden distance vs. time.

Figure 20.3 depicts the mole fraction distribution of methane on the imaginary interface at different times, from which one can observe that methane is more likely to aggregate at the upper part of the reservoir, and the aggregation of methane would evolve over time.

After gas is injected, a transition zone is formed between the injected gas and the condensate gas as the result of mass transfer process, and the transition zone is further widened over time. Figure 20.1 shows a typical composition contour plots of injected methane. In this paper, the mixture width is defined as the distance between the position where the mole fraction of injected gas is 0 and the position where the mole fraction of injected gas is 0.99. It can be noticed from Figure 20.1 that with the injection of methane, the mixture zone composed of methane and condensate gas emerges, and its width expands from the initial 15m on day 50 to 124 m on day 800 (Figure 20.4). One can also observe that the width increases fast at earlier stage and slows down in the later period.

20.3.2 Sensitivity Analysis

In this section, we investigated the influence of density differences on gravity override, which were reflected in the choice of different injected gases (dry gas, nitrogen and carbon dioxide).

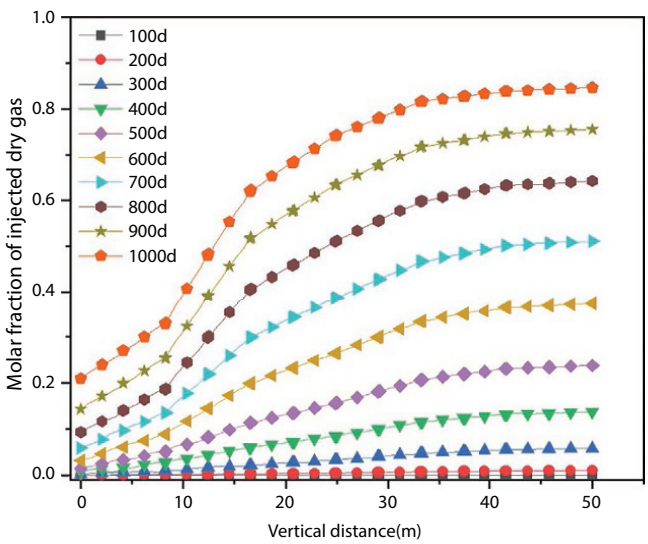

Figure 20.3 Molar fraction distribution along the z direction.

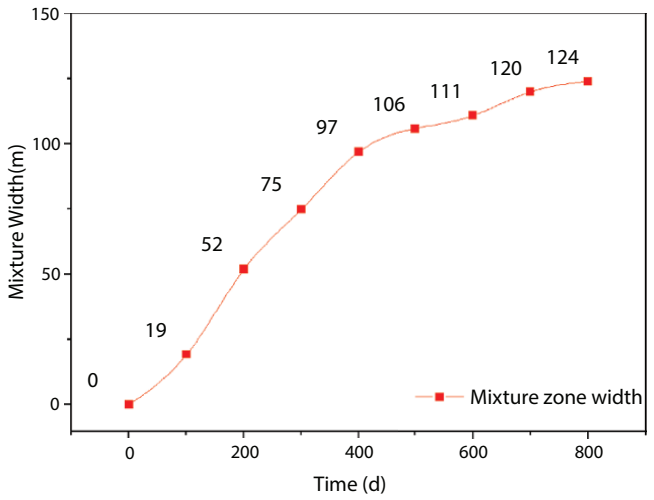

Figure 20.4 Development of the mixture zone.

20.3.2.1 The Influence of Density Difference on Gas Override

In this section, the effect of density difference on gas override was reflected by different injected gases. Three typical gas agents (methane, nitrogen and carbon dioxide) were chosen for that purpose. The primary differences among those agents lie in their different densities under formation condition, which are 246 kg/m^3, 321 kg/m^3, and 731 kg/m^3 for dry gas, nitrogen and carbon dioxide, respectively. As the density of condensate gas in this study is 309 kg/m^3, the density ratios between injected gases and condensate gas are 0.80, 1.04 and 2.37 for dry gas, nitrogen and carbon dioxide.

Figure 20.5 shows the molar fraction distributions of CO_2, N_2 and C_1 at producer on day 1000. It can be seen that along the z direction, from

Figure 20.5 Typical molar distribution of differennt injected gases.

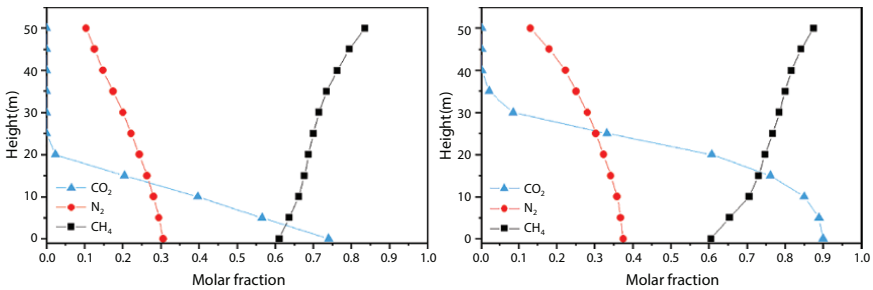

Figure 20.6 Molar distribution of injected gas at producer.

z= 0m to z= 50m, the molar fraction of dry gas increases from 0 to 0.225, with the one for nitrogen decreases from 0.306 to 0.104 and the one for CO_2 decreases from 0.740 to 0, indicating that injected dry gas would cause the most severe overburden, and N_2 can relieve the override in a large scale. Furthermore, for the case of CO_2, it can even lead to a reverse override. When the time comes to day 1200, the vertical molar fraction difference for methane, nitrogen and carbon dioxide along the z-axis are 0.270, -0.239 and -0.883, respectively. In other words, the overburden of the three injected gases all become stronger over time.

20.4 Conclusions

The mathematical model in this study provides a quick and appropriate solution to the gas override phenomenon in the development of condensate gas reservoir, facilitating the prediction and prevention of the unfavorable results the gas override might bring. Some of the conclusions are drawn as follows.

1. A transition zone is formed between the injected gas and the condensate gas as the result of mass transfer process, and the transition zone is further widened over time.
2. Among the various factors involved in the development of gas override, the density difference is the largest contributor. The dry gas would surpass the original condensate gas and CO_2 would flow along the bottom of the original condensate gas.

References

1. Abdelgawad, K.Z. and Mahmoud, M.A., *In-situ generation of CO 2 to eliminate the problem of gravity override in EOR of carbonate reservoirs.* SPE Middle East Oil & Gas Show and Conference, 2015, Society of Petroleum Engineers, 2015.
2. Spivak, A., Gravity Segregation in Two-Phase Displacement Processes. *Soc. Petrol. Eng. J.*, 14, 06, 619–632, 1974.
3. Nzekwu, B.L. and Bennion, D.W., Mobility Control in Dynamic Gravity Segregation Flow Systems. *J. Can. Petrol. Technol.*, 26, 04, 1987.
4. Xia, T.X., Greaves, M., Turta, A.T., Ayasse, C., THAI—A 'short-distance displacement' *in situ* combustion process for the recovery and upgrading of heavy oil. *Chem. Eng. Res. Des.*, 81, 3, 295–304, 2003.
5. Rossen, W.R., Zeilinger, S.C., Shi, J.X., Lim, M.T., Simplified Mechanistic Simulation of Foam Processes in Porous Media. *SPE J.*, 4, 03, 279–287, 1999.
6. Shi, J.X. and Rossen, W.R., Simulation and Dimensional Analysis of Foam Processes in Porous Media. *SPE Reserv. Eval. Eng.*, 1, 02, 148–154, 1998.
7. Boeije, C.S. and Rossen, W., Gas-injection rate needed for SAG foam processes to overcome gravity override. *SPE J.*, 20, 01, 49–59, 2014.
8. Shi, J.X. and Rossen, W.R., *Improved surfactant-alternating-gas foam process to control gravity override.* SPE/DOE improved oil recovery symposium, 1998, Society of Petroleum Engineers, 1998.
9. Stone, H.L., *Vertical, conformance in an alternating water-miscible gas flood.* SPE annual technical conference and exhibition, 1982, Society of Petroleum Engineers, 1982.
10. Jenkins, M.K., *An analytical model for water/gas miscible displacements.* SPE enhanced oil recovery symposium, 1984, Society of Petroleum Engineers, 1984.

21

Research on the Movable Water in the Pores of Tight Sandstone Gas Reservoirs

Guodong Zou[1], Weiyao Zhu[1]*, Wenchao Liu[1], Yunqing Shi[2] and Jin Yan[2]

[1]Institute of Applied Mechanics, University of Science and Technology Beijing, Beijing, China
[2]SINOPEC Exploration and Development Research Institute, Beijing, China,

Abstract
In conventional reservoir assessment, porosity and permeability are generally used as characterizations of reservoir properties. The test of the movable water and the core flooding experiments show that for the low-permeability and ultra-low-permeability reservoirs, it is deficient to evaluate the reservoir physical properties only by porosity and permeability. As a supplementary parameter, the content of movable water can better characterize the physical properties and seepage characteristics of tight sandstone gas reservoirs. To study the movable water in the rock pores, a combination of gas flooding experiments and nuclear magnetic resonance (NMR) technique are adopted in this paper. After each gas flooding experiment, the core is weighed, and NMR is used to test the water distribution. Experiments show that the water in the tight sandstone gas core greatly reduces its effective permeability, and there is remarkable negative correlation between the permeability loss and the core permeability. Secondly, when the injection pressure is greater than the critical pressure, the movable water in the pores will all be driven out, and as the injection pressure increases, the residual water will also be partially driven out.

Keywords: Tight sandstone gas reservoirs, low permeability, water saturation, movable water

21.1 Introduction

Most tight sandstone gas reservoirs in China have the characteristics of low porosity, low permeability, high water saturation, high stress

**Corresponding author*: weiyaook@sina.com

Ying Wu, John J. Carroll, Mingqiang Hao and Weiyao Zhu (eds.) Gas Injection into Geological Formations and Related Topics, (343–350) © 2020 Scrivener Publishing LLC

sensitivity, high capillary pressure, and the reservoir geological conditions are very complicated. Seepage theory and gas reservoir engineering method can no longer meet the needs of low-permeability gas reservoir development. The seepage mechanism of low-permeability gas reservoirs is quite different from that of medium-high permeability gas reservoirs [1]. The influencing factors are numerous and the situation is complicated. At present, gas-water seepage law, the changing characteristics of reservoirs in the development process, and the gas supply mechanism in different regions of heterogeneous reservoirs are still not clear. It is necessary to continue to study, grasp the development mechanism and laws, and take corresponding countermeasures to effectively improve the development benefits of low permeability sandstone gas reservoirs.

The initial water saturation of the tight sandstone gas reservoirs is generally high, and the water/gas ratio of gas wells is also high at the same time. Whether it is Sulige gas field or Guang'an gas field in China, gas wells generally produce water, and some have high water production [2]. It is indicated that part of movable water is produced from the stratum. In order to study the mechanism of water production, different types of cores are selected in this paper, and gas flooding experiments with different pressure are carried out to analyze the change of water saturation and its mobility in the pores.

21.2 Experimental

21.2.1 Experimental Equipment

The experiment was conducted under normal temperature and pressure. The confining pressure system uses a high-precision multi-stage plunger displacement pump (Teledyne isco100-DX) for pressure control. A DXD high-precision digital pressure sensor is used for pressure measurement, and a high linear differential pressure sensor is used to accurately collect the pressure across the core. Back pressure control system uses BP-100 air spring back pressure valve manufactured by an American company and uses high-precision multi-stage piston displacement pressure pump to control. In order to simulate the characteristics of formation stress, the experiment adopts three-axis core holder. Gas metering using soap-film flow meter. The experimental equipment diagram is shown in Figure 21.1.

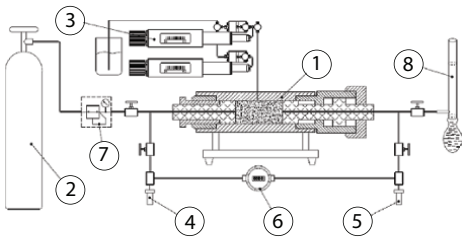

1 - core gripper, 2 - gas cylinder, 3 - multi-stage plunger pump,
4 and 5 - pressure sensors, 6 - high linearity differential pressure sensor,
7 - pressure-regulating valve, 8 - soap-film gas meter

Figure 21.1 Experimental equipment diagram.

21.2.2 Experimental Procedure

Cores with different physical properties (Table 21.1) were selected to conduct gas percolation experiments (dry cores) and gas flooding experiments (water-saturated cores).

(1) gas percolation experiments (dry cores): Put the dry cores into the holding unit, keep the net confining pressure to 3.0MPa, and set the gas drive pressure to 0.05, 0.1, 0.2, 0.3, 0.4, 0.5, 0.6, 0.7, 0.8, 0.9, 1.0, 1.5, 2.0, 3.0 MPa (from low to high) for gas flooding, when the gas flow rate is fixed at certain gas drive pressure, increase the drive pressure to the next point

(2) gas flooding experiments (water-saturated cores): after the above step, cores are vacuumed to fully saturate the brine, and then repeat the step 1.

The flow rate of the dry cores increases linearly with the increase of the gas drive pressure (Figure 21.2), indicating that the gas percolation in the dry cores is linear percolation.

Table 21.1 Cores physical parameters.

Core number	Length/cm	Diameter/cm	Porosity/%	Permeability/ $\times 10^{-3}\mu m^2$
GA110-1	3.60	2.55	15.0	7.41
GA110-2	6.48	2.55	14.2	4.71
GA111-5	3.61	2.56	10.9	0.628
GA110-3	4.41	2.55	8.18	0.048

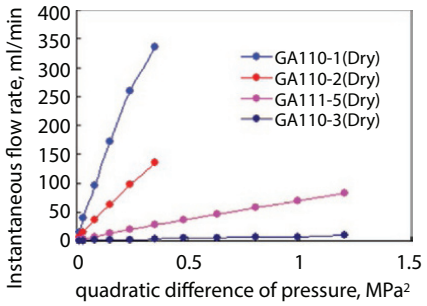

Figure 21.2 Relationship between gas drive flow and pressure of dry cores.

21.3 Results and Discussion

21.3.1 Change of the Saturated Water

Under the same gas drive pressure, the gas flow rate passing through the fully saturated water cores is much smaller than the flow rate through the dry cores (Figure 21.3), indicating that the water inside the core has a resistance to the gas flow, the gas cannot flow as the drive pressure is too low to overcome the capillary force of water. The efficient flow may happen only when the pressure is high enough to drive the water in the maximum pore throat, and the pressure is the pseudo starting pressure.

The change of the water saturation in the core under various drive pressure difference is shown in Figure 21.4. According to Darcy's law, on the same core, the seepage velocity is proportional to the drive pressure difference, so the pressure difference is actually a reflection of the seepage velocity. As shown in Figure 21.3 and Figure 21.4, when a certain initial pressure difference is reached, the water in the core begins to flow, and the water saturation decreases drastically. After that, the displacement pressure difference increases (that is, the airflow velocity increase), there is a small drop in water saturation. This phenomenon indicates that when the displacement pressure is low, the water in the relatively large pores is driven first. As the displacement pressure increases, the water in the smaller pores starts to flow. And the pressure continues to increase, the water production is no longer increased, the remaining water in the pores is the residual water.

This indicates that for the reservoir which has good conditions of physical character, when the water saturation is high, the gas starts to flow, which will drive part of the water flow in the pores under a certain pressure difference. And the larger the production pressure difference (the

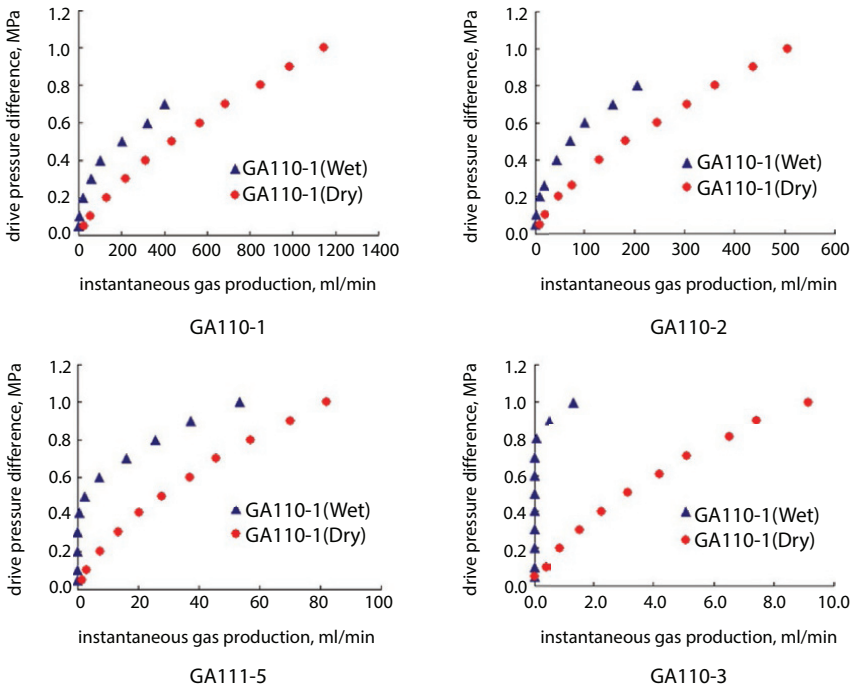

Figure 21.3 Comparison of dry and wet cores.

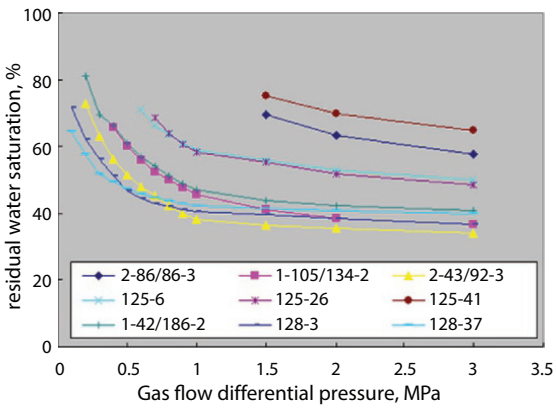

Figure 21.4 Relationship between flow differential pressure and residual water saturation.

higher the gas well production), the more water is produced, when it is below a certain production pressure difference (the output is reduced), the water in the pores stops flowing, and the gas well stops producing water. This indicates that the irreducible water saturation of the low permeability gas reservoir is not a fixed value in the development process,

but a physical quantity relative to the gas seepage velocity. As the gas flow velocity increases, the water saturation decreases gradually, which increases the gas phase permeability. Therefore, in some low permeability gas reservoirs, the gas phase permeability may increase with the development of the gas field.

The relationship between residual water saturation and flow pressure difference is shown in Figure 21.4, which can be adopted to determine whether a certain type of gas layer produces water under various production pressure difference. For example, the sample 2-43/92-3(Φ=12.58%, K=1.51mD), if the initial water saturation is 50%, the water will not flow when the production pressure difference is less than 0.5MPa, and the water in the pores begins to flow when the production pressure difference is above 0.5MPa. The upper part the curve is in the figure, the worse the physical properties of the sample is, indicating that under the same production pressure difference, the physical properties are poorer, the immovable water saturation is higher in the reservoir. From the perspective of accumulation, the water in the tight reservoir is not easily discharged in the process of accumulation, so the residual water saturation is high. (The physical properties of the cores in the figure: porosity is 7.75% to 14.45%, permeability is 0.049 to 20.8mD.)

21.3.2 Test of the Movable Water

In conventional reservoir assessment, porosity and permeability are generally used as characterizations of reservoir properties. The test of the movable water and the core flooding experiments show that for the low-permeability and ultra-low-permeability reservoirs, it is deficient to evaluate the reservoir physical properties only by porosity and permeability. As a supplementary parameter, the content of movable water can better characterize the physical properties and seepage characteristics of tight sandstone gas reservoirs.

To study the movable water in the rock pores, a combination of gas flooding experiments and nuclear magnetic resonance (NMR) technique are adopted in this paper. After each gas flooding experiment, the core is weighed, and NMR is used to test the water distribution.

Figure 21.5 shows the water saturation profiles of the four cores (GA110-1, GA110-2, GA111-5, and GA110-3) under different gas flooding pressures. It can be seen that the permeability of GA110-1 and GA110-2 is relatively high (greater than 1.0mD), the water saturation begins to decrease when the gas flooding pressure is 0.05MPa. But the permeability of GA111-5, GA110-3 is small (less than 1.0mD), the gas flooding pressure at which the

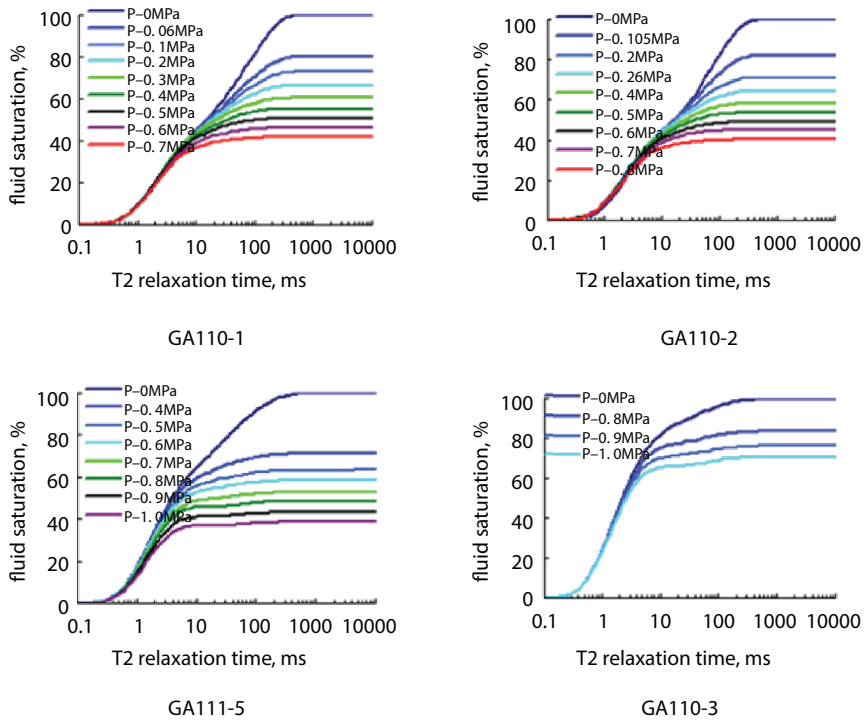

Figure 21.5 Water saturation profiles of cores.

water saturation begins to decrease is relatively large, the pressure at which the water saturation of GA111-5 begins to decrease reaches 0.4MPa, and GA110-3 reaches 0.8 MPa. It can also be seen from the figure that the water saturation decreases greatly in the initial stage of gas flooding. As the gas flooding pressure increases, the decreasing extent of the water saturation is reduced. And the eventual decreasing extent of the water saturation is proportional to the permeability of cores. For low permeability gas fields, it is difficult to drive water out when the gas flooding pressure is low, indicating that the water in the small pores is difficult to drive out as the binding force (capillary force) is strong.

21.4 Conclusion

(1) The water inside the core has a resistance to the gas flow, the gas cannot flow as the drive pressure is too low to overcome the capillary force

of water. The efficient flow may happen only when the pressure is high enough to drive the water in the maximum pore throat.

(2) The irreducible water saturation of the low permeability gas reservoir is not a fixed value in the development process, but a physical quantity relative to the gas seepage velocity. As the gas flow velocity increases, the water saturation decreases gradually, which increase the gas phase permeability.

(3) For low permeability gas fields, it is difficult to drive water out when the gas flooding pressure is low, the water in the small pores is difficult to drive out as the binding force (capillary force) is strong.

References

1. Wang, J., Prospects for the large sized tight sandstone gas bearing regions in China. *Nat. Gas Ind.*, 2000.
2. Kang, Y.L. and Luo, P.Y., Current status and prospect of key techniques for exploration and production of tight sandstone gas reservoirs in China. *Petrol. Explor. Dev.*, 34, 2, 239–245, 2007.

22

Probabilistic Petroleum Portfolio Options Evaluation Model (POEM)

Darryl Burns

TAQA North, Calgary, AB, Canada

Abstract

The purpose of this project is to provide petroleum engineers and management teams with a probabilistic model for evaluating projects and portfolios to identify optimal investment options that meet or exceed desired return criteria while remaining within acceptable risk and capital budget. This project would not have been possible without the Probability Management Enterprise SIPmath add-in tools, and mentorship from Dr. Sam Savage. Thank you.

The model consists of an individual Project Economic Evaluation Tool (PEET), and a Portfolio Options Evaluation Tool (POET), both constructed in Microsoft Excel with Enterprise SIPmath add-in available from Probability Management. These tools are provided as a 'beta version'. At this stage of development, these tools are suitable for use by an experienced petroleum engineer who is also familiar with Microsoft Excel and Probability Management Enterprise SIPMath add-in tools. Commodity pricing and royalty calculations built into the tools are specific to the Province of Alberta, Canada. Since the tools are constructed in Microsoft Excel, the libraries and calculations can easily be modified to include additional jurisdictions.

Keywords: Project economic evaluation tool, portfolio options evaluation tool

22.1 Project Economic Evaluation Tool (PEET)

PEET calculates cash flows and reports key profitability indicators for an input individual oil or gas well project. The production forecast, however, is input as a statistical distribution, not as a single forecast. Resulting cash flows and profitability indicators are calculated by Monte Carlo simulation,

Email: Darryl.Burns@taqa.ca

Ying Wu, John J. Carroll, Mingqiang Hao and Weiyao Zhu (eds.) Gas Injection into Geological Formations and Related Topics, (351–360)

and reported as statistical distributions, not single numbers, under a variety of price forecast scenarios. This interactive tool provides investment decision makers with key information including the range of possible outcomes and the statistical distribution, or in other words, the 'chance of whatever' occurring.

PEET results for multiple projects under multiple price forecast scenarios are saved into a library for POET.

22.2 Portfolio Options Evaluation Tool (POET)

POET accepts libraries of projects generated by PEET, and graphically displays risk vs. return and cost of all portfolio combinations under a number of scenarios. The intent is to identify a number of portfolio investment options that meet or exceed desired return criteria while remaining within acceptable risk and budget. Since there are many measures and visualizations of return and risk, steps for constructing POET from a blank Excel workbook are included in the Operating Instructions.

22.3 Program Calculation Procedures

22.3.1 General Cash Flow Calculation and Profitability Indicators

All calculations in PEET are done on a Gross 100% Working Interest basis.

PEET is structured to accept inputs and calculate monthly cash flows as follows:

22.3.1.1 General Cash Flow Calculation

Gross Revenue
- Royalties
- Operating Costs
Operating Cash Income Before Tax (OCIBT)
- Income Tax
Operating Cash Income After Tax (OCIAT)
- Exploration Capital
- Development Capital
Cash Flow After Tax (CFAT)

Profitability indicators are defined as:

Payout = time for accumulated Cash Flow After Tax = 0. Note time value of money ignored.

$$\textbf{\textit{Profit to Investment Ratio}} = \frac{\sum Cash\ Flow\ After\ Tax\ (undiscounted)}{\sum investment\ (Capital)\ (undiscounted)}$$

NPV = Σ CFAT discounted to time 0 using the discount rate.

Internal Rate of Return (IRR) = discount rate at which Σ CFAT=0 (ie rate that makes NPV=0)

$$\textbf{\textit{Value to Investment Ratio}} = \frac{\sum Cash\ Flow\ After\ Tax\ (discounted)}{\sum investment\ (Capital)\ (discounted)}$$

22.4 General Calculation Steps

The PEET worksheet is structured to complete calculations in the following order;

1. Production forecast distribution
2. Trial Raw production forecast
3. Random Walk Price Forecast
4. Gross Revenue before D&A and shut in evaluation
5. Royalty before D&A and shut in evaluation
6. Operating Cost before D&A and shut in evaluation
7. Income Tax before D&A and shut in evaluation
8. Shut In Check
9. Capital Cost (success and D&A cases)
10. D&A and Shut In Corrected Cash Flows
11. Financial Calculations from Corrected Cash Flows

Prospect Number

Prospect number is used for tracking individual projects when evaluating portfolios in POET. Prospect number is also used for incrementing the HDR seed for the D&A distribution, and the production forecast

distribution to avoid coherence in D&A events and production forecast factors between projects.

Shut In Evaluation
Once all components of the General Cash Flow calculation are completed, PEET completes a Shut In Evaluation in each producing month to test whether or not OCIAT, less fixed opex, is positive. If OCIAT, less fixed opex, is negative, production and cash flow calculations are corrected to reflect a shut in condition for that month. Production volume, Gross Revenue, and Royalty are set to 0. Opex is set to reflect fixed operating costs only.

Commodity Price Library
A commodity price library has been constructed to ensure price coherence amongst the individual project and portfolio evaluations. The Chief Probability Officer is the steward of this master file, and is responsible for updating and distributing the Master Commodity Price Forecast and Master Commodity Price History worksheet tables quarterly.

The library contains the following gas, NGL, and oil price forecasts

A) Sproule Escalating
B) Sproule Constant (flat forward)
C) GLJ Petroleum Consultants Escalating
D) Deloitte Escalating

Random Walk Commodity Price Change Distribution and Forecast
Random walk commodity price change distribution and forecast is generated as follows:

1. Monthly oil, gas, and NGL commodity price history from the previous ten years (2009-01 to 2018-12) were collected and entered into the "Price History" tab of the project spreadsheet tool (PEET).
2. Monthly price changes for each commodity were calculated.
3. The monthly price change distribution type for each commodity was evaluated by ordering the price changes from

smallest to largest, dividing the range into 5 equal 'bins', and counting the number of data points in each bin. The shape of the resulting histograms indicated that a normal type distribution would be an acceptable model.

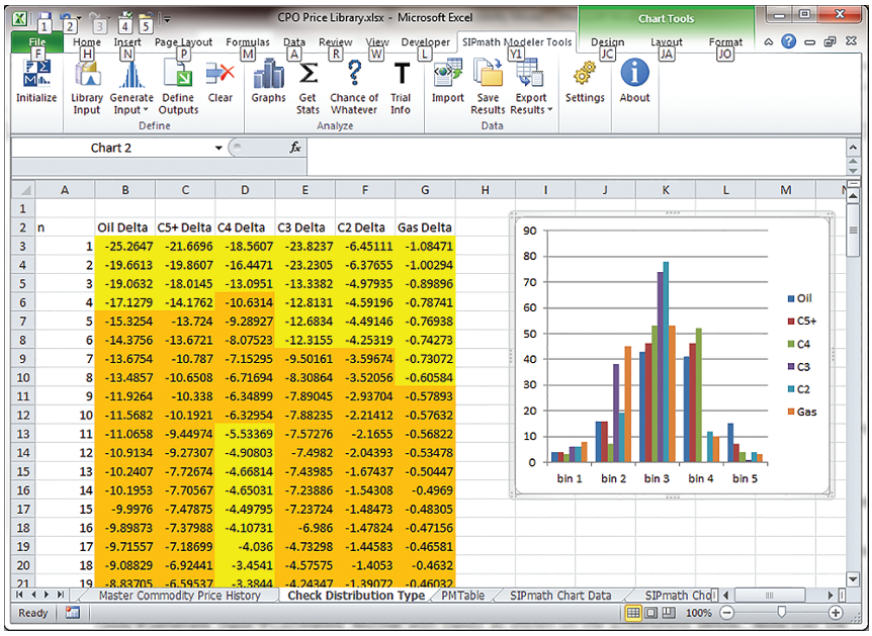

n	Oil Delta	C5+ Delta	C4 Delta	C3 Delta	C2 Delta	Gas Delta
1	-25.2647	-21.6696	-18.5607	-23.8237	-6.45111	-1.08471
2	-19.6613	-19.8607	-16.4471	-23.2305	-6.37655	-1.00294
3	-19.0632	-18.0145	-13.0951	-13.3382	-4.97935	-0.89896
4	-17.1279	-14.1762	-10.6314	-12.8131	-4.59196	-0.78741
5	-15.3254	-13.724	-9.28927	-12.6834	-4.49146	-0.76938
6	-14.3756	-13.6721	-8.07523	-12.3155	-4.25319	-0.74273
7	-13.6754	-10.787	-7.15295	-9.50161	-3.59674	-0.73072
8	-13.4857	-10.6508	-6.71694	-8.30864	-3.52056	-0.60584
9	-11.9264	-10.338	-6.34899	-7.89045	-2.93704	-0.57893
10	-11.5682	-10.1921	-6.32954	-7.88235	-2.21412	-0.57632
11	-11.0658	-9.44974	-5.53369	-7.57276	-2.1655	-0.56822
12	-10.9134	-9.27307	-4.90803	-7.4982	-2.04393	-0.53478
13	-10.2407	-7.72674	-4.66814	-7.43985	-1.67437	-0.50447
14	-10.1953	-7.70567	-4.65031	-7.23886	-1.54308	-0.4969
15	-9.9976	-7.47875	-4.49795	-7.23724	-1.48473	-0.48305
16	-9.89873	-7.37988	-4.10731	-6.986	-1.47824	-0.47156
17	-9.71557	-7.18699	-4.036	-4.73298	-1.44583	-0.46581
18	-9.08829	-6.92441	-3.4541	-4.57575	-1.4053	-0.4632
19	-8.83705	-6.59537	-3.3844	-4.24347	-1.39072	-0.46032

4. Variance (VAR.S) of the commodities and covariance (COVARIANCE.S) amongst the commodities were calculated and entered into a covariance matrix. "Distributions", "Means", and "HDR" column headers were placed adjacent to the covariance matrix.
5. A Correlated Normal distribution of the commodity price changes was generated by SIPmath Modeler Tools→Generate Input→Correlated Normal with inputs as shown on the screenshots below. Note that the Means were set at 0, and Start Var ID = 4362714:

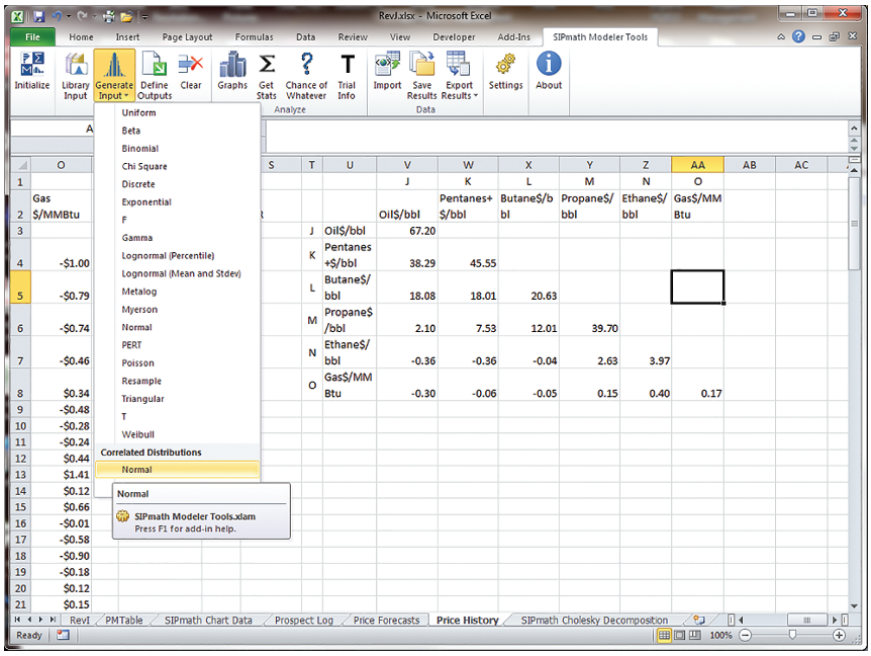
RevI.xlsx - Microsoft Excel
File
Home
Insert
Page Layout
Formulas
Data
Review
View
Developer
Add-Ins
SIPmath Modeler Tools
Initialize
Library Input
Generate Input
Define Outputs
Clear
Graphs
Get Stats
Chance of Whatever
Trial Info
Import
Save Results
Export Results
Settings
About
Analyze
Data
Uniform
Beta
Binomial
Chi Square
Discrete
Exponential
F
Gamma
Lognormal (Percentile)
Lognormal (Mean and Stdev)
Metalog
Myerson
Normal
PERT
Poisson
Resample
Triangular
T
Weibull
Correlated Distributions
Normal
Normal
SIPmath Modeler Tools.xlam
Press F1 for add-in help.
Gas $/MMBtu
Oil$/bbl
Pentanes+ $/bbl
Butane$/bbl
Propane$/bbl
Ethane$/bbl
Gas$/MMBtu
RevI
PMTable
SIPmath Chart Data
Prospect Log
Price Forecasts
Price History
SIPmath Cholesky Decomposition
Ready
100%

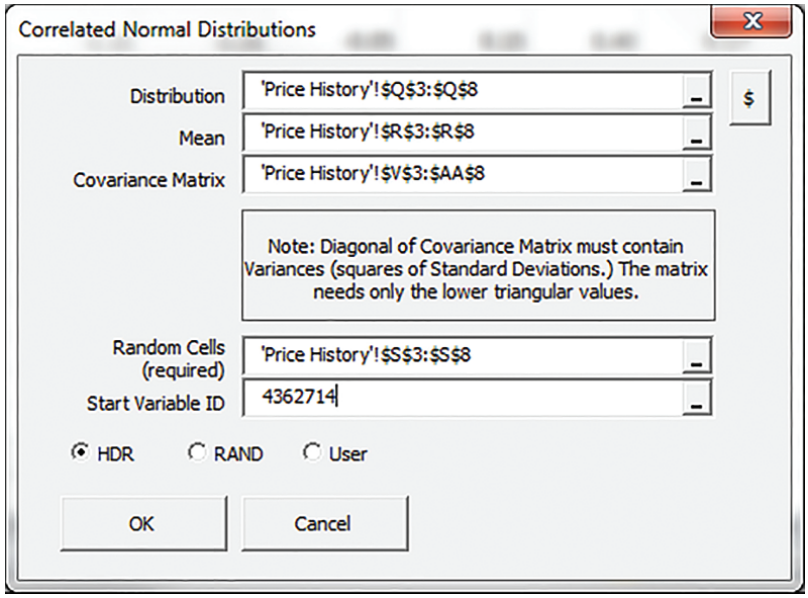
Correlated Normal Distributions
Distribution
'Price History'!$Q$3:$Q$8
$
Mean
'Price History'!$R$3:$R$8
Covariance Matrix
'Price History'!$V$3:$AA$8
Note: Diagonal of Covariance Matrix must contain Variances (squares of Standard Deviations.) The matrix needs only the lower triangular values.
Random Cells (required)
'Price History'!$S$3:$S$8
Start Variable ID
4362714
HDR
RAND
User
OK
Cancel

6. Covariance output distributions of the commodity price differences was then generated by SIPmath Modeler Tools→Define Output with inputs as shown on the screenshot below:

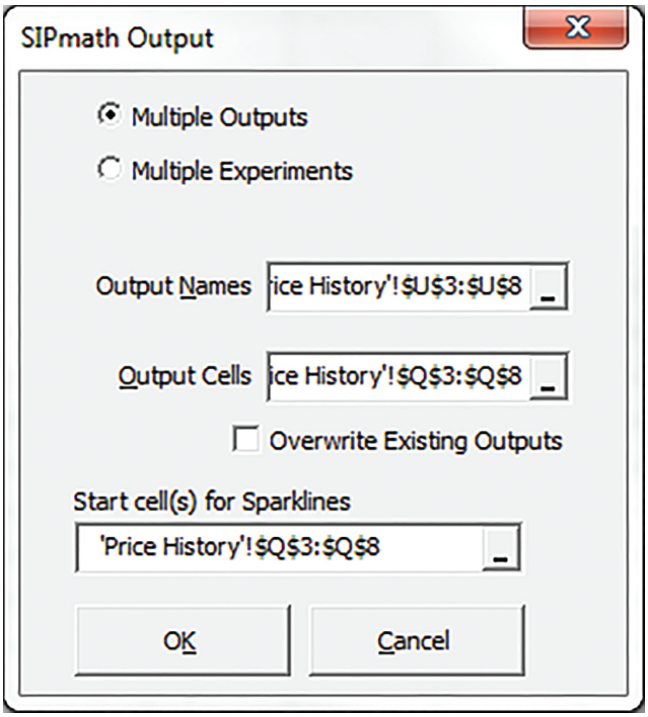

7. A subset of cross plots of commodity price change pairs of the original data, and PMTable correlation results were compared, and found to be in reasonable agreement.
8. For each month of the random walk price forecast section of cash flow calculations, a uniform input distribution was input, and the input distribution multiplied by the number of trials (500 for example) and rounded to the nearest integer so that an 'index' number between 1 and the number of trials (500 for example) is generated to look up a coherent set of commodity price changes. Note that Start Variable ID 4362722 was used.

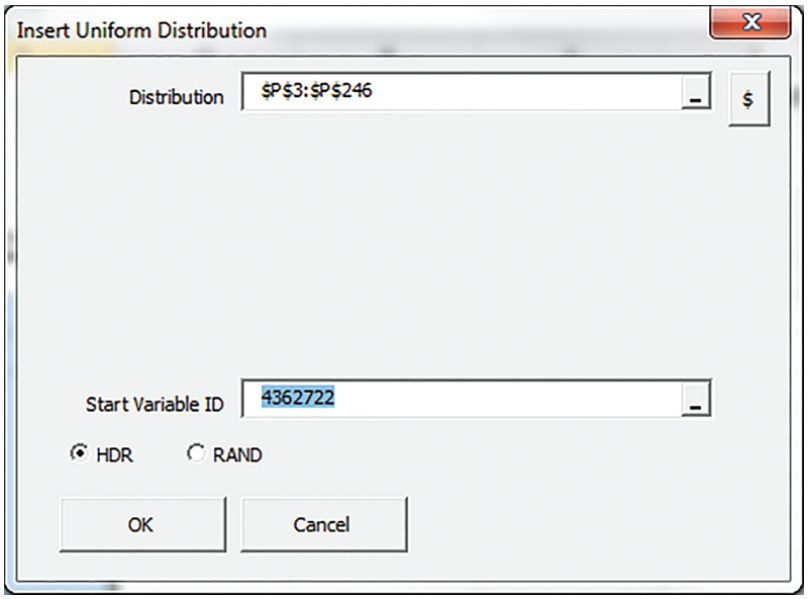

9. This coherent set of commodity price changes is then added to the prior month's commodity prices, and, if the calculated prices are below the maximum and above the minimum price limits, the calculation is carried, otherwise the price is set at minimum if the calculation is below minimum, and maximum if calculation is above maximum limit.
10. Calculated commodity prices at months 1, 6, 12, and annually to production month 120 are defined as outputs, Low and high percentile values as dictated by user input are calculated, and results displayed graphically for each of the commodities.

Production Forecast Statistical Distribution Calculations

PEET is designed to accept results of reservoir engineering evaluation of production data, including decline curve and statistical evaluation. These results are in the form of a multi-segment Arps decline curve fit to the 50th percentile (P50) production forecast, and the Estimated Ultimate Recovery (EUR) of the 90th percentile (P90) production forecast. PEET calculates the P50 EUR from the input decline parameters, and calculates the input lognormal distribution ("LgNrml_RAW_EUR") of the EUR's from the calculated P50 EUR, and the input P90 EUR. The production forecast for each

trial in the Monte Carlo simulation is calculated by multiplying the P50 production forecast by the ratio of trial EUR/P50 EUR, and plotted in a semilog Rate vs. Cumulative production chart for reference.

Gross Revenue Calculations
Monthly Gross Revenue is calculated by multiplying volume x price for each sales product.

Royalty Calculations
Alberta Modernized Royalty Framework for new wells spud on or after January 1, 2017, formulas are used to estimate Crown royalties payable. Rigorous calculation of royalties by fluid recombination from gas and condensate analyses and volumes is outside the scope of this project, but could be added to the model. Sales gas gross heating value is used for heating value of the Gas+Ethane gas equivalent product, and 33%, 50%, and 100% recovery factors of propane, butane, and pentanes+ from the raw gas are assumed.

Operating Cost Calculations
Monthly operating cost consists of two components, fixed and variable. Operating cost is calculated by adding fixed cost to (unit volume cost x volume). Unit volume costs are on a raw gas basis for gas wells, and oil basis for oil wells.

Income Tax
Income tax for this project is assumed to be 0, although the model is structured to accept tax calculations.

Chance of Success Distribution Output
Drill and Abandon, or failure, risk is input, and a uniform input distribution is used to determine whether or not a trial in the Monte Carlo simulation is a D&A, or a success case. (Forecast Factor set to 0 if uniform distribution value for the trial is less than the % D&A chance entered.) The Chance of Success output is compared to the input D&A chance as a check. Chance of Success should equal 1- Chance of D&A.

Raw Cumulative Gas Distribution Output
Raw Cumulative Gas Distribution Output is calculated from the raw gas production forecasts in the Monte Carlo simulation trials. D&A risk, and Shut In corrections are included in this calculation, so the output distribution will be lower than the (unrisked) production forecast distribution input.

Total Sales MBOE Distribution Output
Total Sales MBOE Distribution Output is calculated from the sales product volumes in the Monte Carlo simulation trials. D&A risk, and Shut In corrections are included in this calculation. A conversion factor of 1 boe:6 mcf gas is used to convert MMSCF sales gas to MBOE.

Payout Month Distribution Output
Payout month is the project month that the undiscounted Cumulative Cash Flow After Tax becomes positive. To avoid calculation errors, the payout month is set to 240 in the event of a D&A outcome on a trial. Set the Chance of D&A=0 for accurate undiscounted payout month distribution for the success outcomes.

Index

Also of Interest

Check out these related titles from Scrivener Publishing

Also Available in the *Advances in Natural Gas Engineering Series:*

The Three Sisters: Acid Gas Injection, Carbon Capture and Sequestration, and Enhanced Oil Recovery, edited by Ying (Alice) Wu, John J. Carroll, and Yongle Hu, ISBN 9781119510062. This seventh volume in the series, Advances in Natural Gas Engineering, presents the "three sisters," the three hottest and most important topics in the industry today, both independently and how they're interrelated: acid gas injection, carbon capture and sequestration, and enhanced oil recovery. *NOW AVAILABLE!*

Carbon Dioxide Capture and Acid Gas Injection, edited by Ying Wu and John J. Carroll, ISBN 9781118938669. This sixth volume in the series, Advances in Natural Gas Engineering, offers the most in-depth and up-to-date treatment of CO2 capture and acid gas injection, two of the hottest topics in natural gas engineering. *NOW AVAILABLE!*

Acid Gas Extraction for Disposal and Related Topics, edited by Ying Wu, John Carroll, and Weiyao Zhu, ISBN 9781118938614. This fifth volume in the series, Advances in Natural Gas Engineering, offers the most in-depth and up-to-date treatment of acid gas extraction for disposal, an important innovation in natural gas engineering. *NOW AVAILABLE!*

Gas Injection for Disposal and Enhanced Recovery, edited by Ying Wu, John Carroll, and Qi Li, ISBN 9781118938560. This fourth volume in the series, Advances in Natural Gas Engineering, offers the most in-depth and up-to-date treatment of the disposal and enhanced recovery of natural gas. *NOW AVAILABLE!*

Sour Gas and Related Technologies, edited by Ying Wu, John J. Carroll, and Weiyao Zhu, ISBN 9780470948149. Written by a group of the most well-known and knowledgeable authors on the subject in the world, volume three focuses on one of the hottest topics in natural gas today, sour gas.

This is a must for any engineer working in natural gas, the energy field, or process engineering. *NOW AVAILABLE!*

Acid Gas Injection and Related Technologies, edited by Ying Wu and John J. Carroll, ISBN 9781118016640. Focusing on the engineering of natural gas and its advancement as an increasingly important energy resource, this volume is a must-have for any engineer working in this field. *NOW AVAILABLE!*

Carbon Dioxide Sequestration and Related Technologies, edited by Ying Wu and John J. Carroll, ISBN 9780470938768. Volume two focuses on one of the hottest topics in any field of engineering, carbon dioxide sequestration. *NOW AVAILABLE!*

Other Titles from the Same Authors:

Acid Gas Injection and Carbon Dioxide Sequestration, by John J. Carroll, ISBN 9780470625934. Provides a complete overview and guide on the hot topics of acid gas injection and CO2 sequestration. *NOW AVAILABLE!*

Carbon Dioxide Thermodynamic Properties Handbook 2nd Edition, by Sara Anwar and John J. Carroll, ISBN 9781119083580. This second edition of a contemporary classic is the most comprehensive collection of carbon dioxide (CO2) data ever compiled, with new information added to the revision, a "one stop shop" for any engineer or scientist who works with carbon dioxide in any industry. *NOW AVAILABLE!*